INFORMATION TO USERS

This manuscript has been reproduced from the microfilm master. UMI films the text directly from the original or copy submitted. Thus, some thesis and dissertation copies are in typewriter face, while others may be from any type of computer printer.

The quality of this reproduction is dependent upon the quality of the copy submitted. Broken or indistinct print, colored or poor quality illustrations and photographs, print bleedthrough, substandard margins, and improper alignment can adversely affect reproduction.

In the unlikely event that the author did not send UMI a complete manuscript and there are missing pages, these will be noted. Also, if unauthorized copyright material had to be removed, a note will indicate the deletion.

Oversize materials (e.g., maps, drawings, charts) are reproduced by sectioning the original, beginning at the upper left-hand corner and continuing from left to right in equal sections with small overlaps.

Photographs included in the original manuscript have been reproduced xerographically in this copy. Higher quality 6" x 9" black and white photographic prints are available for any photographs or illustrations appearing in this copy for an additional charge. Contact UMI directly to order.

Bell & Howell Information and Learning
300 North Zeeb Road, Ann Arbor, MI 48106-1346 USA
800-521-0600

The Electronic Structure and Spectroscopy of Rhodium Diatomic Molecules

by

Scott Gregory Fougère
B.Sc., St. Francis Xavier University, 1991
M.Sc., University of Victoria, 1994

A Dissertation Submitted in Partial Fulfillment of the
Requirements for the Degree of

DOCTOR OF PHILOSOPHY

in the Department of Chemistry

We accept this dissertation as conforming
to the required standard

Dr. W. J. Balfour, Supervisor (Department of Chemistry)

Dr. T. E. Gough, Department Member (Department of Chemistry)

Dr. C. X. W. Qian, Department Member (Department of Chemistry)

Dr. G. A. Beer, Outside Member (Department of Physics and Astronomy)

Dr. M. D. Morse, External Examiner (Department of Chemistry, University of Utah)

Supervisor: Dr. Walter J. Balfour

ABSTRACT

This dissertation presents detailed spectroscopic studies of two rhodium diatomic molecular systems, rhodium monocarbide (RhC) and rhodium mononitride (RhN). The spectrum of a third rhodium diatomic species has also been recorded. All evidence suggests that rhodium monoxide (RhO) is the carrier. The rhodium-based molecules have been generated using a laser-ablation/molecular beam source.

Laser-induced fluorescence (LIF) and dispersed fluorescence (DF) techniques have been used to study the visible spectrum of rhodium monocarbide between 530 and 400 nm. $Rh^{12}C/Rh^{13}C$ isotope shifts, DF and excited level lifetime measurements have assisted in classifying the observed bands into three series: the previously known $C^2\Sigma^+ - X^2\Sigma^+$ system and two spin subsystems of a $^2\Pi_i - X^2\Sigma^+$ system.. The C - X system is inherently strong with short excited state lifetimes whereas both components of the $^2\Pi_i - X^2\Sigma^+$ system are very weak and have excited state lifetimes that are very long when compared with the C - X system. With this information, we have employed a time-filtering technique to separate effectively emission from overlapping $^2\Sigma^+$ and $^2\Pi$ levels. The $^2\Pi_{1/2} - X^2\Sigma^+$ component was identified as the B - X system, previously identified as a $^2\Sigma^+ - ^2\Sigma^+$ transition. Many new bands that belong to the $^2\Pi_i - X^2\Sigma^+$ transition have been recorded and analysed. The $^2\Pi_{3/2} - X^2\Sigma^+$ component was not observed previously except through local perturbations in the higher vibrational levels in the C state.

Rhodium mononitride has not been studied in the gas phase prior to this work. Many vibronic bands have been studied in the 700 - 400 nm region using LIF.

Rotational analyses of the stronger bands, excited state lifetime measurements, and $Rh^{14}N/Rh^{15}N$ isotope shifts have enabled identification of three electronic systems: [15.1]1 - $X^1\Sigma^+$, [19.5]0^+ - $X^1\Sigma^+$, and [22.4]0^+ - $X^1\Sigma^+$ with (0,0) bands near 15071, 19489, and 22385 cm^{-1}, respectively. Our assignment of $^1\Sigma^+$ as the symmetry of the ground state agrees with theoretical predictions. Dispersed fluorescence spectra revealed the presence of at least three low-lying electronic states. The three clearly identified states lie at T = 555, 1470, and 3920 cm^{-1} above the ground state. We believe some of these features are likely spin-orbit components of an expected low-lying $^3\Pi$ state and another of these features may be the $^1\Pi$ state that arises from the same electron configuration.

The spectrum of what has been tentatively identified as RhO has been recorded in the 400 - 700 nm region using laser-induced fluorescence. The rhodium monoxide molecules have been produced in the reaction of laser-ablated rhodium metal with oxygen. Molecular orbital arguments suggest that the ground state of RhO be of $^4\Sigma$ symmetry. The bands recorded between 550 and 640 nm appear to have a profile consistent with a $^4\Pi$ - $^4\Sigma$ transition. The high density of lines in several branches near the band centers, however, has prohibited detailed rotational analyses at this time.

Examiners:

Dr. W. J. Balfour, Supervisor (Department of Chemistry)

Dr. T. E. Gough, Department Member (Department of Chemistry)

Dr. C. X. W. Qian, Department Member (Department of Chemistry)

Dr. G. A. Beer, Outside Member (Department of Physics and Astronomy)

Dr. M. D. Morse, External Examiner (Department of Chemistry, University of Utah)

Table of Contents

List of Tables

List of Figures

Acknowledgements

Many people who were of great assistance to me on this journey must be thanked. I would like to express my gratitude to all of you. However, there are certain people who I must single out and say a special "Thank You" to:

Dr. Walter J. Balfour, my supervisor, for granting me the opportunity to study at the University of Victoria. His scientific advice, financial support and enthusiasm for research has made my tenure here a positive experience. Now that I find myself in the academic world, I hope I can follow Dr. Balfour's work ethic and skills as a great teacher who has earned the respect of his peers and his students.

Dr. Charles X. W. Qian for the opportunity to use his lab and for passing on his knowledge of the scientific apparatus used to complete this work. Dr. Qian has also helped me think about my research from a different point of view. His suggestions and comments have proved very useful.

Dr. Chi Zhou and Dr. Jianyang (Bob) Cao, both former members of the Qian group for "showing me the ropes". Without the use of their expertise in general spectroscopic techniques, I certainly would not have been able to produce the spectra that you will see in this dissertation. The discussions we have had about our projects were invaluable.

I would like to thank my other lab mates, both past and present. Past members include Dr. B. J. Shetty, Dr. C. V. V. Prasad, and Mr. Scott J. Rixon. I would like to thank Romey Heuff who is the current member of the Balfour group. Romey took on the task of the RhC deperturbation project and is hopefully furthering the analysis of RhO. Her enthusiasm has kept me on my toes.

I would like to thank Dr. Michael D. Morse (Utah), Dr. Anthony. J. Merer, Dr. Peter F. Bernath, Dr. Ram S. Ram, and Dr. Lester A. Andrews for sharing their, at the time, unpublished results and for their useful discussions.

Dedication

to

Carolyn

whose love and support has made this journey all worth while

I shall be telling this with a sigh
Somewhere ages and ages hence:
Two roads diverged in a wood, and I--
I took the one less traveled by,
And that has made all the difference.

From
The Road Not Taken
by Robert Frost

Chapter 1

Introduction

1.1 Significance of Spectroscopy

Molecular spectroscopy may be defined as the study of the interaction of electromagnetic radiation (light) and matter. Since molecules possess quantized energy levels, they are able to absorb and emit electromagnetic radiation at discrete frequencies. This fact is one of the basic principles of chemistry. One can look at spectroscopy as a way to perform a measurement with electromagnetic radiation as the measuring device.

Spectroscopic studies play an important role in the identification and understanding of molecular structure. Spectroscopy is used both as a tool to probe the structure of molecules as well as to identify new molecules. Electronic spectroscopy yields information about the energy levels in the ground and excited states. Comprehension of a molecule's electronic spectra helps in the understanding of the molecule's physical and chemical properties. Most often, a precise, and sometimes analytical, description of the motion of the electrons (electronic structure) and the nucleus (vibrational and rotational structure) of a molecule can be obtained from a study of the molecule's spectrum. Each time a new molecule is discovered and analyzed, insight into the nature of molecular bonding is enhanced.

Investigation of the molecular spectra of diatomic (and small polyatomic) molecules formed by the reaction of a transition metal (TM) with various ligands such as carbon, nitrogen, hydroxides, or even cyclopentadienyls is an important starting point to creating a foundation that deals with the chemical bonding between a transition metal and another atom (ligand). Comprehension of the "simple" bonding models will aid in the understanding of the way larger organometallic complexes form. To date, several studies

of diatomic molecules involving TMs and main group elements (H, C, N, O, F) have been carried out. Previous studies on the TM monocarbides (M-C) and mononitrides (M-N) will be discussed in the chapters concerning RhC and RhN respectively.

The study of diatomic systems has certainly benefitted from the developments in experimental techniques. Prior to the development of lasers and molecular beam techniques, emission spectra photographed on photographic plates served as the main method of spectroscopic analysis. Conventionally the metals were vaporized in high temperature ovens. The metal vapor was then allowed to react with various gases to form the desired products [1]. Because of the high temperature conditions necessary to produce the metal vapor, the spectra were often complex and the information obtained from the low J rotational levels was often hidden due to the congestion. Laser ablation followed by supersonic expansion of a molecular beam has resulted in much colder spectra that in turn has reduced the spectral congestion [2].

Laser ablation/molecular beam techniques have not solved all of the problems associated with the analyses of spectra associated with TMs. Since transition metals have unpaired *d* electrons, a number of close-lying electronic states can arise from promotion of one of these electrons. Many of these states can interact with each other affecting the appearance of the spectra. These interactions are not limited to TM molecules [3]. Excited states of the TM molecules usually have irregular energy level patterns as a result of such interactions. Such complications can render the analysis of the spectra very difficult.

Detailed *ab initio* calculations on transition metal containing molecules, like

analyses of the experimental data, are also complicated by the interactions of various electronic states. Theoretical calculations have not yet advanced to the point where the calculations can predict accurately all of the experimentally measurable quantities, particularly for transition metal molecules such as rhodium monocarbide (RhC), rhodium mononitride (RhN), and rhodium monoxide (RhO). Even small changes in the methods used to calculate the spectra can have a dramatic effect on the appearance and position of the spectra. One such example is Shim's calculation of the low-lying electronic states of RhN [4]. In that study, three very similar techniques produced three very different orderings and energies of the electronic states of RhN. Nevertheless, *ab initio* calculations, in conjunction with the various experimental techniques, have proved very useful in solving molecular spectra.

1.2. Transition Metals

Since this dissertation involves the spectroscopy and electronic structure of rhodium based diatomic molecules, a background to rhodium should be given. Rhodium is classified as a transition element. "Transition elements" can be described as three series of elements that arise from the filling of the 3*d*, 4*d*, and 5*d* shells [5] with electrons. The *d*-block elements, as they are sometime referred to, follow the alkaline earth metals and precede the *p*-block elements in the periodic table (group 3 to 12)[1], hence, the alternative name "transition." Because all the elements of the *d*-block series are metallic,

[1] The notation used is based on the IUPAC notation [6]. The traditional notation would be group IIIA to VIIIA, IB and IIB. The Chemical Abstracts Service notation [6] is IIIB to VIIIB, IB and IIB.

these elements became known as the transition metals (TM). The first nine transition elements (scandium to copper) of the first row (3*d*) with incomplete 3*d* orbitals form the *first transition series*. The second row elements (yttrium to silver) form the 4*d* (*second*) *transition series* and the *third transition series* (5*d*) contain, across the row, the elements lanthanum to gold. Though the group 12 elements (zinc, cadmium, and mercury) are considered transition metals, they are excluded from the transition series due to their filled *d* orbitals [5]. Some texts adopt a broader definition to include the partly filled *f* and *d* orbitals (the lanthanides and actinides). The lanthanides and actinides are known as the "inner-transition elements" and interrupt Periods 6 and 7 respectively. However, for this dissertation, the trends and properties of the lanthanides and actinides will not be considered.

Although each group of transition metals, and for that matter each metal, has its own properties, the transition metals exhibit many common characteristics [7]. The most common property, as mentioned above, is that these elements are all metals. The early elements of the transition series resemble the alkaline earth metals while those found late in the series have similar characteristics to the early *p*-block elements. Some of these common properties are:

1. The TMs are all hard and strong. They are usually quite lustrous.
2. The metals have high melting and boiling points (> 1000 K).
3. They have high thermal and electrical conductivities.
4. Most TMs exhibit numerous oxidation (valence) states where their ions and compounds display a variety of colors.

5. TM have an inclination to form coordination compounds with Lewis bases.

6. Because of the partially filled orbitals, the elements form some paramagnetic compounds that may exhibit magnetic properties.

1.2. A Little About Rhodium...

The discovery of rhodium occurred almost two hundred years ago. In 1803, W. H. Wollaston [5] recognized that a black residue remained after crude platinum was dissolved in aqua regia. The isolated residue was later identified as a new element. Wollaston named the element rhodium for the Greek word *rhodon* (rose) as a consequence of the rose-red color that appeared in the aqueous solutions of its salts. Rhodium is very rare, comprising less than 0.0004 ppm of the earth's crust [5, 8] and is usually found in the same location as other platinum metals. The earth's main sources of rhodium are the nickel-copper sulfide ores (Rh composition ~ 0.1 %) mined in South Africa and Sudbury, Canada. Rhodium is separated from the ores by a complex procedure similar to that used to separate other platinum metals from platinum concentrate [5, 8].

Rhodium, like the other platinum metals, is a silvery-white lustrous metal. Its atomic number is 45 and relative atomic mass is 102.9055. The melting and boiling points of rhodium are 2236 and 3970 K respectively. Like the other transition metals, rhodium has high thermal and electrical conductivities. As for acid/base properties, rhodium is considered amphoteric. A summary of some physical and chemical properties associated with elemental rhodium is shown in Table 1.1.

Table. 1.1. Some physical and chemical properties of elemental rhodium [5, 9].

Rhodium (Rh)	
Atomic Number	45
Number of Naturally Occurring Isotopes	1
Relative Atomic Mass	102.9055
Electronic Configuration	$[Kr]4d^{8}5s^{1}$
Atomic Radius (nm)	0.134
Atomic Volume (cm^3/mol)	8.30
Density (g/cm^3 at 300 K)	12.39
Electronegativity	2.28
1st Ionization Potential (kJ/mol) (eV)	719.66 7.46
Melting Point (K)	2236
Boiling Point (K)	3970
Heat of Vaporization (kJ/mol)	495.39
Heat of Fusion (kJ/mol)	21.76
Specific Heat Capacity ($Jg^{-1}K^{-1}$)	0.242
Thermal Conductivity ($Wcm^{-1}K^{-1}$ at 298.2 K)	1.50
Atomic Crystal Packing	face-centered cubic (fcc)

Rhodium, next to platinum, is one of the most active elements in the area of catalysis. It is not surprising then to see that rhodium has a variety of uses in the catalysis industry. The automobile industry employs rhodium to control exhaust emissions [5]. Rhodium has found other industrial applications. Some examples include the manufacture of glass and ammonia synthesis. Organometallic uses of rhodium include the replacement of ligands in phosphine complexes [$(Ph_3P)_3RhCl$], otherwise known as

Wilkinson's catalyst [10], hydrogenation [5, 7], and hydroformylation reactions [5, 7].

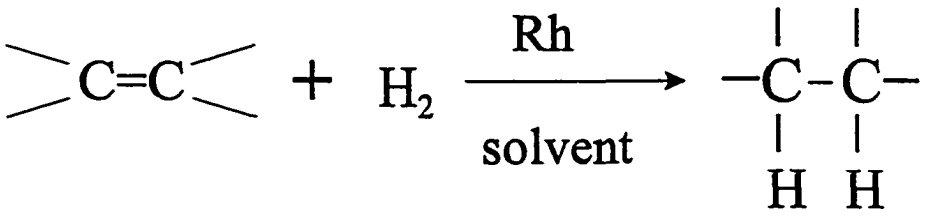

Hydrogenation

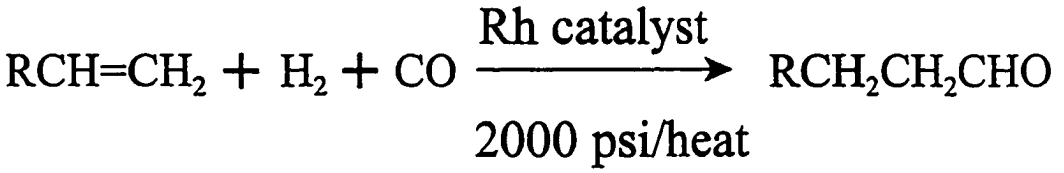

Hydroformylation

Rhodium has also found uses in medicinal chemistry [11]. Rhodium-cobalt alloys have found uses in magnetic (EMF) therapy. The extent and nature of this process has yet to be scientifically determined but the market for such remedies has flourished in the last few years.

Rhodium, as well as the other transition metals, is special in that the energy gaps between the metal *nd* and (n+1)*s* orbitals are small and that many TMs have unpaired electrons. These unpaired electrons allow the metal to participate as a catalyst in chemical reactions by forming activated complexes with lower potential energies than if no metal were present. Consequently, many transition metals are used as catalysts.

Transition metal containing molecules are very important in astrophysics. Astrophysicists and chemists want to know about the mechanisms that form the elements and what factors control their distribution in the earth (universe). The process by which the elements are formed is called *nucleosynthesis*. The earth's crust has been the major contributor to what is presently known. To attempt to explain the origin of the chemical elements, scientists have turned their attention to the "heavens." They believe exploration of the solar system and beyond is one of the keys to discovering the formation of the earth, stars and the elements found in them. The most direct insight in the analyses of solar system's composition has come from the analyses of meteorites [4].

Iron is one of the most abundant transition metals found in the solar system. The ^{56}Fe nucleus is the most stable nucleus in terms of binding energy per nucleon, so that it is the largest element that can be formed by fusion. This makes iron a prime candidate for extraterrestrial spectroscopic research [12-15]. Elements larger than iron require energy (*i.e.*, neutron capture and radioactive decay) to promote further element building.

Although the terrestrial abundance of rhodium is very minute, there is the possibility that rhodium-based molecules exist extraterrestrially. With 29 transition elements known to occur naturally on earth, it is hard to believe that these elements are not found elsewhere in the universe. Transition metal diatomic molecules such as TiO and VO and small metal polyatomic molecules such as MgCN and MgNC [16,17] have been discovered in the spectra of stars and gas envelopes of stellar media.

Even more important to the search for new molecules in space is the development of a spectroscopic database of metal containing species that can be used as a frame of

reference for the spectroscopic analyses. Prior to the mid 1990s, only a few examples of TM diatomic monocarbides and mononitrides have been identified in the laboratory domain. However, over the last few years, this number has now increased such that over half the transition metal monocarbides and mononitrides (chapters 4 and 5) have been spectroscopically characterized. This has formed a solid foundation for the spectroscopic database mentioned above. The steady increase in identification of TM-containing diatomic systems in conjunction with advancements made in search techniques should inspire further exploration for these types of molecules in various stellar media. The spectroscopic analysis carried out by the *Hubble Space Telescope* [18] is just one example of this inspiration/desire to find out more about the composition of the universe.

Figure 1.1 shows the principal uses of rhodium in the world today.

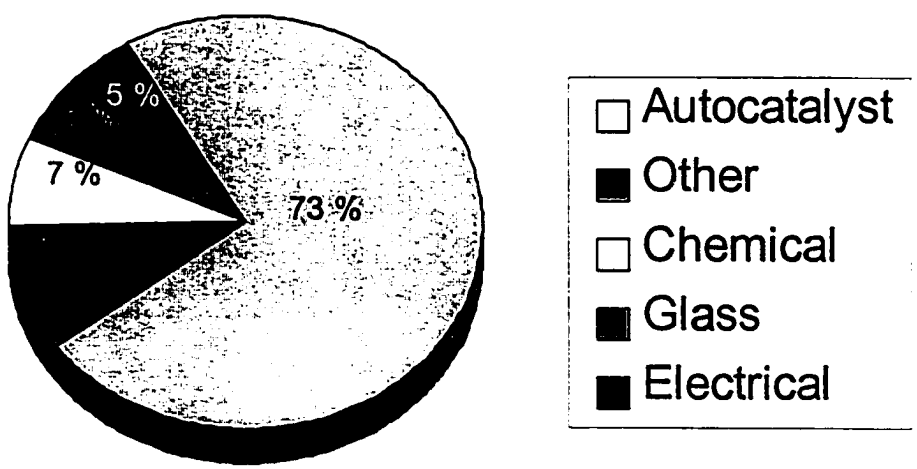

Fig. 1.1. The principal uses of rhodium in the western world (adapted from reference [5]).

With a few of the applications of transition metals (specifically Rh) mentioned, a comprehension of the bonding between the metal atom and other atoms/compounds is essential in understanding the catalytic reactions and organometallic reactions. This understanding has presented considerable challenges to experimental and theoretical chemists. Knowledge of the bonding in simple diatomic systems should provide a solid foundation in understanding the bonding in larger systems.

1.4. Outline and Goals of this Project

Spectroscopic analyses of transition metal diatomic molecules has been the focus of research in Dr. Balfour's group since 1974 [19]. Our interest in rhodium diatomic species stemmed from a visit to the laboratory of Dr. Albin Lagervist and Dr. Rosemary Scullman in 1975. Dr. Scullman was first to report works on diatomic transition metal monocarbides in 1965 when she published the spectra of PtC [20]. A year later, Lagerqvist and Scullman (LS) published their work on the RhC species [1]. The spectrum of what was believed to be RhO was photographed around that time but no analysis was done. Copies of these spectra were given to Dr. Balfour to attempt an analysis. After completion of my M.Sc. thesis, I became involved in the study of RhO. The spectrum was very congested. With the ability to record the laser induced fluorescence spectra of jet-cooled molecules, we attempted to record the spectrum of RhO to simplify the analysis of the molecule.

With a rhodium rod in our possession, we wanted to record the spectrum of RhC to calibrate the spectra of other transition metal monocarbides produced in our lab since

the exact positions of RhC bands were already reported. To our surprise, spectral impurities (extra bands) appeared in the spectrum of RhC and these were later identified to be RhN. At the time, this was the first identification of a mononitride. Since methane and ammonia were used to react with rhodium to produce RhC and RhN respectively, the molecule RhH was also produced as a side product in the ablation process.

Hopefully, the work presented in this dissertation will lead to a deeper understanding of transition metal containing diatomic molecules. The importance of rhodium in industry, nature, and astrophysics warrants the detailed structural analysis of rhodium-containing molecules presented in this work. Spectral identification and characterization of three rhodium-based diatomic molecules will be presented. In chapter 2, the basic theory behind diatomic molecules will be presented followed by a description of the experimental apparatus and methods (chapter 3) used to obtain the spectra of the Rh-X molecules. In chapter 4, the electronic spectrum and structure of rhodium monocarbide (RhC) will be reexamined in the light of experimental evidence of new transitions identified in our work on rhodium diatomic species. Chapter 5, will discuss the spectrum and structure of rhodium mononitride (RhN). The spectra of rhodium oxide (RhO), to date, will be presented in chapter 6. Finally in Chapter 7, a global look at the bonding in rhodium-based diatomic species will be presented.

Chapter 2

Basic Theories of the Diatomic Molecule

2.1. The Electromagnetic Spectrum and Molecular Processes

All spectra arise from transitions between energy states and molecular spectroscopy is concerned with the change in energy that occurs when a molecule interacts with (absorbs or emits) discrete amounts of electromagnetic radiation. Electromagnetic radiation covers a range of frequencies called the electromagnetic spectrum. Regions of the spectrum (Fig. 2.1) are classified according to the manner in which the radiation is generated or detected. The associated molecular processes vary according to the region studied. A summary of the interactions between the incident radiation and the type of change the molecule undergoes upon "excitation" is included in Fig. 2.1. The electromagnetic radiation used in laser induced fluorescence and most forms of electronic spectroscopy lies in the visible and ultraviolet regions.

Analysis of a molecule's electronic spectrum leads to information about electronic structure and the vibrational and rotational motions of the nuclei, *i.e.*, the study of electronic spectra provides important information about a molecule's geometry and the nature of its electronic structure.

2.2. Electronic Structure of Diatomic Molecules

(i) Determination of Molecular States of Diatomic Molecules

Before classification and discussion of the molecular states involved in the transitions studied in this dissertation, the terms and notation associated with the states must be mentioned. A brief overview will be given in this section. For detailed descriptions of the terms and theory associated with the classifications of electronic

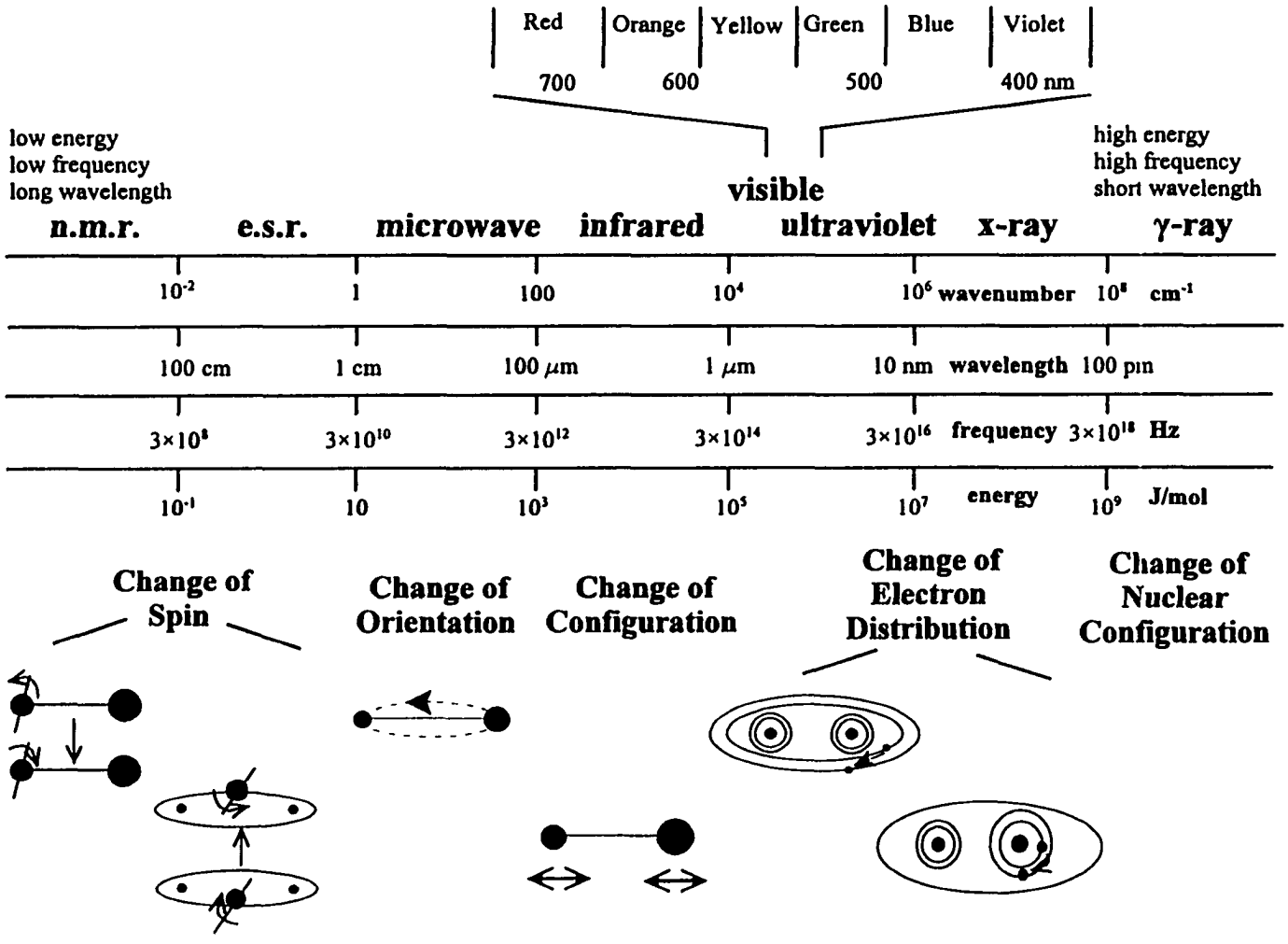

Fig. 2.1 The regions of the electromagnetic spectrum and the molecular processes associated with each region of the spectrum.

spectra, the reader can refer to references [21 to 26].

Molecular state classifications can be traced back to Niels Bohr. Bohr, in 1913, first proposed a theory for the electronic structure of the hydrogen atom. He suggested that the electron in hydrogen could only exist in certain orbits and that the electron had a definite energy based on the energy level which it was in. Later, quantum theory showed that the energy of an electron in an orbital could be characterized by three quantum numbers: n (principal quantum number), l (orbital quantum number), and m_l (magnetic quantum number). The orbital and spin angular momenta of the electrons in atoms couple via their magnetic moments.

The same principle applies to electrons in diatomic molecules [21]. The electrons in a molecule possess angular momenta due to both orbital motions and their electron spins. The total orbital angular momentum (L) is represented by the vector sum of all the individual electron orbital angular momenta.

$$\bar{L} = \sum_i \bar{l}_i, \qquad \left|\bar{L}\right| = \sqrt{L(L+1)}\hbar \tag{2.1}$$

As the symmetry is reduced (from spherical to axial) in a diatomic molecule, the electrons with orbital angular momentum, begin to precess about the internuclear axis (Fig. 2.2). With increasing field (magnetic) strength, L precesses faster about the axis. This means that l is no longer a good quantum number, but the projection of l onto the internuclear axis (m_l) is. In the case of a multiple electron system, the vector sum of m_l becomes M_L and can have values of

$$M_L = L, L\text{-}1, L\text{-}2, \ldots. -L \tag{2.2}$$

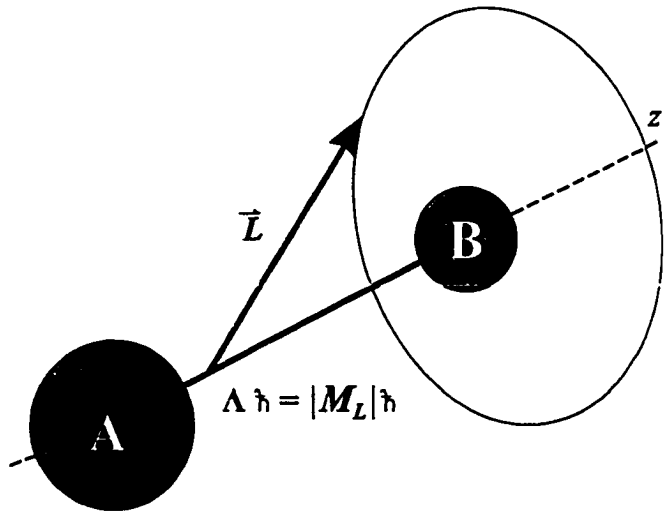

Fig. 2.2. The precession of orbital angular momentum (L) about the internuclear axis.

From equation 2.2, M_L can take on values of $+L$ to $-L$. The sign of M_L is determined by the direction of motion about the axis (clockwise/ counter-clockwise). The direction of the motion about the axis does not affect the energy, so there is a degeneracy for states with the same M_L but of opposite signs. It is therefore more useful to label the electronic states in terms of M_L instead of L. It is common convention to denote the projection along the internuclear axis by λ for a single electron and Λ for many electrons such that

$$|m_l| = \lambda \quad \text{and} \quad |M_L| = \Lambda \tag{2.3}.$$

For a given value of L, the quantum number Λ can have the values

$$\Lambda = 0, 1, 2, 3, ... L \tag{2.4}.$$

Capital Greek letters designate the molecular states of diatomic molecules such that when $\Lambda = 0, 1, 2, 3, ...$, we have Σ, Π, Δ, Φ, ...states.

Multiplet structures are a result of more than one unpaired electron in a molecule (or atom). Similar to the total orbital angular momentum, the resultant spin of the

electrons is the vector sum of the spins of the individual electrons:

$$\vec{S} = \sum_i \vec{s}_i, \qquad \left|\vec{S}\right| = \sqrt{S(S+1)}\hbar \tag{2.5}$$

When the situation arises that $\Lambda \neq 0$, a magnetic field in the direction of the internuclear axis results from the orbital motion of the electrons. This motion causes a precession of S about the direction of the field with a constant component of $M_S\hbar$. With molecules, the Greek letter Σ represents M_S ($M_S = \Sigma$). The quantum number Σ can have $2S + 1$ values:

$$\Sigma = S, S - 1, S - 2, \ldots -S \tag{2.6}$$

The quantum number Ω denotes the total electronic angular momentum about the internuclear axis. The magnitude of the component of the total electronic angular momentum about the axis is given by $\Omega\hbar$, where

$$\Omega = \Lambda + \Sigma \tag{2.7}$$

and

$$\Omega = (\Lambda + S), (\Lambda + S - 1), (\Lambda + S - 2), \ldots(\Lambda - S) \tag{2.8}$$

Integral or half-integral values can result for Ω. This definition of Ω is only valid for $\Lambda > 0$ since the traditional usage is to set $\Omega = |M_s|$ for Σ states.

With this information, the notation (terms) for the electronic states of diatomic molecules can be presented. Similar to the description of atomic states ($^{2S+1}L_J$, the term symbol for a molecular state is written

$$^{2S+1}\Lambda_\Omega \tag{2.9}$$

with S, Λ, and Ω described earlier in the text.

(ii) Molecules from Atoms... Determining the Parentage of Molecular States from Electron Configurations

A diatomic molecule is formed by bringing two atoms together. Each of the two atoms is in a particular atomic state and linear combinations of the atomic orbitals (AOs) give the molecular orbitals (MOs) of the diatomic molecule.

Theoretically, there are three possible models in which one can construct the molecular states of diatomic molecules from the nuclei and electrons of atoms: the "separated atom," "united atom," and the "building-up" principles. Only a brief summary will be included in this work since Herzberg [21], and others [25, 26], have described these models in detail. Only heteronuclear diatomics need be considered for our work on rhodium based diatomic species.

In the separated atom approach, two individual atoms with their own values of L and S can be brought together from an infinite separation to form the diatomic molecule. In this process a molecular axis is formed (z of Fig. 2.2). From the combination of all the possible values of $\sum M_{Li}$, all the values of Λ can be obtained. The multiplicity of the particular molecular state is determined from the vector sum of the spins of the individual atoms. As an example, consider the coupling of one atom with $L_A = 0$ (S atomic state) and the second atom with $L_B = 1$ (P atomic state). The values of M_L are 0 for atom A and $0, \pm 1$ for atom B. The resultant value of $\Lambda = 0$ gives a Σ state and the values of $\Lambda = \pm 1$ correspond to the degenerate components of a Π molecular state.

In a united atom approach, an atom with appropriate nuclear charge and proper number of electrons is hypothetically split. The spherical symmetry of the united atom is

lost. At this point, the direction of the molecular axis can be defined and we can measure the component of the orbital angular momentum along this axis. The magnitude of the component M_L is given by equation 2.2. With regards to spin, the value of S remains the same as in the atomic state from which the molecular state results. This model is used to describe diatomic hydrides. Hydrides can be thought to form from the abstraction of a proton from a large united atom [25] since the hydrogen atom is so small that it is considered a small disturbance.

The "building-up" model has the atoms at a fixed distance and the molecular orbitals are constructed from the linear combinations of the atomic orbitals of the atoms (known as the LCAO method- *linear combination of atomic orbitals*). Since the atoms have specific values of n and l, we can use these quantum numbers to distinguish between the atomic orbitals. The electrons are placed into the molecular orbitals. The filling of the MOs leads to a electron configuration from which the possible molecular states can be derived. The values of Λ are determined as the absolute value of the sum of the individual orbital angular momenta, m_{li}. The multiplicities of the molecular states are determined in a similar manner. For any closed shell system ($...\sigma^2$, $...\pi^4$, $...\delta^4$), a $^1\Sigma^+$ results.

The relative energies of the MOs vary in different molecules and are dependent upon the energies of the atomic orbitals and the degree of mixing among the atomic orbitals. For most diatomic molecules studied today this method is used qualitatively to determine the possible electronic structures of their ground states and excited states. Specific descriptions using this method as it applies to the ground and excited states of

RhC and RhN will be discussed in their respective chapters.

2.3. The Structure of Electronic Transitions

The Born-Oppenheimer approximation allows for the separation of the motion of the electrons from the motion of the nuclei, based on the disparity in the masses of the electron and the nuclei in the molecule, such that:

$$\Psi_{total} = \psi_{electronic} \cdot \psi_{vibrational} \cdot \psi_{rotational} \qquad (2.10).$$

The total energy, then, to a very good approximation, may be given by the sum of the electronic (E_e), vibrational (E_v), and rotational (E_r) energies:

$$E_{total} = E_{electronic} + E_{vibrational} + E_{rotational} \qquad (2.11).$$

Each term for a given electronic state can be written as:

$$T = T_e + G(v) + F(J) \qquad (2.12).$$

The symbol T is called the *term value* of an energy level and G(v) and F(J) are the vibrational and rotational term values of the respective energy levels with quantum numbers v and J. The energy of the transitions is written as

$$E/hc \text{ (in } cm^{-1}) = \nu = T' - T''$$

$$= (T_e' - T_e'') + [G'(v') - G''(v'')] + [F'(J') - F''(J'')] \qquad (2.13)$$

$$= \nu_{electronic} + \nu_{vibrational} + \nu_{rotational} \qquad (2.14).$$

The symbols (') and (") refer to quantities/quantum numbers of the upper state and ground state respectively. The quantity $T_e' - T_e''$ is called the system origin and is described by the term $\nu_{electronic}$. The band origin (ν_0) is given by the term

$$\nu_0 = \nu_{electronic} + \nu_{vibrational} \qquad (2.15)$$

with

$$\nu_{vibrational} = G'(v') - G''(v'') \qquad (2.16).$$

(i) Vibrational Energy Levels

The vibrational term of equation 2.12 should be described in further detail. A vibration can be treated as the expansion and compression of a "spring-like" structure [22]. The oscillation of the nuclei occurs about an equilibrium position (r_e). For a small change in bond distance ($r-r_e$), the potential energy can be expressed by the first few terms of a Taylor expansion series. The shape of the potential is best described by a parabolic-like curve and is approximated by the second order derivative such that

$$U(r) = \tfrac{1}{2}k(r-r_e)^2, \text{ where } k = \{d^2U/d(r-r_e)^2\}_0 \qquad (2.17)$$

where U(r) is the potential energy and k is the *force constant* of the bond which, in turn, determines the shape of the potential well. The subscript "0" indicates that the derivative is evaluated at the equilibrium bond length. The energy (in cm^{-1}) for such a harmonic oscillator can be described by

$$G_{vib} = \omega_{osc}(v + \tfrac{1}{2}), \quad v = 0, 1, 2, 3, \ldots \qquad (2.18)$$

where v is the vibrational quantum number. The vibrational frequency (ω) is related to the force constant k:

$$\omega_{osc} = (2\pi c)^{-1}(k/\mu)^{1/2} \quad cm^{-1} \qquad (2.19)$$

where μ is the reduced mass of the diatomic molecule and c is the speed of light.

Real molecules do not exactly follow the simplistic nature of the harmonic oscillator. As the nuclei approach each other ($r \rightarrow 0$), Coulombic repulsions of the nuclei

cause the potential curve to rise more steeply than in the harmonic oscillator. This repulsive force is less significant as $r \rightarrow \infty$ resulting in a curve that is not as steep. The departure from the ideal harmonic behavior is termed anharmonicity. Generally, the energy levels are no longer equally spaced but get closer as v increases. The vibrational energy, if anharmonicity is taken into account, is described by equation 2.20:

$$G_{vib} = \omega_e(v + \tfrac{1}{2}) - \omega_e x_e(v + \tfrac{1}{2})^2 + \omega_e y_e(v + \tfrac{1}{2})^3 + \ldots \qquad (2.20).$$

with x_e known as the first order anharmonicity factor and y_e as the second order anharmonicity factor. The spacing between adjacent vibrational levels in a given electronic state is then given by

$$\Delta G(v + \tfrac{1}{2}) = G(v+1) - G(v) = \omega_e - 2\omega_e x_e - 2\omega_e x_e v + \ldots \qquad (2.21).$$

A picture of the anharmonic potential curve is shown in Fig. 2.3. The wavenumber ($\nu_{v'v''}$) of a vibrational transition ($v' - v''$) is

$$\nu_{v'v''} = \nu_e + \omega_e'(v' + \tfrac{1}{2}) - \omega_e' x_e'(v' + \tfrac{1}{2})^2 + \ldots - \omega_e''(v'' + \tfrac{1}{2}) + \omega_e'' x_e''(v'' + \tfrac{1}{2})^2 - \ldots \quad (2.22).$$

(ii) Vibrational Isotope Effect

For diatomic molecules in which at least one of the nuclei has more than one naturally occurring isotope, the vibrational frequencies of the different isotopic molecules will be different. If a heavier reduced mass is used in equation 2.19, the isotopic molecule will have a smaller vibrational frequency. Any quantity associated with the isotopic molecule is denoted by an italicized superscript i (^{i}). The vibrational frequencies for two isotopomers molecules are related by

$$\frac{\omega_{osc}^{i}}{\omega_{osc}} = \sqrt{\frac{\mu}{\mu^{i}}} = \rho \qquad (2.23)$$

The vibrational constants for the isotopomer and "ordinary" molecule are related such that:

$$\omega_e^i = \rho\omega_e \tag{2.24}$$

$$\omega_e^i x_e^i = \rho^2 \omega_e x_e \tag{2.25}.$$

For the isotopomer the vibrational energy can be given by a slight modification of equation 2.20 such that:

$$G_{vib} = \rho\omega_e(v + ½) - \rho^2\omega_e x_e(v + ½)^2 + \rho^3\omega_e y_e(v + ½)^3 + \ldots \tag{2.26}.$$

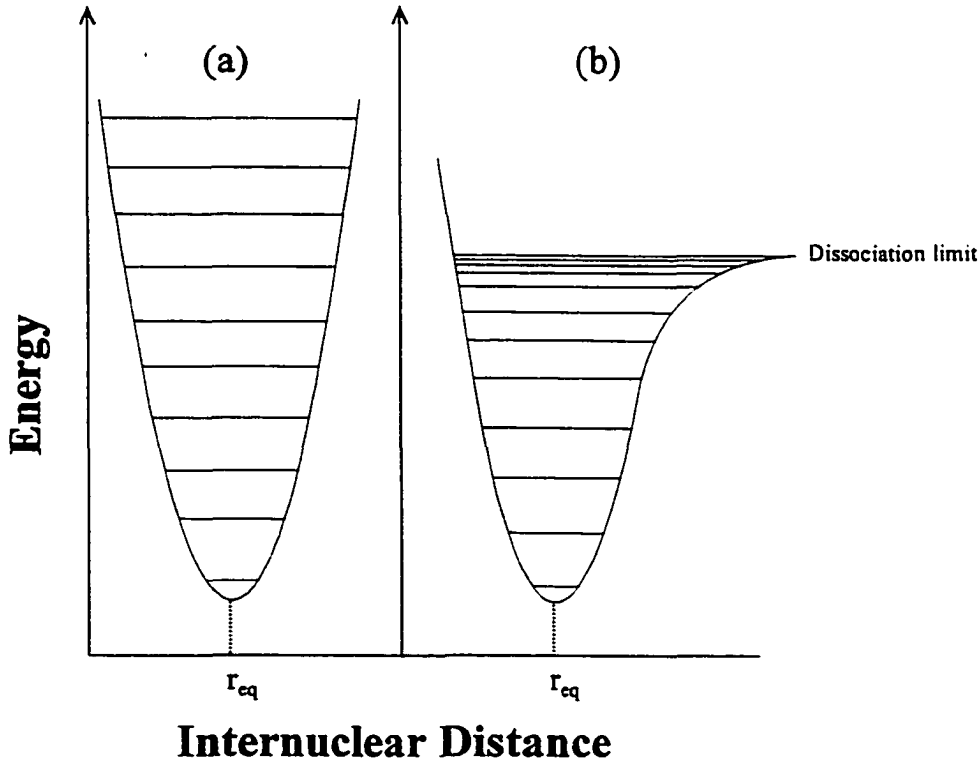

Fig. 2.3. Diatomic oscillator potentials. In (a), the shape of a harmonic oscillator potential for a diatomic is shown and in (b), the shape of the anharmonic potential.

The vibrational isotope shift ($\Delta\nu$) is

$$\Delta\nu = \nu - \nu' = (1-\rho)[\omega_e'(v' + \tfrac{1}{2}) - \omega_e''(v'' + \tfrac{1}{2})]$$
$$- (1-\rho^2)[\omega_e'x_e'(v' + \tfrac{1}{2})^2 - \omega_e''x_e''(v'' + \tfrac{1}{2})^2]$$
$$+ \text{higher order terms} \qquad (2.27).$$

The vibrational isotope shift is particularly useful in the assignment of vibrational quantum numbers to a band when the spectra of two isotopomers are simultaneously recorded.

(iii) Rotational Energy Levels

In the previous paragraphs the vibrational contribution to the overall energy was discussed while the rotation of the diatomic molecule was neglected. At a first approximation, the energy of the rotations and vibrations of a diatomic molecule can be treated independently (equation 2.14).

The simplest model used to describe a rotating molecule is to consider that the bond length (r) is constant . The energy of rotation for the diatomic rigid rotor is quantized such that the allowed energy levels (for a $^1\Sigma^+$ state) are given by the expression:

$$E_r = \frac{\hbar^2}{2I}J(J+1) = \frac{\hbar^2}{2\mu r^2}J(J+1) = BJ(J+1), J = 0,1,2,... \qquad (2.28).$$

where I is the moment of inertia and the rotational constant B, in units of cm^{-1}, is

$$B = \frac{h}{8\pi^2 c\mu r^2}, \quad I = \mu r^2 \qquad (2.29)$$

and J is the rotational quantum number. In practice the chemical bond is not rigid [23]

and higher order terms need to be added to the expression in equation 2.28 such that

$$F(J) = BJ(J+1) - DJ^2(J+1)^2 + \ldots \qquad (2.30)$$

where D represents the centrifugal distortion constant and accounts for the stretching of the bond as the speed of rotation increases (increasing *J*).

With F(*J*) so-defined, the rotational component of equation 2.13 can now be written as

$$\nu_{\text{rotational}} = F'(J') - F''(J'') = B'J'(J'+1) - B''J''(J''+1) + \ldots \qquad (2.31).$$

As the bond stretches with vibration, the change in the moment of inertia results in a change of the rotational constant, *B*. The *B* value in a particular vibrational level will be somewhat smaller than the equilibrium rotational constant B_e. The dependence of the rotational constant on the vibrational quantum number is expressed, to a first approximation, as a power series,

$$B_v = B_e - \alpha_e(v + \tfrac{1}{2}) + \text{higher order terms} \ldots \qquad (2.32)$$

where B_v is the rotational constant in the v^{th} vibrational and α_e is a constant that accounts for the vibration-rotation interaction.

(iv) Rotational Isotope Effect

The rotational constant *B* in the rotational term values will be different in two isotopomers since they have different reduced masses. The *B* value for the isotopomer will be

$$B^i = \rho^2 B \qquad (2.33).$$

2.4. Combination Differences

When one vibronic band of a molecule has been rotationally analyzed, the identification and rotational assignments of other bands which share either a common upper state or a common lower state is facilitated by the use of combination differences [21]. The differences in line positions are very useful in that they depend only on the upper or lower state constants.

For the lower state combination differences (Fig. 2.4), the emissions share a common upper state level such that

$$\begin{aligned}\Delta_2 F''(J) &= \nu_R(J-1) - \nu_P(J+1) = F_v''(J-1) - F_v''(J+1) \\ &= B''(J+1)(J+2) - B''(J-1)(J) \\ &= 4B''(J+\tfrac{1}{2})\end{aligned} \tag{2.34}.$$

The upper state combination differences are determined in a similar manner and are given by

$$\Delta_2 F'(J) = 4B'(J+\tfrac{1}{2}) \tag{2.35}.$$

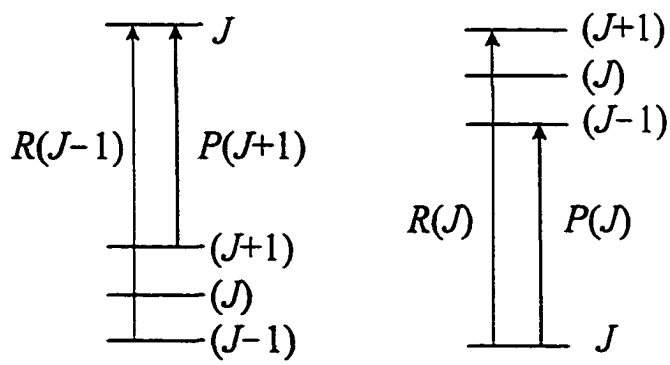

Fig. 2.4. $\Delta_2 F$ ground state and excited state combination differences.

A plot of $\Delta_2 F$ against J is linear at low J but may curve slightly at high J. Deviation from linear behavior for the combination differences is due to centrifugal distortion (D). In our studies D is on the order of 10^{-6} cm^{-1} or smaller. Limitations in experimental resolution prohibit accurate determinations of D. In "hotter" spectra, where there are many J values, D can be determined from a plot of $\Delta_2 F/(J + ½)$ versus $(J + ½)^2$. The intercept of such a graph yields $4B_v$ and the slope is $8D_v$.

Once the combination differences for a specific band are determined, the search for other bands with identical upper or lower combination differences can take place in order to aid in vibronic assignments. With the rotational assignments made for the original band, the rotational assignments for the "related" bands are made unambiguously. This applies to transitions associated with $\Delta\Omega = 0, \pm 1$. Transitions with $\Delta\Omega = \pm 1$ also have combination relations involving the Q branch.

For the ground state we have

$$\begin{aligned} R(J) - Q(J+1) &\approx Q(J) - P(J+1) \\ &= F_v''(J+1) - F_v''(J) = \Delta_1 F'' \end{aligned} \tag{2.36}$$

while in the excited state

$$\begin{aligned} R(J) - Q(J) &\approx Q(J+1) - P(J+1) \\ &= F_v'(J+1) - F_v'(J) = \Delta_1 F' \end{aligned} \tag{2.37}.$$

Equations 2.36 and 2.37 give the separation between successive rotational levels. Since the Q branch goes to a Λ component of a Π state different from the R and P branches, the Q branch lines will have a slightly different upper state than the R and P branches (see

Fig. 2.5) and hence the combination relations in equations 2.36 and 2.37 may not hold exactly. The deviations are called "combination defects" and are a result of Λ-type doubling. The phenomenon of Λ-type doubling is described further on in the text.

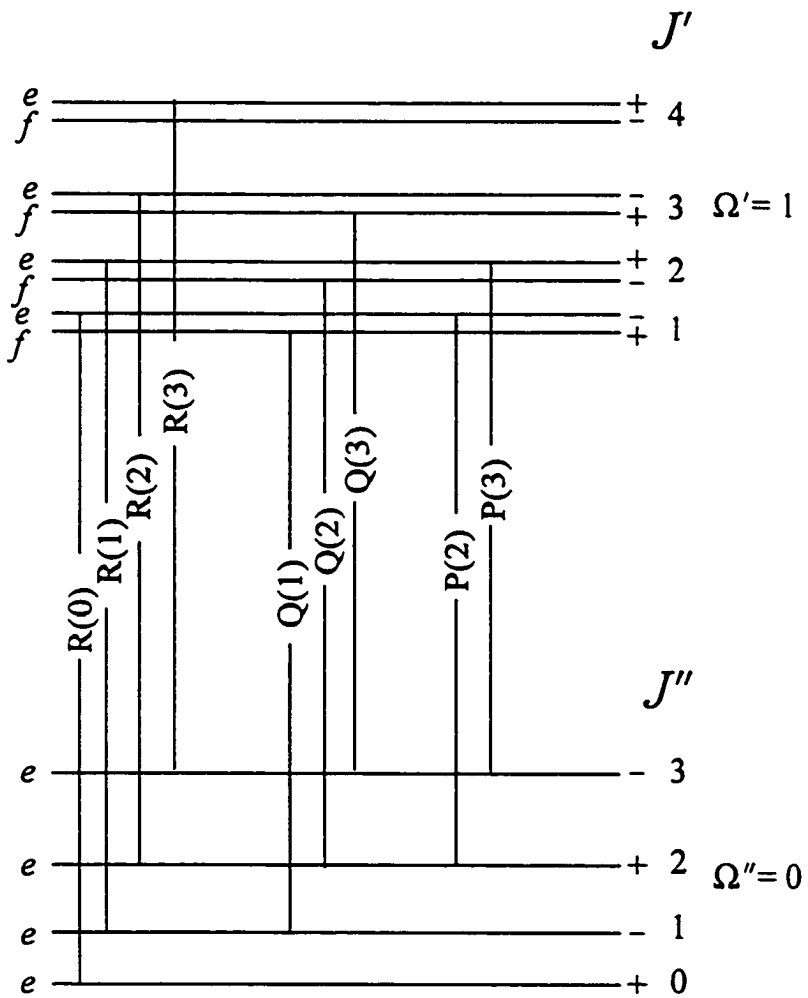

Fig. 2.5. A schematic energy level diagram showing the first few rotational lines of all three branches of a vibronic band of an $\Omega' = 1 - \Omega'' = 0^+$ transition. The $\Lambda(\Omega)$ -type doubling in the upper state is greatly exaggerated. The +/− and *e/f* labels refer to the parity of each rotational level [21].

2.5. Selection Rules for Electric Dipole Transitions

The interaction between electromagnetic radiation (photons) and diatomic molecules causes transitions to occur between electronic states of the molecular system. Excitations will occur if the energy of the photon matches the energy of the gap between the states of the transition:

$$h\nu \text{ (photon)} = E_{\text{excited state}} - E_{\text{ground state}} \qquad (2.38)$$

In a process similar to absorption, the molecule in an excited state can emit to the ground state (or any lower state) by emitting a photon to carry away the excess energy. The observable molecular spectra will depend on which states couple through electromagnetic radiation. Certain requirements must be met in order for molecular states to couple. These requirements are known as *selection rules* and they arise from symmetry considerations and the requirements for conservation of angular momentum during the absorption or emission process. If the selection rules are known, quantum numbers and symmetries of the states can be determined from the spectra. For an electronic transition between two states to occur, the selection rules dictate that the transition moment between the two states is nonzero. Only the selection rules for heteronuclear diatomics need be mentioned as we are only concerned with molecules of this type. A summary of the important selection rules is given in Table 2.1.

Table 2.1. General selection rules for heteronuclear diatomic molecules.

General Selection Rules:	
total angular momentum:	$\Delta J = 0, \pm 1$ but $J = 0 \nleftrightarrow J = 0$
molecular symmetry wavefunctions for a transition between rotational levels	$+ \leftrightarrow -$ but $+ \nleftrightarrow +$ and/or $- \nleftrightarrow -$
Hund's case (a) and case (b)	
$\Delta\Lambda = 0, \pm 1 \quad \Delta S = 0$	
for $\Sigma - \Sigma$ transitions: $^1\Sigma^+ \leftrightarrow {}^1\Sigma^+$, $^1\Sigma^- \leftrightarrow {}^1\Sigma^-$ but $^1\Sigma^+ \nleftrightarrow {}^1\Sigma^-$	
Hund's case (a)	
$\Delta\Sigma = 0 \quad \Delta\Omega = 0, \pm 1 \quad \Omega = 0 \nleftrightarrow \Omega = 0$ for $\Delta J = 0$	
Hund's case (b)	
$\Delta R = 0, \pm 1$	
for $\Sigma - \Sigma$ transitions $\Delta R \neq 0$	
Hund's case (c)	
$\Delta\Omega = 0, \pm 1$; $\Delta J = 0, \pm 1$, $J' = 0 \nleftrightarrow J'' = 0$	
$0^+ \leftrightarrow 0^+$, $0^- \leftrightarrow 0^-$ but $0^+ \nleftrightarrow 0^-$	
i.e., for e/f parities:	
$\Delta J = \pm 1$: $e \leftrightarrow e$, $f \leftrightarrow f$, $e \nleftrightarrow f$	
$\Delta J = 0$: $e \leftrightarrow f$, $f \nleftrightarrow f$, $e \nleftrightarrow e$	

2.6. Vibronic Transitions ... The Franck- Condon Principle

Equation (2.13) represents the energy of the possible vibronic transitions that can occur between two electronic states. Diatomic vibrational transitions that accompany

electronic transitions (called *vibronic*[1] transitions) are not restricted by changes in vibration quantum number [21], *i.e.*, any vibrational level of the upper state may combine with any vibrational level of the lower state.

The probability and intensity of any vibronic transition is governed by the *Franck-Condon (FC) principle.* It uses the Born-Oppenheimer approximation to separate the electronic motion from the vibrational motion. Classically, vibronic transitions are considered to be "vertical" such that no nuclear motion (hence no vibration) occurs during electronic excitation so the molecule initially will have the same internuclear distance in the excited state as it does in the ground state. After the excitation the bond can be considered to be "compressed" and in order to relieve the stress on the bond the molecule begins to vibrate.

Qualitatively, the FC principle allows for an estimation of the shape of the potential energy wells. Where the transition dipole moment is constant (independent of R) the intensity of any vibronic transition is proportional to the square:

$$\left|\int \psi'_{vib}\psi''_{vib}dR\right|^2 = \left|\langle v'|v''\rangle\right|^2 = q_{v'v''} \qquad (2.39).$$

with $q_{v'v''}$ known as the Franck-Condon factor which is the square of the overlap of the vibrational wave functions of the two states involved in the transition. The qualitative picture that shows the "vertical" transition and overlap of the wave functions is shown in Fig. 2.6. It should be noted however, that equation 2.39 is only valid for cases in which the transition dipole moment is constant, independent of R.

---

[1] *Vibronic* transitions refer to vibrational transitions that accompany electronic transitions. *Rovibronic* transitions refer to the rotational transitions that accompany vibronic transitions.

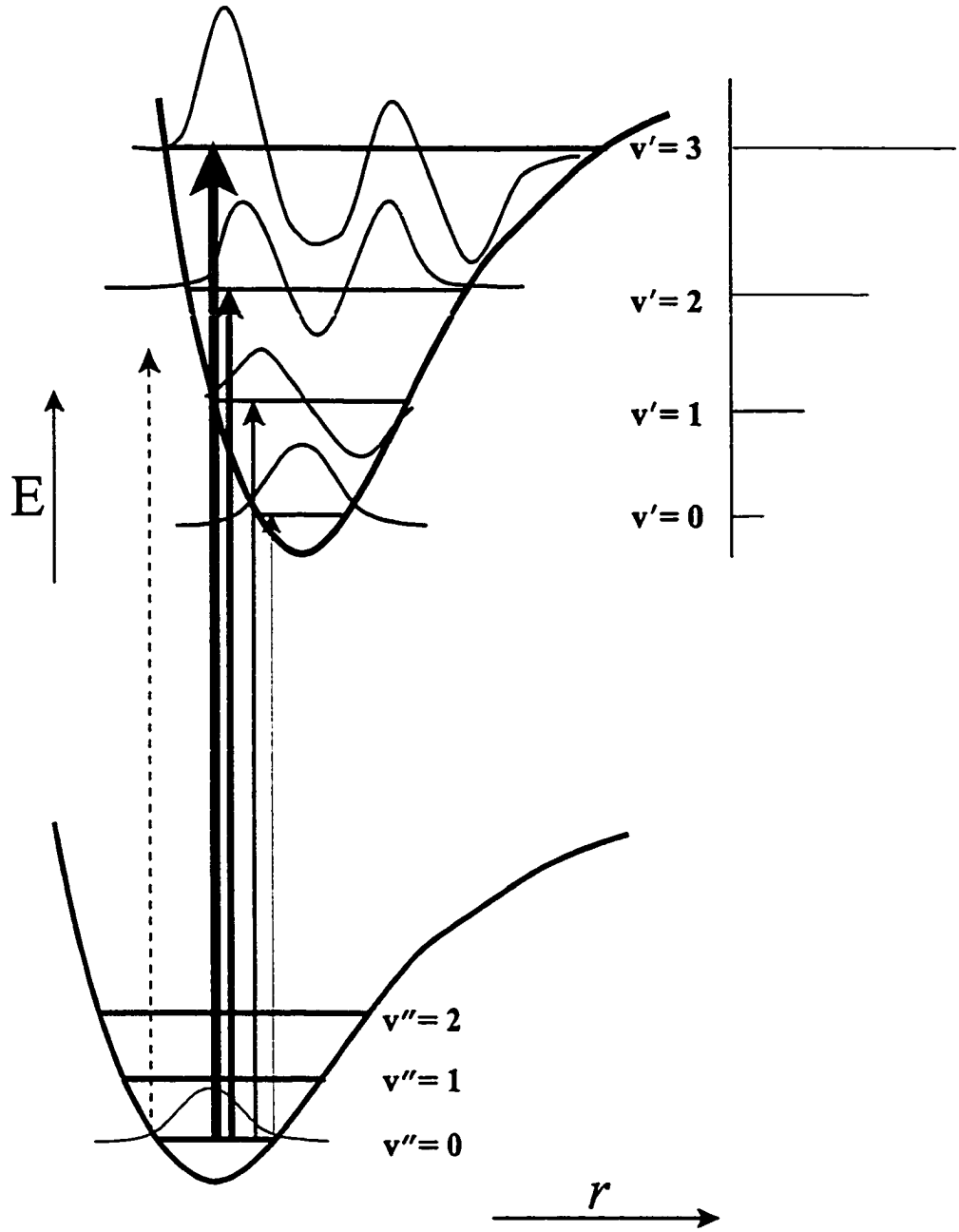

Fig. 2.6. The basis of the Franck-Condon Principle. The most probable transition occurs from the initial ground state vibrational wave function to an excited state vibrational level with a wave function that resembles the ground state the most. The thickness of the lines represents the intensity of the transition. The stick spectrum on the right shows the vibrational intensity pattern of the transitions. The more the states are displaced from each other (the greater the difference in bond lengths), the longer the vibrational progression.

2.7 Angular Momentum Coupling Cases: Hund's Cases (a), (b), and (c)

When molecules possess electronic orbital and/or spin angular momentum the rotational structure of molecules is more complicated than for the $^1\Sigma$ state where the energy is given by $BJ(J+1)$ [21]. The various angular momenta can couple together in such a way that causes a splitting of the rotational energy levels that exist in that electronic state. The manner and degree of the splitting depends upon how the various angular momenta couple.

Hund has considered the possible coupling schemes and recognized that diatomic molecules could be classified according to several coupling cases. The cases are characterized according to which of the different types of interaction predominates. The schemes are known as Hund's coupling cases and range from case (a) through case (e). Most diatomic molecules follow one of three coupling cases: Hund's case (a), case (b), and case (c). For the present work, only these three cases need be described.

(i) Hund's Case (b)

Diatomic molecules with $\Lambda = 0$ and $S \neq 0$ generally belong to Hund's coupling case (b). However, there are exceptions. Where strong off-diagonal spin-orbit coupling to another state exists, a Σ state can belong to Hund's case (a), as is found for example in MoN and WN. Hund's case (b) also applies to molecules where the magnetic field associated with the orbital angular momentum is too weak to induce the electron spin to couple to the internuclear axis. As a result Σ and, therefore, Ω are not defined. They are no longer good quantum numbers. The coupling of $\boldsymbol{S}$ and $\boldsymbol{R}$ gives the total orbital angular

momentum J, which can take all integer values from $R + S$ to $|R - S|$. The coupling is depicted in Fig. 2.7.

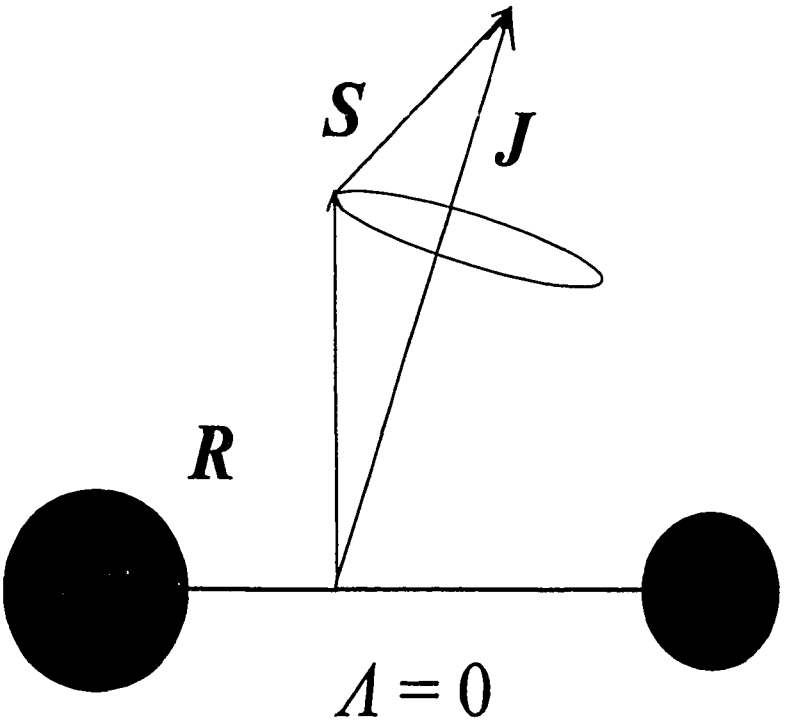

Fig. 2.7. Hund's case (b) coupling for Λ = 0.

(ii) Hund's Case (a)

This coupling scheme, shown in Fig. 2.8, is only appropriate for states with $\Lambda > 0$. The projection of the orbital angular momentum (L) on the internuclear axis is $\Lambda\hbar$ and of electron spin (S) is denoted by $\Sigma\hbar$. These angular momenta couple (equation 2.10) to give the component of the total (orbital + spin) angular momentum along the internuclear axis ($\Omega\hbar$), where

$$\Omega = \Lambda + \Sigma \qquad (2.40).$$

The molecular rotational angular momentum **R**, which is perpendicular to the molecular axis, couples to **Ω** to give the total angular momentum ***J***:

$$J = \Omega, \Omega + 1, \Omega + 2 \ldots \qquad (2.41).$$

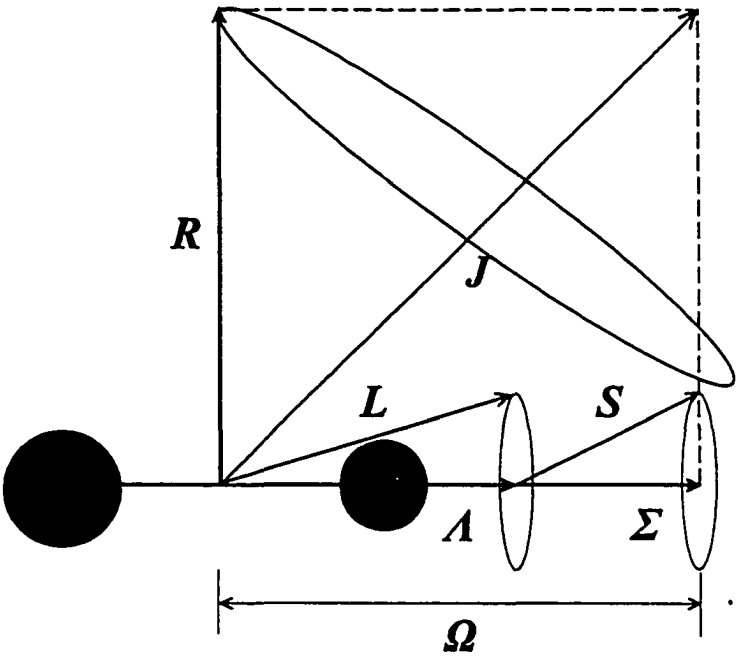

Fig. 2.8. Hund's case (a) coupling.

(iii) Hund's Case (c)

Hund's coupling case (c) is similar to case (a). Case (c) coupling, shown in Fig. 2.9, usually occurs in the excited states of heavier molecules (*i.e.* molecules with at least one heavy atom). This interaction between ***L*** and ***S*** is stronger than the interaction with the internuclear axis. The quantum numbers Λ and Σ are no longer defined. The spin-

orbit coupling is so large that the spin (S) and orbital angular momenta (L) couple strongly together to give a resultant J_a, the total electronic angular momentum. This result will then couple to the axis with a projection $\Omega\hbar$. As in case (a), the electronic angular momentum Ω and the rotational angular momentum R couple to yield the total angular momentum J. [2]

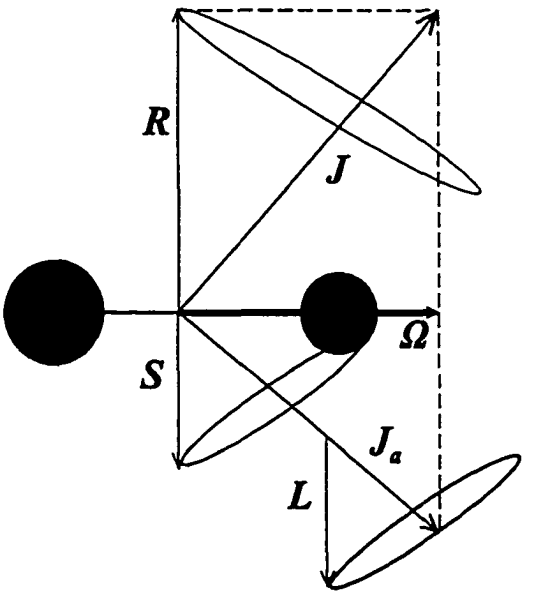

Fig. 2.9. Hund's case (c) coupling.

2.8. Perturbations

By definition, a perturbation can be thought of as anything that causes an irregular behavior in any observable or anything that causes disorder to a system [27]. In quantum mechanical terms, most systems of interest can be described by Hamiltonian equations

[2] When spin- orbit interaction is sufficiently large to cause severe mixing of states with different values of S, Λ, and Σ, it may not be possible to define J_a.

(energy operators). Solution of the Schrodinger equation give the energy levels of a system. The equation, however, can only be solved rigorously for a two-body problem. However, small corrections to a simple system that resembles the real system may be enough to solve the problem. If the wavefunctions (ψ) and energies (E) of the simpler system are known, it is possible to adjust them (by an amount ΔE) so that they are distorted enough to resemble the true wavefunctions. With perturbation theory useful algebraic relationships can be developed to aid in understanding systems.

In spectroscopy, a molecule originates in a state with a definite energy and when excited (via electromagnetic radiation) the molecule is in another state for a brief period. The energy levels, to a first approximation, can be described by a zero-order model ($\hat{H}^0$) [22]. The model neglects interactions, coupling terms and perturbations in the system. To account for these "disturbances" in the system, the model has to be expanded to correct for these interactions. We can loosely summarize the corrections as

$$\hat{H} = \hat{H}^0 + \hat{H}^1 + \hat{H}^2 \tag{2.42}$$

$$E = E^0 + E^1 + E^2 \tag{2.43}$$

with

$$E^1 = \Delta E = \int \psi^{0*} \hat{H}^1 \psi^0 d\tau \tag{2.44}$$

where the "^{0}" superscript refers to the unperturbed (zeroth-order) system. The "^{1}" and "^{2}" superscripts are first and second order corrections which are very small in comparison to E^0. Thus equation 2.44 transforms, to a first approximation,

$$E = E^0 + \int \psi^{0*} \hat{H}^1 \psi^0 d\tau + \text{higher order terms} \tag{2.45}.$$

One does not have to look far to find examples of perturbations in electronic spectroscopy. The higher order terms associated with the vibrational (anharmonicity) and rotational (centrifugal distortion) energy terms are actually perturbations of the "pure" vibrational and rotational motion of the molecule. The energy of an observed spectroscopic transition is really a group of an infinite number of the above corrections. The reason these terms (corrections) are included is to fit the observed transitions as exactly as possible while at the same time confirm line assignments and overall assignment of the transition.

There are various mechanisms that result in perturbations. In this study, there are basically two types of perturbations: (1) those which exist locally in the rotational band structure and (2) global interactions between vibronic levels of different electronic states. It should be noted that the second type of perturbation is a very general classification.

Rotational perturbations in a band may appear in different forms. The most common is the displacement of a spectral line or several successive lines associated with the rotational branch structure of a band. In some cases a rotational line may be split. Also, an intensity perturbation may occur in which one or more of the lines appear weaker than the normal intensity distribution. It is not uncommon for a band to have a perturbation that involves a combination of these anomalies.

The normal course of a progression in a band system can be disturbed through interaction with another electronic state. Essentially, the vibrational levels of the observed electronic state are displaced because of interaction(s) with vibrational levels of another state. As in rotational disturbances, the vibrational levels can be displaced and/or

the intensity of the band associated with those levels can be diminished (or enhanced). The shift in energies of the vibronic levels depends on how close the energies of the unperturbed states are. The closer the states are to being degenerate, the more the states interact and hence, the greater the repulsion. Perturbations may not always be physically evident in a molecule's spectrum. Besides intensities, the excited state lifetimes of vibrational levels may be affected by the interaction of another state's vibrational level. Excited state lifetimes will be discussed later in this chapter. Given the density of states associated with transition metal spectra, the presence of some type of disturbance (either one or both types of perturbations) is not uncommon.

Perturbations, like spectroscopic transitions, are governed by selection rules based on the quantum numbers and symmetry properties of the states/levels involved in the interaction [21]. Interactions must take place between states that have the same total angular momentum J and the same parity (+ ↮ -). Both states must have $\Delta\Omega = 0$ or ± 1. In cases where the two states have the same value of Ω, the perturbation is considered homogeneous. When the states have Ω values that differ by ± 1, the perturbation is heterogeneous. The last restriction is only valid under Hund's case (a) or (b) formalism. For Hund's case (c), since Λ and S are not defined, the selection rules are based on the values of Ω ($\Delta\Omega = 0$ or ± 1).

At the beginning of this section, a "dictionary" definition of a perturbation was given. Under that definition, any interactions that occur as a result of angular momenta coupling in the molecule could be considered a "perturbation". Such phenomena as spin-orbit coupling and spin-rotation interactions are two such examples that apply to the

investigations presented in this dissertation.

(i) Spin - Rotation Interaction

As mentioned earlier, most multiplet Σ molecular states belong to Hund's coupling case (b). The energy levels of a $^1\Sigma$ state are given by $BJ(J+1)$. In the case where a Σ molecular state has one or more unpaired electrons, a term for spin(S)-rotation(R) interaction must be included in the overall description of the system. The Hamiltonian for the spin-rotation interaction ($\hat{H}_{sr}$) can be included as a perturbation of the rotational energy term values [22]:

$$\hat{H} = \hat{H}_0 + \hat{H}'_{sr} \tag{2.46}$$

$$\hat{H}'_{sr} = \gamma R \cdot S \tag{2.47}$$

where γ is the spin-rotation coupling constant and is usually quite small ($\sim 10^{-2}$ cm^{-1}) in relation to the rotational constant B for transition metal diatomic monocarbides, mononitrides, and monoxides. Most texts that describe spin-rotation interactions use the $^2\Sigma^+$ state as the "typical" example for spin-rotation interaction. From Fig. 2.5, we know that $J^2 = (R + S)^2$ so

$$R \cdot S = \tfrac{1}{2}[J^2 - R^2 - S^2] \tag{2.48}$$

therefore

$$E'_{sr} = \left\langle RJS\Lambda \middle| \hat{H}'_{sr} \middle| RJS\Lambda \right\rangle = \tfrac{1}{2}\gamma[J(J+1) - R(R+1) - S(S+1)] \tag{2.49}$$

The effect that spin-rotation interaction has on the rotational energy levels is that there

will be multiple values of J for each rotational quantum number N.

The situation is a little more complicated when we have a molecule that has more than one unpaired electron in a molecular orbital (*i.e,* for molecular states with multiplicities greater than 2). An extra term would be added to equation 2.49 to account for the interaction between the unpaired electrons (spin-spin coupling).

(ii) Spin - Orbit Interaction

Molecule states that follow Hund's case (a) coupling undergo a splitting into 2S+1 components because of the possible values that Ω can have due to the magnitude of $\Lambda + \Sigma$. The splitting can be viewed as a perturbation of the electronic states involved in the transition since the coupling removes the degeneracy of the different Ω-levels. To a first approximation, the coupling between the orbital and spin motions along the axis is linearly proportional to Λ and Σ such that the Hamiltonian for this spin-orbit splitting is

$$\hat{H} = \hat{H}_0 + \hat{H}'_{so}, \text{where } \hat{H}'_{so} = A\Lambda\Sigma = E'_{so} \tag{2.50}$$

where A is the spin-orbit coupling constant. The spin orbital coupling constant determines the magnitude of the multiplet splitting. When its value is positive ($A > 0$), the molecular state is "regular" and when $A < 0$ negative, the state is "inverted."

(iii) Λ-*Type Doubling*

All states that have $\Lambda > 0$ are doubly degenerate due to the energy associated with the orbital motion (clockwise or counter-clockwise) of the electrons about the internuclear axis ($\pm \Lambda$). The degeneracy is removed by interaction of the electronic and

rotational motions of the molecule. As a result one of the degenerate rotational levels is designated (+) and the other (-). The ± description (parity) of the levels refers to the behavior of the wavefunctions under the space-fixed inversion operator.

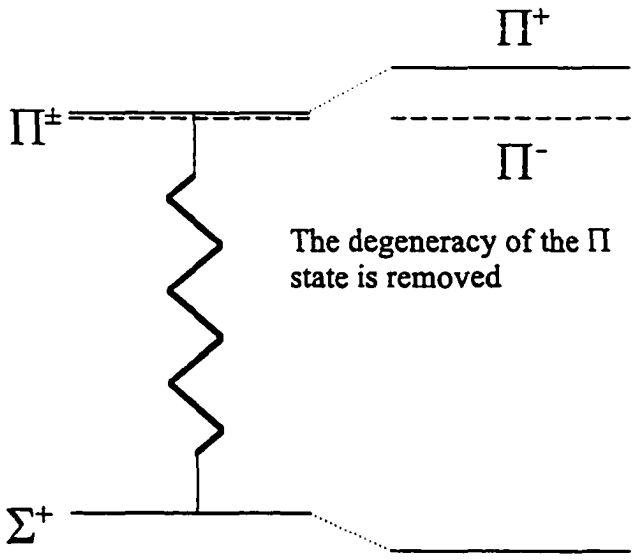

Fig. 2.10. Λ-type doubling.

In the case of a $^1\Pi$ state, the degeneracy is lost when the molecule begins to rotate. If a $^1\Sigma^+$ state is in the vicinity, the interaction between the $^1\Pi^+$ component of the $^1\Pi$ state and the $^1\Sigma^+$ state causes the $^1\Pi^+$ levels to be displaced while the $^1\Pi^-$ component remains unaffected. This uncoupling phenomenon is known as *Λ-type doubling*. Figure 2.10. shows the splitting. The (+) levels are perturbed and the degeneracy of the $^1\Pi$ state is lost as is shown in Fig. 2.5. The splitting usually increases with increasing J and differs for the different multiplet components of the molecular terms. The rotational term energies

(of the $^1\Pi$ state) are given by

$$F_{\pm}(J) = BJ(J+1) \pm qJ(J+1) \tag{2.51}$$

where q[3] is the Λ-type doubling constant and is given by what is called the "Van Vleck pure precession formula" [21]:

$$q = \frac{2B^2 L(L+1)}{(E_{\Pi} - E_{\Sigma})} \tag{2.52}.$$

The value of q is also given by the difference in B values of the two components of the $^1\Pi$ state

$$q = B_{(+)} - B_{(-)} \tag{2.53}.$$

Λ-type doubling is analogous to the spin-rotation splitting observed in multiplet Σ states under Hund's case (b) coupling. The splitting between the levels varies in the different components of the multiplet state.

In the case of Hund's case (c) coupling, the Λ-type doubling is called Ω-type doubling since Λ is no longer a good quantum number.

2.9. Lifetimes of the Excited States

Traditionally, most spectroscopic studies have focused on the transition frequencies. Often overlooked is the information contained in transition intensities and excited state lifetimes which can contribute to the overall picture. In some circumstances (*e.g.* when the excited states are strongly perturbed), every observable quantity may be needed to unravel the electronic structure of a particular molecule.

---

[3] Some authors prefer to write equation 2.51 as: $F_{\pm}(J) = BJ(J+1) \pm \frac{1}{2} qJ(J+1)$.

The majority of lifetime studies involves first-order or pseudo-first-order kinetic processes [28]. The LIF signal intensity curve represents the excitation of the initial population (at time zero) and the decay of the excited state population. The signal intensity can be described by a simple exponential function of time

$$I(t) = I_0 \exp(-\frac{t}{\tau}) \tag{2.54}$$

where I_0 is a constant scaling factor and τ^{-1} is the lifetime of the excited state, *i.e.*,gives the rate at which the population of a particular excited state level decays.

In laser-induced fluorescence experiments it is not always evident from the recorded spectra that molecular interactions are taking place. It is in these instances that lifetimes measurements aid in the analysis of the electronic structure. In a situation where there is no interaction between excited state vibrational levels, the lifetimes of all the observed levels of a given electronic state should be the same (within experimental limits). Lefebvre-Brion and Field [3] present an extensive treatment of the intensity/lifetime relationship.

The fitting of the decay curves is described in the experimental procedure.

Chapter 3

Experimental Details

3.1. Introduction

The origin of TM spectroscopic studies can be traced back almost 150 years. Masson, in the early 1850s, studied the "electric" spectra of metals and confirmed that metals have characteristic spectra [29]. Soon after, Anders Ångstrom discovered that Masson's spectra were actually overlapping spectra consisting of the metal of the electrode in question and the gas that surrounded it. Perusal of Herzberg's Table 39 in his book *Molecular Spectra and Molecular Structure: Spectra of Diatomic Molecules* [21] shows that the study of electronic spectra of molecules via emission studies has taken off in the late 1920s. Not only have these studies played an important role in understanding the physical and chemical properties of molecules, they have also "lent a hand" in the development of quantum theory.

Early emission spectra were obtained by exciting the sample to various excited electronic states. As the molecules relax, the emitted radiation is dispersed by a grating and focused onto a photographic film. The calibration of the spectra was usually achieved by recording adjacent a previously known atomic spectrum. In the introduction the difficulties associated with the analyses of emission spectra of TM diatomic molecules were mentioned. With the introduction of lasers to spectroscopic research in the late 1960's, the collection techniques associated with spectroscopic methods have changed. The 1980s saw the advent of the laser ablation/molecular beam technique to synthesize and characterize small metal clusters [30] and later, the jet-cooled spectra of diatomic transition metal molecules [31]. Since then, the study of diatomic transition metal species has flourished. The appeal of this technique is that any metal or metal

mixture is readily vaporized by the ablation source. The resultant metal plasmas can produce small metal clusters (*e.g.*, M_x and M_xX_n) or mix with reactant gas mixtures to produce various metal-containing molecules (*e.g.*, $M + CH_4 \rightarrow MC + MH$ etc...).

In this chapter, a summary of the experimental setup that combines the techniques of laser vaporization in a molecular beam and probe techniques will be presented.

3.2. Experimental Apparatus

A schematic of the experimental apparatus used to produce the rhodium based diatomic species is shown in Fig. 3.1. The setup can be sectioned into three components. The first component is the ablation laser/molecular beam source. Its function is to produce the molecules for study. The second component consists of an excitation source and a detection unit. A pumped dye laser is used to excite the molecules produced in the molecular beam and a monochromator/photomultiplier assembly is used to detect the laser induced fluorescence (LIF). The third unit is the data processing system that manipulates the LIF signal for processing.

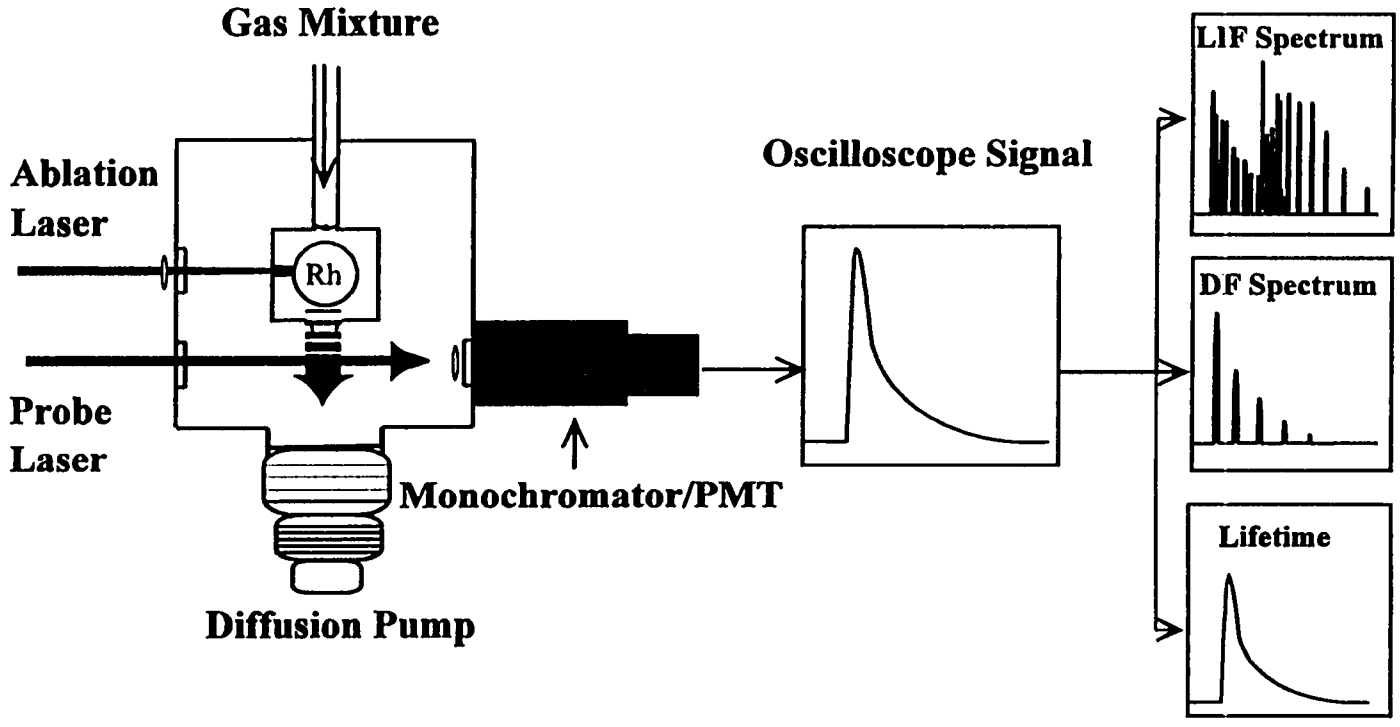

Fig. 3.1. The experimental set-up used to record the spectra of rhodium-based diatomic molecules. Details of the experiments are found in the text.

(i) Ablation Laser Molecular Beam Source

The ablation laser/molecular beam source consists of a high vacuum expansion chamber, a sample gas inlet system, a pulsed molecular beam valve, a mounted, motor-driven rotating and translating rhodium rod, a diffusion pump that is backed by a mechanical pump and a Nd:YAG laser. The valve and motor/rod assembly are directly housed within the chamber with the gas inlet system and pump attached externally. The laser is also positioned external to the chamber.

The walls of the vacuum chamber are made of black anodized aluminum in a cubic shape with dimensions of 30cm×30cm×30cm. The chamber is mounted on an Edwards diffstack 160 diffusion pump (16 cm throat) which is connected to an Edwards E2M8 mechanical backing pump. The pressure in the chamber is monitored by an ion pressure gauge (Granville-Phillips 270006). Typical chamber pressures of ~10^{-5} Torr are monitored with the molecular beam switched off. With the valve in operation, the pressure in the chamber roughly increases by a factor of ten.

The sample inlet system (gas mixture preparation chamber) consists of a 10-liter gas bulb with two outlets. Typically, the gases used in preparation of the sample (*i.e.*, CH_4 for RhC, NH_3 for RhN, and O_2 for RhO) are seeded in a carrier gas. Helium was used as the carrier gas in all our experiments. The concentration of the reactant gas in helium is usually small (~ 3 - 10 %) to a total pressure of one atmosphere. One outlet is connected to a series of inlet valves that enables the input of a particular gas. The second outlet leads to the molecular beam apparatus. Teflon tubing is used to connect the outlets to the valve and the gas inlet valves. On average, with a fresh sample mixture (filled

bulb), two to three days worth of experiments can be carried out (approximately 40 to 60 scans) before the gas mixture has to be replenished. The length of time between fillings, of course, depends upon the type of experiment carried out.

The pulsed molecular beam valve is a piezoelectric device. Its design and construction followed the blueprint of Proch and Trickl [32]. The valve allows the gas mixture to expand into a nozzle head (reaction chamber). We employ a variety of nozzle heads. Each nozzle head has three perpendicular channels. A 2-mm (diameter) opening is standard to the nozzle heads. The main difference among the different heads is found in the length of the main channel. Channel length seems vital in the formation of different molecular species. For instance, RhC/RhN are easily formed with a short nozzle head (17 mm channel length) whereas the formation of RhO is maximized by a longer nozzle head (25 mm channel length). The second channel has a diameter of 5.5 mm and is the home of the metal rod. A third channel intersects the path of the translating and rotating rod. This channel serves as a pathway for the ablation laser.

The second harmonic (532 nm) of a Continuum NY61 Nd:YAG laser is used as the vaporization source. A convex (converging) lens with a focal length of 50 cm is used to focus the output of the laser on to the surface of the rod. The second harmonic (532 nm) has sufficient energy (~ 200 mJ/pulse) to vaporize most metals. Some of the metals used in molecular studies in our lab have been: Fe; b.p. = 3135 K [9], Rh; b.p. = 3970 K [9], and Re; b.p. = 5869 K [9].

The rhodium plasma is produced downstream of the nozzle valve by ablating the surface of the rhodium rod (Goodfellow, 99.9%, d = 5 mm, length = 30 mm). A stepping

motor translates and rotates the rod in and out of the path of the ablation laser. The function of the stepping motor is to provide continuously a smooth, fresh surface for ablation. Without the continuous motion of the rod, the laser would drill a hole through the rod. After every laser shot (the pulse duration is ~ 10 ns), the vaporized rhodium atoms are expanded into the channel together with the reactant gases. It is there that reactions take place. The timing of the gas pulse (pulse width ~ 200 μs) relative to the vaporization laser pulse is adjusted to maximize the production of the species to be studied.

(ii) Excitation of the Sample and Data Collection

All of our spectra were recorded using a pulsed dye laser system. A Lumonics HY600 Nd:YAG laser operating at 355 nm is used to pump a tunable Lumonics HD-300 dye laser. The dispersing element consists of a 2400 groove/mm grating. The wavelength and energy outputs of the dye laser depend on the laser dye used. With a large region of the near uv-visible spectrum (390 - 700 nm) to scan, a variety of dyes is used. Table 3.1 gives a summary of the dyes used and their optimized operating conditions. The dyes were purchased from Exciton Inc.

The jet-cooled sample is excited at a right angle to the axis of the molecular beam expansion. Excitation pulses were synchronized with the pulses of the molecular beam with a digital delay generator (Princeton Applied Research: EG & G 9650). The delay varies from molecule to molecule and is adjusted to maximize product formation.

Table 3.1. A list of the dyes utilized in the LIF/DF scans of RhX molecules. All dyes were pumped by the third harmonic of a Nd:YAG laser (Lumonics HY600).

Dye	Lasing Wavelength		Solvent	Concentration		Power(mJ) (± 5mJ)
	Max (nm)	Range (nm)		Molarity	mg/L*	
LDS750	718	699-743	M	3×10^{-4}	145	40
LDS698	692	659-732	M	3×10^{-4}	113	40
DCM	643	611-685	PC/M (1/4)	5×10^{-4}	152	20
R640	643	607-640	M	2×10^{-3}	1182	30
KR620	596	594-641	M	1×10^{-3}	581	25
R610	600	588-632	M	5×10^{-4}	252	20
R590	574	563-597	M	6×10^{-4}	318	10
C540A	543	523-586	M	3.5×10^{-3}	1082	10
C485	529	499-565	M	1.5×10^{-3}	386	10
C500	504	481-550	M	1.5×10^{-3}	257	10
C480	477	458-507	M	8×10^{-4}	204	5
C460	459	443-485	M	4×10^{-4}	92	5
C450	452	436-467	M	3×10^{-4}	66	5
C440	435	422-459	M	4×10^{-4}	70	5
EXA428	426	415-436	D	5×10^{-5}	52	5
EXA417	416	406-425	D	3×10^{-5}	25	5
EXA411	411	402-419	D	3.7×10^{-5}	24	5
EXA404	404	396-413	D	7.5×10^{-5}	50	5

*** The concentrations are quoted in mg/L. Actual volumes used were 500 mL.**

M = methanol PC = propylene carbonate D = dioxane

LDS = (pyridine 1) DCM = dicyanomethylene R = rhodamine
KR = kiton red (sulforhodamine) C = coumarin EXA = exalite

Typical values for RhC and RhN were in the 30 to 40 microsecond range.

The LIF signal is collected perpendicular to the plane of the excitation laser and molecular beam axis by means of a collecting lens, filtered by a monochromator, and converted to an electrical signal by a photomultiplier (PMT). A collecting lens (diameter = 50 mm) has a focal length of 75 mm and is positioned inside the vacuum chamber. The purpose of this lens is to image the fluorescence onto the entrance slit of the monochromator.

A Jobin-Yvon H20 monochromator was utilized as a band pass filter. Depending on the experiment, the monochromator was used in three modes. The first mode was as a broad bandwidth filter (~ 30 nm) that allows all emissions to many lower vibronic states to be collected while at the same time reducing the amount of scattered light from both the excitation and ablation lasers. Further filtering can be achieved by placing slits with various slit widths at the entrance and exit ports of the monochromator. A second mode of operation allowed for the fluorescence to be collected with the monochromator fixed at a specific wavelength. In this manner, emission to a particular vibronic state can be monitored. The advantage of recording spectra via this method will be discussed later in the chapter. A third method of operation is to fix the laser at a particular wavelength and let a stepping motor rotate the grating of the monochromator. Two slits sizes are used. With the "wide" (1 mm) slits in place, the bandwidth of the monochromator is approximately 100 cm^{-1}. The "narrow" slits (0.5 mm) allow the monochromator a bandwidth of <50 cm^{-1}. This resolution is sufficient to provide data of a quantity to allow for a vibrational analysis of the ground state.

The fluorescence that is allowed to pass through the monochromator is detected using a photomultiplier. The Hamamatsu R1477 model with a spectral range of 185 - 900 nm was utilized in our experiments. The signal is converted to an electric signal and sent to the oscilloscope.

The signal that arrives from the PMT is detected and digitized on a digital oscilloscope (Tektronix 2440). The sampling interval consists of 1024 channel-voltage data points with up to a 2 ns resolution between points. From there, the signal was transferred to a 386 MHz IBM PC computer that was equipped with a general purpose interface bus (GPIB) board to transfer data from the oscilloscope to the computer, an A/D (analog to digital) converter (Laboratory Technologies: PCL-711s) and an Advantech PCL-830 timer card. The GPIB board is equipped with a Quick Basic driver and similarly, the timer card also has its own driver. A Quick Basic program (TIMER.BAS) was written in which each pulse width and delay time could be adjusted to the desired settings.

Timing of events in the experiment is crucial. The triggering of events is controlled by the clock of the timer card (set to 10 Hz). The timer card triggers a series of events. The two Nd:YAG laser (ablation and pump laser) flash lamps are triggered by two channels of the timer board. The nozzle driver is also triggered by the timer card by another channel. The timer card also triggers a delay generator (Princeton Applied Research, EG & G 9650) which, in turn, triggers the Q-switches of both lasers. As mentioned earlier, the delay time between the laser pulses of both lasers is set such that an optimal signal is achieved. This delay time was usually adjusted after each cleaning of

the nozzle head and subsequent laser realignment. The generator also triggers the scope with the first pulse of the ablation laser (t = 0 of the scope).

3.2.3 Data Processing System

The position of individual spectral transitions was determined from the recorded spectra using a simple computer program. The program identifies local maxima in the LIF signal and the position of the peak is identified in terms of air wavelength (λ_{air}) as determined by the dye laser. Conversion of the peak wavelengths (nm) into vacuum wavenumbers (cm^{-1}) was achieved by the same program [34].

All the spectra were plotted using one of two graphing programs: Genplot® or Microsoft Excel®. Microsoft Excel® was also used to calculate and graphically fit the experimental combination differences used to determine the molecular parameters reported in this thesis.

3.3. Experimental Procedure

Three types of experiments were performed in our investigation of RhX diatomic species. Some of the experiments were customized to facilitate our analyses. The first type involved the collection of excitation spectra; the second dealt with the recording of dispersed fluorescence spectra and the third was the determination of excited state lifetimes through recorded LIF decay curves.

3.3.1 Laser Induced Fluorescence (LIF) Spectra

It was mentioned earlier that the development of laser techniques has changed spectroscopic studies dramatically in the last thirty years. Laser induced fluorescence is one spectroscopic method that has developed as a result of laser techniques. There have been a number of LIF techniques developed since Kinsey [35] first reviewed the concept in 1977. Demtröder [36] and Andrews [37] have summarized some of the "standard" LIF techniques as well as recent developments.

In the LIF technique, a tunable dye laser is used to excite the molecules, jet-cooled in our case, from a particular low-lying vibronic level to some excited state. When the laser is brought into resonance with a spectroscopic transition to an electronically excited vibronic level, molecules in the lower state will be excited to the higher state. The molecules in the excited state decay spontaneously to various vibronic levels governed by the selection rules. The spontaneous fluorescence decay signal is monitored at a particular wavelength (in our experiments the monochromator is set manually). The signal that appears on the oscilloscope is a result of the emission. The fluorescence is interpreted in terms of the initial population of the ground state. If the laser wavelength is not tuned to a specific rovibronic transition, then the spectral intensity is zero and no LIF signal is detected. For this reason, the LIF method is highly sensitive. A schematic of the LIF technique is shown in Fig. 3.2.

Apart from the different types of spectra recorded, two different filtering strategies for recording LIF spectra have been used in this study of RhX molecules. Both types of filtered spectra are less congested and reveal different pieces of information

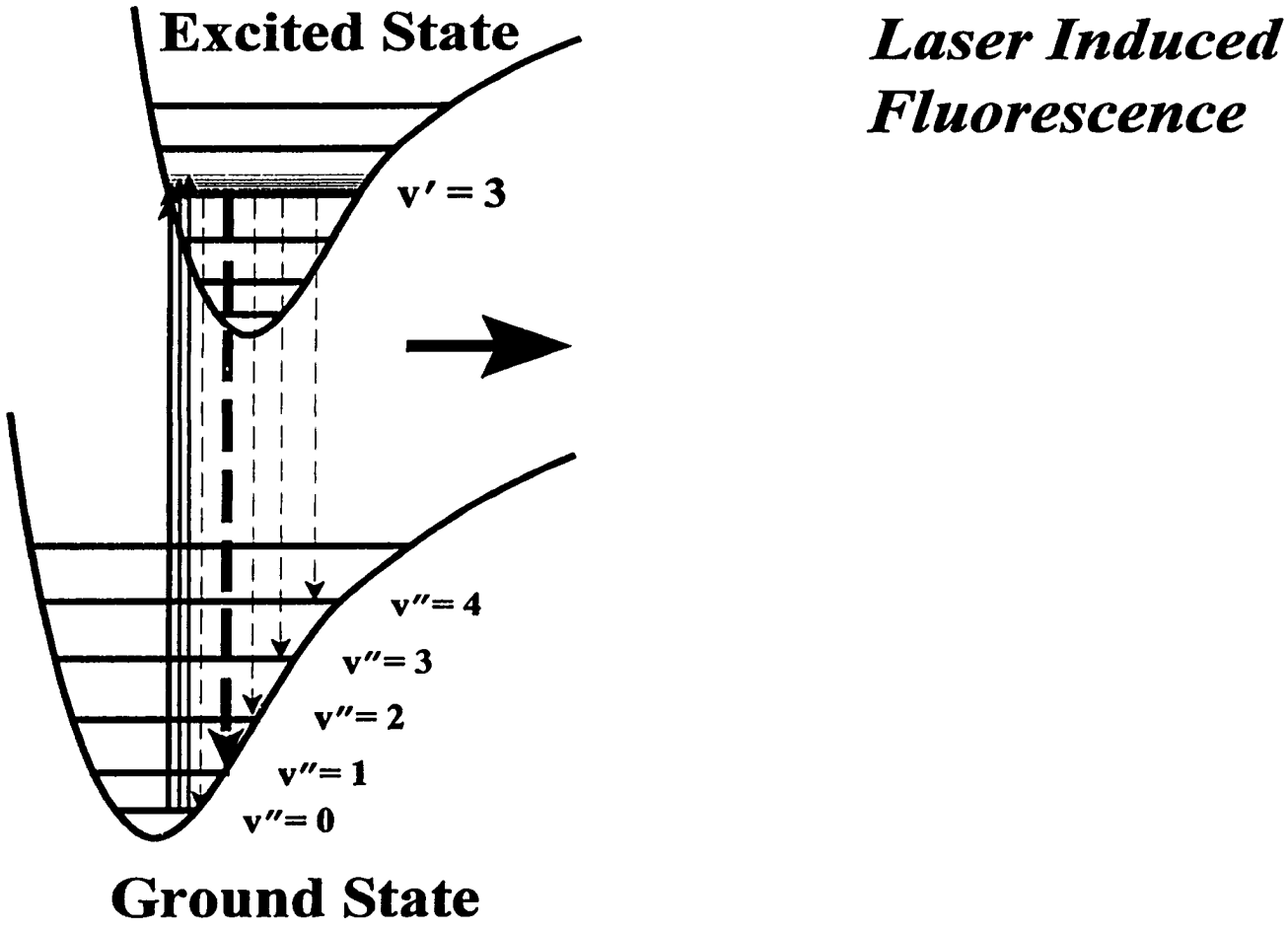

Fig. 3.2. The fluorescence process in an LIF experiment. The monochromator is fixed at a specific wavelength that corresponds to a low-lying vibronic level.

about interactions among different states. The first strategy involves monitoring the fluorescence with the monochromator fixed at a specific wavelength (frequency). Wavelength-filtering laser induced fluorescence (WF-LIF) is a useful technique since different excited states emit differently to different low-lying states. In this way the band related to a particular transition can be isolated. Figure 3.3 demonstrates the WF-LIF technique which has been used successfully in this lab on different occasions [38, 39]. In Chapter 5, we show how the WF-LIF technique was used to suppress, effectively, the contribution of one transition in overlapping bands to obtain a spectrum for the second band so it could be rotationally analyzed.

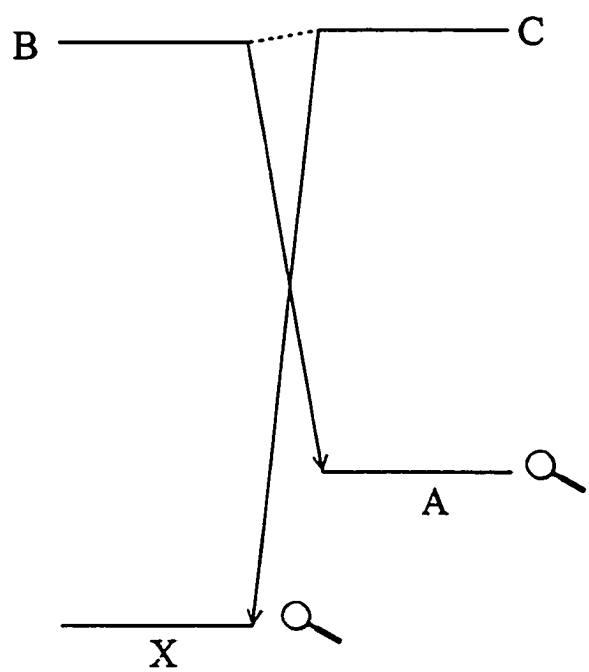

Fig. 3.3. Wavelength filtering: emission from two close-lying states (B & C) may be separated by monitoring the fluorescence to different lower states (X or A).

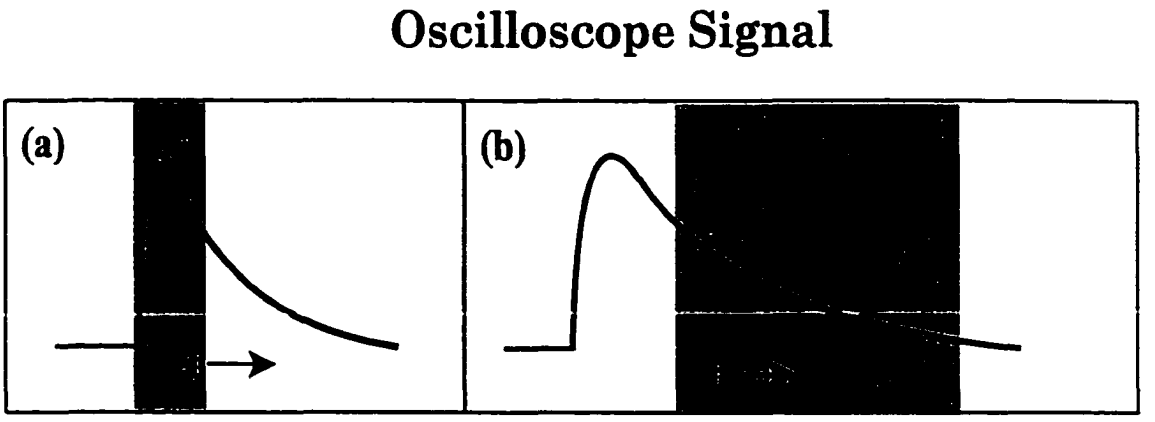

Fig. 3.4. The principle behind the TF-LIF technique. The LIF signal in (a) collected in the shaded region and processed to produce the LIF spectrum. In (b), the LIF spectrum is recorded by recording the LIF signal of the later part of the decay curve. Emission from a band with a shorter lifetime is essentially eliminated.

The second technique depends on the lifetimes of the excited states involved in the observed transitions. This spectroscopic technique is called time-filtering. The time-filtering technique is useful in separating emissions that belong to different electronic states. The principle behind the TF-LIF technique is shown in Fig. 3.4. Maximum efficiency of the technique is achieved when the excited states have significantly different lifetimes and emit to the same lower state. The technique involves the collection of fluorescence in different time domains. In the case where two states are mixed, yet have very distinct lifetimes, the time windows used to collect the emission can be adjusted to filter emission from the transition whose excited state has a short lifetime from the state with the longer lifetime. The time-filtered method proved invaluable in the analysis of the RhC spectrum (Chapter 4).

The spectra were recorded in a straightforward manner. The method used to record the LIF spectra was the same, despite the LIF techniques used. Once the LIF signal was optimized, the wavelength scan was initiated. Any search for new molecules usually begins with the recording of a survey spectrum. From these low resolution scans, it is possible to identify vibronic bands associated with a particular molecule. In this domain, the spectra are usually recorded in 10 or 20 nm increments with a scan step of 0.01 nm. Typically, no more than five laser shots are used to average waveforms for a particular wavelength. The resulting waveforms, which reflect the LIF decay curves, are averaged and integrated to obtain a mean LIF intensity for the molecule at that wavelength. Signals are then digitized and displayed on a PC as a LIF spectrum.

The spectra of specific bands of interest are then recorded in the same manner just mentioned but under more scrutiny. Typically, these slow scans are undertaken in increments of 0.001 nm. Waveforms are normally averaged and integrated using a minimum of 15 laser shots.

For the LIF, WF-LIF, and TF-LIF spectra, the absolute transition frequencies should be accurate within 1 cm^{-1}. The relative position of individual rotational lines should be accurate to within 0.1 cm^{-1}. These estimations are based on the known positions of the RhC bands reported by Lagerqvist and Scullman. Mixed spectra of RhC/RhN were recorded simultaneously to calibrate the RhN spectra.

3.3.2 Dispersed Fluorescence (DF) Spectra

Dispersed LIF spectroscopy uses the same experimental apparatus as normal LIF

spectroscopic techniques but differs in the information collected for analysis. The main uses of the technique are to map out the vibrational levels of the ground state and survey for low-lying electronic states near the ground state. The DF spectra may also provide insight into the transition intensities (Franck-Condon overlap) from the observed dispersal pattern (profile). An illustration of the DF principle is shown in Fig. 3.5.

The DF spectrum is recorded as a function of the fluorescence wavelength. The excitation source (laser) is tuned to a specific rovibronic transition to populate a particular state. The fluorescence from this state is then dispersed and recorded. With a source fixed to a specific excitation wavelength, DF spectroscopy has an experimental approach similar to Raman spectroscopy [37]. However, DF spectroscopy involves the analysis of spontaneous emission whereas Raman spectroscopy deals with "scattered" light. In the DF method, the monochromator (driven by a stepping motor) scans in steps of 0.5 nm from a predetermined wavelength. Usually, the scan begins about 20 to 30 nm shorter than the excitation wavelength and the monochromator is allowed to scan to the wavelength limit of the monochromator (900 nm). The DF analysis is a "cheap and easy" way to detect hot bands in a normally congested spectrum. In a typical scan, 20 laser shots are used to obtain an average waveform for integration at a particular wavelength. A dye amplifier cell was employed to obtain a satisfactory signal to record the DF spectra for several of the weaker bands. The calibration of the wavelength scale of the DF spectra was checked with the aid of the second order peak associated with the excitation wavelength. The uncertainties associated with the DF spectra are estimated to be less than 20 cm^{-1} based on the observed hot bands that appear in the RhC spectrum.

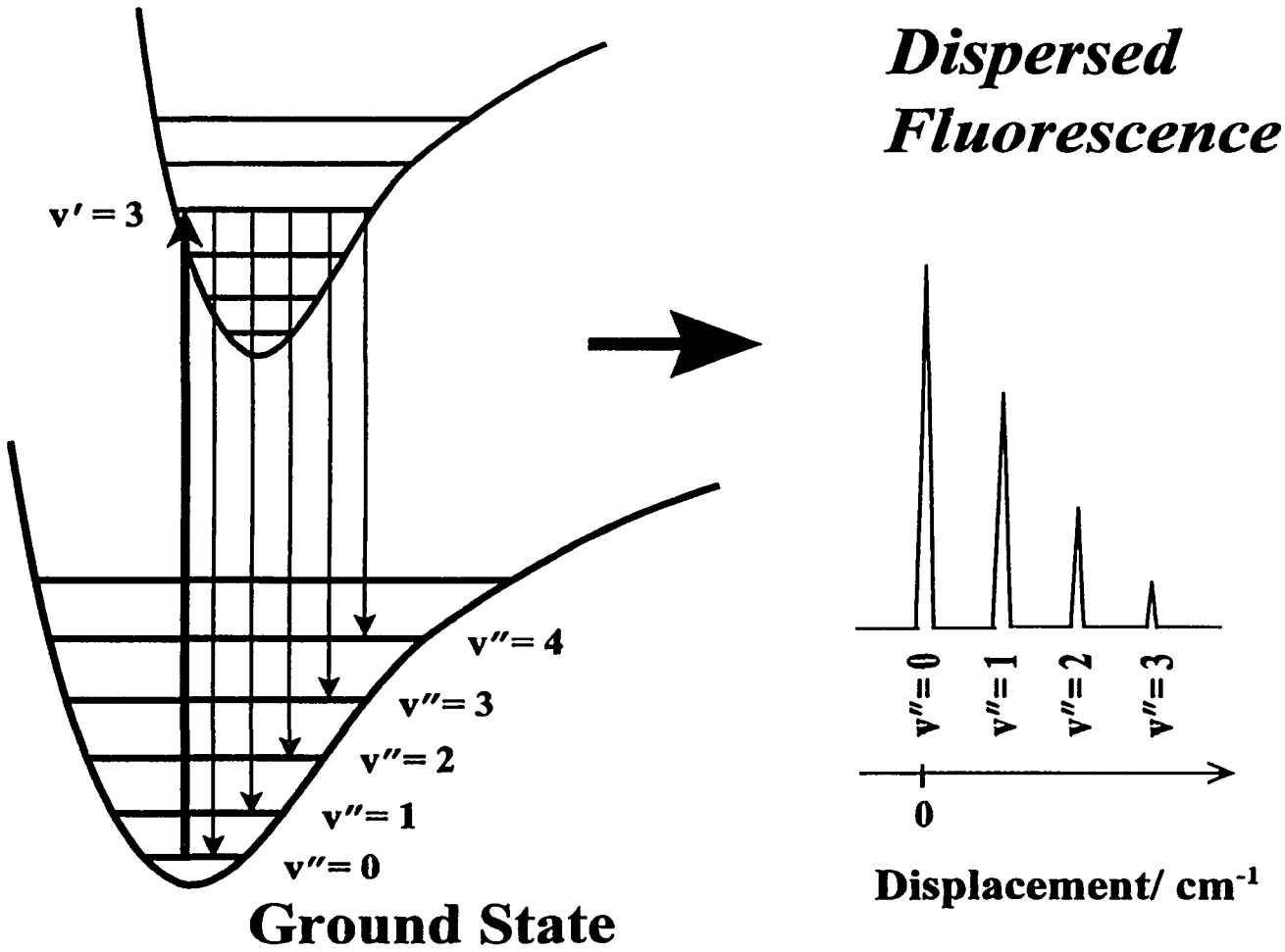

Fig. 3.5. The principle behind dispersed fluorescence spectroscopy. The "0" on the displacement scale represents the fixed excitation wavelength of the dye laser.

3.3.3 LIF Decay Signal and Excited State Lifetime Determination

A typical LIF decay profile is shown in Fig. 3.4 and specific examples are found in chapters 4 and 5. The excited state lifetimes were obtained by averaging waveforms transmitted from the oscilloscope. As with the recording of spectra in the DF technique, the excitation laser is fixed to coincide with a specific rovibronic transition. For the determination of the excited state lifetimes for rhodium diatomic species (RhC/RhN), the laser wavelength was most frequently tuned to correspond with the R-branch band head. The waveforms observed on the oscilloscope were averaged over 2000 laser shots and then recorded on the computer. These waveforms reflect the LIF decay curves associated with a particular excited state and therefore represent the lifetime of the excited state.

One assumption that is made is that the majority of the lifetime measurements involve first-order or pseudo-first-order decay processes. The rate of such a decay is given by

$$d[D^*]/dt = -k[D^*] \qquad (3.1).$$

The time dependence of [D*], the excited state is

$$[D^*]_t = [D^*]_0 \exp(-t/\tau) \qquad (3.2).$$

where $[D^*]_0$ is the initial [D*] and τ is the inverse of the slope k. Equation 3.2 is the standard method of analyzing kinetic data [26, 28]. If we plot ln ([D*]) against time (t), a linear plot is obtained with a slope -k. Since $k = \tau^{-1}$, the inverse of the slope yields the lifetime of the excited state. Deviations from linear behavior are a good indication that there is mixing between the excited state being studied and some other nearby state.

The accuracy in the lifetime measurements is somewhat limited in cases where the

lifetimes are extremely long. The path of the molecule is such that it spends only a limited time in the viewing zone of the collection optics. Therefore, the fluorescence of an excited state is probed only for a portion of each decay curve. Reproducibility of the lifetime data for each excited state was monitored by averaging the lifetimes of several trials (minimum of five trials). The standard deviation of the data was then used to calculate the uncertainty associated with the lifetime of a particular state.

With the explanation of the experimental methods completed, we can share our observations and analyses for various rhodium diatomic species explored in this thesis.

Chapter 4

The Electronic Structure and Spectrum of Rhodium Monocarbide

4.1. Introduction to RhC

There are more known compounds of carbon than of any other element except hydrogen [7]. Most are identified as organic substances (*e.g.*, benzene C_6H_6). Another class of carbon chemistry is organometallic chemistry. Organometallic chemistry is a discipline of chemistry that bridges the fields of organic and inorganic chemistry. Compounds that fall under this classification contain a metal bonded to some organic moiety. One such compound is $W(CH_3)_6$ [7]. The direct interaction of carbon with a metal yields compounds that fall under a subclass of organometallic compounds that are generally known as *metal carbides* (M-C).

Despite the important role that transition metal centers play in catalytic and organometallic chemistry, knowledge relating to the simplest metal carbide bonds is limited. Diatomic transition metal carbides are simple systems that can be used as models toward a more detailed understanding of the bonding between a metal and a carbon atom. It is surprising that not more spectroscopic work had been carried out on the transition metal monocarbides prior to five years ago. However, it seems like every year since then the data base of TM carbides has had new members added. Information, whether it is through theoretical calculations or experimental means, is being collected regularly such that a new, deeper understanding of how a metal center interacts with a carbon atom is being achieved.

Of the 3*d* transition metal monocarbides, only FeC [40 - 42], CoC [43, 44], and NiC [45] have been characterized by gas phase spectroscopic studies. Theoretically, ScC [46], VC [47], TiC [48], CrC [49], FeC [50] and NiC [51] have been examined.

The 4*d* transition series has been studied more extensively than its 3*d* and 5*d* counterparts. Yttrium carbide [52] was the first metal carbide to be characterized in molecular beam experiments, in 1994. However, the majority of the gas phase spectroscopic studies on transition metal carbides have taken place over the last three years. Simard (NRC) has studied NbC [53]. The group under M.D. Morse (Utah) has recently studied MoC [54], RuC [55] and PdC [56]. Rhodium carbide had been studied previously by Lagerqvist, Scullman and Kaving [1, 57] and Brom *et al.* [58]. The silver and cadmium monocarbides have yet to be identified in molecular beam experiments.

A good correlation between experimental and theoretical studies exists for the 4*d* TM monocarbides. Theoretical studies have been performed on YC [59], NbC [53], MoC [60], TcC [61] and RuC [62]. Palladium carbide [63 - 67] has been the focus of five separate theoretical studies to date. Rhodium carbide has itself been the focus of two theoretical investigations. Shim and Gingerich [68] used all-electron Hartree-Fock (HF)/ configuration interaction (CI) calculations to study the RhC ground state and sixteen excited states. Balasubramanian *et al.* [69] used the complete-active-space multi-configuration self-consistent field (CASMCSCF) followed by first-order configuration interaction (FOCI) calculations to study the properties of the ground state and twenty-three excited states of RhC. The results of these calculations will be discussed later in this chapter.

The 5*d* series is the least studied of all the monocarbides. Experimentally, IrC [70 - 72] and PtC [73 - 78] have been examined via gas phase studies. With respect to theoretical investigations, Balasubramanian *et al.* have performed similar CASMCSCF

and FOCI calculations on TaC [79] and IrC [80] which is isoelectronic to RhC.

The intent of this chapter is to report on the extended analyses on RhC. The previous work by Lagerqvist and Scullman [57] has been reinvestigated due to reasons that will become apparent in the following sections. The re-examination of the RhC spectrum has led to new results. The new results, in conjunction with what was previously reported [1, 57], and *ab initio* calculations [68, 69], have provided a new outlook on the electronic structure of RhC in the visible region.

4.2. RhC ..... A Historical Perspective

Rhodium carbide has a storied history behind it. If literature accounts are correct, the first metal carbide molecule studied spectroscopically was PtC [73] in 1965. Soon after, RhC was spectroscopically identified in the gas phase by Lagerqvist (L), Scullman (S), and Kaving(K) [1]. Over the next two years, Scullman *et al.* studied the IrC [70, 71] and RuC [81, 82] molecules. In what can be viewed as a pioneering study, Lagerqvist, Scullman, and Kaving (LSK) used a high-temperature King furnace to produce these diatomic TM carbides. Lagerqvist *et al.* rotationally analyzed many bands recorded on photographic plates in the infrared and visible region. The spectra were often complex because of high temperature conditions in the experiments and numerous perturbations.

The emission spectrum of RhC certainly fits the observations of the high-temperature spectra mentioned in the previous paragraph. Lagerqvist, Scullman, and Kaving classified the bands observed in the RhC spectrum into three electronic systems. The (0,0) band of the $A^2\Pi - X^2\Sigma^+$ transition, the lowest energy system, was observed at

9800 cm^{-1}, in the near-infrared region. A vibrational analysis was performed on twenty-eight bands, of which, ten were rotationally analyzed. The spectrum of RhC proved to be very rich in the 400 - 500 nm region with no less than thirteen bands being observed. These bands were assigned to two $^2\Sigma^+ - X^2\Sigma^+$ transitions. The (0,0) band heads for the B - X and C - X transitions were reported at 21285 and 21452 cm^{-1} respectively. Two bands of the B - X system and eight bands of the C - X system were rotationally analyzed. According to the authors, the B and C excited states perturb each other in a way that both states were thought to be heavily mixed. Evidence for a fourth state, named the D state, was obtained through local perturbations in the C state. This D state was inferred to be of $^2\Sigma^-$ symmetry. A summary diagram illustrating the energies and assignments of the B, C, and D excited states observed by LS is shown in Fig. 4.1.

At this point the reader may wonder why the present study of RhC was undertaken. With the ongoing study of metal-based diatomic carbide molecules and other Rh-X species in Victoria, a spectrum of rhodium carbide was recorded in 1994 during a study of FeC [40] to test the quality of the laser ablation molecular beam source. The spectrum of RhC could be used as a wavemeter to help calibrate our other Rh-X spectra since the RhC spectrum is so rich in the 500 - 400 nm region. This interest in rhodium diatomic molecules led to a detailed examination of the RhC literature. As the literature concerning the visible region was scrutinized, some aspects of the original interpretation were deemed questionable. These concerns about the analysis led to our reassessment of the original problem and hence our exploration of the electronic structure of RhC. Some of these difficulties with the published interpretation are discussed below. With the

ground state of RhC firmly established under a $^2\Sigma^+$ symmetry, four of the five states detected by Scullman *et al.* were characterized as $^2\Sigma^+$ states. Even the original authors found this puzzling. Only the A state, a $^2\Pi_r$ state had a symmetry different from the other identified excited states. A molecule having many $^2\Sigma$ states may not seem puzzling; it is, however, where these states are energetically located that caused suspicion. The B and C excited states were observed to be only 168 cm^{-1} apart and, after a deperturbation analysis, the states were calculated to be only 15 cm^{-1} apart. If both states are of $^2\Sigma^+$ symmetry, it is surprising that states of the same symmetry lie so close in energy. Configuration interactions dictate that these states should mix and be driven further apart.

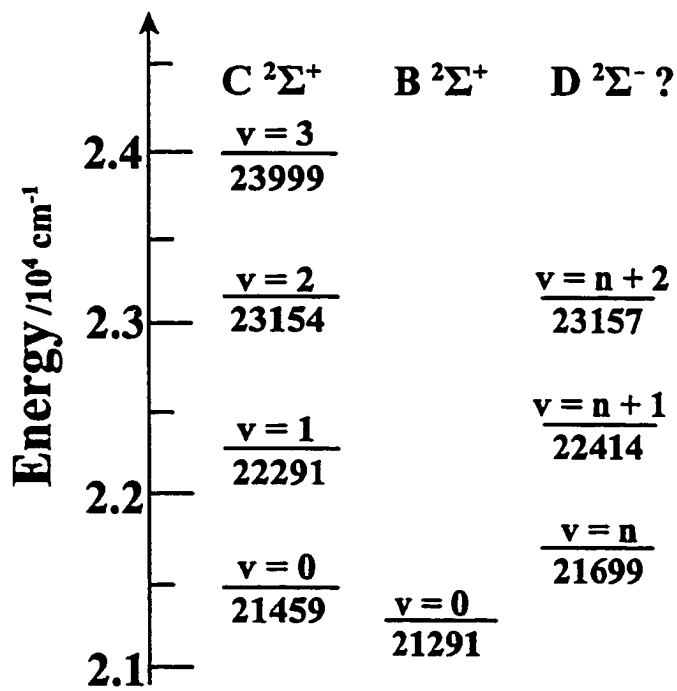

Fig. 4.1. The excited state energy levels and assignments of RhC as suggested by Lagerqvist and Scullman [1].

Of the bands that were rotationally analyzed for the B - X and C - X systems of RhC, only two were attributed to the B state and both shared $v' = 0$. This is a strange

to the B state and both shared $v' = 0$. This is a strange observation considering the (0,0) bands of both B - X and C - X transitions had very similar intensities and several vibrational levels associated with the C state were observed. Franck-Condon arguments ($r_B \neq r_X$) also favor the idea that higher vibrational levels of the B state should have been observed. The question that arises from these facts is why were no other vibrational levels of the B state observed. One can speculate that since the $v' = 0$ levels of the B and C states are heavily mixed the oscillator strength of the B-X transition is very small or nearly zero and the B state should have a long radiative lifetime.

Our next concern involves the value of the spin-rotation constant γ reported by Lagerqvist and Scullman for the $v'= 0$ level of the B state. Their deperturbed value ($+1.03$ cm^{-1}) is two orders of magnitude larger than and is opposite in sign to the value of γ_C (-0.03 cm^{-1}). The large value is not characteristic of γ reported for other metal carbides. For instance, the ground state of RhC [1] has a value of -0.06 cm^{-1} and for CoC [43], γ_X is -0.041 cm^{-1}. Since the other rotational constants associated with the B and C states mimic each other, the values of γ for both states should also be similar but this is not the case. The important observation is the fact that LS's spin-rotation constant (γ_B) is almost exactly twice the value of the rotational constant.

The fact that γ_B is roughly twice the rotational constant suggests that the symmetry of the B state is not $^2\Sigma^+$ as LS assigned but rather $^2\Pi$. A comparison of the rotational energy expressions for the $^2\Sigma^+$ and $^2\Pi$ states suggests the B state might be of $^2\Pi$ symmetry. The correlation between the spin-rotation constant and the rotational constant results from the rearrangement of the $^2\Pi$ energy level expression into a $^2\Sigma^+$ expression:

$$F_1^e(N) = BN(N + 1) - DN^2(N + 1)^2 + \tfrac{1}{2}\gamma N \quad (4.1)$$

$$F_2^f(N) = BN(N + 1) - DN^2(N + 1)^2 - \tfrac{1}{2}\gamma(N + 1) \quad (4.2).$$

Substitution of $J - \frac{1}{2}$ in equation 4.1 and $J + \frac{1}{2}$ in equation 4.2 for N yields

$$F_1^e(J) = B(J - 1/2)(J + 1/2) - D(J - 1/2)^2(J + 1/2)^2 + \tfrac{1}{2}\gamma(J - 1/2) \quad (4.3)$$

$$F_2^f(J) = B(J + 1/2)(J + 3/2) - D(J + 1/2)^2(J + 3/2)^2 + \tfrac{1}{2}\gamma(J + 3/2) \quad (4.4).$$

The splitting between the $F_2^f(J)$ and $F_1^e(J)$ levels ($\Delta\nu_{fe}$) would be:

$$\Delta\nu_{fe} = 2B(J + 1/2) - 4D(J + 1/2)^3 - \gamma(J + 1/2) \quad (4.5).$$

If a very small separation exists between the *e* and *f* rotational levels for the first values of J such that the levels are nearly degenerate, then $\gamma \approx 2B$. We have made two assumptions in the previous statement. First, the values of the D terms are so small they can be neglected and second, the Λ-type doubling is assumed to be very small or nearly zero. LS determined the γ value for the v = 0 level of the B state as 1.03 cm^{-1}, nearly twice that of the determined rotational constant of 0.5067 cm^{-1}.

In 1972, six years after the original LS work, the electron spin resonance (ESR), near-infrared, and electronic spectra of RhC in neon and argon matrices (at 4 K) were studied by Brom *et al* [58]. The bands of the C - X system were found to lie approximately 350 - 400 cm^{-1} higher than their gas phase counterparts as is often the case. Besides the bands of the C - X system, two other electronic systems in the 460 - 400 nm region were observed. The positive value determined for $\Delta g_\perp$ from ESR work is consistent with what is observed for a $^2\Pi_i$ state. Brom's results indicated that an unknown excited state of $^2\Pi_i$ symmetry was coupled to the ground state. The determined $\Delta g_\perp$ is related to the ground state through the spin-doubling constant (γ_X) by [83]

$$\gamma = -2B_v \Delta g_\perp \qquad (4.6)$$

where B_v is the mean of the rotational constants of the two states involved. The value of γ_X calculated through equation 4.6 is in good agreement with γ_X determined by LS's analysis.

During the time we were recording the LIF spectrum of RhC, an *ab initio* calculation detailing the electronic states/potential energy surfaces of RhC [69] appeared in the literature. In the calculation, Balasubramanian *et al* predicted just one $^2\Sigma^+$ state to lie near 20,000 cm^{-1}. The results of the calculation thus contradict the observations of Scullman *et al.* More importantly, the calculations predict a $^2\Pi$ state very close in energy to the $C^2\Sigma^+$ state. A $^2\Pi$ state in this energy region had not been identified by Lagerqvist and Scullman. Also, the *ab initio* results do not mention the $^2\Sigma^-$ state that Scullman *et al* referred to as the D state. It was peculiar that a $^2\Sigma^-$ symmetry was assigned to the state observed at 460 nm. Typically, interactions between states of $^2\Sigma^+$ and $^2\Sigma^-$ symmetries do not take place since these interactions would violate the selection rules for perturbations [3]. The true nature of the D state clearly needed to be investigated.

The anomalies outlined above, along with the recent *ab initio* study, have led us to question the RhC state assignments. Since other studies of rhodium diatomic species were taking place concurrently in our lab, it was decided to reinvestigate the RhC spectrum in the region 400 nm to 500 nm. It was hoped that the spectroscopic tools at our disposal could be used to clarify the RhC problem. Optimism existed that besides reproducing the bands previously reported, other vibrational levels of the B state would be discovered. Excited states lifetimes were recorded for all the bands originally reported

by LS. The information obtained from the lifetime measurements led to the discovery of several new bands that have been subsequently vibrationally and rotationally analyzed. With our reinvestigation, we have been able to shed new light on an old problem. The following sections will deal with how the RhC enigma was unraveled.

4.3. Reinterpretation of the RhC Spectrum....unraveling the RhC Mystery

(i) Reproduction of the RhC Spectrum

In most spectroscopic studies, analysis is made by focusing on the observed transition frequencies. However, since the original investigation posed many questions, a different approach would have to be taken if any headway were to be made. If one considers the anomalies of the original analysis as a mystery, the investigator would follow the principle of "leaving no stone unturned" no matter how trivial it may seem until the mystery was solved.

The spectra of transition metal carbides (as well as TM nitrides and oxides) can be very complicated because of the large number of excited states that result from the many unpaired *d* electrons. With the possibility of many excited states, a high degree of probability exists that interactions occur between them. To solve these problems, one should look at all the experimental evidence including transition intensities and excited state lifetimes.

Nonetheless, the first task undertaken was the reproduction of the RhC spectrum by means of LIF. A portion of the RhC spectrum (480 - 440 nm) is shown in Fig. 4.2. The bands observed by Lagerqvist and Scullman are present in this scan. Upon closer

inspection, extra features are present in the spectrum that were not observed in the original analysis. The nature of the new bands at 477.33, 452.34 and 460.51 nm along with the parentage of the excited states will be explained further on in the results section. Two of the bands in Fig. 4.2 are marked for RhH and C_2 impurities that result from the Rh + CH_4 ablation reaction.

The next step in our RhC investigation was to focus on the two bands reported to be heavily mixed, namely the transitions to the $v' = 0$ levels of the B and C states. To this end, the excited state lifetimes were measured by recording the LIF decay curves for all of the vibronic levels observed by Lagerqvist and Scullman. The experimentally determined lifetimes are listed in Table 4.1. As one can see the $v' = 0$ level of the C state has a lifetime that is decidedly longer (approximately twice as long) than the higher vibrational levels of the C state. Its lifetime is closer to that of the $v' = 0$ level of the B state. This result points to strong coupling between the B($v' = 0$) and C($v' = 0$) vibrational levels. If the C($v' = 0$) level were unperturbed, its excited state lifetime would be approximately 50 ns as in the other vibrational levels of the C state.

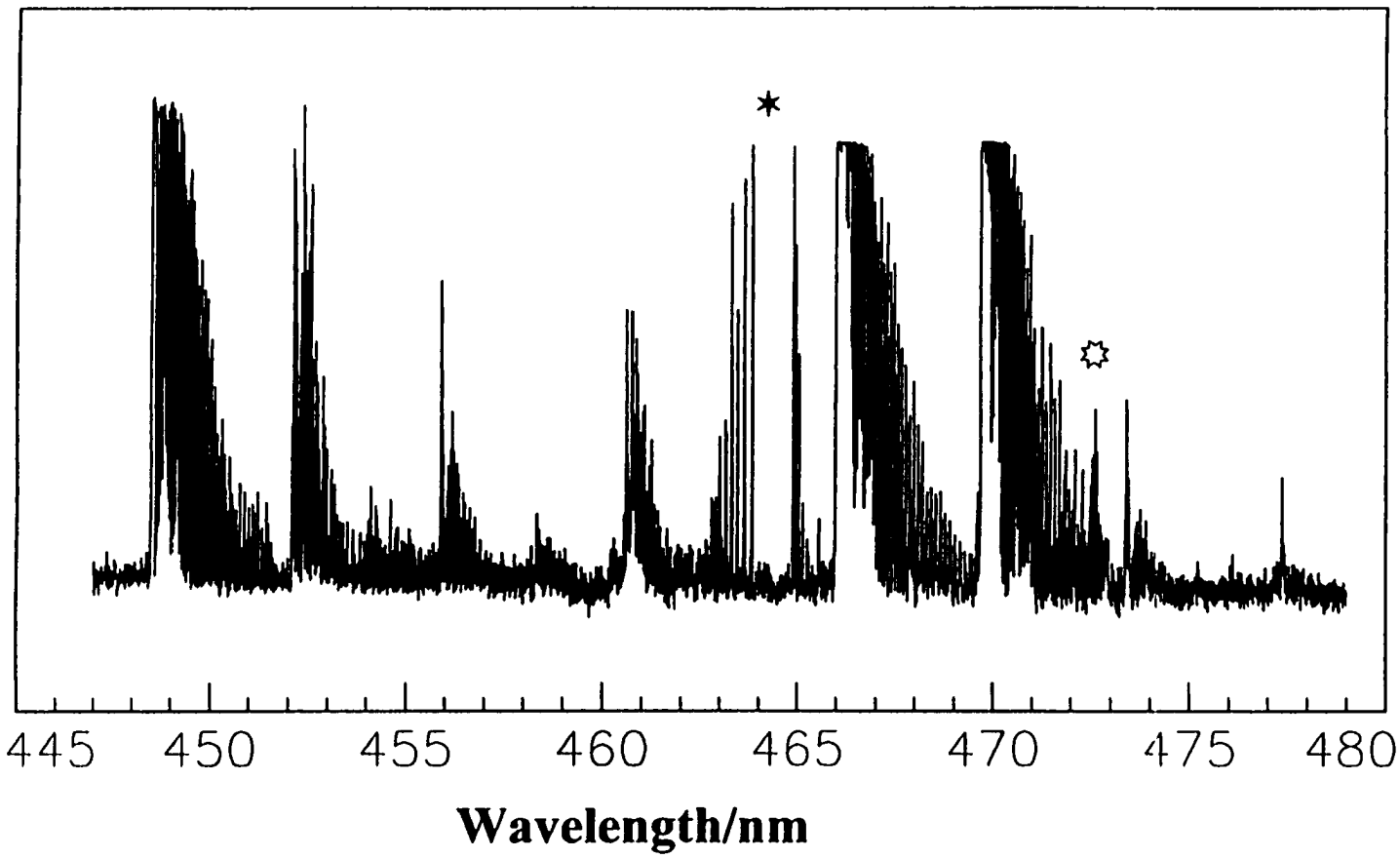

Fig. 4.2. The LIF spectrum of $Rh^{12}C$ recorded between 480 and 448 nm. The bands at 465.87, 455.87, 452.08, and 448.49 nm are the (0,0), (3,2), (2,1), and (1,0) bands of the Lagerqvist and Scullman C - X system respectively. The 469.55 nm band is their (0,0) band of the B - X system. The bands marked with a (*) and (✡) come from RhH and C_2 respectively. These molecules are side products of the Rh + CH_4 ablation reaction.

Level	Band measurement (nm)	Lifetime (± 5 ns)
$B^2\Sigma^+$ v = 0	469.55	100
$C^2\Sigma^+$ v = 0	465.87	80
$C^2\Sigma^+$ v = 1	448.49	50
$C^2\Sigma^+$ v = 2	431.77	50
$C^2\Sigma^+$ v = 3	416.57	50
$C^2\Sigma^+$ v = 4	403.17	50

If we consider two uncoupled electronic states such that the C-X transition has an appreciable oscillator strength and the B-X transition has very little oscillator strength, we expect to observe two very distinct transitions each with very different intensities and distinct upper state lifetimes. In other words, the rate of fluorescence (k_{FC}) from the C state would be appreciable whereas the rate of fluorescence (k_{FB}) from the B state would be nearly zero. The overall fluorescence signal would then be from the C-X transition. The unperturbed B-X transition intensity will be very weak (if observed at all) and its excited state lifetime very long. This example is illustrated in Fig. 4.3a. In this case the wavefunctions are not mixed. For the C-X and B-X transitions we have, respectively

$$|\langle\Psi_X|\mu|\Psi_C\rangle|^2 \propto (k_{FC}) \neq 0 \tag{4.7}$$

$$\text{and } |\langle\Psi_X|\mu|\Psi_B\rangle|^2 \propto (k_{FB}) \approx 0 \tag{4.8}.$$

However, if the states interact to the extent that they are equally mixed, as alluded to by Lagerqvist and Scullman, the intensities of the two transitions would be the same, as the weaker B-X transition would gain intensity at the expense of the stronger C-X

transition. The phenomenon is commonly called "intensity borrowing." A scheme representing this mixing situation is shown in Fig. 4.3.b. The rate of fluorescence for the B-X transition is now nonzero and approximately equal to $\frac{1}{2}k_{FC}$. The lifetime associated with the $v' = 0$ level of the B state would increase as a result of this mixing.

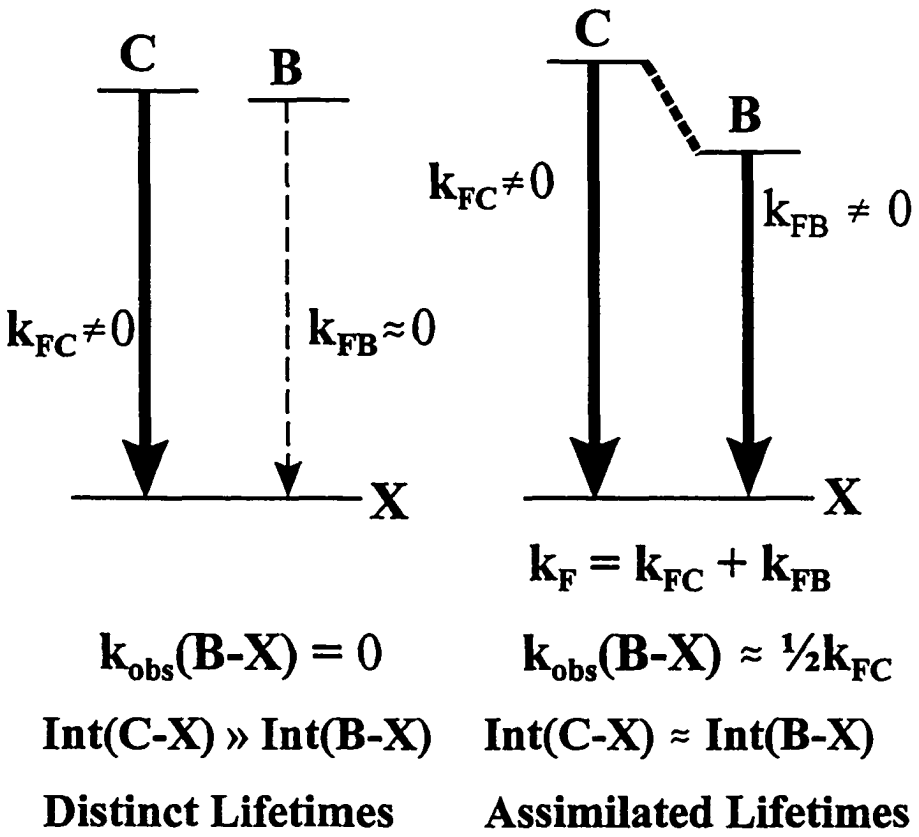

Fig. 4.3. Depiction of (a) the characteristics of uncoupled electronic states and (b) the characteristics and properties of interacting electronic states. The terms with k represent the rates of radiative fluorescence. The dark arrows indicate strong transitions while the lighter arrow represents a transition with very little oscillator strength.

The original wavefunctions Ψ_C and Ψ_B are no longer pure and therefore change to

accommodate this mixing. The wavefunctions for the mixed states can now be written as:

$$\Psi_C' = (1/\sqrt{2})(\Psi_B + \Psi_C) \tag{4.9}$$

$$\text{and } \Psi_B' = (1/\sqrt{2})(\Psi_B - \Psi_C) \tag{4.10}.$$

Substitution of Ψ_B' for Ψ_B in equation 4.8 yields:

$$|\langle\Psi_X|\mu|\Psi_B'\rangle|^2 = |\langle\Psi_X|\mu|(1/\sqrt{2})(\Psi_B - \Psi_C)\rangle|^2 \tag{4.11}.$$

If we expand the right hand side of equation 4.11, we find that

$$|\langle\Psi_X|\mu|\Psi_B'\rangle|^2 \cong \tfrac{1}{2}|\langle\Psi_X|\mu|\Psi_C\rangle|^2 = \tfrac{1}{2}k_{FC}' \tag{4.12}$$

since the parts of the equation involving Ψ_B would vanish as k_{FB} is equal to zero. Neglecting any nonradiative decay processes, we can use the relationship $\tau^{-1} = k_F$ to find that the lifetime of the $v' = 0$ level of the B state is about twice that of the unperturbed levels of the C state. This correlates well with the observed lifetimes presented in Table 4.1.

Lefebvre-Brion and Field [3] describe how the lifetime of the unperturbed B state can be estimated since the $v' = 0$ lifetimes of the mixed states and those of the unperturbed C state vibrational levels are known. Essentially, in a two level system, the coupled wavefunctions representing the B and C states (equations 4.9 - 4.12) can be written such that the general solutions are linear combinations:

$$\Psi_C' = \cos\theta\Psi_C + \sin\theta\Psi_B \tag{4.13}$$

$$\text{and } \Psi_B' = -\sin\theta\Psi_C + \cos\theta\Psi_B \tag{4.14}.$$

The excited state lifetimes (neglecting nonradiative decay processes) can be related to the lifetimes of the perturbed states as

$$(\tau_C')^{-1} = \cos^2\theta/\tau_C^0 + \sin^2\theta/\tau_B^0 \quad (4.15)$$

$$(\tau_B')^{-1} = \sin^2\theta/\tau_C^0 + \cos^2\theta/\tau_B^0 \quad (4.16)$$

$$(\tau_B')^{-1} + (\tau_C')^{-1} = (\tau_B^0)^{-1} + (\tau_C^0)^{-1} \quad (4.17)$$

where τ_B^0 and τ_C^0 are the lifetimes of the unperturbed levels. If we assume our experimental data to be correct (*i.e.*, $\tau_C^0 \approx 50$ ns, $\tau_B' \approx 100$ ns, and $\tau_C' \approx 80$ ns), a lifetime of approximately 400 ns is obtained for the unperturbed levels of the B state. The whole point of calculating the *unperturbed* lifetime of the B state is to confirm that its vibronic levels will have considerably longer lifetimes and that transitions to and from them are likely to be very weak in comparison to those of the C state. To facilitate detection of these very weak bands associated with the unperturbed levels of the B state, our experimental methods would have to be modified to accommodate the expected weaker signal intensity and long decay times. With this new insight on the vibrational levels of the B state, a search for new transitions was undertaken. The results are described in the following section.

(ii) New Bands Associated with the RhC Spectrum

We began the search for new transitions associated with the B electronic state by modifying our signal collection method. We employed the time-filtering method described in section 3.3(*i*). The integration window was offset so that the signal could be collected with $100 \leq t \leq 800$ ns in contrast to normal running conditions where the integration window is set to accumulate the signal between $0 \leq t \leq 50$ ns. By offsetting and widening the integration window (Fig. 3.4) more of the signal can be averaged and

any interference from the $C^2\Sigma^+ - X^2\Sigma^+$ emission could be minimized. Collection of more shots over the weaker portion of the fluorescence signal allowed for optimum data collection and therefore, a better signal to average to produce the spectrum.

The first area of the RhC spectrum to be resurveyed under these new experimental conditions, was the vicinity of the two (0,0) transitions. If the B and C states are truly $^2\Sigma$ states as LS suggest, then the chance of observing any other bands in this region would be minuscule. However, if the symmetry of the B state is other than $^2\Sigma^+$ symmetry, then the other multiplet component of the state should be nearby. Our survey efforts were rewarded. Two new transitions were detected. The intensities of these transitions are much weaker than those associated with the $C^2\Sigma^+ \leftarrow X^2\Sigma^+$ system. The TF-LIF and DF spectra for the newly observed red degraded RhC band at 477.33 are shown in Fig. 4.4 and Fig. 4.5 and the TF-LIF and DF spectra for the 460.51 nm band are shown in Fig. 4.6 and Fig. 4.7. Inspection of Fig. 4.4 and Fig. 4.6 reveals that the branch structure of these new bands is more complicated than the four branches expected for a $^2\Sigma^+ \leftarrow {}^2\Sigma^+$ transition. We were able to identify six branches in both instances. The branch structure of these new bands is more characteristic of a $^2\Pi \leftarrow {}^2\Sigma^+$ transition than a $^2\Sigma^+ \leftarrow {}^2\Sigma^+$ transition. The DF spacings confirmed the transitions belong to $Rh^{12}C$. The absence of any nodal structure in the DF spectrum (Fig. 4.5) of the 477.33 nm vibronic level indicates that the upper state involved in this transition has $v' = 0$. The DF spectrum of the 460.51 nm level (Fig. 4.7) shows one node. Its upper level is therefore assigned to a $v' = 1$ vibronic state.

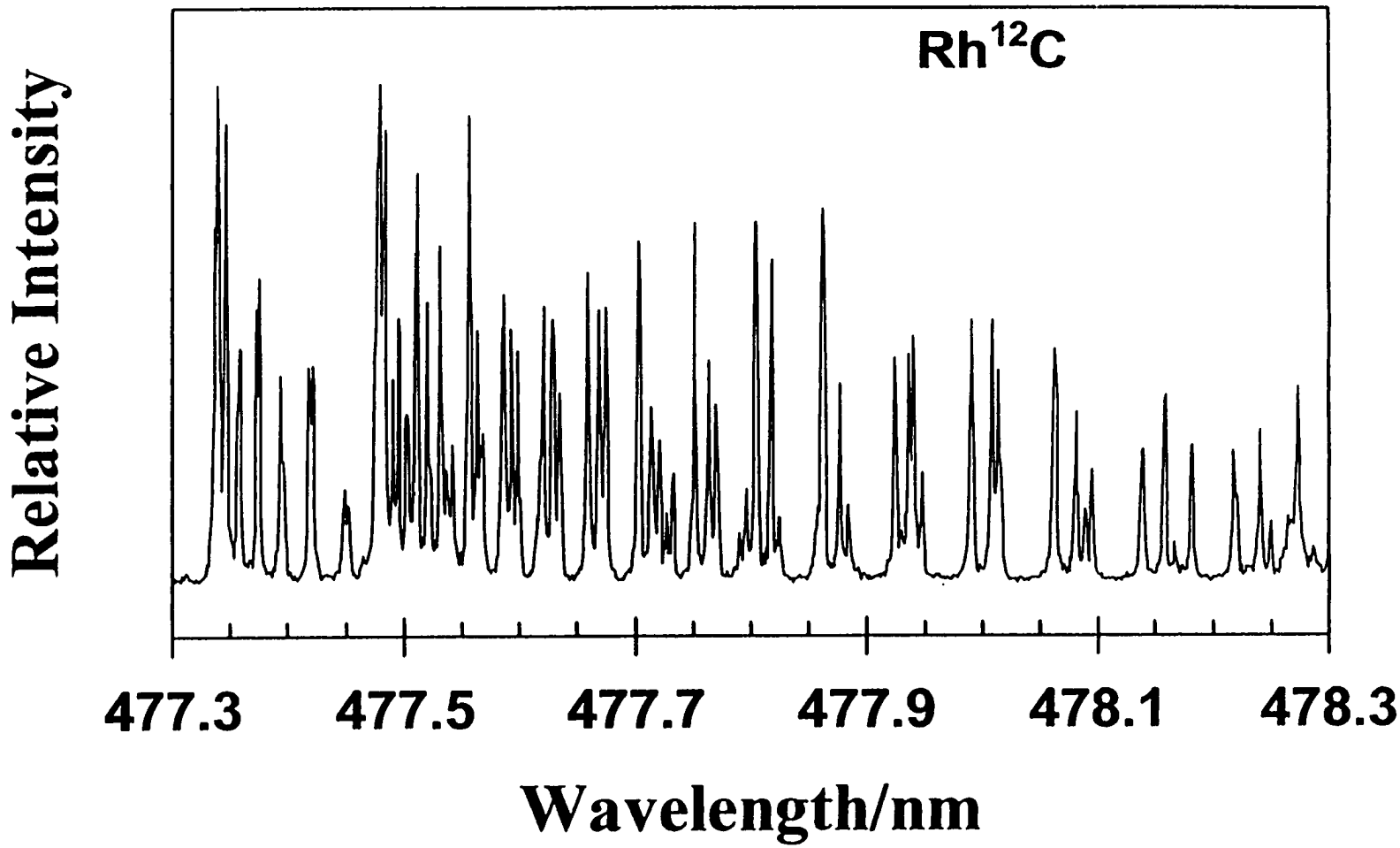

Fig. 4.4. The results of the application of the TF-LIF technique to record the spectrum of $Rh^{12}C$. The TF-LIF spectrum for the 477.33nm band is shown. More than four branches are present.

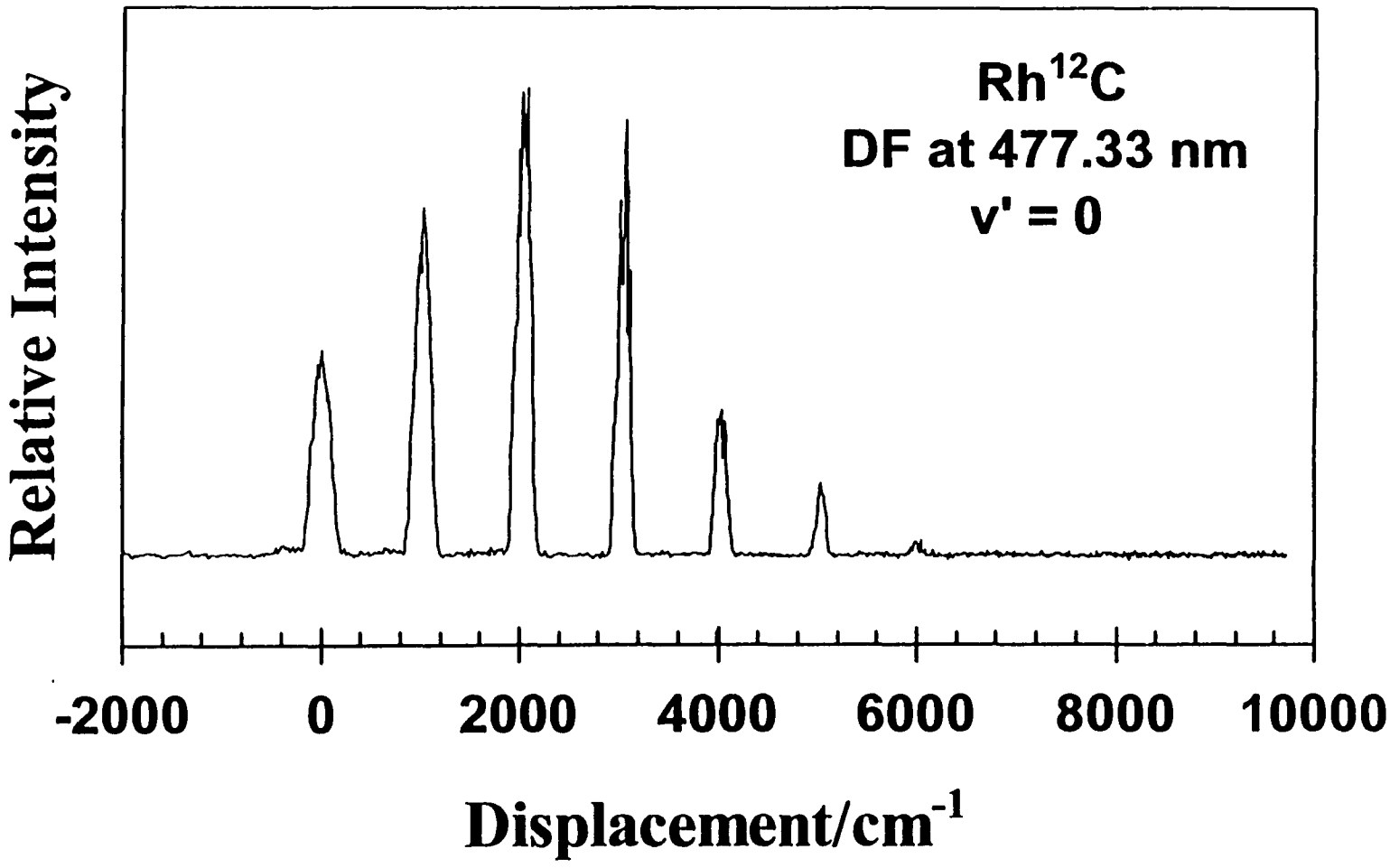

Fig. 4.5. The DF spectrum recorded for this vibronic level with the excitation laser fixed at 477.33 nm. The absence of nodal structure indicates the upper state has $v' = 0$.

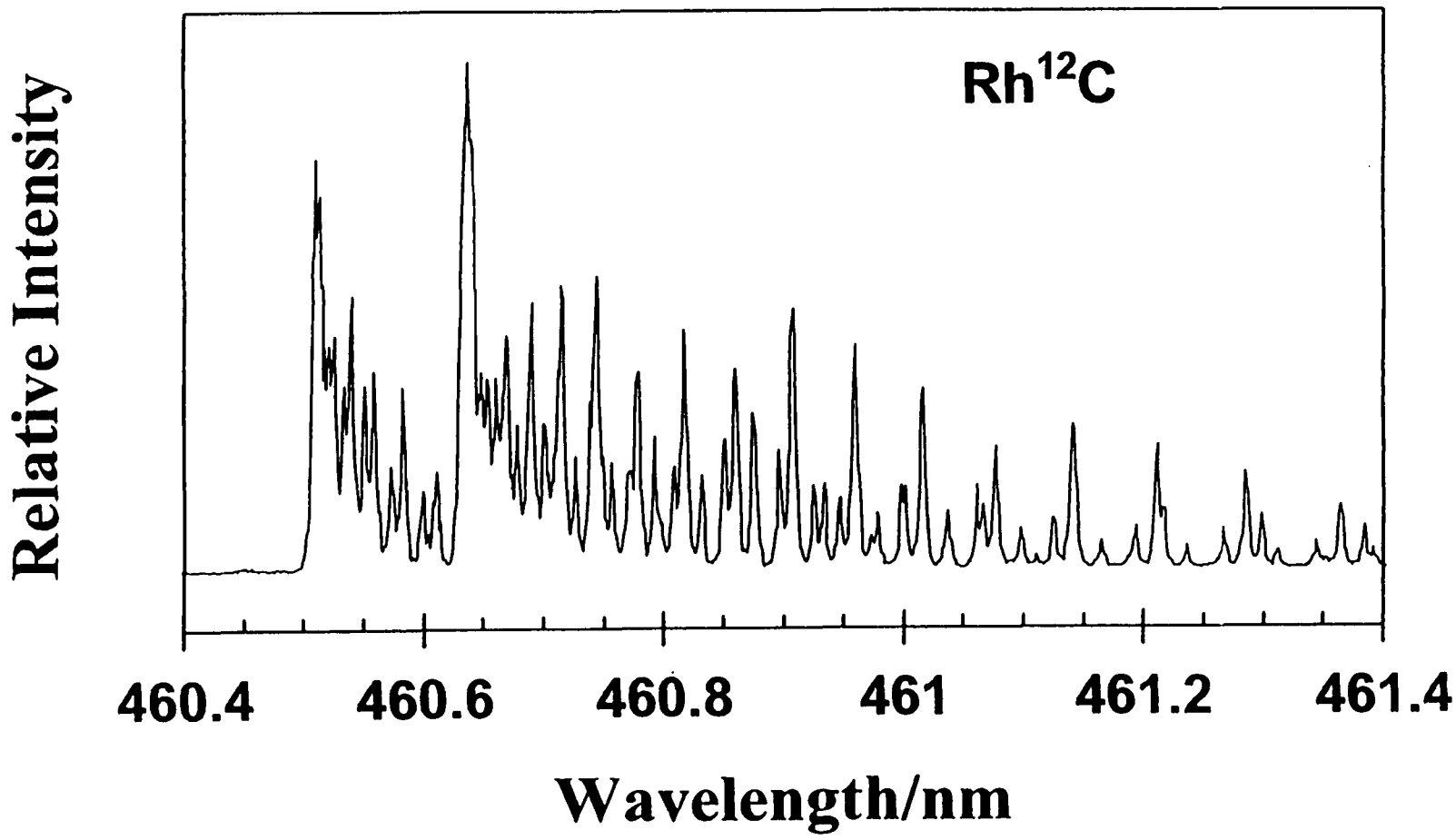

Fig. 4.6. The results of the application of the TF-LIF technique to record the spectrum of $Rh^{12}C$. The TF-LIF spectrum for the 460.51 nm band is shown. More than four branches are present.

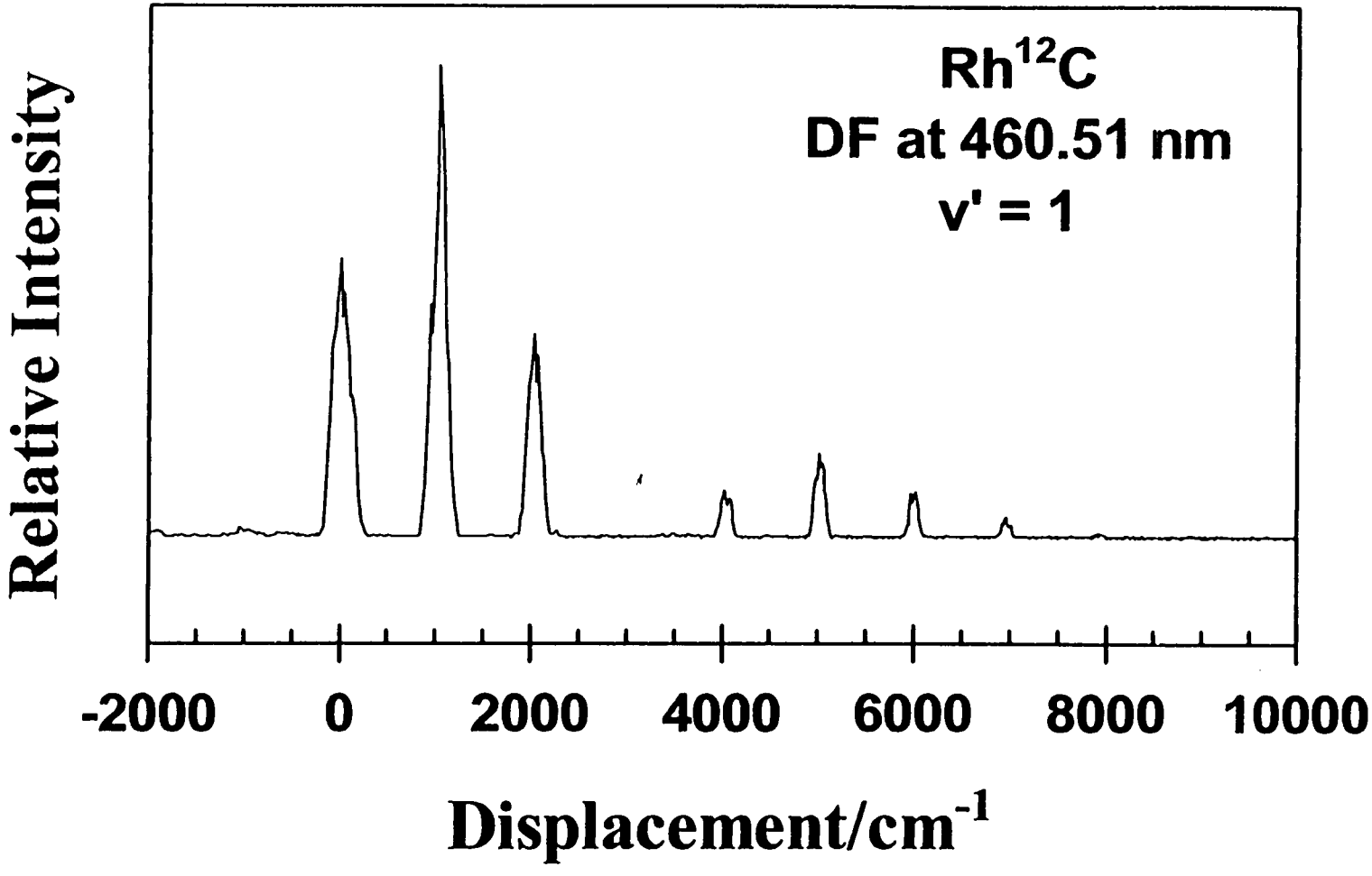

Fig. 4.7. The DF spectrum recorded for this vibronic level with the excitation laser fixed at 460.51 nm. The presence of one node in the intensity distribution suggests the upper state has v' = 1.

The branch structure of the 477.33 nm (0,0) band was mentioned in the previous paragraph. Since the 477.33 nm band fitted the criteria of what was expected for the bands of unperturbed vibrational levels of the B state, we wanted to compare and contrast the properties of the 477.33 nm band to the bands observed by Lagerqvist and Scullman. In Fig. 4.8 we show (a) the (2,0) band observed at 431.77 nm for the $C^2\Sigma^+$ - $X^2\Sigma^+$ system, (b) the newly detected 477.33 nm (0,0) band and (c) the 469.55 nm band assigned by LS [1] as the (0,0) bands of the $B^2\Sigma^+ \leftarrow X^2\Sigma^+$ system. From Fig. 4.8, one can see differences present in the branch structure of each spectrum. The (2,0) band of the apparently unperturbed $C^2\Sigma^+$ - $X^2\Sigma^+$ system (Fig. 4.8a) has a "simple" structure with two R and two P branches with the low J lines of the R branches so closely spaced that only one band head is evident. The spectrum displayed in Fig. 4.8b (also presented in Fig. 4.4) shows that the 477.33 nm band has a more complicated branch structure, with what looks like two R-branch heads. There are marked differences in relative intensities of the three bands. The 477.33 nm band is by far the weaker of the three. The (0,0) band of the B - X system is displayed in Fig. 4.8c. The band's structure is interesting. It has features that resemble both of the bands just described. The intensity of the 469.55 nm band is comparable to the 431.77 nm band and both bands have four branches. However, the 469.55 nm band's outward appearance is more like the 477.33 nm band but with fewer branches. If the $v' = 0$ level of the B state were not mixed with the $v' = 0$ level of the C state, the (0,0) B-X transition would be expected to be much weaker, like the transition represented by the 477.33 nm band.

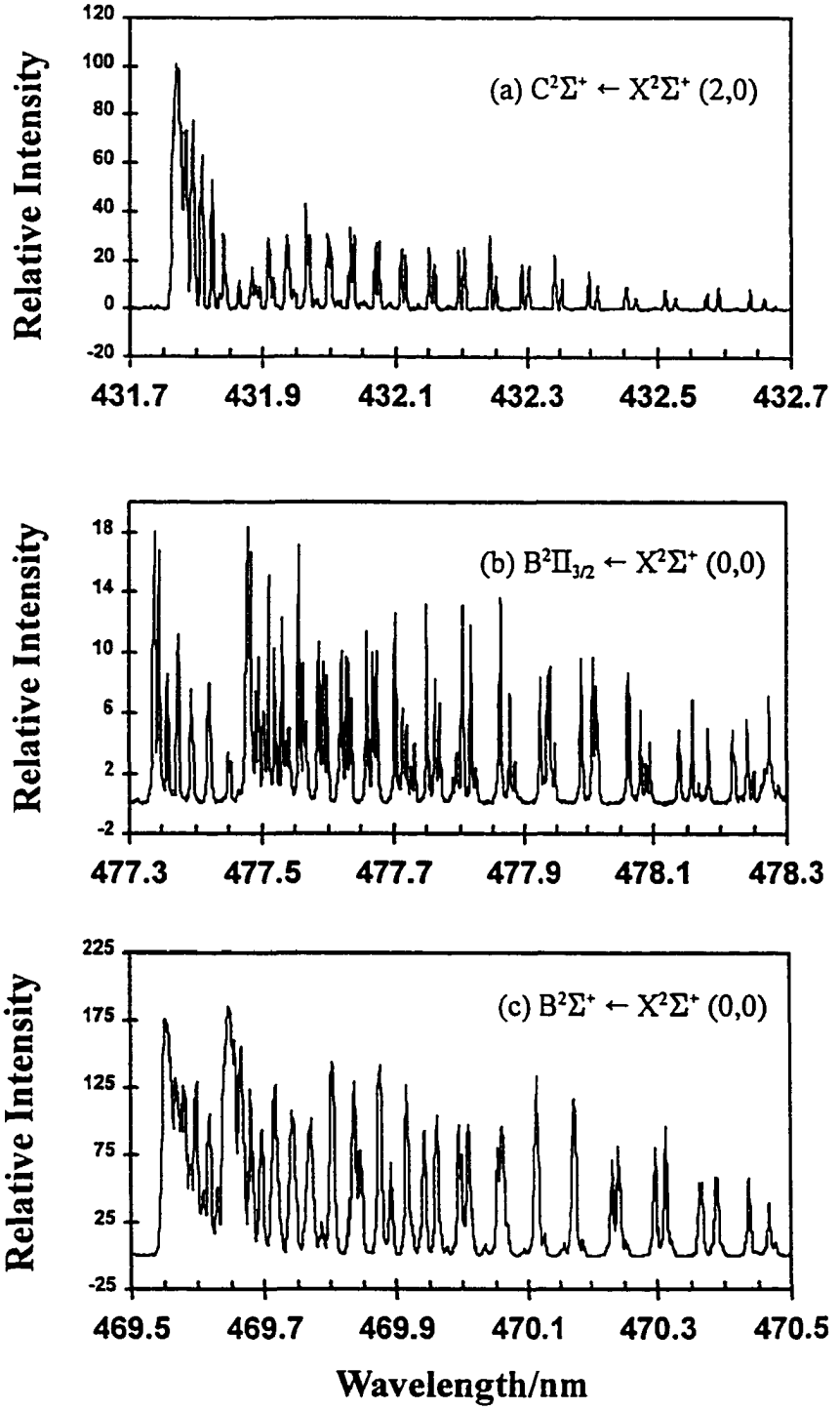

Fig. 4.8. Comparison of the band profiles of RhC. The spectrum shown in (a) is the (2,0) band of the unperturbed $C^2\Sigma^+ \leftarrow X^2\Sigma^+$ system. In (b) the newly observed band at 477.33 nm is shown. The branch structure shows that the transition is too complicated for a $^2\Sigma^+ \leftarrow X^2\Sigma^+$ transition. The band shown in (c) was assigned by LS as the (0,0) band of the $B^2\Sigma^+ \leftarrow X^2\Sigma^+$ system.

The energy separation between the vibronic levels represented by the 477.33 nm and 460.51 nm bands is approximately 760 cm^{-1}. This energy separation is reasonable for v and (v + 1) that belong to the same electronic state. The vibrational information obtained from the DF spectra also suggest that the 477.33 nm and 460.51 nm bands involve vibronic levels belonging to the same upper electronic state. The lifetimes of the two levels are distinctively longer than the levels of the C state. A comparison of the LIF decay curves and excited state lifetimes will be given in the next paragraph.

The next logical course of action was to record lifetimes for these two levels. The LIF decay curves were recorded at 416.57 nm ($v' = 3$, C state), 469.55 nm ($v' = 0$, B state), and 477.33 nm (newly observed band) to compare the lifetimes of the three transitions. These wavelengths correspond to the highest energy branch heads in each of the three bands shown in Fig. 4.8. The decay curves are displayed for comparison on the same time scale in Fig. 4.9. The top portion of the figure (Fig. 4.9a) represents the decay curve for the apparently unperturbed $v' = 3$ level of the C state. This curve is almost identical to those recorded for the other unperturbed levels of the C state ($v' = 1$, 2, and 4). The middle plot (Fig. 4.9b) is the decay curve of the perturbed $v' = 0$ level of the B state. It is somewhat broader in profile than (a). All the vibrational levels of the C state and the $v' = 0$ level of the B state observed by LS have lifetimes in the 50 to 100 ns range. The decay curve recorded at 477.33 nm is displayed in Fig. 4.9c. One can immediately see that the decay curve at 477.33 nm is quite different than the two curves in Fig. 4.9a and 4.9b. The lifetime of this upper state level was determined to be ~ 800 ns; about an order of magnitude larger than the lifetimes associated with the Lagerqvist

and Scullman bands. A similar lifetime was determined for the vibronic level associated with the 460.51 nm band (1100 ns).

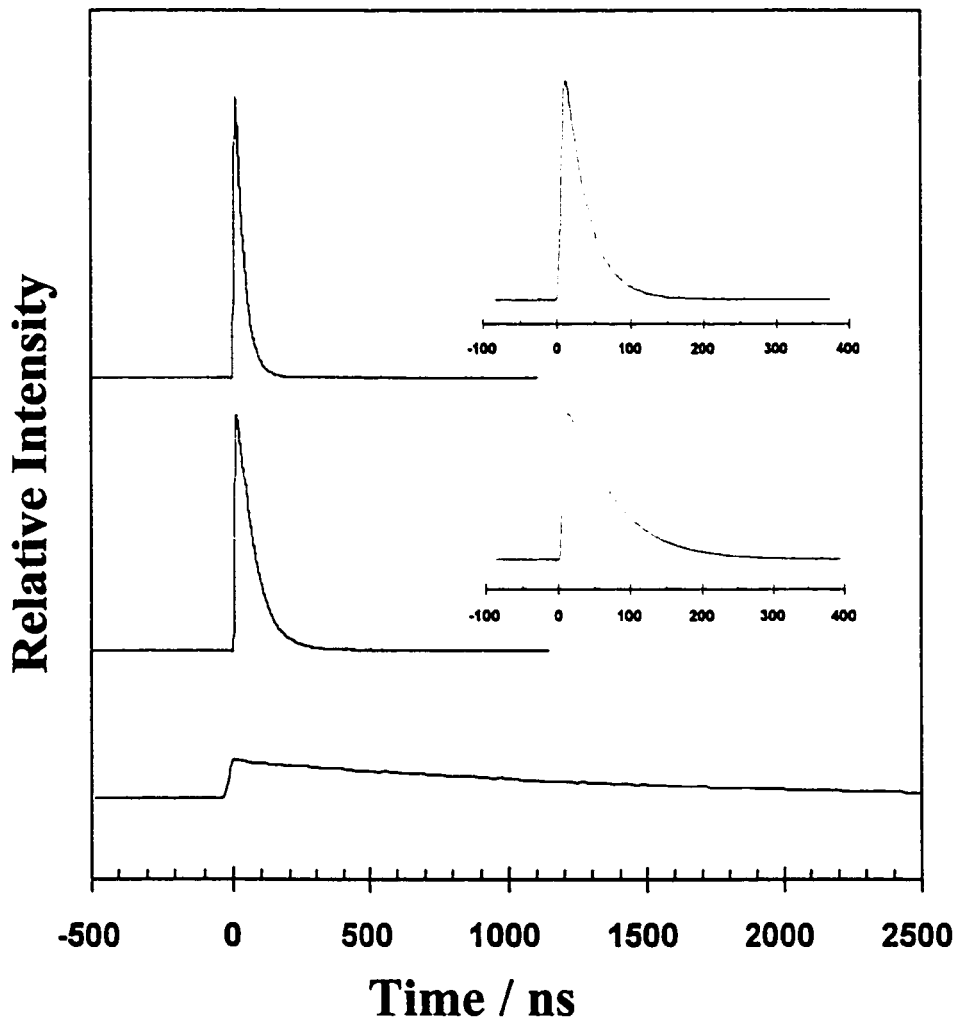

Fig. 4.9. The LIF decay curves obtained at (a) 416.57 nm, (b) 469.55, and (c) 477.33 nm. The insets of (a) and (b) are reproductions on a smaller time scale. The lifetimes for all the vibronic levels of the B and C states are reported in Table 4.1 and Table 4.3.

The lifetimes associated with the 477.33 and 460.51 nm bands approximate the expected lifetimes of unperturbed vibrational levels of the B state. With the contrast in signal intensities for these transitions, it is easy to understand how the bands associated with the unperturbed levels of the B state could be easily overlooked in a global scan (large scan step).

The $Rh^{12}C$ LIF spectrum between 530 - 400 nm appears very congested because the bands of the C-X system are so intense. The $Rh^{12}C$ LIF spectrum we recorded has 21 bands that involve transitions between various vibrational levels of the $C^2\Sigma^+$ state and $X^2\Sigma^+$ ground state, thirteen of which were observed by LS. The emission spectrum photographed by Lagerqvist and Scullman [1] displayed the same congestion in the 500 - 400 nm region. Since their studies employed a King furnace to produce $Rh^{12}C$, the emission spectrum they photographed appeared at a very high temperature. As a result, the $Rh^{12}C$ spectrum they photographed suffered even more spectral congestion than we observed. We believe this to be the reason why Lagerqvist and Scullman did not detect any of the new bands. Because of this spectral congestion, the TF-LIF technique is especially useful in any "hunt" for new bands. The ultimate usefulness of the time-filtering technique is illustrated in Fig. 4.10. In this figure we present part of the $Rh^{12}C$ spectrum near the C-X (2,0) band at 431.77 nm. The "normal" LIF spectrum is presented in Fig. 4.10a whereas, in Fig. 4.10b, a TF-LIF spectrum is shown. As mentioned in the description of the technique, we have suppressed most of the signal contribution due to the $C^2\Sigma^+ - X^2\Sigma^+$ transition. The TF-LIF technique gave us the chance to record quality spectra which could be used to perform rotational analyses.

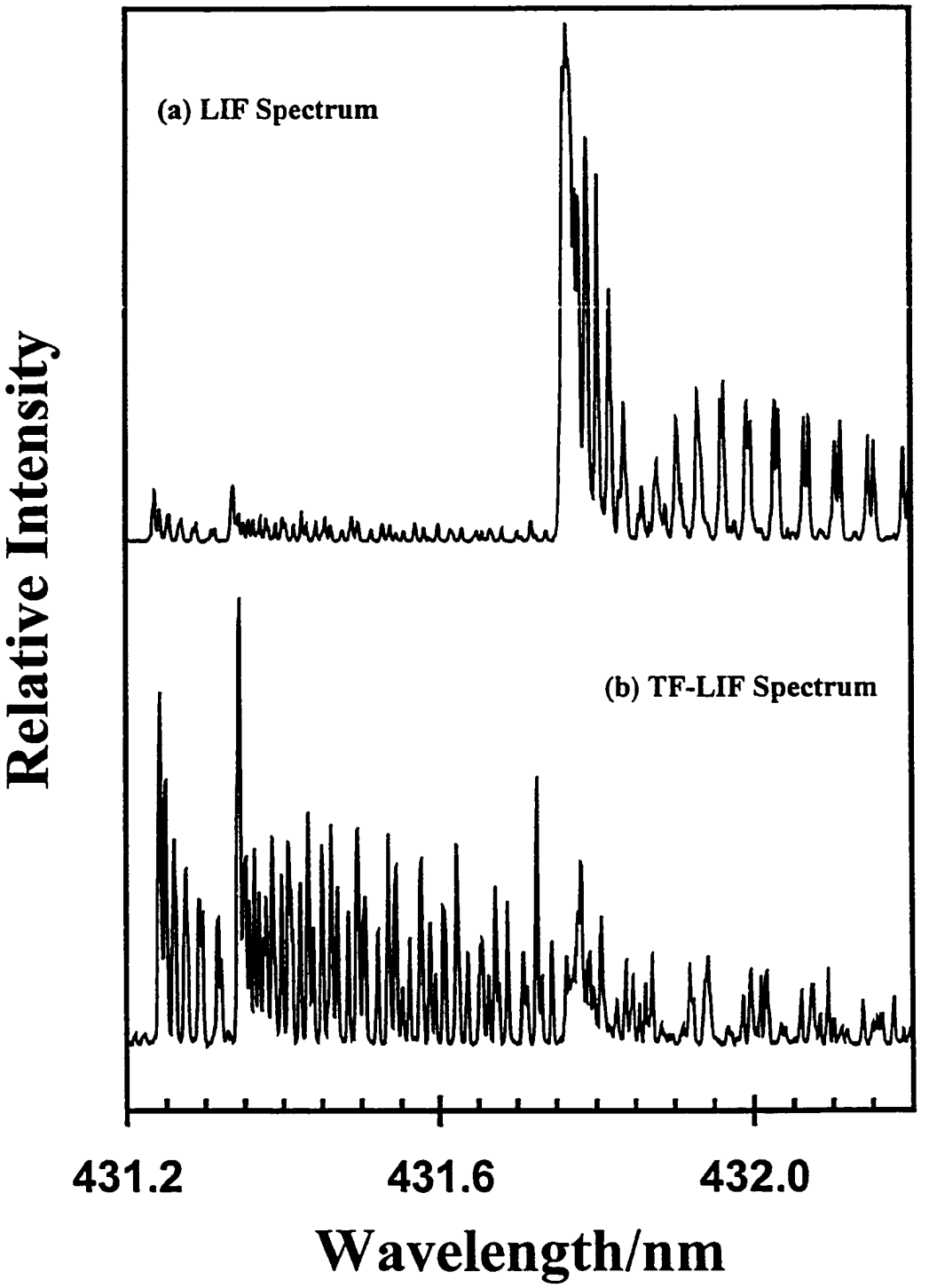

Fig. 4.10. $Rh^{12}C$ spectra recorded with two different time windows. The upper spectrum (a) was collected with $0 \leq t \leq 50$ ns and is dominated by $C^2\Sigma^+ - X^2\Sigma^+$ emission from the (2,0) band with the head at 431.77 nm. The weaker feature to higher energy is the emission belonging to the (3,0) band of the $^2\Pi - X^2\Sigma^+$ system. The contribution to the signal from the C - X emission in lower spectrum (b) has been effectively eliminated by averaging the signal in the range $100 \leq t \leq 800$ ns.

Our reinvestigation of the 530 - 400 nm region of $Rh^{12}C$ spectrum via the TF-LIF technique has led to the discovery of twelve new transitions. All of these bands degrade towards to the red. The vibronic levels associated with these new bands have lifetimes that are much longer (> 500 ns) than the lifetimes associated with the vibrational levels of the $C^2\Sigma^+$ electronic state. The newly detected bands have profiles that are similar to the 477.33 nm and 460.55 nm bands (see Fig. 4.4 and Fig. 4.6). The locations of these bands are represented by stick spectra displayed in Fig. 4.11. The top part of Fig. 4.11 shows the C- X bands previously observed by Lagerqvist and Scullman. The bottom part of Fig. 4.11 shows the new bands observed in this work. The vibrational spacings allowed for estimations of ω_e and $\omega_e x_e$ for both progressions. A fit of the vibrational intervals of the lowest energy progression yielded values of 768 and 6.3 cm^{-1} for ω_e and $\omega_e x_e$ respectively. Values of 831 and 15.5 cm^{-1} were obtained for ω_e and $\omega_e x_e$ vibrational constants of the second progression. The values for the second progression are to be taken with a grain of salt because this substate interacts with the levels of the $C^2\Sigma^+$ state. Vibrational assignments are also included in Fig. 4.11. The assignments were based on $Rh^{12}C/Rh^{13}C$ isotope shifts and DF spectra. Fig. 4.12 shows the isotope shifts for selected RhC bands in the LIF spectra for the region 499 to 486 nm for the $Rh^{13}C$ (top) and $Rh^{12}C$ molecules (bottom). Band positions, vibrational assignments, and isotopic data are listed in Table 4.2. The lifetimes for the upper vibrational levels of these new bands are listed in Table 4.3.

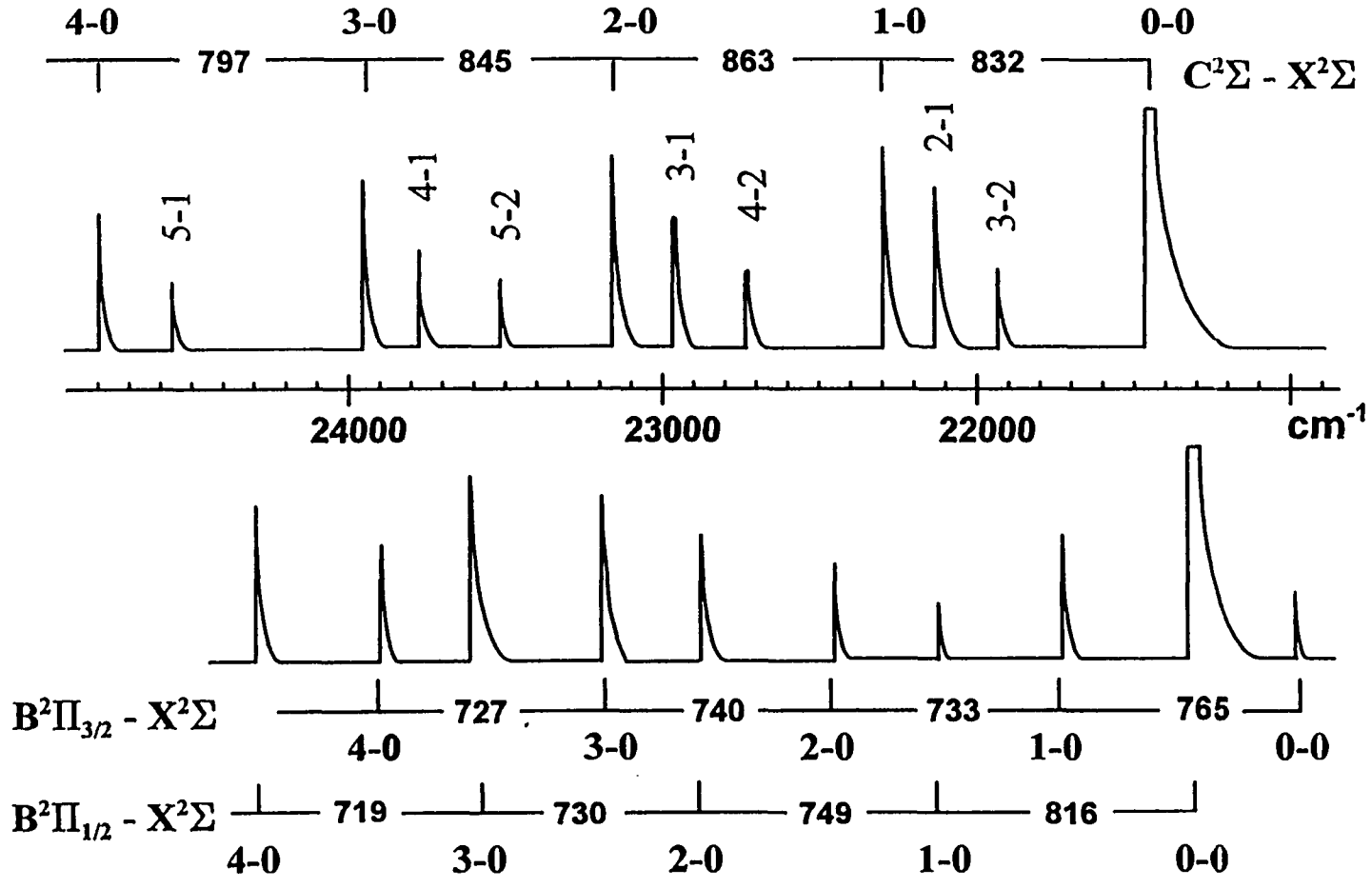

Fig. 4.11. A schematic illustrating the observed spectrum of $Rh^{12}C$ in the 400 - 480 nm region. The upper spectrum represents the bands observed by LS (levels with short lifetimes) whereas the bottom spectra represent the new bands (levels with long lifetimes). Vibrational assignments and values of the vibrational spacings are included.

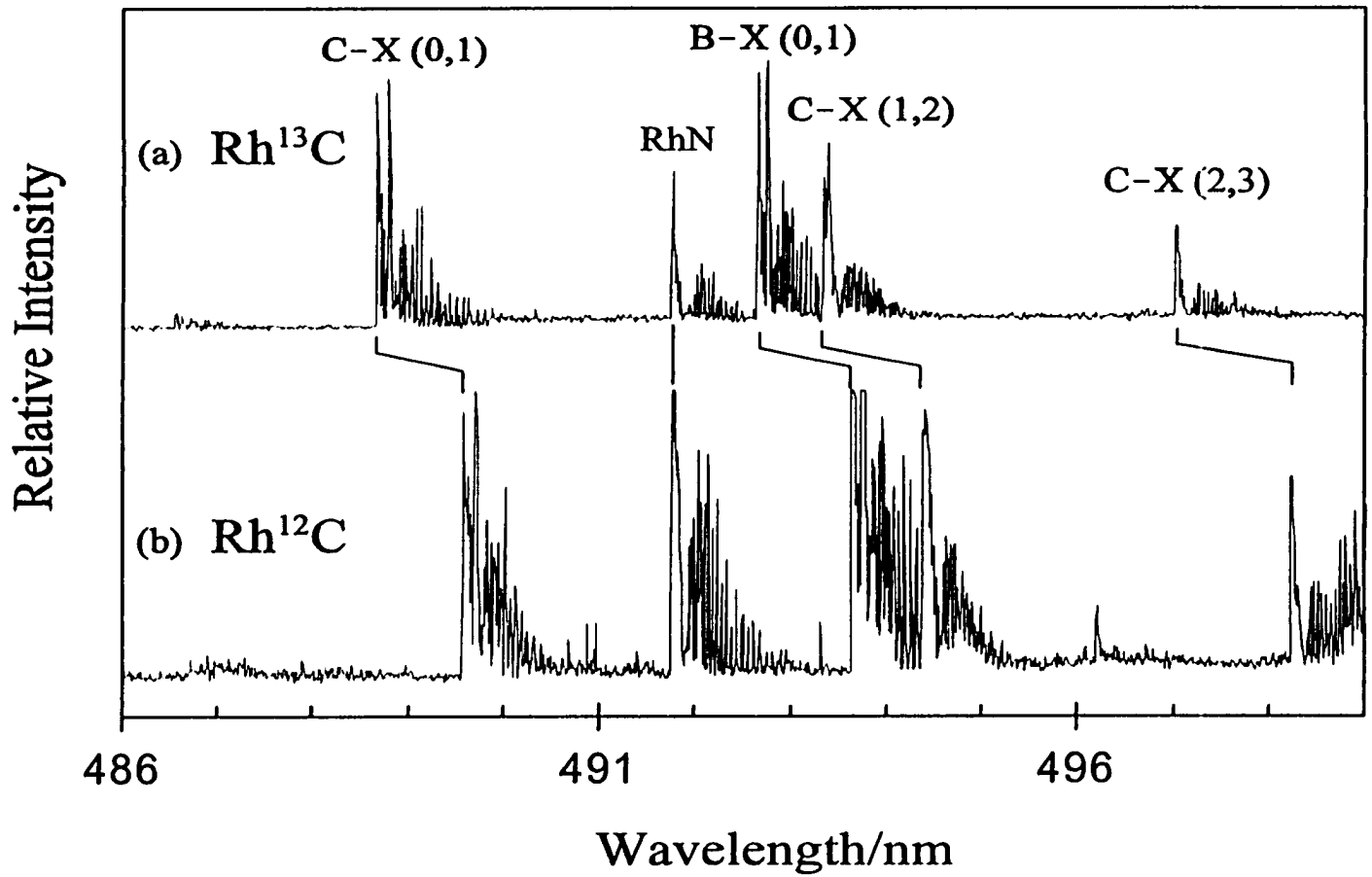

Fig. 4.12. The LIF spectra of (a) $Rh^{13}C$ and (b) $Rh^{12}C$ in the 499 - 486 nm region. The isotope shifts are marked along with the band assignments. The band at 491.70 nm is the (1,0) band of the [19.4] - $X^1\Sigma^+$ system of RhN observed as an impurity in the RhC spectra.

Table 4.2. Band Heads* in the 530-400 nm spectrum of $Rh^{12}C/Rh^{13}C$.

λ_{air} (nm)	ν_{vac} (cm^{-1})	Assignment	$\lambda_{air}(Rh^{13}C)$ (nm)	ν_{vac} (cm^{-1})	$\Delta\nu$ $Rh^{12}C$-$Rh^{13}C$ (cm^{-1})
528.92	18901	$C^2\Sigma^+$-X, 3-5	526.32	18995	-94
524.66	19055	$C^2\Sigma^+$-X, 2-4	522.27	19142	-87
520.63	19202	$C^2\Sigma^+$-X, 1-3	518.64	19276	-74
520.07	19222	$B^2\Pi_{1/2}$-X, 0-2	518.12	19295	-73
515.59	19390	$C^2\Sigma^+$-X, 0-2	513.61	19465	-75
498.24	20065	$C^2\Sigma^+$-X, 2-3	496.94	20118	-53
494.37 †	20222	$C^2\Sigma^+$-X, 1-2	493.32	20265	-43
493.65 †	20252	$B^2\Pi_{1/2}$-X, 0-1	492.62	20294	-42
489.58 †	20420	$C^2\Sigma^+$-X, 0-1	488.68	20458	-38
478.11 †	20910	$C^2\Sigma^+$-X, 3-3			
477.33	20944	$B^2\Pi_{3/2}$-X, 0-0			
474.50	21069	$B^2\Pi_{1/2}$-X, 1-1			
474.14	21085	$C^2\Sigma^+$-X, 2-2			
469.55 †	21291	$B^2\Pi_{1/2}$-X, 0-0	469.58	21290	+1
465.87 †	21459	$C^2\Sigma^+$-X, 0-0	465.80	21462	+3
460.51	21709	$B^2\Pi_{3/2}$-X, 1-0	461.03	21684	+25
455.87	21930	$C^2\Sigma^+$-X, 3-2	456.39	21905	+25
452.34	22107	$B^2\Pi_{1/2}$-X, 1-0			
452.08 †	22114	$C^2\Sigma^+$-X, 2-1	452.45	22096	+18
448.49 †	22291	$C^2\Sigma^+$-X, 1-0	449.04	22263	+28
445.47	22442	$B^2\Pi_{3/2}$-X, 2-0	446.36	22397	+45
443.49	22542	$B^2\Pi_{1/2}$-X, 3-1			
439.91	22726	$C^2\Sigma^+$-X, 4-2			
437.40	22856	$B^2\Pi_{1/2}$-X, 2-0			
435.44	22959	$C^2\Sigma^+$-X, 3-1	436.24	22917	+42
431.77 †	23154	$C^2\Sigma^+$-X, 2-0	432.73	23103	+51
431.25	23182	$B^2\Pi_{3/2}$-X, 3-0			
429.71	23265	$B^2\Pi_{1/2}$-X, 4-1			
425.23	23510	$C^2\Sigma^+$-X, 5-2			
423.86	23586	$B^2\Pi_{1/2}$-X, 3-0			
420.80	23758	$C^2\Sigma^+$-X, 4-1			
418.14	23909	$B^2\Pi_{3/2}$-X, 4-0			
416.57 †	23999	$C^2\Sigma^+$-X, 3-0			
411.32	24305	$B^2\Pi_{1/2}$-X, 4-0			
407.39	24540	$C^2\Sigma^+$-X, 5-1			
403.17	24796	$C^2\Sigma^+$-X, 4-0			

*The head to shortest wavelength.

†Observed by Lagerqvist and Scullman

Two groups of bands have been identified besides those of the $C^2\Sigma^+ - X^2\Sigma^+$ system. The first progression is anchored at 477.33 nm and the second is the B-X (0,0) bands at 469.55 nm. These new progressions have led to the reassignment of the B - X system. Direct observation of these two new progressions has led us to deduce that the new bands may represent vibronic levels of substates that belong to the same electronic state, *i.e.*, the spin-orbit components of a $^2\Pi$ state. The 469.55 nm band previously assigned by LS as the (0,0) band of the $B^2\Sigma^+ - X^2\Sigma^+$ system is actually one of the (0,0) bands associated with $^2\Pi - X^2\Sigma^+$ transition. The other (0,0) band associated with the other spin orbit component of the $^2\Pi - X^2\Sigma^+$ transition is the band located at 477.33 nm. It so happens that the energies of the $v' = 1, 2$ and 3 levels of the progression starting at 477.33nm lie very close in energy to the levels of the $D^2\Sigma^-$ state tentatively assigned by LS.

The experimental evidence presented to this point along with the predictions of the *ab initio* calculations [69] and the inference of an excited state of $^2\Pi_i$ symmetry from matrix work/ESR measurements [58] cast doubt on LS's respective assignments of $^2\Sigma^+$ and $^2\Sigma^-$ symmetries for the B and D states.

Table 4.3. $Rh^{12}C$ lifetimes for the vibronic levels of the newly observed bands detected using the TF-LIF technique.

Level	Band measurement (nm)	Lifetime (± 25 ns)
$B^2\Pi_{3/2}$ v = 0	477.33	800
$B^2\Pi_{3/2}$ v = 1	460.51	1100
$B^2\Pi_{3/2}$ v = 2	445.47	975
$B^2\Pi_{3/2}$ v = 3	431.25	950
$B^2\Pi_{3/2}$ v = 4	418.14	525
$B^2\Pi_{1/2}$ v = 0	469.55	100
$B^2\Pi_{1/2}$ v = 1	452.34	525
$B^2\Pi_{1/2}$ v = 2	435.44	700
$B^2\Pi_{1/2}$ v = 3	423.86	600
$B^2\Pi_{1/2}$ v = 4	411.32	525

(iii) Rotational Analysis of the New Bands of $Rh^{12}C$

The rotational constants for the $^2\Sigma^+$ ground state of RhC (B, D, and γ) have been previously established by Lagerqvist and Scullman [1], and Scullman and Kaving [57]. They used the method of combination differences (means of the values of all the observed bands) to determine B and D from plots of $\Delta_2F''(N)/4(N+½)$ as a function of $(N+½)^2$. The B values obtained for the v = 0 to v = 3 allowed for the evaluation of the ground state vibration-rotation interaction constant (α) according to the equation

$$B_v = B_e - \alpha_e(v + ½) \qquad (4.18).$$

Values of 0.6027(5) and 0.00396(3) cm^{-1} were obtained for $B_e^{\cdot}$ and $\alpha_e^{\cdot}$ respectively. The ground state spin-splitting constants (γ_v) were obtained from the differences of the combination differences [1]

$$\Delta_2F_1(N) - \Delta_2F_2(N) = 2\gamma_v \qquad (4.19).$$

The value of $2\gamma_0$ for the ground state was -0.13(1) cm^{-1}.

Rotational analyses have been carried out for most of the new bands. The analysis of bands in the progression anchored at 477.33 nm was rather straightforward. The (0,0) and (1,0) bands of this progression have been described previously and are displayed in Fig. 4.4 and Fig. 4.6. Six branches are easily identified in each band. The branches of these bands are those of a $^2\Pi_{3/2} - {}^2\Sigma^+$ transition associated with one component of a $^2\Pi_i - {}^2\Sigma^+$ transition namely R_{11}, Q_{11}, P_{11}, $^QR_{12}$, $^PQ_{12}$, and $^OP_{12}$. First lines of the $^2\Pi_i - {}^2\Sigma^+$ transitions are illustrated in Fig. 4.13. The (2,0) band of this $^2\Pi_{3/2} - {}^2\Sigma^+$ system, with labeled branch structure, is shown in Fig. 4.14. The first lines of this band are labeled on the spectrum. All the bands in this progression have similar profiles and

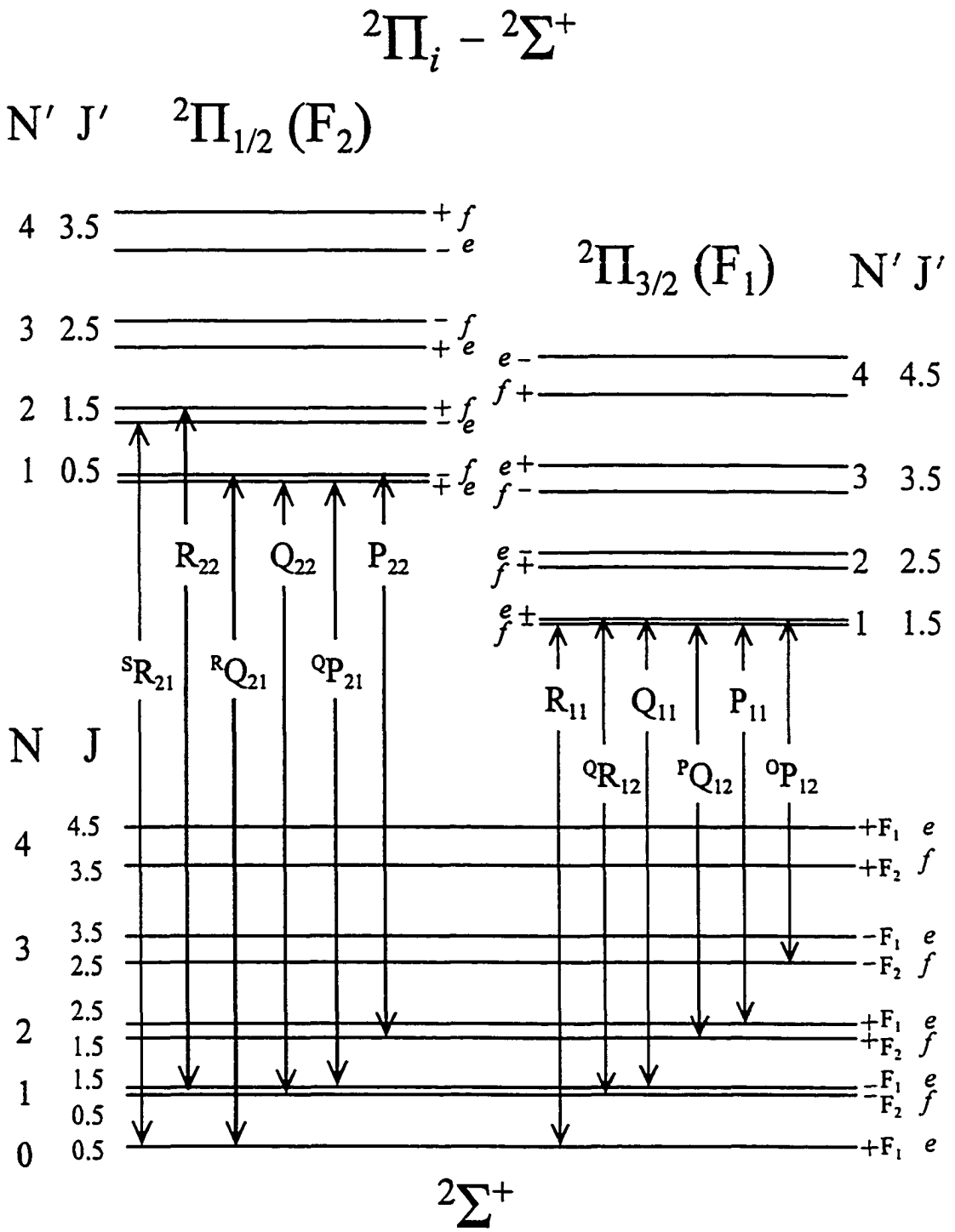

Fig. 4.13. The energy level diagram for a $^2\Pi_i - X^2\Sigma^+$ transition. First lines in each branch are indicated. The diagram is drawn for an excited state following Hund's case (a) coupling. The splittings are greatly exaggerated.

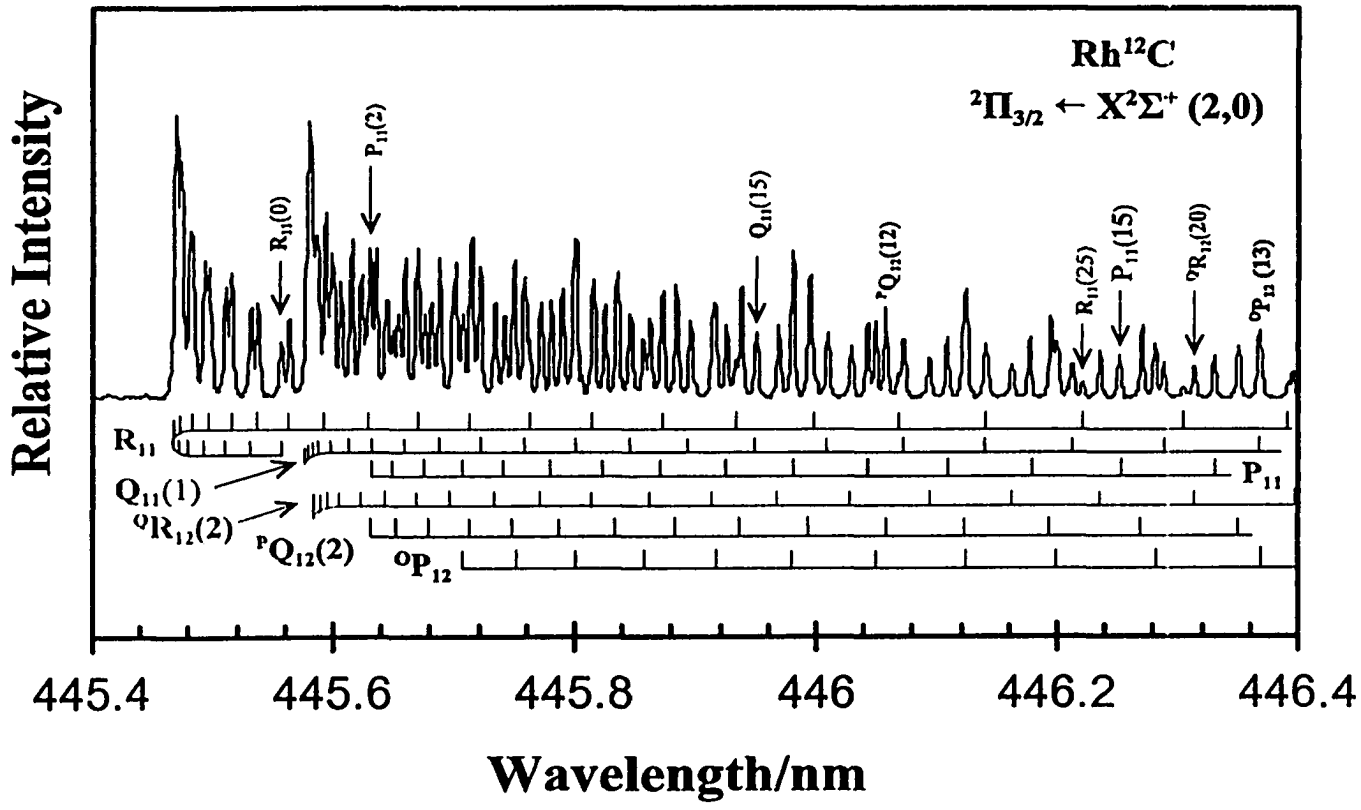

Fig. 4.14. The (2,0) band of the $^2\Pi_{3/2} \leftarrow X^2\Sigma^+$ subsystem. The branches are identified according to a $^2\Pi_{3/2} \leftarrow X^2\Sigma^+$ transition shown in Fig. 4.13.

branch structures to that shown for the (2,0) band in Fig. 4.14. The transition frequencies and rotational lines assignments for the (0,0), (1,0), (2,0), (3,0) and (4,0) bands of this subsystem are listed in Table 4.4.

The rotational constants for the bands of this $^2\Pi_{3/2} - {}^2\Sigma^+$ system were determined by using

$$\Delta_2F_i'(J) = R_i(J) - P_i(J) = 4B_v(J+½) - 8D_v(J+½)^3 \qquad (4.20).$$

The effective B and D values can be obtained by averaging the Δ_2F', $\{½[\Delta_2F_1' + \Delta_2F_2']\}$, values for the components of the $^2\Pi$ state. Figure 4.15 shows the plot used to obtain the B and D rotational constants for the 445.47 nm (2,0) band of the $^2\Pi_{3/2}$ substate. The bands of this subsystem exhibited no measurable Λ-type doubling.

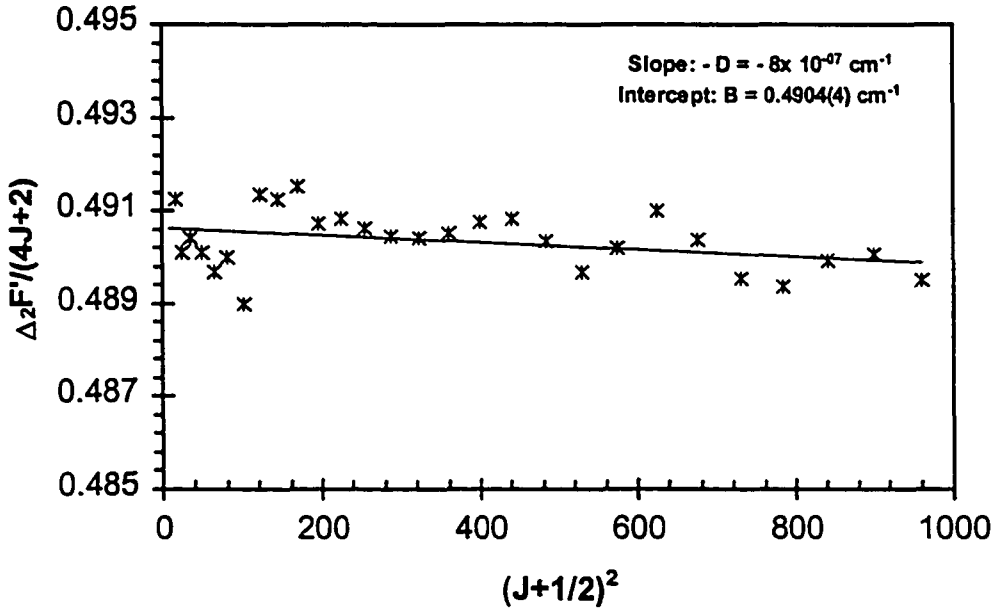

Fig. 4.15. Determination of the rotational constants B and D for the v′ = 2 level of the $B^2\Pi_{3/2}$ state.

Table 4.4. Rotational assignments and vacuum wavenumbers (cm^{-1}) for the $^2\Pi_{3/2} - X^2\Sigma^+$ system of $Rh^{12}C$.

	(0,0) band at 477.33 nm						(1,0) band at 460.51 nm						
N	$R_1(N)$	$Q_1(N)$	$^QR_{12}(N)$	$P_1(N)$	$^PQ_{12}(N)$	$^OP_{12}(N)$	N	$R_1(N)$	$Q_1(N)$	$^QR_{12}(N)$	$P_1(N)$	$^PQ_{12}(N)$	$^OP_{12}(N)$
0	20939.00	-	-	-	-	-	0	21704.24	-	-	-	-	-
1	940.36	20937.85	20937.85	-	-	-	1	705.56	21703.06	21703.06	-	-	-
2	941.45	937.85	937.78	20935.56	20935.34	-	2	706.69	703.06	703.06	21700.41	21700.52	-
3	942.36	937.78	937.61	934.47	934.79	20931.85	3	707.59	703.24	703.06	699.48	699.39	21696.66
4	943.11	937.61	937.30	933.17	933.49	929.54	4	708.25	702.92	702.50	698.26	698.26	694.54
5	943.63	937.13	936.78	932.18	932.50	927.01	5	708.72	702.26	701.89	696.66	696.66	691.86
6	943.94	936.43	936.04	929.97	930.29	924.26	6	709.00	701.51	701.09	694.92	694.54	689.04
7	944.02	935.56	935.08	928.05	928.37	921.30	7	709.00	700.52	700.05	692.94	692.52	686.03
8	943.94	934.47	933.94	925.96	926.28	918.16	8	708.81	699.39	698.83	690.83	690.59	682.83
9	943.63	933.11	932.59	923.61	923.93	914.72	9	708.48	697.98	697.41	688.43	687.86	679.44
10	943.11	931.63	931.02	921.12	921.44	911.24	10	707.87	696.33	695.72	686.03	685.18	675.78
11	942.45	929.97	929.28	918.42	918.74	907.54	11	707.07	694.54	693.84	683.07	682.32	671.93
12	941.54	928.05	927.27	915.51	915.83	903.58	12	706.03	692.52	691.76	680.11	679.31	667.90
13	940.49	925.96	925.13	912.41	912.73	899.49	13	704.81	690.26	689.46	676.87	676.02	663.63
14	939.13	923.61	922.74	909.02	909.34	895.06	14	703.06	687.86	686.97	673.44	672.55	659.08
15	937.61	921.13	920.17	905.63	905.95		15	701.51	685.18	684.24	669.78	668.84	654.48
16	935.96	918.42	977.38	901.88	902.20		16	699.69	682.32	681.33	665.93	664.89	649.56
17	934.03	915.51	914.44	897.93	898.25		17	697.64	679.31	678.18	661.89	660.81	644.50
18	931.68	912.41	911.24	893.84	894.16		18	695.44	676.02	674.85	657.63	656.45	639.16
19	929.28	909.02	907.84	889.50	889.82		19	692.94	672.55	671.28	653.17	651.90	633.69
20	926.75	905.50	904.23	885.02	885.34		20	690.08	668.84	667.57	648.48		
21	924.00	901.75	900.54	880.34	880.66		21	687.21	664.89	663.63	643.56		
22	921.12	897.84	896.45	875.30	875.62		22	684.14	660.81	659.35	638.46		
23	917.90	893.71	892.23	870.14	870.46		23	680.72	656.45	654.95	633.17		
24	914.50	889.37	887.80	864.72	865.04		24	677.18	651.90	650.40			
25	910.98	884.81	883.24	859.22	859.54		25	673.44	647.17	645.53			
26	907.19	879.99	878.38	853.38	853.70		26	669.40	642.25	640.57			
27	903.23	875.17	873.48	847.53	847.85		27	664.89	637.15	635.32			
28	899.06	869.97	868.02				28	660.81	631.77				
29	894.71	864.42	862.69				29	656.64	624.86				
30	890.11	858.97	857.03				30	652.09					
31	885.33	853.12					31	647.17					
32	880.34	847.15					32	642.35					
33	875.17						33	637.15					
34	869.80						34	631.77					
35	864.12												
36	858.36												

Table 4.4. continued. Rotational assignments and vacuum wavenumbers (cm^{-1}) for the $^2\Pi_{3/2} - X^2\Sigma^+$ system of $Rh^{12}C$.

	(2,0) band at 445.47 nm						(3,0) band at 431.25 nm						
N	$R_1(N)$	$Q_1(N)$	$^QR_{12}(N)$	$P_1(N)$	$^PQ_{12}(N)$	$^OP_{12}(N)$	N	$R_1(N)$	$Q_1(N)$	$^QR_{12}(N)$	$P_1(N)$	$^PQ_{12}(N)$	$^OP_{12}(N)$
0	22437.64	-	-	-	-	-	0	23178.17	-	-	-	-	-
1	438.91	22436.42	22436.42	-	-	-	1	179.40	23176.94	23176.94	-	-	-
2	440.02	436.42	436.42	22433.94	22433.94	-	2	180.47	176.79	176.84	23174.65	23174.43	-
3	440.84	436.42	436.42	432.98	432.72	22430.04	3	181.37	176.84	176.67	173.55	173.31	-
4	441.44	436.17	435.77	431.61	431.36	427.86	4	181.91	176.46	176.25	172.14	171.82	23168.35
5	441.90	435.51	435.16	430.04	429.68	425.33	5	182.28	175.88	175.55	170.59	170.17	165.79
6	442.05	434.70	434.30	428.32	427.86	422.49	6	182.28	175.07	174.65	168.78	168.30	162.97
7	442.05	433.69	433.18	426.29	425.83	419.56	7	182.28	174.01	173.53	166.75	166.22	159.83
8	441.90	432.47	431.91	424.06	423.51	416.17	8	181.91	172.67	172.14	164.46	163.88	156.52
9	441.44	431.00	430.39	421.63	421.08	412.73	9	181.37	171.23	170.59	162.06	161.32	153.01
10	440.63	429.13	428.67	419.00	418.34	408.93	10	180.57	169.42	168.78	159.19	158.55	149.23
11	439.77	427.40	426.75	416.17	415.41	405.09	11	179.66	167.45	166.75	156.21	155.51	145.12
12	438.66	425.33	424.52	413.03	412.27	400.95	12	178.38	165.26	164.46	153.01	152.21	141.08
13	437.29	423.00	422.19	409.74	408.93	396.60	13	176.74	162.97	162.06	149.60	148.75	136.56
14	435.77	420.47	419.56	406.20	405.34	392.06	14	175.23	160.31	159.40	145.93	144.97	131.89
15	433.94	417.73	416.77	402.46	401.50	387.26	15	173.21	157.48	156.52	142.10	141.03	-
16	431.91	414.70	413.74	398.52	397.51	382.26	16	171.23	154.02	153.54	138.00	136.94	121.90
17	429.68	411.51	410.45	394.28	393.27	377.02	17	167.78			133.64	132.52	116.59
18	427.20	408.07	407.01	389.88	388.77	371.62	18	166.22			129.12	127.95	111.23
19	424.52	404.48	403.27	385.29	384.08	365.98	19	163.50			124.34	123.12	105.92
20	421.63	400.59	399.33	380.45	379.24	360.04	20	160.41			119.30	118.07	
21	418.59	396.60	395.19	375.46	374.09	353.95	21	157.22			114.15	112.82	
22	415.41	392.16	390.84	370.16	368.80	347.66	22	153.75				107.30	
23	411.71	387.61	386.25	364.62	363.21		23	150.08				101.63	
24	408.07	382.97	381.46	358.93	356.42		24	146.19				95.80	
25	403.98	378.03	376.46	351.63	351.43		25	142.10				89.71	
26	399.83	372.88	371.22		345.30		26					83.40	
27	395.34	367.44	365.78				27						
28	390.84	361.85	360.04				28						
29	385.90	356.01	354.20										
30	380.80	349.97	348.11										

Table 4.4. continued. Rotational assignments and vacuum wavenumbers (cm^{-1}) for the $^2\Pi_{3/2} - X^2\Sigma^+$ system of $Rh^{12}C$.

(4,0) band at 418.14 nm

N	$R_1(N)$	$Q_1(N)$	$^QR_{12}(N)$	$P_1(N)$	$^PQ_{12}(N)$	$^OP_{12}(N)$
0	23905.38	-	-	-	-	-
1	906.70	23904.35	23904.35	-	-	-
2	907.68	904.17	904.17	23901.81	23901.81	-
3	908.49	903.94	903.90	900.66	900.53	23898.25
4	909.01	903.77	903.46	899.28	899.11	895.60
5	909.35	903.08	902.72	897.73	897.44	893.08
6	909.47	902.22	901.81	895.95	895.55	890.15
7	909.35	901.12	900.66	893.88	893.36	887.04
8	909.15	899.74	899.28	891.52	891.01	883.65
9	908.49	898.25	897.73	889.00	888.36	880.15
10	907.57	896.49	895.95	886.24	885.55	876.36
11	906.53	894.40	893.71	883.20	882.51	872.29
12	905.27	892.21	891.35	879.98	879.29	868.05
13	903.77	889.63	888.82	876.54	875.73	863.69
14	901.93	887.04	886.07	872.86	872.00	858.99
15	900.14	883.94	883.02	868.96	868.05	854.06
16	897.73	880.84	879.81	864.83	863.86	848.85
17	895.49	877.40	876.26	860.48	859.45	843.47
18	892.73	873.78	872.58	855.95	854.81	837.86
19	889.84	869.94	868.79	851.14	849.88	831.97
20	887.40	865.98	864.66	846.10	844.84	825.85
21	883.54	861.62	860.31	840.78	839.52	819.57
22	879.98	857.15	855.84	835.29	833.91	813.00
23	876.36	852.40	851.14	829.63	828.14	
24	872.58	847.53	846.10	823.68	822.20	
25	868.39	842.44	840.78	-	815.97	
26	864.15			811.06		
27	859.62					
28	854.81					

The second set of bands was assigned to the other spin-orbit component, the $^2\Pi_{1/2}$ - $^2\Sigma^+$ subsystem. Seven new bands associated with the $^2\Pi_{1/2}$ excited state were observed: (0,2), (1,1), (1,0), (2,0), (3,1), (3,0), and (4,0). Rotational analyses concentrated on those bands whose vibrational levels were not yet characterized. The rotational analyses of the $^2\Pi_{1/2}$ - $X^2\Sigma^+$ bands of this second subsystem proved more difficult due to the various degrees of mixing between the levels of the $^2\Pi_{1/2}$ state with nearby vibrational levels of the $C^2\Sigma^+$ state. The bands could be placed into one of three categories based on the extent of the mixing: (i) where the state interacts strongly with the levels of the $C^2\Sigma^+$ state ($v' = 0$ of the $^2\Pi_{1/2}$ state); (ii) where the interaction of the levels of the $C^2\Sigma^+$ state with the $^2\Pi$ excited state ($v' = 1$ and 2) appears to be minuscule or negligible and (iii) where the levels of the $^2\Pi_{1/2}$ state interacts slightly with the levels of the $^2\Sigma^+$ state.

Analysis of the strongly perturbed (0,0) band had been carried out by LS. LS dealt in depth with the interaction of the $v' = 0$ levels of the B and C states. Their detailed deperturbation analysis is essentially correct except for mistaking the symmetry of the B state. The (0,0) band of the B-X system is shown in Fig. 4.16. The branch structure is deceptive. Only four branches appear in the spectrum which is what is expected for a $^2\Sigma^+$ - $^2\Sigma^+$ transition and the spacings are not that much different from the other bands of the C - X system. This is quite likely one of the reasons behind the LS assignment.

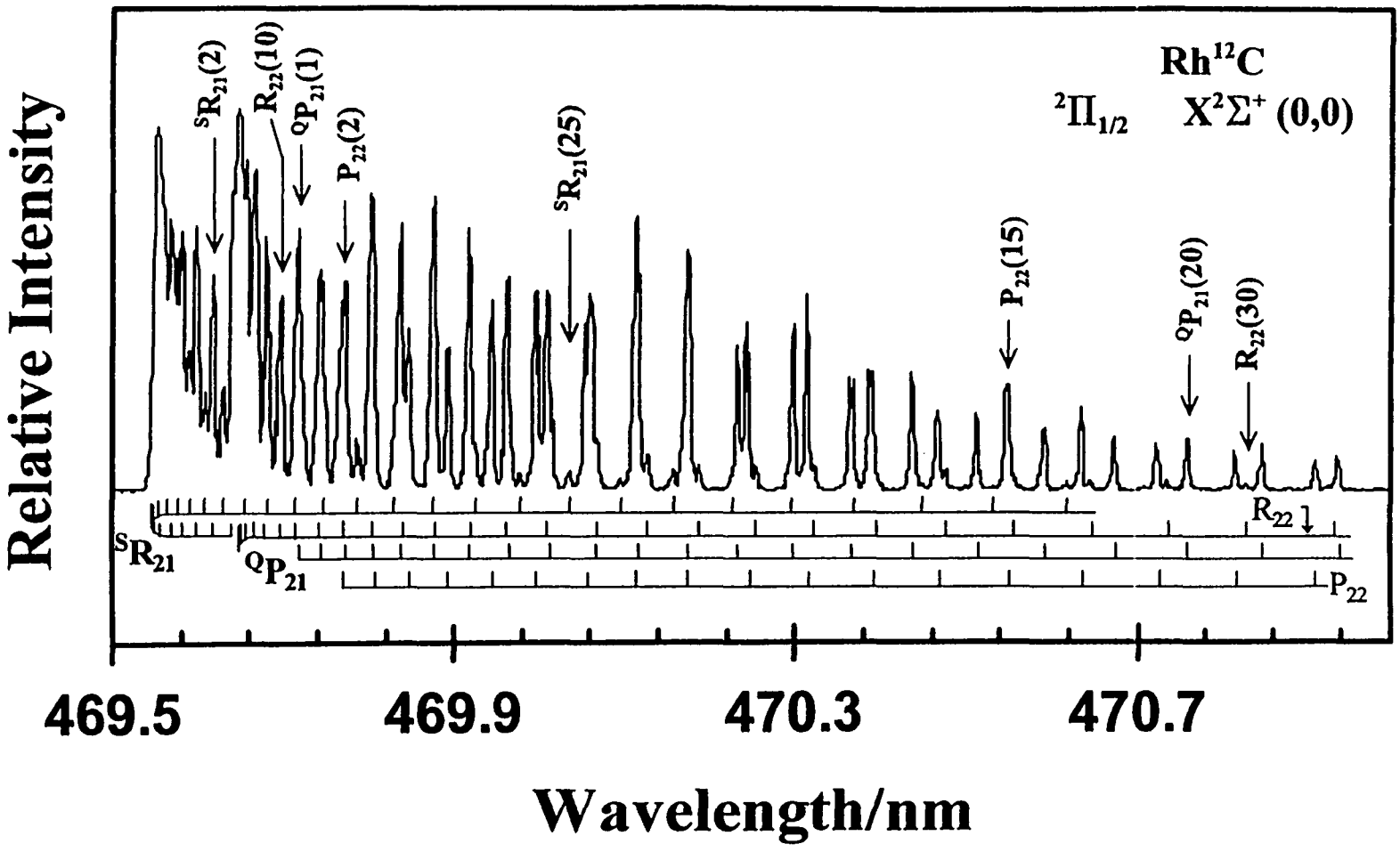

Fig.4.16. The (0,0) band of the $B^2\Pi_{1/2} \leftarrow X^2\Sigma^+$ system. Where possible, the first lines are marked. This band was previously observed by Lagerqvist and Scullman. However, they did not report transitions involving the low-lying rotational levels.

The analysis of the bands that do not appear to be perturbed was carried out in the same manner as the analyses of the bands discussed above. Six branches were identified in the (1,1), (1,0), and (2,0) bands of the $^2\Pi_{1/2} - X^2\Sigma^+$ system (Fig. 4.12). A reproduction of the (2,0) band at 437.40 nm is shown in Fig. 4.17. The values of B and D for these bands were calculated according to equation 4.20.

The $^2\Pi_{1/2} - X^2\Sigma^+$ bands can be distinguished from the bands of the $^2\Pi_{3/2} - X^2\Sigma^+$ bands by using the combination defect relations [21]. These relations determine the magnitude of the Λ-type doubling in both states. By examining the first combination differences, a measure of the splitting can be made for the upper state:

$$R_i(J) - Q_i(J) = Q_i(J+1) - P_i(J+1) + \varepsilon \approx \Delta_1 F_i'(J) \qquad (4.21).$$

The Λ-type doubling can also be measured by using the upper state term values to calculate the energy differences ($\Delta\nu_{fe} = F_1'(J)-F_2'(J)$) of the corresponding "*e*" and "*f*" levels (see Fig. 4.13) . For a $^2\Pi_{1/2}$ state, the $\Delta\nu_{fe}$ splitting is linear with J+½. The Λ-type doubling for the v′ = 2 level of the $^2\Pi_{1/2}$ state associated with the $^2\Pi_{1/2} - X^2\Sigma^+$ system is shown in Fig. 4.18. The bands associated with the $^2\Pi_{1/2}$ state that did not appear to be perturbed were fit to the equation:

$$F(J) = T_v + B_vJ(J + 1) - D_vJ^2(J + 1)^2 \mp \tfrac{1}{2}(p_v+2q_v)(J + \tfrac{1}{2}) \qquad (4.22).$$

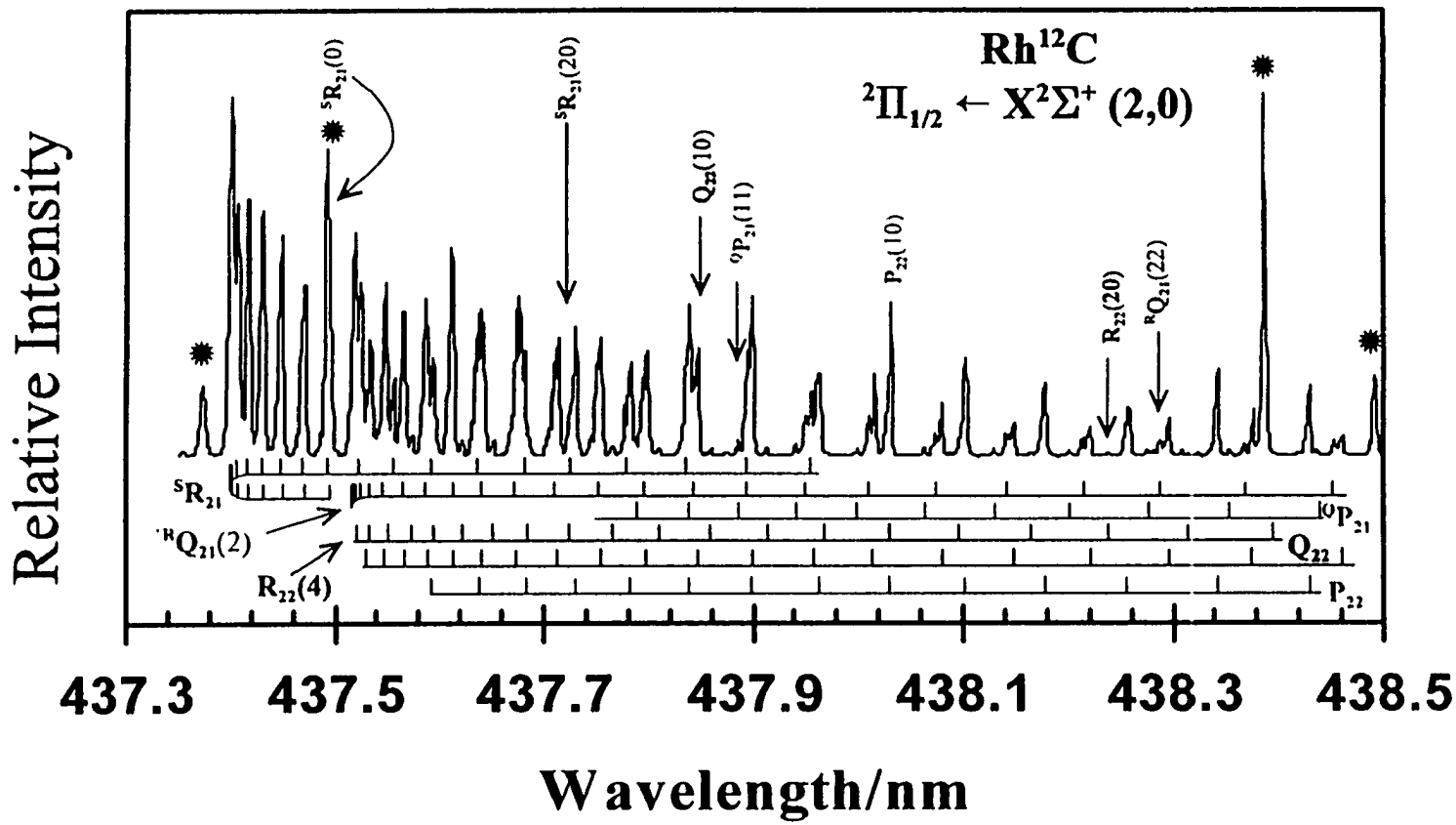

Fig. 4.17. The (2,0) band of the $B^2\Pi_{1/2} \leftarrow X^2\Sigma^+$ system at 437.40 nm. The branches are assigned according to a $^2\Pi_{1/2} \leftarrow {}^2\Sigma^+$ transition as shown in Fig. 4.13. The (✹) symbol denotes rotational lines of the RhH spectrum.

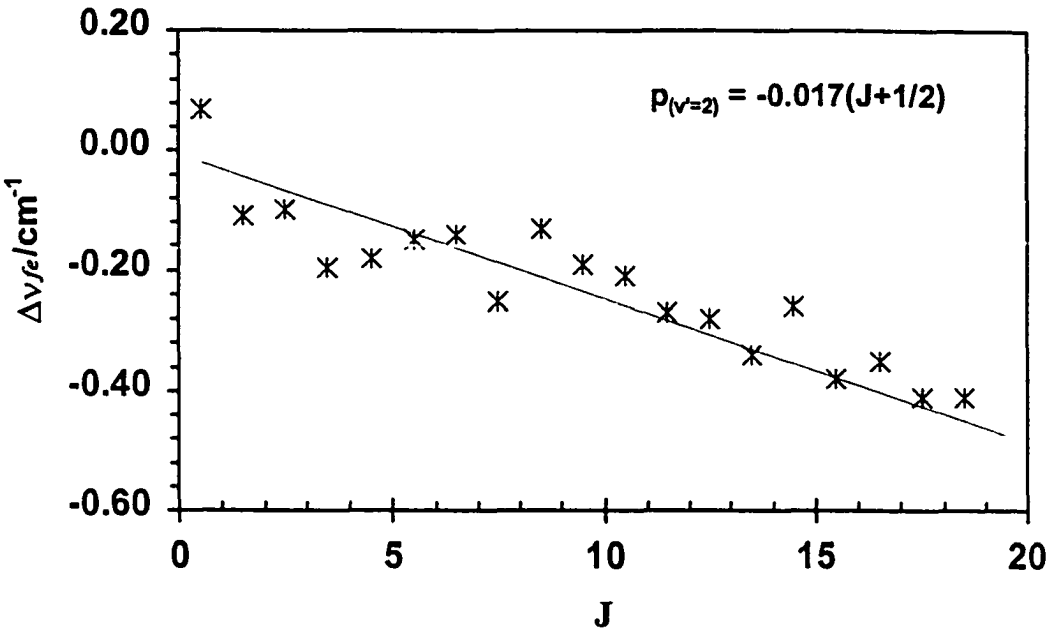

Fig. 4.18. The Λ-type doubling in the v′= 2 level of the $^2\Pi_{1/2}$ - $X^2\Sigma^+$ system. The uncertainty associated with the value of the slope is ± 0.007 cm^{-1}.

The last bands associated with the $^2\Pi_{1/2}$ state to be investigated were those categorized according to the scenario that the levels of the $^2\Pi_{1/2}$ state undergo moderate interaction with levels of the $C^2\Sigma^+$ state. These bands were the most difficult to analyze. Because of the mixing between the $^2\Pi$ and $^2\Sigma^+$ states, the transitions are neither pure $^2\Pi$ - $^2\Sigma^+$ or $^2\Sigma^+$ - $^2\Sigma^+$ transitions. The effective mixing of the $^2\Sigma^+$ levels with the $^2\Pi$ levels and the fact that the oscillator strength of the $^2\Sigma^+$ - $^2\Sigma^+$ transition is much larger than that of the unperturbed $^2\Pi$ - $^2\Sigma^+$ transition causes the bands associated with these "mixed" levels to appear with features of both transitions. The (4,0) band of the $^2\Pi_{1/2}$ - $X^2\Sigma^+$ system at 411.32 nm is one example of this type of band. The band shown is displayed in Fig. 4.19.

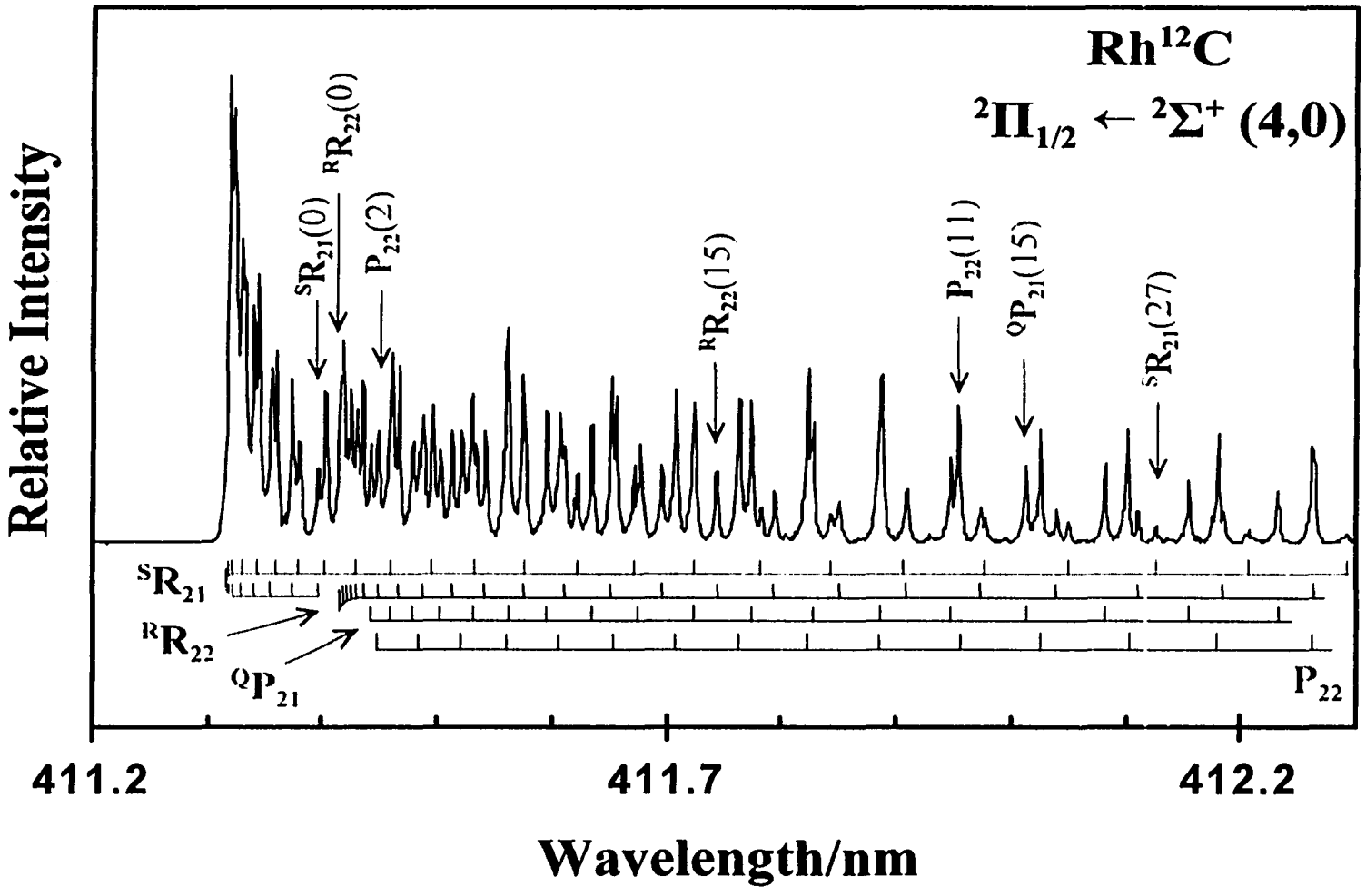

Fig. 4.19. The (4,0) band of the $^2\Pi_{1/2} \leftarrow X^2\Sigma^+$ subsystem. The branches are identified according to a $^2\Pi_{1/2} \leftarrow X^2\Sigma^+$ transition. Where possible, the first lines are marked.

Only four branches appear in its spectrum. The branches are assigned as $^{S}R_{21}$, R_{22}, $^{Q}P_{21}$, and P_{22}. These four branches correlate with the R_{11}, R_{22}, P_{11}, and P_{22} branches of an unperturbed $^2\Sigma^+ - {}^2\Sigma^+$ transition. Only the four branches associated with the unperturbed $^2\Sigma^+ - {}^2\Sigma^+$ transition are seen because the strength of the $^2\Sigma^+ - {}^2\Sigma^+$ transition greatly outweighs that of the $^2\Pi - {}^2\Sigma^+$ transition. These four branches involve transitions to "bright" rotational levels and it is these branches that are observed in the spectrum . Since the ground state combination differences were already known, the rotational assignments of the upper state could be made and hence the combination differences calculated. With the combination differences of the upper state established, the rotational constants of the upper state were determined. Rotational line assignments and line positions for the bands of the $^2\Pi_{1/2} - X^2\Sigma^+$ system are listed in Table 4.5.

In Fig. 4.20, the splitting due to Λ-type doubling in the $v' = 3$ $^2\Pi_{1/2}$ upper state is shown. A comparison of the plots displayed in Fig. 4.18 and Fig. 4.20 shows that the Λ-type doubling for the two levels are of opposite signs. It is likely that the Λ-doubling observed in the $v' = 2$ and $v' = 3$ levels in the $^2\Pi_{1/2}$ state is caused by the same vibrational level (of a $^2\Sigma^+$ state) positioned somewhere between the $v' = 2$ and $v' = 3$ $^2\Pi_{1/2}$ levels. The (2,0) band of the $C^2\Sigma^+ - X^2\Sigma^+$ system is observed between the (2,0) and (3,0) bands of the $^2\Pi_{1/2} - {}^2\Sigma^+$ system in question. This makes the $v' = 2$ level of the C state the most likely source of the Λ-doubling. The $v' = 2$ level of the $^2\Sigma^+$ state pushes the "+" rotational levels of the $v' = 2$ vibrational level to lower energy while the "+" rotational levels of the $v' = 3$ vibrational level are pushed to higher energy.

Table 4.5. Rotational assignments and vacuum wavenumbers (cm^{-1}) for the $^2\Pi_{1/2} \leftarrow X^2\Sigma^+$ system of $Rh^{12}C$.

	(1,1) band at 474.50nm						(1,0) band at 452.34 nm					
N	$^SR_{21}(N)$	$^QQ_{22}(N)$	$^QP_{21}(N)$	$^RQ_{21}(N)$	$^RR_{22}(N)$	$^PP_{22}(N)$	$^SR_{21}(N)$	$^QQ_{22}(N)$	$^QP_{21}(N)$	$^RQ_{21}(N)$	$^RR_{22}(N)$	$^PP_{22}(N)$
0	21063.11	-	-	-	-	-	22101.79	-	-	-	-	-
1	64.45	21062.08	21062.08	-	-	-	103.16	22099.01	22099.15	-	-	-
2	65.61	62.35	62.26	21059.63	21059.64	21057.93	104.28	98.08	98.28	22100.72	22100.62	-
3	66.54	62.26	62.08	58.51	58.38	55.92	105.26	96.91	97.15	100.91	100.72	22094.47
4	67.39	62.08	61.77	57.22	57.08	53.65	105.94	95.64	95.88	100.72	100.52	101.64
5	67.97	61.77	61.37	55.79	55.52	51.24	106.48	94.08	94.47	100.42	99.98	100.08
6	68.38	61.23	60.83	-	53.78	48.66	106.87	92.37	92.81	99.69	99.35	87.25
7	68.64	60.52	60.07	52.49	52.05	45.81	107.07	90.52	91.00	98.91	98.47	96.52
8	68.64	59.59	59.09	50.48	49.99	42.72	107.02	88.42	88.91	97.98	97.45	94.42
9	68.55	58.51	57.98	48.39	47.77	39.70	106.87	86.13	86.66	96.91	96.23	78.18
10	68.24	57.22	56.59	46.07	45.40	36.32	106.48	83.64	84.32	95.49	94.81	89.64
11	67.71	55.79	55.08	43.53	42.78	32.80	105.94	80.96	81.64	94.05	93.20	86.96
12	67.04	54.10	53.34	40.82	40.06	29.07	105.11	78.18	78.86	92.27	91.44	67.22
13	66.14	52.29	51.47	37.92	37.12	25.20	104.09	75.16	75.94	90.27	89.44	
14	65.12	50.22	49.37	34.89	34.00	21.02	103.01	71.95	72.82	88.13	87.25	
15	63.87	48.08	47.10	31.65	30.71	16.75	101.60	68.49	69.41	85.78	84.81	
16	62.48	45.76	44.65	28.18	27.20	12.31	100.03	64.90	65.91	83.30	82.27	
17	60.83	43.04	42.06	24.57	23.46	7.69	98.47	61.09	62.11	80.62	79.54	
18	59.09	40.33	39.21	20.79	19.59	2.85	96.62	57.10	58.17	77.64	76.57	
19	57.08	37.43	36.28	16.84	15.59		94.47	52.97	54.11	74.57	73.45	
20	54.94	34.32	33.03	12.62	11.29			48.49	49.81	71.41	70.14	
21	52.62	31.02	29.64	8.31	6.98			43.98	45.29	67.90	66.54	
22	50.04	27.46	26.04	3.74	2.41			39.26	40.67	64.20	62.84	
23	47.36	23.73	22.26					34.40	35.85	60.45	58.90	
24	44.47	19.26	18.35					29.20	30.70	56.32	54.81	
25	41.35	15.73	14.17					23.90	25.50	51.99	50.54	
26	38.06	11.55	9.86					18.35	20.00	47.57	46.06	
27	34.67	6.98	5.38							42.96	41.26	
28	31.02	2.41	0.77							38.15	36.40	
29	27.20									33.15	31.30	
30	23.15									27.90	27.10	
31	18.93									22.50	20.50	
32	14.53											
33	9.86											
34	5.38											

Table 4.5. continued. Rotational assignments and vacuum wavenumbers (cm^{-1}) for the $^2\Pi_{1/2} \leftarrow X^2\Sigma^+$ system of $Rh^{12}C$.

	(2,0) band at 437.40 nm						(3,0) band at 423.86 nm				
N	$^{S}R_{21}(N)$	$^{Q}Q_{22}(N)$	$^{Q}P_{21}(N)$	$^{R}Q_{21}(N)$	$^{R}R_{22}(N)$	$^{P}P_{22}(N)$	N	$^{S}R_{21}(N)$	$^{R}R_{22}(N)$	$^{Q}P_{21}(N)$	$^{P}P_{22}(N)$
0	22850.97	-	-	-	-	-	0	23587.47	-	-	-
1	852.07	22848.05	-	-	-	22847.78	1	582.72	-	23578.75	-
2	853.22	847.16	-	-	-	845.70	2	583.87	-	577.82	23576.42
3	854.16	846.06	-	22849.56	-	843.40	3	584.74	23580.22	576.68	574.18
4	854.83	844.76	-	849.30	-	841.11	4	585.39	580.22	575.37	571.89
5	855.36	843.19	22838.51	848.83	-	838.55	5	585.88	579.89	573.80	569.33
6	855.72	841.37	-	848.05	22847.63	835.84	6	586.04	579.35	572.05	566.62
7	855.72	839.44	839.91	847.16	846.67	832.87	7	586.04	578.58	570.15	563.68
8	855.72	837.35	837.87	846.06	845.65	829.79	8	585.88	577.66	567.92	560.53
9	855.36	835.01	835.53	844.76	842.18	826.46	9	585.55	576.42	565.58	557.21
10	854.83	832.45	832.95	843.30	842.62	822.86	10	584.96	575.16	562.97	553.63
11	854.16	829.79	830.42	841.47	840.70	819.17	11	584.19	573.52	560.20	549.88
12	853.22	826.77	827.55	839.59	838.86	815.21	12	583.16	571.80	557.21	545.86
13	852.07	823.65	824.48	837.46	836.73	811.10	13	581.91	569.77	554.06	541.63
14	850.97	820.31	821.15	835.16	834.38	806.63	14	580.49	567.59	550.69	537.34
15	849.30	816.77	817.71	832.71	831.72	802.10	15	578.86	565.09	547.00	532.73
16	847.63	812.97	812.01	830.00	828.96	797.32	16	577.06	562.54	543.20	527.91
17	845.85	809.07	810.11	827.03	826.05	792.34	17	575.16	559.71	539.19	522.92
18	843.72	804.86	806.06	823.91	822.90	787.19	18	572.76	556.67	535.01	517.77
19	841.00	800.49	801.74	820.42	819.25	781.80	19	570.26	553.52	530.51	512.36
20	838.86	795.97	797.32	817.14	815.80	776.19	20	567.59	549.99	525.90	506.79
21	836.10	791.19	792.49	813.39	811.95	770.33	21	564.71	546.40	521.08	500.94
22	-	786.16		809.49	808.10	764.32	22	561.61	542.50	516.04	494.94
23	830.11	780.97		805.28	803.92	758.11	23	558.30	538.48	510.79	488.68
24		775.62		800.86		751.64	24	554.88	534.25	505.38	
25		769.97		796.39		744.91	25	551.13	530.69	499.70	
26		764.11		791.56		738.08	26	547.16	525.03	493.81	
27		758.11		786.57		730.95	27		520.16	487.70	
28		751.79		781.49		723.72	28		515.07		
29		745.32		776.19			29		509.87		
30		738.17		770.40			30				

Table 4.5. continued. Rotational assignments and vacuum wavenumbers (cm^{-1}) for the $^2\Pi_{1/2} \leftarrow X^2\Sigma^+$ system of $Rh^{12}C$.

(4,0) band at 411.32 nm

N	$^SR_{21}(N)$	$^RR_{22}(N)$	$^QP_{21}(N)$	$^PP_{22}(N)$
0	24300.05	24298.58	-	-
1	301.39	298.88	24297.36	-
2	302.44	298.88	296.35	24294.90
3	303.32	298.76	295.19	292.74
4	303.91	298.41	293.85	290.40
5	304.32	297.82	292.21	287.71
6	304.49	297.00	290.40	284.90
7	304.49	295.95	288.40	281.87
8	304.32	294.72	286.07	278.60
9	303.79	293.26	283.52	275.09
10	303.09	291.57	280.87	271.36
11	302.15	289.64	278.01	267.45
12	301.04	287.53	274.86	263.31
13	299.69	285.14	271.36	258.87
14	298.12	282.57	267.80	254.27
15	296.30	279.76	264.01	249.49
16	294.26	276.79	259.98	244.37
17	292.03	273.52	255.73	239.13
18	289.54	270.01	251.24	233.66
19	286.83	266.28	246.52	227.96
20	283.97	262.43	241.57	222.02
21	280.87	258.29	236.39	215.81
22	277.49	253.92	247.10	209.42
23	273.92	249.40	225.45	202.80
24	270.19	244.60	219.64	196.07
25	266.11	239.53	213.54	
26	261.85	234.24	207.39	
27	257.36	228.83		
28	252.70	223.13		
29	247.74	217.14		
30	242.67	211.16		
31	237.20	204.66		
32	231.68	198.22		

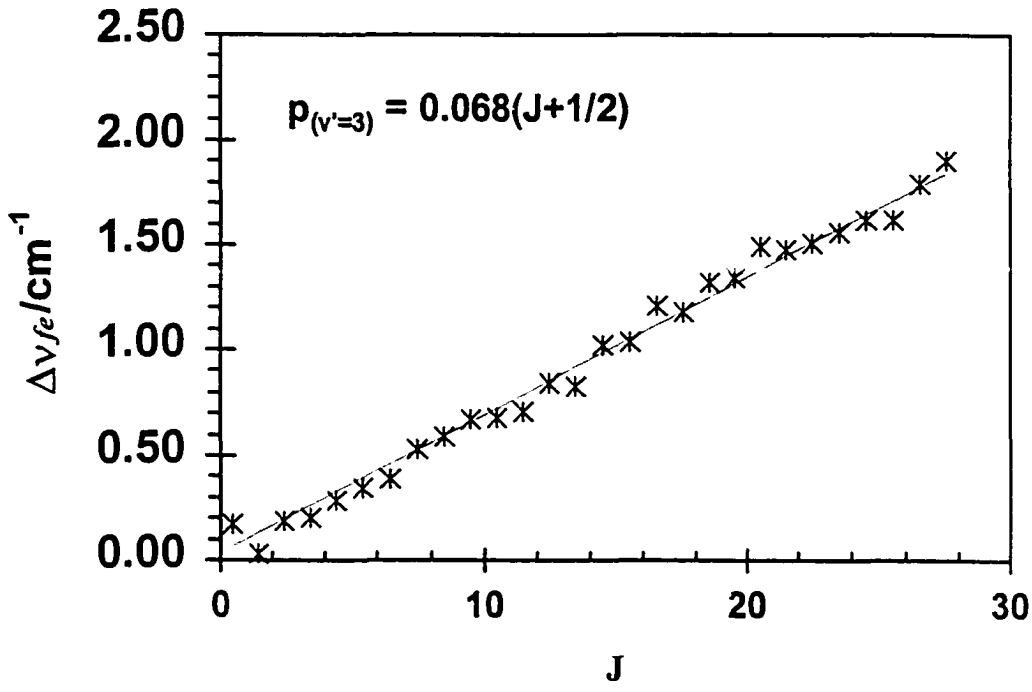

Fig. 4.20. The Λ-Type Doubling in the v′= 3 level of the $^2\Pi_{1/2}$ - $X^2\Sigma^+$ system. The uncertainty of the slope is 0.002 cm^{-1}.

Besides the bands of the $^2\Pi_{3/2}$ - $X^2\Sigma^+$, $^2\Pi_{1/2}$ - $X^2\Sigma^+$, and $C^2\Sigma^+$- $X^2\Sigma^+$ systems, a weak band with its R-head at 413.90 nm is observed in the $Rh^{12}C$ spectrum. This band is not part of the three band systems just mentioned. The DF spectral pattern is shown in Fig. 4.21. Since the vibrational intervals of the lower state associated with the 413.90 nm band, as determined from the DF spectra, match those recorded for the bands of the C-X and $^2\Pi$ - $^2\Sigma^+$ systems, the band belongs to a $Rh^{12}C$ transition. Ground state combination differences confirmed the carrier of the spectrum to be RhC with the v″= 0 level of the $X^2\Sigma^+$ state as the lower state of the transition. The excited state has a very long lifetime (600 ± 25 ns). The DF spectral pattern shown in Fig. 4.21 the upper state vibrational quantum number might be two. However, given the nature of the interactions of the

levels of the excited states and their effect on the DF spectral patterns, the "assignment" is purely speculative without further proof.

Six branches were identified and the structure of the band is very similar to the structure of the $^2\Pi_{3/2}$ - $X^2\Sigma^+$ bands described previously. Rotational analysis yields a B′ value of 0.5067(7) cm^{-1} and there is no measurable Λ-type doubling. Two other bands, too weak to be characterized, have been observed at 427.32 nm and 442.22 nm. These three uncharacterized vibronic bands are suitably situated to be vibrationally related.

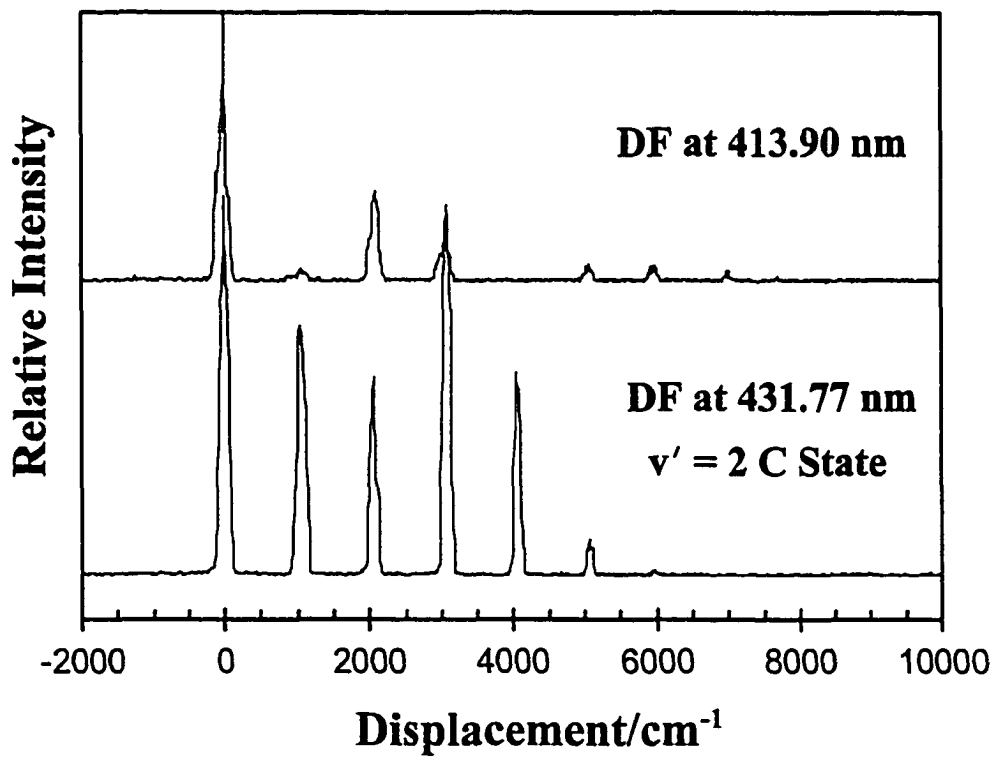

Fig. 4.21. The DF spectrum recorded following excitation to the 413.90 nm band. The DF spectrum for the C-X (2,0) band at 431.77 nm is shown for comparison.

We have determined the observed molecular constants for the new bands associated with the $^2\Pi_{1/2}$ - $X^2\Sigma^+$ and $^2\Pi_{3/2}$ - $X^2\Sigma^+$ systems. The spectroscopic constants for the ground state and new excited states of $Rh^{12}C$ are listed in Table 4.6. To present a complete picture the constants determined by LS are also listed.

Table 4.6. Rotational constants (cm^{-1}) for the observed levels of $Rh^{12}C$. The rotational constants for the ground state, taken from reference [1], are included for completeness.

State	Constant	v = 0	v = 1	v = 2	v = 3	v = 4
$X^2\Sigma^+$	B_v	0.6007	0.5967	0.5928	0.5899	—
	γ	- 0.067(3)	- 0.065(4)	- 0.064(7)	- 0.065(6)	—
$B^2\Pi_{1/2}$	B_v	0.5067	0.5045(5)	0.4982(7)	0.4973(9)	0.4926(5)
	p	—	0.045(4)	- 0.017(7)	0.068(2)	0.070(2)
$B^2\Pi_{3/2}$	B_v	0.4983(5)	0.4948(6)	0.4904(4)	0.4871(6)	0.4852(6)
$C^2\Sigma^+$	B_v	0.5479(6)	0.5420(4)	0.5365(6)	0.5299(4)	—
Unclassified level						
[24.2]	B			0.5067(7)		

4.4. Discussion

(i) Molecular Orbitals, Electron Configurations and Dispersed Fluorescence Spectra

The dispersed fluorescence (DF) spectrum for each of the important $Rh^{12}C$ bands was recorded. These spectra are displayed in Figs. 4.22 to 4.24. In Fig. 4.22 the DF spectra after excitation to the $v' = 0$, 1, 2, and 3 vibronic levels of the $C^2\Sigma^+$ state are displayed. Figure. 4.23 shows the DF spectra recorded from the $v' = 0$ to 3 levels of the $^2\Pi_{1/2}$ state and Fig. 4.24, the DF spectra recorded from the $v' = 0$ and 1 levels of the $^2\Pi_{3/2}$ state.

Only one progression can be identified in the DF spectra recorded to 9000 cm^{-1} for all the bands. The progression is identified with the vibrational levels of the $X^2\Sigma^+$ ground state. In some DF spectra, we were able to detect fluorescence all the way from the $v' = 0$ to $v' = 11$ of the ground state. The peak displacements are listed in Table 4.7. The large number of levels observed in the DF spectra is in agreement with what is expected from Franck-Condon arguments ($r_C \approx r_B > r_X$). The change in bond length between the ground state and the various vibrational levels of the B and C states is $\geq$ 0.06 nm.

Two very weak progressions starting at displacements of 9400 and 10340 cm^{-1} are observed in the DF spectra of the higher energy levels associated with B and C states. These progressions are associated with the spin-orbit components of the $A^2\Pi_r$ state studied by Kaving and Scullman [57]. The lower energy progression originating at 9400 cm^{-1} is assigned to the $^2\Pi_{1/2}$ substate and the progression anchored at 10340 cm^{-1} is the $^2\Pi_{3/2}$ substate. The DF features associated with the $A^2\Pi$ state may be seen in Fig. 4.25.

Table 4.7. Summary of the observed vibronic levels of $Rh^{12}C$ from dispersed fluorescence spectra.

Lower State	Displacement (±20cm^{-1})	Separation (cm^{-1})
$X^2\Sigma^+$ v′ = 0	0	
		1050
1	1050	
		1010
2	2060	
		1020
3	3080	
		1000
4	4080	
		1000
5	5080	
		990
6	6070	
		980
7	7050	
		980
8	8030	
		960
9	8990	
		960
10	9950	
		950
11	10900	
$A^2\Pi_{1/2}$ v′ = 0	9400	
		940
1	10340	
		930
2	11270	
$A^2\Pi_{3/2}$ v′ = 0	10180	
		920
1	11100	

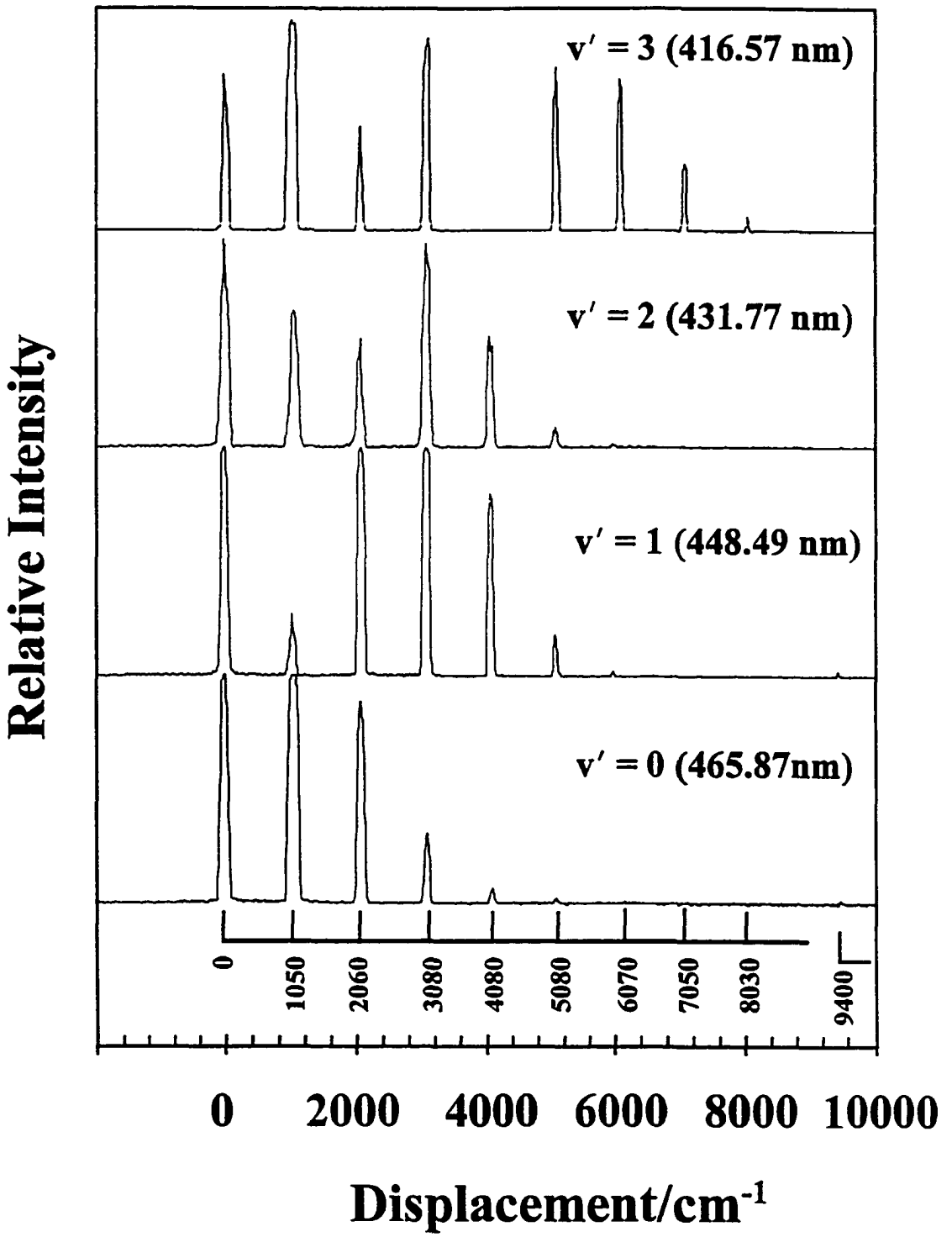

Fig. 4.22. Dispersed fluorescence spectra of $Rh^{12}C$ following the excitation to the vibronic levels of the $C^2\Sigma^+$ state. The vibrational energies for the ground state are included.

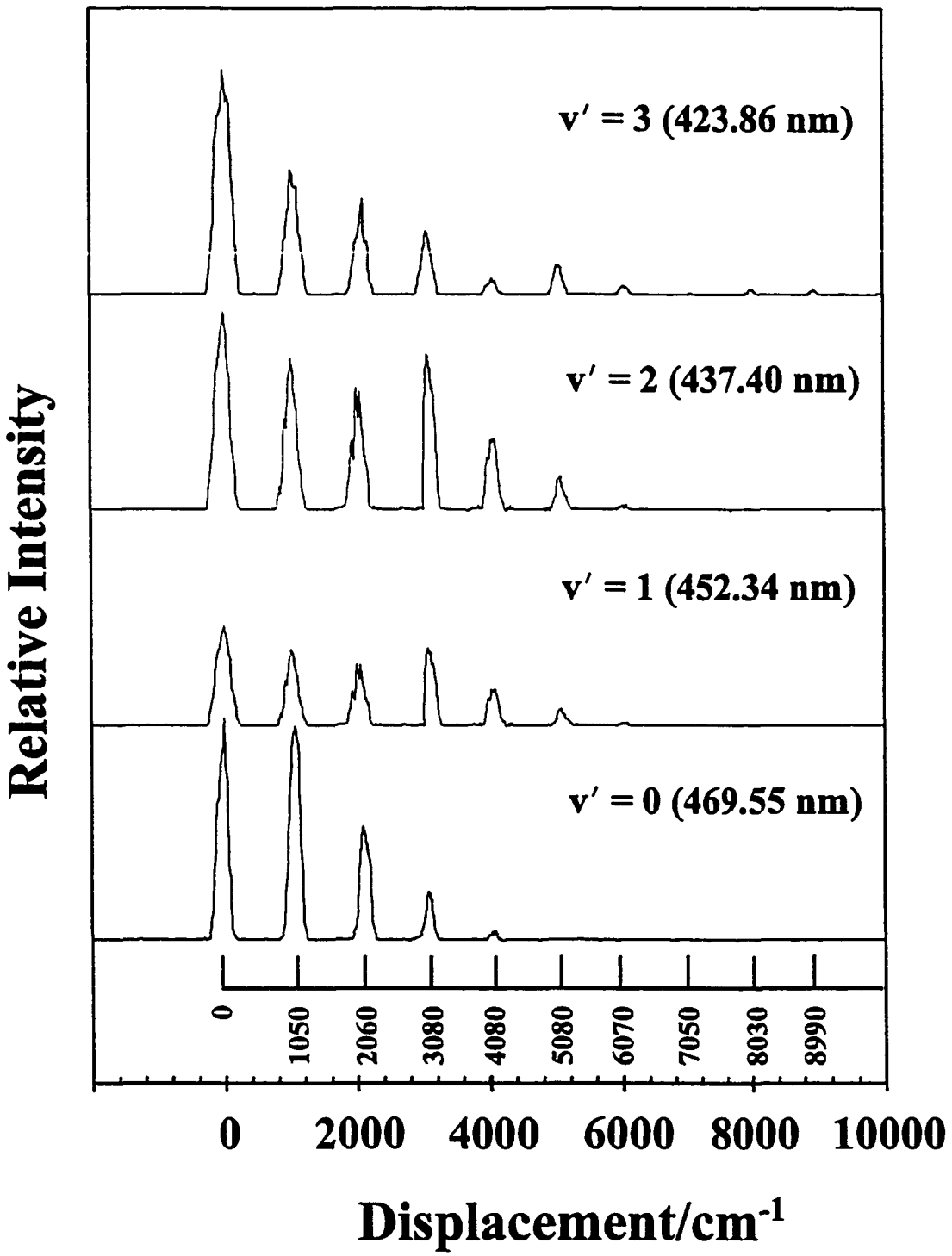

Fig. 4.23. Dispersed fluorescence spectra of $Rh^{12}C$ following the excitation to the vibronic levels of the $B^2\Pi_{1/2}$ substate. The vibrational energies for the ground state are included.

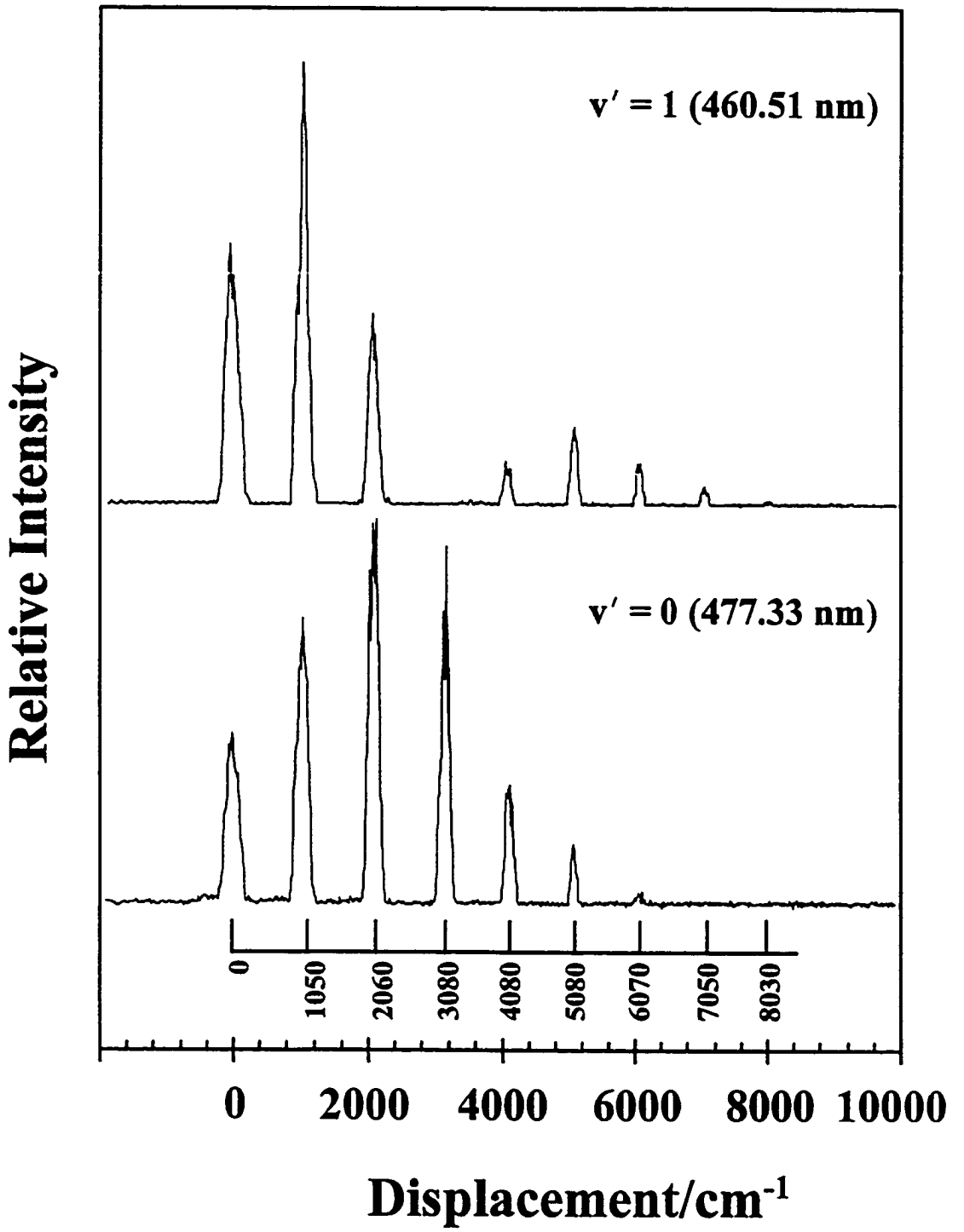

Fig. 4.24. Dispersed fluorescence spectra of $Rh^{12}C$ following the excitation to the vibronic levels of the $B^2\Pi_{3/2}$ substate. The vibrational energies for the ground state are included.

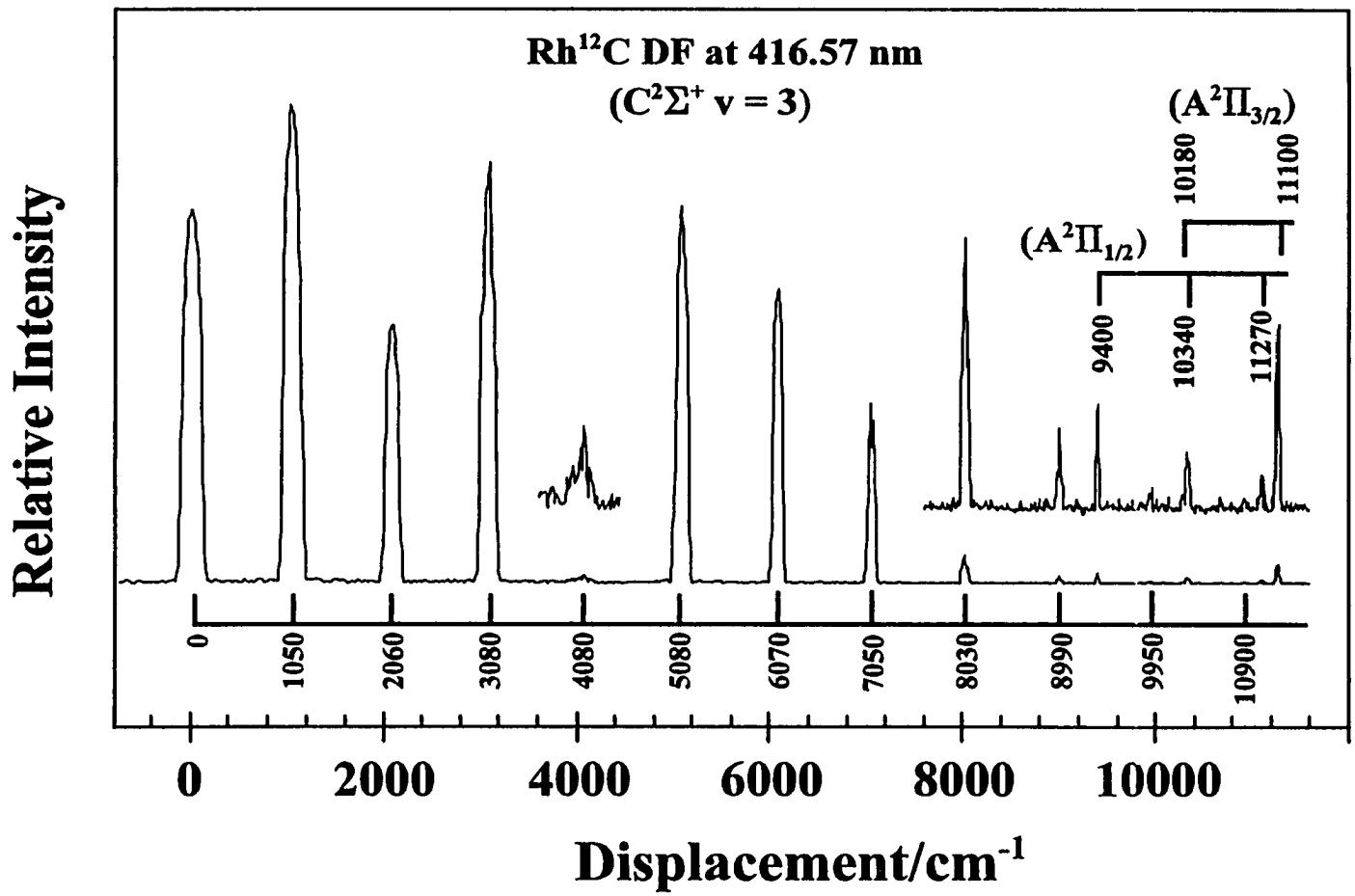

Fig. 4.25. Dispersed fluorescence spectrum of the v′ = 3 of the $C^2\Sigma^+$ state. The vibrational energies of the $X^2\Sigma^+$ and $A^2\Pi$ states are shown. The insets are 10x magnifications.

In their original analyses, LS [1] considered the symmetries of the ground and excited states of RhC based on the ground states of the carbon and rhodium atoms. The molecular states that correlate with a coupling of the ground state terms of the carbon (^{3}P-$2s^22p^2$) and rhodium (^{4}F- $4d^85s^1$) atoms are:

$$^4F(Rh) + {}^3P(C) \rightarrow {}^{2,4,6}[\Sigma^+(2), \Sigma^-, \Pi(3), \Delta(3), \Phi(2), \Gamma].$$

Although there are thirty-six states that arise from coupling of the carbon and rhodium ground state terms, many of these states are likely to lie well above the ground state and need not be considered as possible symmetries of the ground state. LS's rotational analysis confirmed the ground state to be of $^2\Sigma^+$ symmetry. They did not, however, assign a particular electron configuration to the ground state but did mention that a $^2\Sigma^+$ state could arise from a "$(5s\sigma)(5p\pi)^4$" configuration. Scullman and Kaving [57] later suggested that a single electron in a π molecular orbital was responsible for the $^2\Pi_r$ state observed near 10,000 cm^{-1}. The electronic configuration responsible for this electronic state will be discussed further on in this section.

As our reinvestigation of the RhC spectrum progressed, Balasubramanian *et al.* [69] published detailed calculations on the electronic states and potential energy curves of rhodium carbide. The calculations established the symmetries, electronic energies, spectroscopic constants, and bond lengths of twenty-three electronic states. Their prediction of a $^2\Sigma^+$ground state and $^2\Pi$ state as the lowest energy excited state are in good agreement with the previous experimental observations.

A qualitative molecular orbital diagram for RhC is illustrated in Fig. 4.26. The diagram was constructed based on (*i*) a molecular orbital scheme similar to that used by

Merer [84] for transition metal oxides, (*ii*) the MO diagrams of other transition metal carbides [44, 53, 55] and (*iii*) a comparison to the proposed scheme in the isovalent RuN radical [85]. Due account has been taken of the fact that the carbon 2*s* and 2*p* atomic orbitals are closer in energy than the corresponding AOs in oxygen. Any *s* - *p* hybridization may influence the MOs with σ symmetry. Also, the ionization potential of carbon is much closer to that of transition metals of the second row than oxygen. The metal-carbon orbital interaction (*dπ* - *pπ*) should be stronger than the corresponding oxygen-metal interaction. As a result, the π anti-bonding molecular orbital of RhC (6π) is much higher in energy than it is in RhN and even higher than it is in RhO. This interaction is reflected in the MO diagrams of RhC and RhN (Fig.5.26). As can be seen in the MO diagram of RhC, the 5π and 6π MOs are the bonding and anti-bonding pair that form from the mixing of the 4*dπ* (Rh) and 2*pπ* (C) AOs. Chapter 7 will deal with the comparison between rhodium diatomic molecules in further detail. The 11σ (bonding) and 13 σ (anti-bonding) orbitals form as a result of interaction between the 4*dσ* (Rh) and 2*pσ* (c) atomic orbitals with, perhaps a very small contribution from the 5sσ (Rh) orbital. The 2δ orbital is the nonbonding metal-based 4*dδ* (Rh) orbital since there is no nearby counterpart on the ligand for this orbital to mix with.

The eleven valence electrons completely fill the 11σ, 5π, and 2δ MOs with the remaining electron occupying the 12σ orbital. Based on this molecular orbital picture, a $^2\Sigma^+$ state is expected for the ground state of RhC. A $^2\Sigma^+$ symmetry is the sole molecular term that arises from the $11\sigma^2 5\pi^4 2\delta^4 12\sigma^1$ electron configuration. The MO argument agrees with the results of more sophisticated calculations and experimental results.

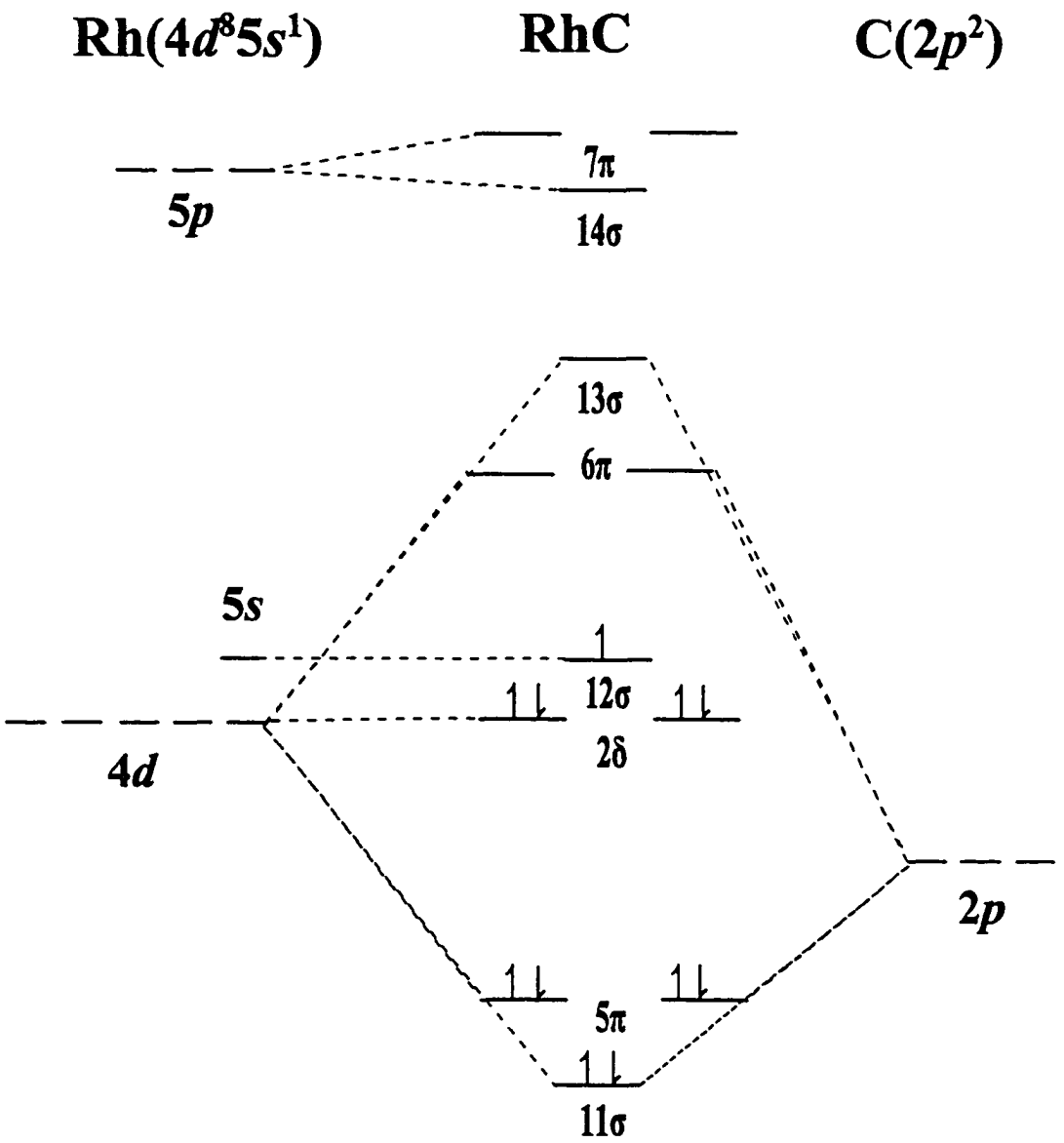

Fig. 4.26. The qualitative MO diagram for the RhC molecule and the electronic configuration of the $^2\Sigma^+$ground state.

If the MO picture we present in Fig. 4.26 is qualitatively correct, four possibilities exist for the lowest-lying electronic states. These are:

(i) $11\sigma^2 5\pi^4 2\delta^3 12\sigma^2$ $\{^2\Delta_i\}$; a $\delta \rightarrow \sigma$ transition

(ii) $11\sigma^2 5\pi^4 2\delta^4 6\pi^1$ $\{^2\Pi_r\}$; a $\sigma \rightarrow \pi$ transition

(iii) $11\sigma^2 5\pi^4 2\delta^4 13\sigma^1$ $\{^2\Sigma^+\}$; a $\sigma \rightarrow \sigma$ transition

(iv) $11\sigma^2 5\pi^4 2\delta^3 12\sigma^1 6\pi^1$ $\{^2\Pi(2), ^2\Phi(2), ^4\Pi, ^4\Phi\}$; a $\delta \rightarrow \pi$ transition.

Ab initio calculations predict energies of 12240, 13313, 15677, and 17804 cm^{-1} for the $^2\Delta$, $^2\Pi$, $^4\Phi$, and $^4\Pi$ states respectively, the four lowest energy electronic states. Scullman and Kaving have identified both spin-orbit components of a $^2\Pi_r$ state at 9416 and 10190 cm^{-1}. Configuration (ii) is the likely configuration for this $^2\Pi_r$ state. Our DF spectra (see Fig. 4.21- Fig. 4.25) revealed no evidence for any electronic states below 9000 cm^{-1}. Two progressions originating at 9400 and 10180 cm^{-1} are observed in our spectra (shown in Fig. 4.25). These progressions represent the components of the $^2\Pi$ state observed by Scullman and Kaving [57]. Transitions to the quartet states would be spin-forbidden. A $^2\Delta - ^2\Sigma^+$ transition is also forbidden and should not be seen in emission or LIF studies. Although the $^2\Pi - ^2\Delta$ transition is allowed, our DF studies did not reveal any evidence for the $^2\Delta$ electronic state.

We now turn our attention to the states identified in the LIF experiments. The only excited states observed in our LIF spectra were those associated with the $B^2\Pi - X^2\Sigma^+$ and $C^2\Sigma^+ - X^2\Sigma^+$ systems. With the $11\sigma^2 5\pi^4 2\delta^4 6\pi^1$ electron configuration already assigned to the $A^2\Pi$ state at 9463 and 10243 cm^{-1}, there is only one reasonable configuration to be considered responsible for the $^2\Pi$ symmetry of the B state: $11\sigma^2 12\sigma^1 5\pi^4 2\delta^3 6\pi^1$. This configuration leads to an inverted $^2\Pi$ state {*i.e.* with $E(^2\Pi_{3/2}) < E(^2\Pi_{1/2})$}. Our analysis has confirmed the lower energy spin component of the $B^2\Pi$ state to be the $^2\Pi_{3/2}$ substate {(0,0) band at 477.33 nm} with the $^2\Pi_{1/2}$ substate observed at a higher energy {(0,0) band at 469.55 nm}. Both the *ab initio* calculations and simple

molecular orbital arguments suggest the assignment is reasonable. The *ab initio* calculated energy for this state is 23043 cm^{-1}. This transition is about 2000 cm^{-1} higher than the observed $^2\Pi$ state but a similar energy difference is observed when comparing the calculated (23598 cm^{-1}) to the observed (21459 cm^{-1}) energy of the $C^2\Sigma^+ - X^2\Sigma^+$ transition. Further support for the preference of the $11\sigma^2 12\sigma^1 5\pi^4 2\delta^3 6\pi^1$ configuration as the parentage of the B state is given in more detail later in the discussion.

For RhC, there are two possible configurations that could be responsible for the $C^2\Sigma^+$ state observed at 21459 cm^{-1}. The first is the $11\sigma^2 5\pi^4 2\delta^4 13\sigma^1$ configuration and the second, an $11\sigma^2 5\pi^3 2\delta^4 13\sigma^1 6\pi^1$ configuration. With the interaction between the metal $d\pi$ and the carbon $p\pi$ orbitals expected to be large, the resulting 5π and 6π MOs should be well separated. In fact, Balasubramanian calculated the energy of the $^4\Sigma^+$ state that arises from the same $\pi^3\sigma^1\pi^1$ configuration as the $^2\Sigma^+$ state to be 28749 cm^{-1} and this $^4\Sigma^+$ state is expected to be lower in energy than the $^2\Sigma^+$ state from the same configuration. In light of these calculations, the $11\sigma^2 5\pi^4 2\delta^4 13\sigma^1$ configuration is the more appealing choice for the dominant configuration of the $C^2\Sigma^+$ state. The $C^2\Sigma^+$ excited state then results from the promotion of an electron in the 12σ orbital to the 13σ orbital. Table 4.8 lists the symmetries, dominant electron configurations and calculated energies of the expected electronic states from 0 to 25,000 cm^{-1}. At this point one should note the labeling differences between the experimental literature and theoretical work. The $B^2\Pi_r$ state in Table 4.8 refers to the $A^2\Pi_r$ state observed by Scullman and Kaving [57]. The $B^2\Pi$ and $C^2\Sigma^+$ states studied by LS in reference [1] correspond to the $D^2\Pi$ and $E^2\Sigma^+$ states listed in Table 4.8 respectively. To avoid confusion, throughout this text, and to remain consistent

with the original LS work we have kept the "B" and "C" labels for the $^2\Pi$ and $^2\Sigma^+$ states originating with (0,0) bands at 469.55 and 465.87 nm.

The nature of the excited state associated with the 413.90 nm $^2\Pi$ - $X^2\Sigma^+$ band remains unclassified at this time.

Table 4.8. Summary of the calculated[a] and observed electronic states of RhC and their electron configurations. The labels for the electronic states are those adopted by Balasubramanian [69]. The labels used by Lagerqvist and Scullman and Scullman and Kaving are listed below their respective electronic state assignments.

Electronic State Assignment	Calculated Energy/cm^{-1}	Observed Energy/cm^{-1}	Valence Shell Configuration					
			11σ	12σ	13σ	5π	6π	2δ
$X^2\Sigma^+$	0	0	2	1	0	4	0	4
$A^2\Delta$	12240	-	2	2	0	4	0	3
$B^2\Pi$ (LS: A state)	13313	9463, 10243[b]	2	0	0	4	1	4
$a^4\Phi$	15677	-	2	1	0	4	1	3
$b^4\Pi$	17804	-	2	1	0	4	1	3
$C^2\Phi$	20192	-	2	1	0	4	1	3
$D^2\Pi$ (LS: B state)	23043	20944[c], 21291[c,d]	2	1	0	4	1	3
$E^2\Sigma^+$ (LS: C state)	23598	21459[d]	2	0	1	4	0	4
$c^4\Delta$	25900	-	2	1	1	4	0	3

[a] See reference [69].
[b] Taken from reference [57].
[c] This work.
[d] Taken from reference [1].

(ii) Molecular Constants of $Rh^{12}C$.

In Fig. 4.27, the rotational constants for the vibrational levels of the $^2\Pi_{3/2}$ and $^2\Pi_{1/2}$ substates are plotted. The equilibrium rotational constants (B_e) have been calculated for each of the substates by plotting the observed rotational constants (B_v) for each level against the vibrational quantum number. The B_v values follow the equation

$$B_v = B_e - \alpha_e(v + \tfrac{1}{2}) \qquad (4.23).$$

As one can see from Fig. 4.27, the values of B_v for the $^2\Pi_{3/2}$ substate vary smoothly whereas there are apparent deviations in the B_v values for the vibrational levels of the $^2\Pi_{1/2}$ state.

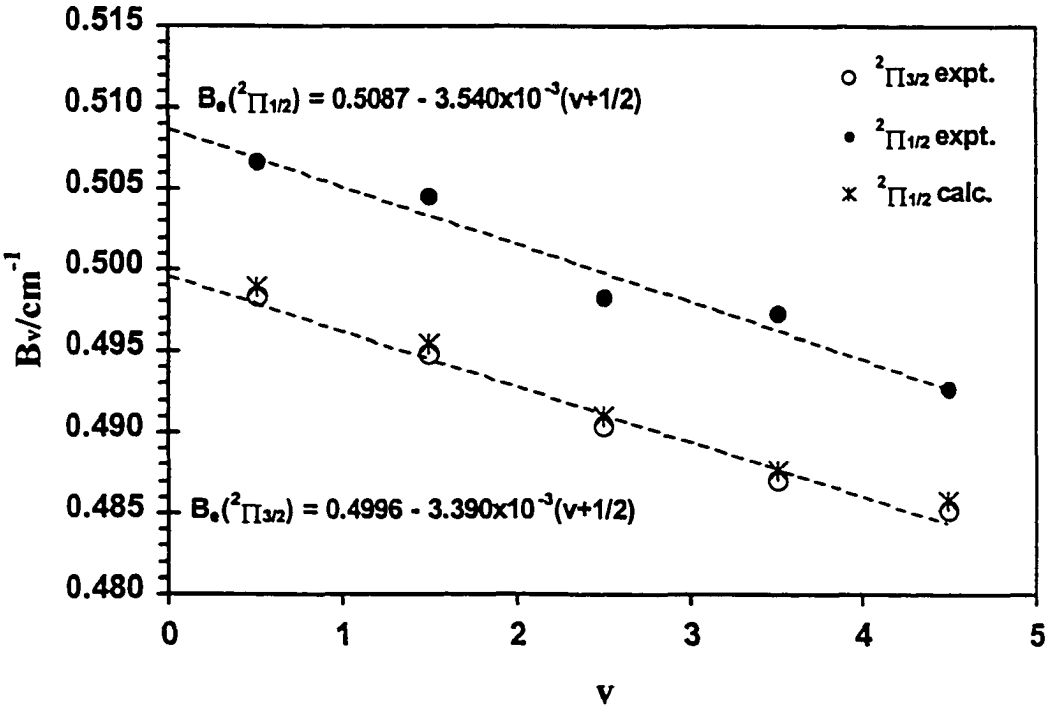

Fig. 4.27. Observed rotational constants of the $^2\Pi_i$ vibrational levels. The B values calculated from the spin-orbit constant for the $^2\Pi_{1/2}$ substate are also shown (*). The dashed lines are the best fits of the observed data. The uncertainties of the fits are: $^2\Pi_{1/2}$ (± 0.0006) and $^2\Pi_{3/2}$ (± 0.0005).

The effective rotational constants for each substate are related to the spin-orbit coupling constant (A) and the B value through the relation [21]

$$B_v(^2\Pi_{3/2}) - B_v(^2\Pi_{1/2}) \approx 2B_v^2/A\Lambda) \qquad (4.24)$$

A value of -400 cm^{-1} for A is estimated from the average experimental splitting in the v′ = 1 to 4 levels observed in the $B^2\Pi_i$ state. The v′ = 0 splitting was excluded because of the strong interaction between the v′ = 0 levels of the $B^2\Pi_{1/2}$ and $C^2\Sigma^+$ states.

If the $^2\Pi_{3/2}$ component is unperturbed and B_v is assumed to be $\approx B_v(^2\Pi_{3/2})$, then equation 4.24 predicts the $B_v(^2\Pi_{1/2})$ values expected in the absence of perturbation. These unperturbed $B_v(^2\Pi_{1/2})$ values are represented by (*) in Fig. 4.27. As one can see from the Fig. 4.27, there is a discrepancy between $B_v(^2\Pi_{1/2})$ calculated according to equation 4.23 and $B_v(^2\Pi_{1/2})$ calculated from equation 4.24. The differences in the calculated and observed B values of the $^2\Pi_{1/2}$ substate are larger than expected. The discrepancies must be attributed to the interactions between the $^2\Pi_{1/2}$ substates, the $^2\Sigma^+$ state and other $\Omega = ½$ states. With the coupling between the $^2\Pi_{3/2}$ and the $^2\Sigma^+$ states expected to be minuscule, the rotational constants of the $^2\Pi_{3/2}$ substate are expected to be unperturbed while those of the $^2\Pi_{1/2}$ substate are expected to be heavily influenced by the $^2\Sigma^+$ state. The difference in molecular constants was one of the concerns we had with the original analysis. The B values for the $^2\Pi_{1/2}$ substate will be greater than expected as the rotational constants of the $C^2\Sigma^+$ state are larger than the unperturbed B values of the $^2\Pi_{3/2}$ substate. The mixing of the $^2\Pi_{1/2}$ and $^2\Sigma^+$ states is thought to be quite extensive. If one compares the spectra for the bands involving the $^2\Pi_{1/2}$ levels, those bands whose levels are mixed with the levels of the $^2\Sigma^+$ state exhibit a different appearance. As mentioned earlier, the four branches that

appear in the spectrum are the branches that are found in the $^2\Sigma^+ - {}^2\Sigma^+$ transitions. The two other branches, if present, appear as weak satellites. A separate research project by another member of our group is investigating the specific details of this mixing.

The observed spin-orbit splittings for the v' = 0, 1, 2, 3, and 4 levels of the $B^2\Pi_i$ state are -347, -398, -414, -404, and -396 cm^{-1}. A value of approximately -400 cm^{-1} can be taken for the value of A from these splittings. The varying degrees of interactions between the levels of the B and C states account for the spread in the observed values.

Scullman and Kaving determined the value of A for the $^2\Pi_r$ state at 10,000 cm^{-1} to be +776 cm^{-1} [57]. In a $^2\Pi$ state resulting from a π^1 configuration, Lefebvre-Brion and Field [3] have shown that the spin orbit constant A is equal to the molecular spin-orbit parameter a_π ($A = a_\pi$). Theory predicts a $^2\Delta$ state to lie in the vicinity of the $^2\Pi$ state. Any spin-orbit mixing between the $\Omega = 3/2$ components of this $^2\Delta$ state and the $A^2\Pi$ state will contribute to the $^2\Pi_{3/2} - {}^2\Pi_{1/2}$ separation. If such mixing is important then the value of a_π which is characteristic of the 6π molecular orbital may not be correctly represented by the experimental A value.

If we look at the B-X ($2\delta \rightarrow 6\pi$) and C-X ($12\sigma \rightarrow 13\sigma$) transitions, a two-electron difference exists between the configurations of the C state ($13\sigma^1 2\delta^4$) and the B excited state ($12\sigma^1 2\delta^3 6\pi^1$). As a result there will be no direct spin-orbit coupling between the configurations of the two excited states. The observed coupling between the B and C states must occur through interaction with other states. Given that many electronic states are calculated to lie within 10,000 cm^{-1} of these two states [69], it is reasonable to hypothesize that mixing of the wavefunctions occurs to some extent.

Figure 4.28 summarizes the points described in the previous two sections. The newly observed bands associated with the $^2\Pi_{3/2}$ and $^2\Pi_{1/2}$ substates are actually the B and D states originally observed by Lagerqvist and Scullman and the v′ = 0 levels of the $B^2\Pi_{1/2}$ and $C^2\Sigma^+$ states interact strongly with each other.

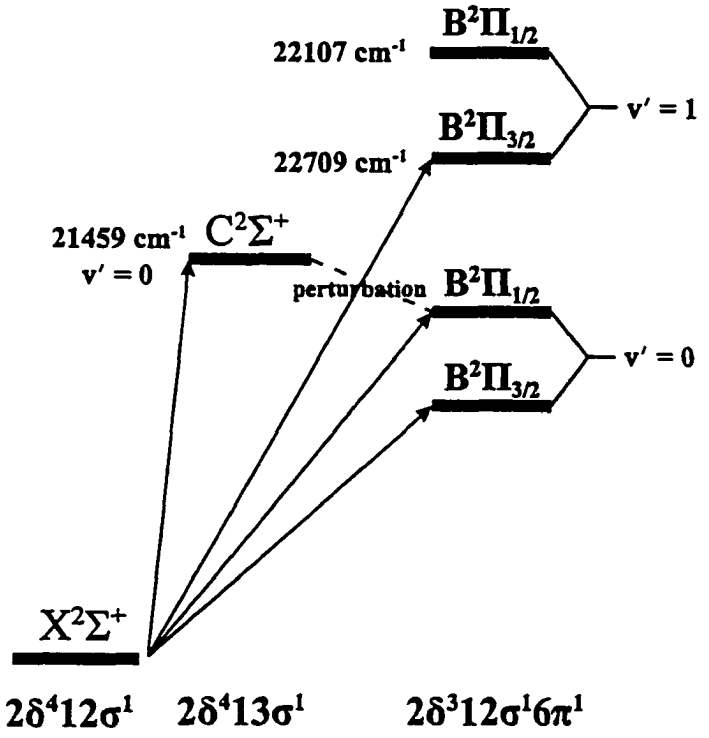

Fig. 4.28. The vibronic energies of the lowest-lying levels of the observed states and the configurations responsible for their symmetries.

4.5. Concluding Remarks.

In this chapter, we have described a reinvestigation of the $Rh^{12}C$ spectrum in the 500 - 400 nm region. Careful reading of the original literature published by Lagerqvist and Scullman in 1966 left us with questions that cast doubt on their assignment of the $B^2\Sigma^+$ state. Through measured excited state lifetimes we were able to confirm that the v'= 0 levels of the B and $C^2\Sigma^+$ states are indeed perturbed. From our lifetime analysis, we predicted that the unperturbed levels of the B state should have much longer lifetimes than the unperturbed levels of the C state.

A *time-filtering* LIF technique was employed to suppress any contribution to the LIF signal from the $C^2\Sigma^+ - X^2\Sigma^+$ transition. With the TF-LIF technique, we observed two "new" transition systems in the $Rh^{12}C$ spectrum. These have been characterized and shown to involve a $B^2\Pi_i$ state lying close to the C state with transitions to the ground state which were very weak and whose excited state lifetimes were very long compared to the strength of the C - X transitions and lifetimes associated with the levels of the $C^2\Sigma^+$ state. We ascertained that the $^2\Pi_{1/2} - X^2\Sigma^+$ component was the "$B^2\Sigma^+ - X^2\Sigma^+$" system of LS's original analysis. It was proven that their v' = 1 and 2 levels of the "D state" are actually the corresponding vibrational levels of the $^2\Pi_{3/2}$ substate.

Vibrational and rotational analyses, as well as lifetime measurements, have been carried out on the bands of the $B^2\Pi_i - X^2\Sigma^+$ system. However, the determined molecular constants should be viewed with some caution. Perturbations and interactions among the different electronic states disguise the properties associated with the unaffected levels of the states in question. The picture that arises from this research has certainly confirmed

that the B state is of $^2\Pi$ symmetry and not $^2\Sigma^+$ symmetry as originally proposed. A deperturbation analysis should provide insight on the true molecular properties of the $B^2\Pi$ state.

Chapter 5

The Electronic Structure and Spectrum of Rhodium Mononitride

5.1. Introduction

Nitrogen is without a doubt one of the most important elements in nature. Transition metals play a vital role in nitrogen fixation in biological systems [87], industrial processes such as the production of ammonia [7], and pollution control [5]. A basic understanding of the chemical bonds between nitrogen and various transition metals is therefore important. In comprehending the basic principles of small model systems such as diatomic TM mononitrides, a greater understanding of larger complex molecules and reactions can also be attained. Correlation of the molecular data within the transition series will provide a better understanding of the nature of the metal- nitrogen bond. Thus, it is not surprising that the study of transition metal mononitrides has received much interest at the experimental and theoretical levels.

Over the last ten years, the experimental database of TM nitrides has increased dramatically to include work on the early metals of the 3*d* series such as ScN [88], TiN [89 - 92], VN [93 - 96] and CrN [38, 96 - 98]. The theoretical database of these nitrides is somewhat more abundant with published works on ScN [99], TiN [99 - 102], VN [99], CrN [98, 99], FeN [103], and CuN [104]. The same trend in studies has taken place for the 4*d* series of TM mononitrides. Experimental studies on the early 4*d* TM nitrides include YN [105], ZrN [106 - 108], NbN [109, 110], MoN [111 - 115], and most recently, RuN [85]. Theoretical studies have been performed on YN [116], NbN [117], MoN [118], RuN [85], and RhN [4, 119].

Experimentally, the 5*d* transition metal mononitride series has been studied more extensively than either of the 3*d* or 4*d* series. Gas phase spectroscopic studies have been

reported for HfN [120], TaN [121], WN [122], ReN [123, 124], OsN [125], IrN [72, 126 - 128], and PtN [78, 129]. To date, no theoretical work has been published for the 5*d* series except for Balasubramanian's work on PtN [130].

Besides the gas phase studies, several matrix isolation studies have been carried out on TM nitrides. Andrews *et al.* have "cornered the market" for the first and third row transition metals. His group has studied first row metal nitrides such as VN [98], CrN [98], MnN [98], FeN [131], CoN [132], and NiN [132]. Third row metal nitrides of TaN [133], and WN [134] have also been studied. For the second row TM nitrides, matrix isolation studies have been carried out on ZrN [135], MoN [136, 137], and NbN [138].

This chapter reports the discovery and characterization of the 4*d* transition metal mononitride, RhN. To date for rhodium, only RhC [1, 57, 58] has been extensively studied by gas phase spectroscopic methods. Anion photoelectron spectroscopic studies of RhC, RhN, and RhO [139] have appeared recently. The results of this study will be referred to in a later section. Also, infrared absorption spectra of RhN in an argon matrix [140] have been observed recently.

5.2. Observations

The laser induced fluorescence (LIF) spectrum of RhN was recorded from 750 - 370 nm (13300 - 27000 cm^{-1}). It is believed that this is the first identification of the RhN radical in this energy region. Since rhodium has only one isotope (^{103}Rh), $^{15}NH_3$ was used to record the spectrum of $Rh^{15}N$ in order to confirm that RhN was the carrier of the spectrum. Vibrational assignments in the spectrum were obtained directly from the observed $^{14}N/^{15}N$ isotope shifts. Examples of the mixed isotope spectra are shown in Fig. 5.1. The RhN spectrum is very rich with more than forty observed bands. Of these, twenty-five bands are of sufficient intensity that rotational analyses could be performed. The region between 410-370 nm is very congested with many overlapping bands. The correlation between $Rh^{14}N$ and $Rh^{15}N$ features is not apparent in this region. Hence, the bands observed in the 405-370 nm region have not been studied at higher resolution.

All the observed bands of appreciable intensity found in the 700-430 nm region are red-degraded and appear to originate from the ground state. The visible spectrum can be divided into three regions based on the observed bands. The grouping of the observed transitions into electronic states was unambiguous for the lower energy systems since they are in regions free of spectral congestion. The bands of the lowest energy system appear in the 665 - 585 nm region. All the vibronic levels associated with the four bands of this transition have very long lifetimes. Since these are the only bands of any intensity that appear in this region, it can be inferred that they belong to the same system.

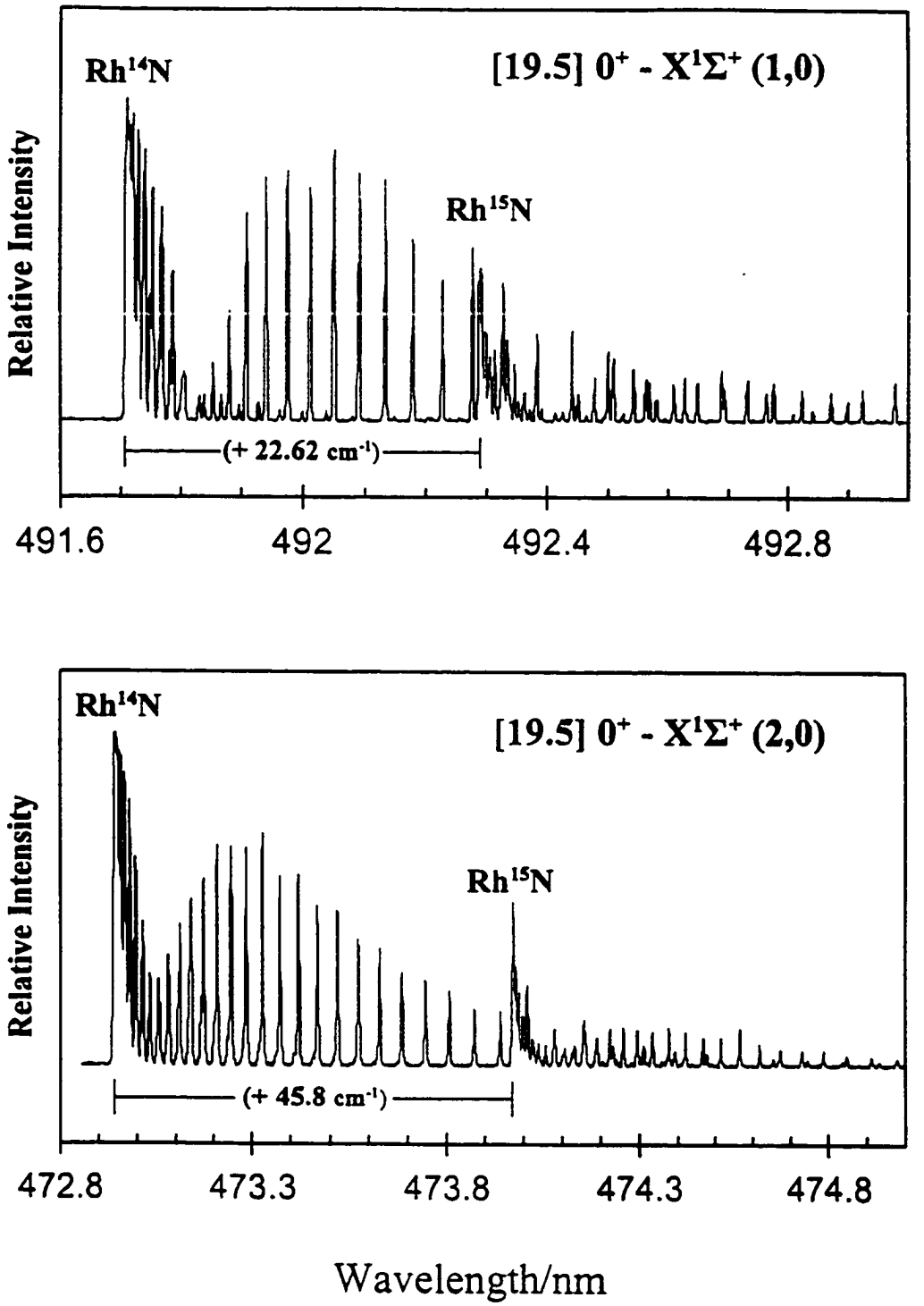

Fig. 5.1. Mixed isotope spectra for the (1,0) and (2,0) bands of the [19.5]0^+ - $X^1\Sigma^+$ system of RhN. Isotopic displacements are displayed. Table 5.1 lists all measured isotope shifts.

The second group of bands is found between 520 - 455 nm. Ten bands are found in this region. Similar to the system described above, the intensities of these bands and the excited state lifetimes suggest that six of the ten bands in this region likely share the same upper and ground states. The other four bands in this region are quite weak and have yet to be assigned to a specific system.

The third region of the RhN spectrum is identified within a wavelength range from 450 to 405 nm. As the lower wavelength region of the spectrum was scanned (<450 nm), the congestion of the RhN spectrum became more apparent. Fifteen bands of varying intensities were observed in this region. Irregular band spacings, along with the congestion, hampered the identification of any vibrational progressions at first glance. However, with the information obtained from the isotope splittings, rotational constants, and excited state lifetimes, we were able to discernibly characterize four of these bands to one specific system.

In addition to the spectrum of RhN, the spectrum of RhH was also recorded in the regions 468-463 nm and 441-437 nm. The formation of RhH is quite conceivable given the conditions of the experiment (Rh + NH_3). The spectrum of RhH is remarkably different from that of RhN due to its larger, more open rotational structure. To date, there is no reported literature dealing with the experimental characterization of RhH. *Ab initio* calculations concerning its ground state have been reported [141]. The analysis of RhH was not undertaken as part of this work and therefore will not be included in this thesis. A separate publication [142] will deal with the characterization and analysis of the RhH spectrum and its corresponding deuteride.

The observed LIF vibronic bands are listed in Table 5.1. The (0,0) band heads of the three systems are found near 663.35, 512.97, and 446.59 nm. A closer look at the bands of the system whose origin is at 663.35 nm reveals the presence of three branches in each of the bands. These branches have been identified as P, Q, and R branches. The other two systems anchored at 512.97 and 446.59 nm have two branches (P and R) associated with each band. Each electronic excited state will be described separately in this section.

The rotational structure was analyzed for each band by fitting the experimental data to the expression:

$$\nu = \nu_0 + B'J'(J'+1) - B''J''(J''+1) \qquad (5.1)$$

to determine values for ν_0, B_v', and B_v''. Several factors influenced the precision with which the molecular constants could be determined: (1) the molecules formed in the molecular beam are rotationally cold ($T \approx 30 - 40$ K), limiting the range of observable J values ($J < 30$); (2) the line width of the dye laser is approximately 0.1 cm^{-1}; (3) the band heads form at low J ($J \approx 7 - 12$). The congestion that results from the returning R-branch lines overlapping with the low J R-branch lines hinders accurate determination of the line positions with our laser resolution. In most circumstances the rotational band structure does not extend to a high enough J value in our experiments to make the determination of the centrifugal distortion constants (D', D") meaningful.

Table 5.1. Band heads (nm) of observed RhN features between 700 and 400 nm.

Wavelength(nm) λ_{air}, ± 0.05	Frequency(cm^{-1}) $\nu_{(vac)}$		Assignment		Lifetime τ(ns) ± 25	Isotope Shift(cm^{-1}) $\Delta\nu(^{14}N\text{-}^{15}N)$
688.600	14518	vvw	[15.1]1-[0.55]	(0,0)		
676.100	14787	vvw				
663.350	15071	mw	[15.1]1 - $X^1\Sigma^+$	(0,0)	965	
658.700	15177	vvw	[15.1]1-[0.55]	(1,0)		
635.470	15732	mw	[15.1]1 - $X^1\Sigma^+$	(1,0)	1225	
629.700	15873	vvw	[15.1]1-[0.55]	(2,0)		
608.521	16429	mw	[15.1]1 - $X^1\Sigma^+$	(2,0)	1300	
608.220	16437	vvw	[15.1]1-[0.55]	(3,0)		
588.400	16990	m	[15.1]1 - $X^1\Sigma^+$	(3,0)	750	
555.955	17982	vvw				
537.700	18592	vw	[19.5]0^+ - $X^1\Sigma^+$	(0,1)	105	-26.32
530.300	18853	vvw			125	
522.900	19124	mw			140	
512.970	19489	vvs	[19.5]0^+ - $X^1\Sigma^+$	(0,0)	105	-0.49
508.350	19666	vvw				
504.400	19820	w			140	
501.800	19921	vw			200	
493.840	20243	vvw	[19.5]0^+ - $X^1\Sigma^+$	(2,1)		
491.710	20331	vs	[19.5]0^+ - $X^1\Sigma^+$	(1,0)	110	22.62
475.700	21016	vvw	[19.5]0^+ - $X^1\Sigma^+$	(3,1)		
472.940	21138	vs	[19.5]0^+ - $X^1\Sigma^+$	(2,0)	105	45.8
465.400	21481	vw	[22.4]0^+ - $X^1\Sigma^+$	(0,1)		
456.190	21915	vs	[19.5]0^+ - $X^1\Sigma^+$	(3,0)	145	62.27
446.590	22385	vvs	[22.4]0^+ - $X^1\Sigma^+$	(0,0)	75	-0.55
444.399	22496	mw			300	36.57
440.716	22684	mw			185	28.6
436.082	22925	mw			160	-4.19
434.434	23012	w				
430.820	23205	s	[22.4]0^+ - $X^1\Sigma^+$	(1,0)	75	22.54
429.850	23294	w			225	
423.143	23626	w			205	
419.873	23810	w			245	
417.820	23927	m			190	
416.497	24003	m	[22.4]0^+ - $X^1\Sigma^+$	(2,0)	80	
411.237	24310	mw			200	
408.331	24483	m			120	
406.191	24612	w			150	
404.416	24720	m	[22.4]0^+ - $X^1\Sigma^+$	(3,0)	85	
402.317	24849	m			140	
400.849	24940	m				

5.3. Results and Analysis

(i) The $X\,^1\Sigma^+$ Ground State

Simple molecular orbital (MO) theory and more detailed calculations predict that the ground state of RhN is a singlet state of Σ^+ symmetry. The rather simple rotational structures of the jet-cooled RhN bands confirm this prediction. The observation of single R(J), P(J) and, where applicable, Q(J) rotational lines confirm the singlet multiplicity of the ground state, i.e., the ground state is of singlet multiplicity with $\Omega''= 0$ and not a 0^- component of a $\Omega = 0^\pm$ pair. The first lines of transitions whose upper state had $\Omega = 0$ were always R(0) and P(1) while those with an upper state of $\Omega = 1$ have R(0), Q(1), and P(2) as their first lines of the system.

The ground state rotational constants ($B_0''$and D_0'') were obtained as averages of the second combination differences via

$$\Delta_2F''(J)/(4J+2) = B_v'' - 2D_v''(J + ½)^2 \qquad (5.2)$$

measurements among all the rotationally resolved bands but excluding those bands for which no upper state electronic assignment could be made. The plot of $\Delta_2F''(J'')/(4J''+2)$ against $(J''+ ½)^2$ [21] according to equation 5.2 yielded values for B_v'' (intercept) and $2D_v''$(slope) respectively. Figure 5.2 shows such a plot for the ground state. Deviations are within accepted experimental parameters (the rotational line width resolution being ± 0.1 cm^{-1}). Bond lengths were extracted from the determined values of B". A value of 0.5075(6) cm^{-1} was obtained for B_0'' corresponding to a bond length of 0.1641(6) nm. The agreement between the theoretical r_e value of 0.1640 nm obtained by Shim *et al.* [4] and the experimentally determined value is most satisfying. The same method was

utilized to fit the ground state data of the $Rh^{15}N$ isotopomer. Analysis of the $Rh^{15}N$ bands yields $B_0'' = 0.4752(7)$ cm^{-1}.

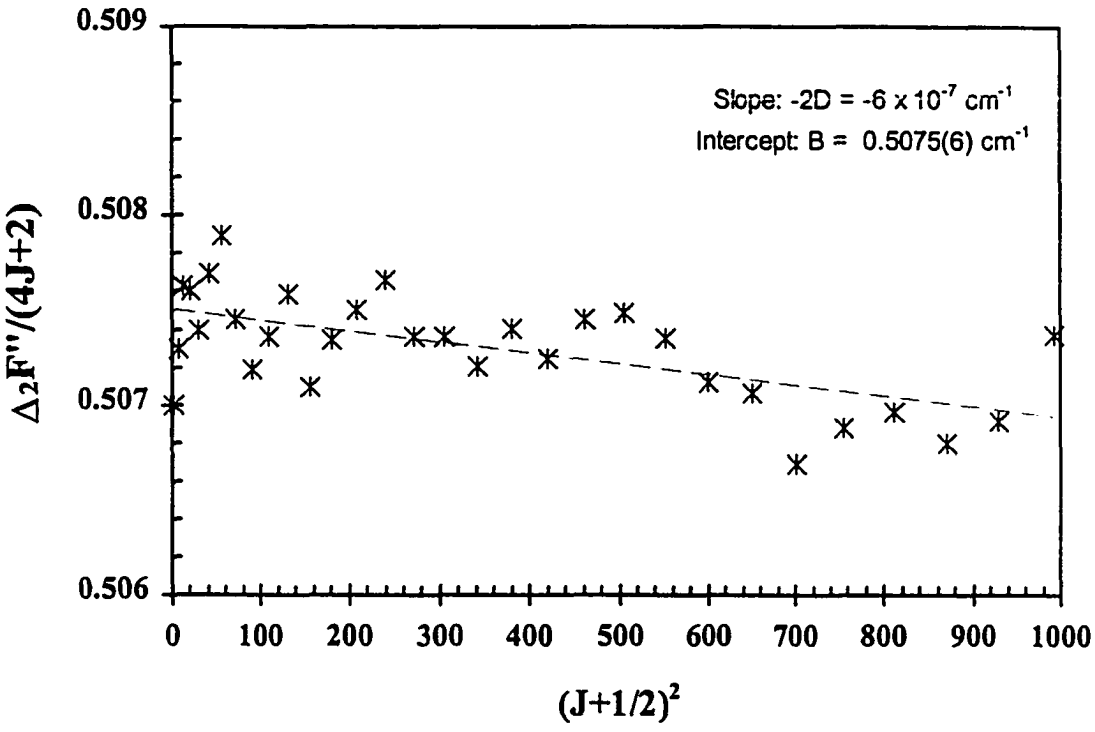

Fig. 5.2. Determination of the ground state rotational constants B and D for $Rh^{14}N$. The uncertainty for the value of the rotational constant B (intercept) is given in parentheses. The slope of the plot gives 2D (centrifugal distortion constant).

The graph in Fig. 5.2 shows a small negative slope as expected. The value of the slope was determined to be 6 x 10^{-7} cm^{-1}. This value corresponds to twice the value of the centrifugal distortion constant ($2D_v$). Although estimation of a centrifugal distortion constant (D_0'') was attempted, the cold spectra did not provide enough J structure to make the determined value meaningful. Varying the values of D_0'' and D_0' did not significantly alter the fitting of the bands even up to J values of 30. The estimated values of D_0'' (~10^{-7} cm^{-1}) parallel those determined for other 4*d* metal nitrides [105 - 115].

The ground state combination differences were helpful in assigning the rotational structure of vibrational levels of the upper electronic states that show local perturbations [21], notably where the R-branch occurred close to the head. Correct rotational numbering in an upper state can be made with a secure knowledge of the ground state rotational numbering,

There are four very weak bands observed in the spectrum that originate from the v = 1 level of the $^1\Sigma^+$ ground state. These transitions combine with the v′ = 0, 2, and 3 vibrational levels of the [19.5] $^1\Sigma^+$ excited state and the v′ = 0 vibrational level of the [22.4] $^1\Sigma^+$ excited state. Their data allowed a value of 897 cm^{-1} to be determined for the v = 0 to v = 1 vibrational interval of the ground state, *i.e.*,

$$\Delta G(\tfrac{1}{2}) = \omega_e'' - 2\omega_e x_e'' = 897 \text{ cm}^{-1} \qquad (5.3).$$

This vibrational frequency for the ground state compares favorably with the argon matrix value of 895 cm^{-1} soon to be reported by Andrews *et al.* [140]. With only one vibrational interval of the ground state available from the LIF spectrum, independent values for ω_e'' and $\omega_e x_e''$ cannot be obtained.

Only one vibrationally hot band for $Rh^{14}N$ was strong enough that it could be rotationally analyzed. The band at 537.7 nm was assigned to the (0-1) transition of the [19.5] $0^+ - X^1\Sigma^+$ system. A value of 0.5041(5) cm^{-1} ($r_1'' = 0.1648$ nm) was determined for the rotational constant (B_1'').

(ii) The [15.1]1 - $X\,^1\Sigma^+$ System

Of the three observed systems, the [15.1]1-$X^1\Sigma^+$ system is by far the weakest. The 680 - 600 nm region of the spectrum is relatively free of spectral congestion. Four red-degraded bands of sufficient intensity for study have been recorded. The strongest band of the red region has its origin at 15065 cm^{-1} (663.35 nm). It is believed that this band is the 0-0 band of the system. The other bands associated with this system are of comparable intensity. Band heads at 15732, 16429, and 16990 cm^{-1} are assigned to the (1,0), (2,0), and (3,0) bands of this system respectively. The (0,0), (1,0) and (2,0) $Rh^{14}N$ bands are shown in Figs. 5.3 - 5.5. Line positions and rotational assignments of these bands are listed in Table 5.2. An irregular vibrational pattern for this system may be noted. Spacings of 661, 687, and 561 cm^{-1} are found between the (0,0), (1,0), (2,0), and (3,0) bands. This anomalous spacing precludes any meaningful calculation of the molecular constants ω_e and $\omega_e x_e$ for this electronic state. Irregular spacings are not surprising in diatomic species such as RhN, especially when many electronic states lie close enough in energy that there may be considerable interaction between the states.

The bands of this system have as their first lines R(0), Q(1), and P(2). This identifies the system as a $\Omega' = 1 - \Omega'' = 0$ transition. By contrast, bands in the [19.5]-X and [22.4]-X systems have only an R and a P branch with R(0) and P(1) as their first lines. This identifies those systems as $\Omega' = 0 - \Omega'' = 0$ transitions.

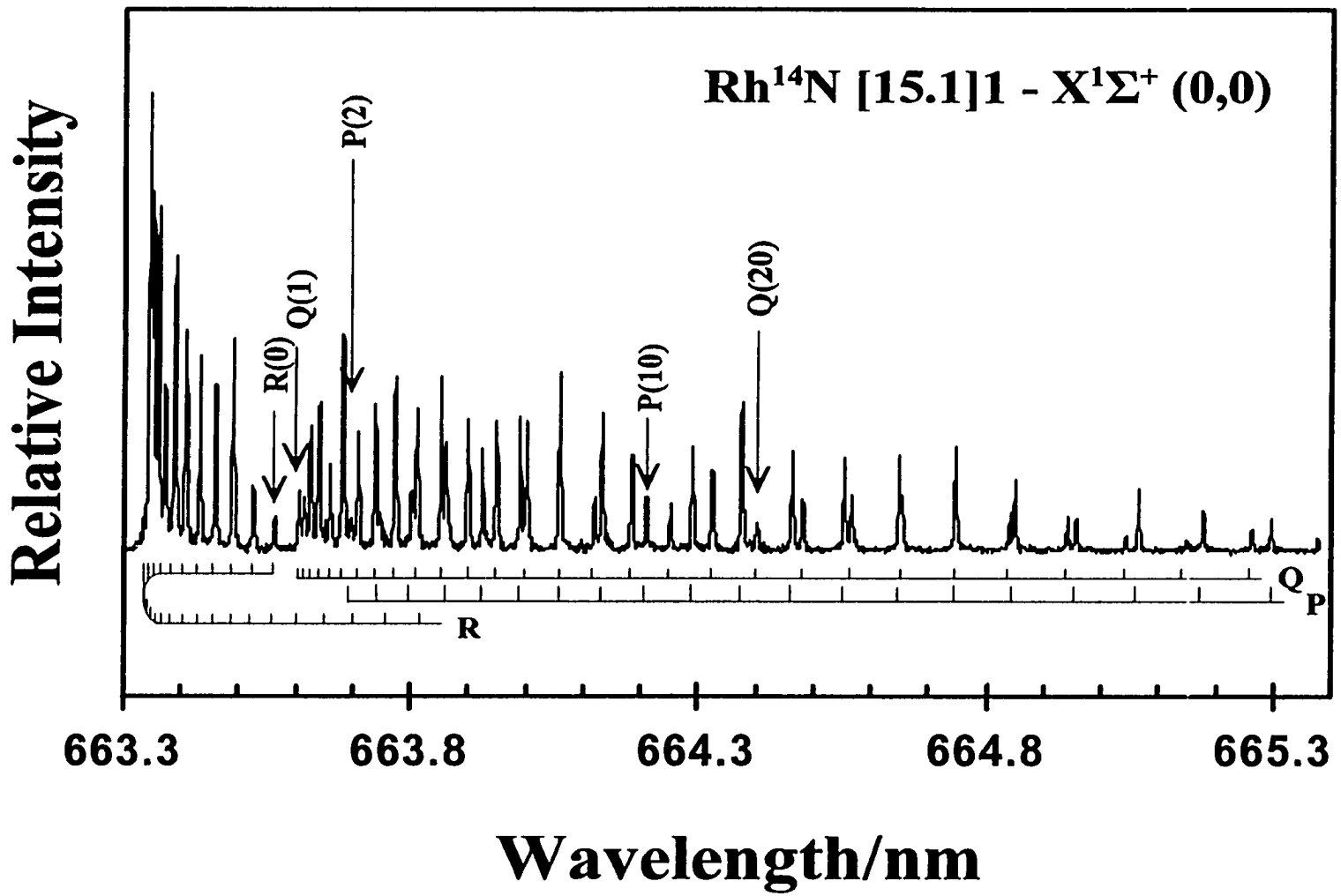

Fig. 5.3. The (0,0) band of the [15.1]1-$X^1\Sigma^+$ system. The first lines of each branch are marked.

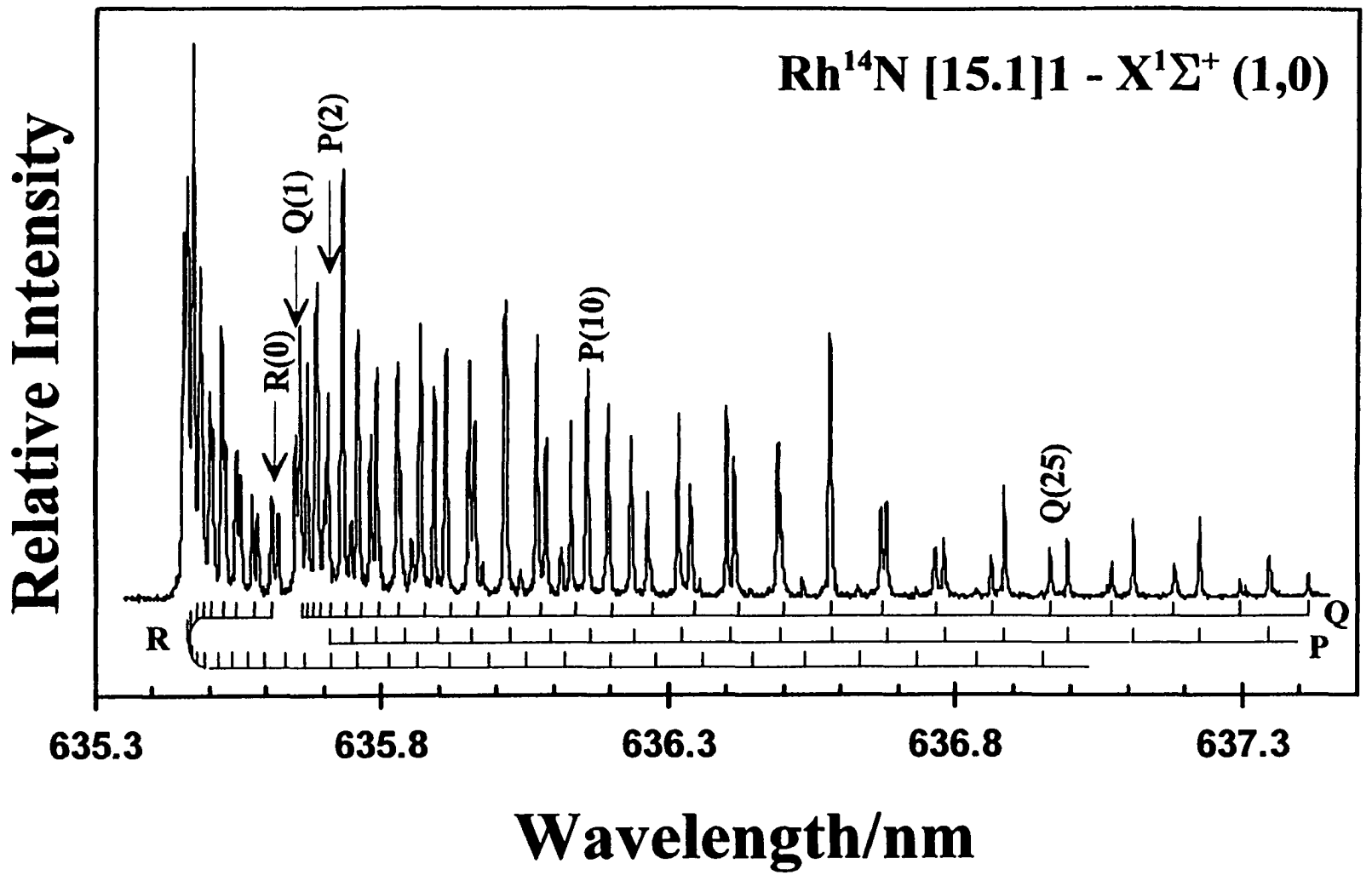

Fig. 5.4. The (1,0) band of the [15.1]1-X$^1\Sigma^+$ system. The first lines are marked.

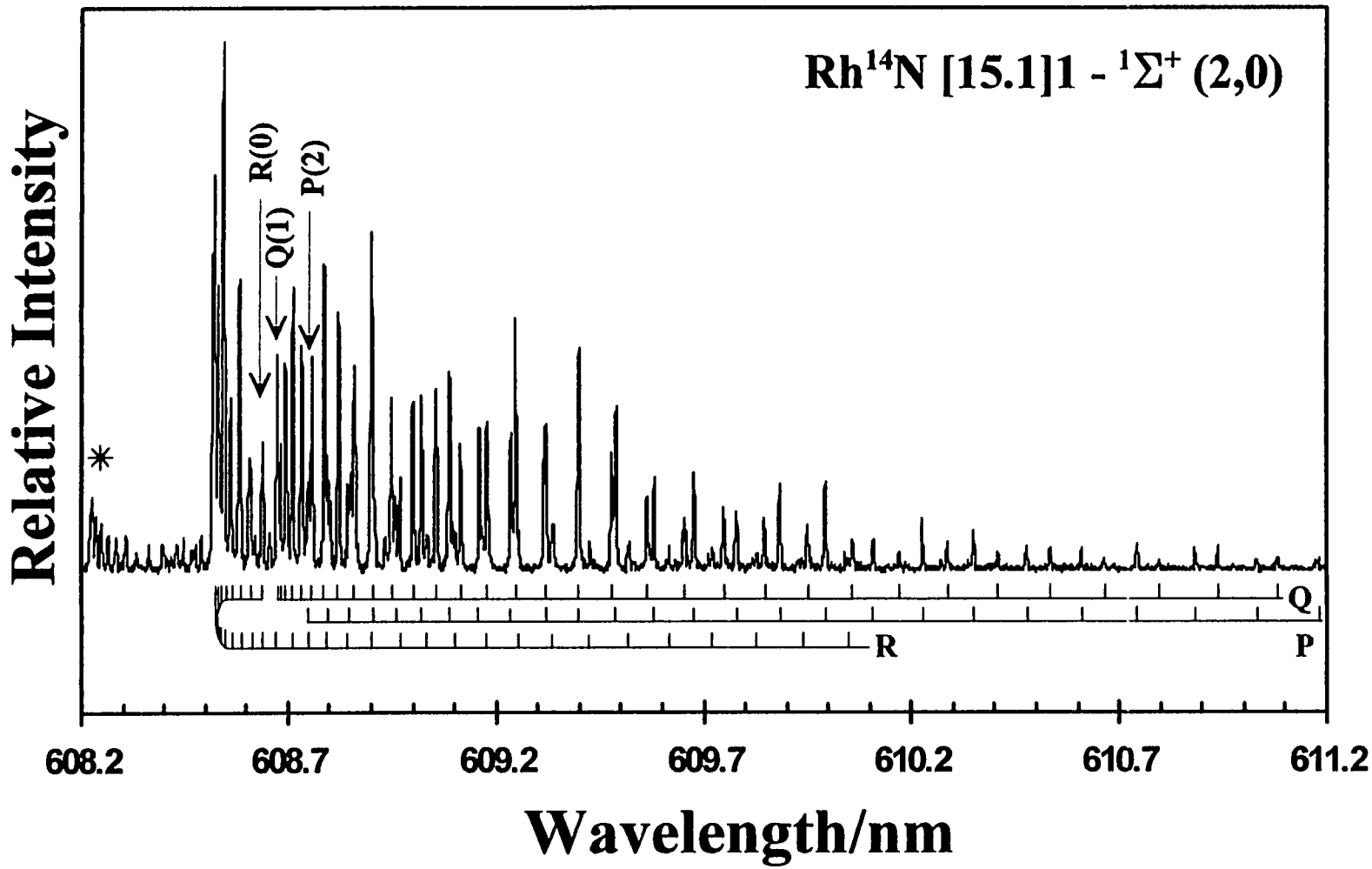

Fig. 5.5. The (2,0) band of the [15.1]1-$^1\Sigma^+$ system. The first lines of each branch are marked. The higher energy feature marked with a (*) is the R-head of the [15.1]1-[0.55] (3,0) band located at 608.22 nm.

The [15.1] - X system differs from the [19.5]-X and [22.4]-X systems in two other respects. The first difference is the striking disparity in the excited state lifetimes of the [15.1] levels in comparison to the other levels in the other systems. The lifetimes of the vibrational levels of the [15.1]1 state are approximately 1 μs. These values are an order of magnitude longer than the lifetimes of vibrational levels of the [19.5]0^+ and [22.4]0^+ states. Very different lifetimes have also been observed in the $B^2\Pi$ and $C^2\Sigma^+$ excited states of RhC mentioned in the previous chapter where the lifetimes of the vibrational levels associated with the $B^2\Pi$ state were found to be significantly longer (by a factor of 10) than in the vibrational levels belonging to the $C^2\Sigma^+$ excited state. The second major difference between the [15.1]1-X and both 0^+-X systems is the appearance of -553 cm-1 "hot" bands associated only with the bands of the [15.1]1-X system. One such "hot" band may be seen in Fig. 5.5. The nature of these "hot" bands is addressed in the discussion of the DF spectra in section 5.5.

Rotational analysis of the bands of the [15.1]1 - $X^1\Sigma^+$ system was straightforward. The bands did not show any local perturbations. The rotational constants (B_v and D_v) of the [15.1]1 state were determined individually for each vibrational band in the same manner described for the ground state. The rotational constants for the $v' = 0$, 1, and 2 vibrational levels of the [15.1]1 excited state are listed at the end of the results section. As was the case in the ground state, a hotter spectrum would certainly have aided in a more accurate determination of D_v'.

First combination differences {$\Delta_1F'(J)$ and $\Delta_1F''(J)$} with the Q-branch reveal that there is a slight combination defect present. The combination relations are represented by

equations 2.51 - 2.53. The Λ-doubling is proportional to J'(J'+1) which is as expected for a state with Ω'= 1 parentage [21]. To account for the splittings, a Λ-doubling term (see footnote on page 44) was added to equation 5.1 for the upper state such that

$$\nu = \nu_0 + B'J'(J'+1) - B''J''(J''+1) \pm \tfrac{1}{2}q'J'(J'+1) \qquad (5.4).$$

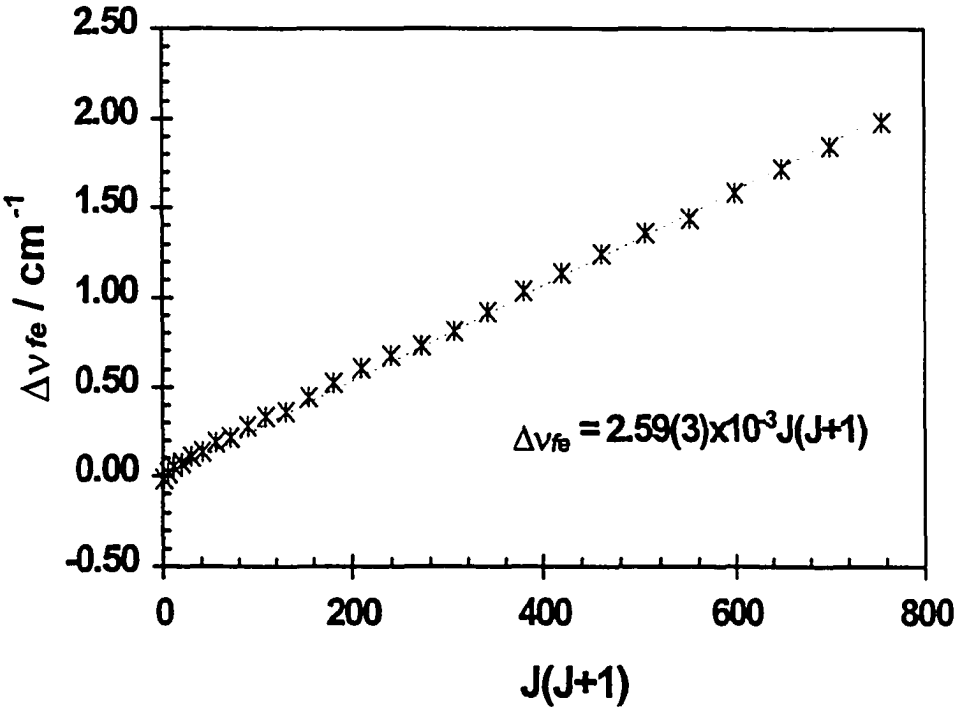

Fig. 5.6. Λ-type doubling in the v = 0 level of the [15.1]1 state of $Rh^{14}N$. The symbols represent the observed splittings. The dashed line represents the fit to the data. The uncertainty in the slope is included in the equation of the slope.

The observed defect (splittings) for the v'= 0 vibrational level of the [15.1] 1 state is shown in Fig. 5.6. The term q' referred to in equation 5.4 is the upper state Λ-doubling parameter. The "±" sign of equation 5.4 accounts for the splitting of the rotational levels in the doubly degenerate Π-state due to the interaction between the orbital and rotational

angular momenta. The upper sign of equation 5.4 refers to the *e* levels of the upper state and the lower sign to the *f* levels. The *e/f* parity labeling scheme for rovibronic wavefunctions is discussed in section 2.9. Since the ground state is a 0^+ state, it possesses only *e* levels. The "−q'" term in equation 5.4 is used to fit the R and P-branches as the selection rules ($e \leftrightarrow e$, $f \leftrightarrow f$) dictate [21]. The lower sign "+q'" is used to fit the Q-branch which is governed by the selection rule $e \leftrightarrow f$ [21].

With the values of rotational constants for each vibrational level (B_v') of the [15.1]1 state determined, an estimation of equilibrium rotational constant (B_e') could be made via

$$B_v' = B_e' - \alpha_e(v + \tfrac{1}{2}) \qquad (5.5).$$

By plotting B_v' against $(v + \frac{1}{2})$ as shown in Fig. 5.7, we obtain the values $B_e' = 0.4708$ cm^{-1} (from the y-intercept) and $\alpha_e = 0.00765(6)$ (from the slope). This B value for $Rh^{14}N$ corresponds to an equilibrium bond length (r_e) of 0.1705 nm.

The position and character of the 588.40 nm band suggests that the band is the (3,0) band of the [15.1]1−$X^1\Sigma^+$ system. No bands of any significant intensity that could be associated with the 588.40 nm band but those of the [15.1]−X system are observed in this region. The irregular vibrational intervals observed for this system have made it almost impossible to confirm or refute if this band belongs to the [15.1] − X system or belongs to another system based on vibrational data alone. An excited state lifetime of 750 ns was determined for this vibronic level. This lifetime is approximately 200 ns shorter than for the other levels of the [15.1]1 state but much longer (by ~ 650 ns) than in the levels associated with the 0^+ states. However, the agreement between the B value

calculated from equation 5.5 (0.4440 cm^{-1}) and that determined from the rotational analysis (0.4566 cm^{-1}) in the upper state level is far from satisfactory. Also, the observed Λ-type doubling for this level is quite large (q = 3.1 $x10^{-3}$ cm^{-1}) in comparison to the v=1 and 2 (~0.6 $x10^{-3}$ cm^{-1}) levels but quite comparable to the value determined for the v=0 level (2.6 $x10^{-3}$ cm^{-1}) of the [15.1]1 state. Interaction(s) with a nearby dark state(s) may explain the anomalous behavior of the rotational constants of this vibronic level.

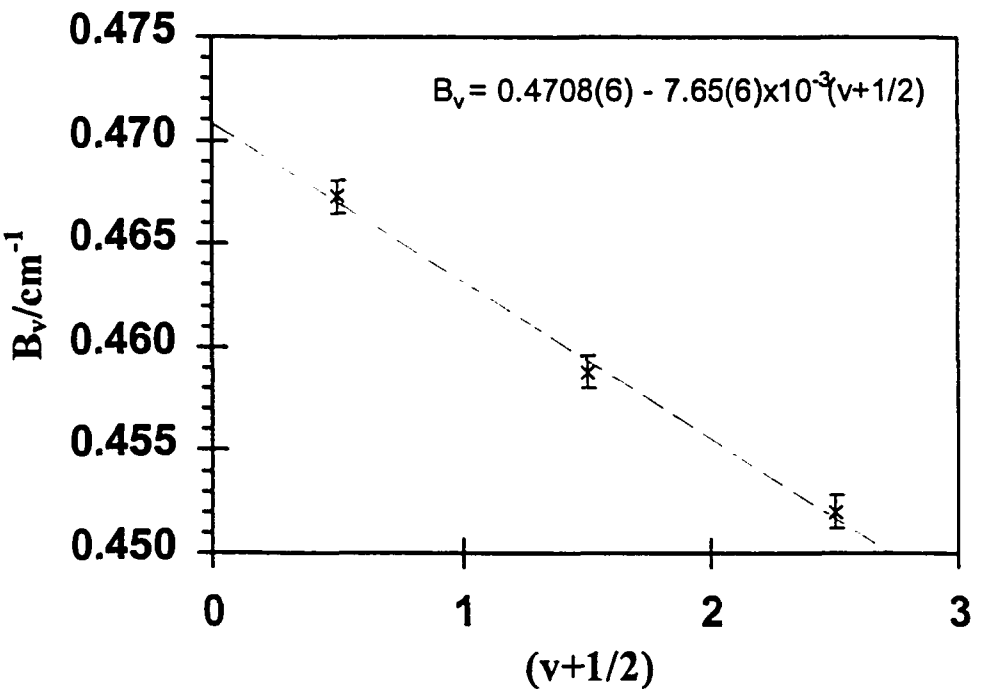

Fig. 5.7. Determination of B_e and α_e for the [15.1]1 electronic state of $Rh^{14}N$.

Mixed isotope spectra were recorded to confirm vibrational assignments for this system but the systems proved to be so weak that $Rh^{15}N$ bands were not observed. Unfortunately, our sample of $^{15}NH_3$ was depleted to the point that a more extensive probe of the region could not be furthered. At this point we have tentatively assigned the

588.40 nm band as the (3,0) band of the [15.1]1- $X^1\Sigma^+$ system. The dispersed fluorescence spectra recorded for this system was inconclusive due to the weak intensity of the feature. Without further evidence or investigation, the possibility that the 588.40 nm band is a (0,0) band of a new system cannot be dismissed.

Table 5.2. Rotational assignments and vacuum wavenumbers (cm^{-1}) for the [15.1]1 - $X^1\Sigma^+$ system of the $Rh^{14}N$ molecule.

	(0,0)			(1,0)		
J	R(J)	Q(J)	P(J)	R(J)	Q(J)	P(J)
0	15066.02			15728.60		
1	15066.88	15065.02		15729.41	15727.58	
2	15067.68	15064.86	15062.98	15730.10	15727.38	15725.55
3	15068.36	15064.59	15061.82	15730.77	15727.06	15724.34
4	15068.97	15064.23	15060.57	15731.19	15726.66	15723.03
5	15069.49	15063.82	15059.21	15731.71	15726.17	15721.62
6	15069.95	15063.32	15057.81	15732.01	15725.55	15720.11
7	15070.34	15062.66	15056.31	15732.26	15724.91	15718.55
8	15070.61	15062.00	15054.72	15732.41	15724.09	15716.80
9	15070.84	15061.23	15053.07	15732.41	15723.20	15715.00
10	15070.95	15060.37	15051.32	15732.41	15722.21	15713.15
11	15070.95	15059.42	15049.51	15732.21	15721.10	15711.12
12	15070.95	15058.40	15047.59	15732.01	15719.89	15709.07
13	15070.84	15057.26	15045.59	15731.64	15718.55	15706.85
14	15070.61	15056.04	15043.51	15731.14	15717.22	15704.60
15	15070.34	15054.72	15041.36	15730.62	15715.71	15702.16
16	15069.95	15053.39	15039.12	15729.96	15714.11	15699.67
17	15069.49	15051.91	15036.81	15729.21	15712.40	15697.08
18	15068.97	15050.37	15034.41	15728.32	15710.62	15694.42
19	15068.36	15048.72	15031.95	15727.38	15708.72	15691.61
20	15067.68	15046.97	15029.40	15726.32	15706.72	15688.73
21	15066.93	15045.18	15026.75	15725.16	15704.60	15685.75
22	15066.02	15043.26	15024.00	15723.94	15702.41	15682.68
23	15065.02	15041.27	15021.22	15722.58	15700.09	15679.50
24	15064.02	15039.16	15018.29	15721.10	15697.65	15676.19
25	15062.93	15037.02	15015.32	15719.52	15695.16	15672.79
26	15061.73	15034.78	15012.29	15717.94	15692.55	15669.33
27	15060.48	15032.45	15009.18	15716.13	15689.81	15665.75
28	15059.21	15030.03	15005.96	15714.25	15686.98	15662.04
29		15027.52	15002.63	15712.33	15684.05	15658.24
30		15024.86		15710.23	15681.05	15654.36
31		15022.22		15707.24	15677.88	15650.37
32		15019.44		15705.74	15674.64	15646.23
33		15016.55		15703.42	15671.32	
34		15013.64		15700.88	15667.59	
35		15010.60			15664.30	
36		15007.47			15660.67	
37					15656.89	
38					15653.06	

Table 5.2 continued. Rotational assignments and vacuum wavenumbers (cm^{-1}) for the [15.1]1 - $X^1\Sigma^+$ system of the $Rh^{14}N$ molecule.

	(2,0)			(3,0)		
J	R(J)	Q(J)	P(J)	R(J)	Q(J)	P(J)
0	16425.55			16986.09		
1	16426.42	16424.64		16986.92	16985.08	16984.15
2	16427.04	16424.42	16422.53	16987.65	16984.87	16983.06
3	16427.66	16424.07	16421.34	16988.31	16984.56	16981.85
4	16428.12	16423.58	16419.92	16988.86	16984.15	16980.60
5	16428.44	16423.02	16418.49	16989.29	16983.63	16979.16
6	16428.66	16422.34	16416.95	16989.67	16983.06	16977.69
7	16428.79	16421.51	16415.25	16989.93	16982.36	16976.11
8	16428.79	16420.62	16413.42	16990.16	16981.56	16974.44
9	16428.66	16419.56	16411.51	16990.16	16980.66	16972.68
10	16428.44	16418.49	16409.48	16990.16	16979.65	16970.83
11	16428.12	16417.19	16407.33	16990.04	16978.53	16968.87
12	16427.60	16415.82	16405.07	16989.81	16977.35	16966.86
13	16427.04	16414.31	16402.67	16989.52	16976.05	16964.73
14	16426.36	16412.72	16400.17	16989.12	16974.64	16962.45
15	16425.55	16411.02	16397.59	16988.63	16973.14	16960.09
16	16424.64	16409.16	16394.85	16988.02	16971.55	16957.68
17	16423.58	16407.22	16392.08	16987.30	16969.83	16955.18
18	16422.53	16405.10	16389.07	16986.55	16968.01	16952.53
19	16421.16	16402.94	16386.00	16985.68	16966.08	16949.86
20	16419.78	16400.63	16382.94	16984.82	16964.09	16947.01
21	16418.22	16398.21	16379.53	16983.78	16961.96	16944.11
22	16416.63	16395.63	16376.10	16982.50	16959.75	16941.13
23	16414.87	16393.04	16372.56	16981.21	16957.42	16938.00
24	16413.20	16390.25	16368.97	16979.86	16955.03	16934.78
25	16411.29	-	16365.14	16978.41	16952.47	16931.51
26	16409.16	16384.34		16976.83	16949.92	16928.13
27	16406.74	16381.20		16975.18	16947.16	16924.66
28	16404.37	16377.90		16973.48	16944.28	16921.08
29	16401.87	16374.57		16971.55	16941.38	16917.39
30	16399.15	-		16969.68	16938.34	16913.64
31	16396.43			16967.58	16935.24	16909.75
32				16965.97	16931.97	16905.77
33				16963.20	16928.59	16901.80
34				16960.84	16925.18	16897.83
35				16958.34	-	16893.85
36					16918.05	16889.88
37					-	

(iii) The [19.5]0$^+$ – X$^1\Sigma^+$ System

In the general description of the $Rh^{14}N$ spectrum (section 5.2), we mentioned that we divided the spectrum into regions that contained groups of bands. In the region 520 - 455 nm, there are four prominent bands. The lowest energy and strongest feature in this region has its head at 512.97 nm. The very small $Rh^{14}N/Rh^{15}N$ isotope shift (-0.49 cm^{-1}) confirmed that this band was the (0,0) band of this system. The measured isotope shifts were used to determine the vibrational numbering of the system. We were able to determine that the $Rh^{14}N$ band heads at 491.70, 472.95, and 456.20 nm share a common lower vibrational level with the 512.97 nm band. We have assigned these three bands as the (1,0), (2,0), and (3,0) bands of this [19.5]-$X^1\Sigma^+$ system respectively.

The vibrational spacings of the [19.5] electronic state appear to be fairly regular. This allowed for satisfactory estimation of the vibrational constants ω_e' and $\omega_e x_e'$: these were determined to be 877 cm^{-1} and 17.0 cm^{-1} respectively. In Fig. 5.8 the measured and calculated isotope shifts for each band of the [19.5]-X system are shown. The agreement between the measured and calculated shifts is satisfactory with a slight deviation for the (3,0) band. The discrepancy between the observed and calculated isotope shift for the (3,0) band is good evidence that the $v' = 3$ level is perturbed.

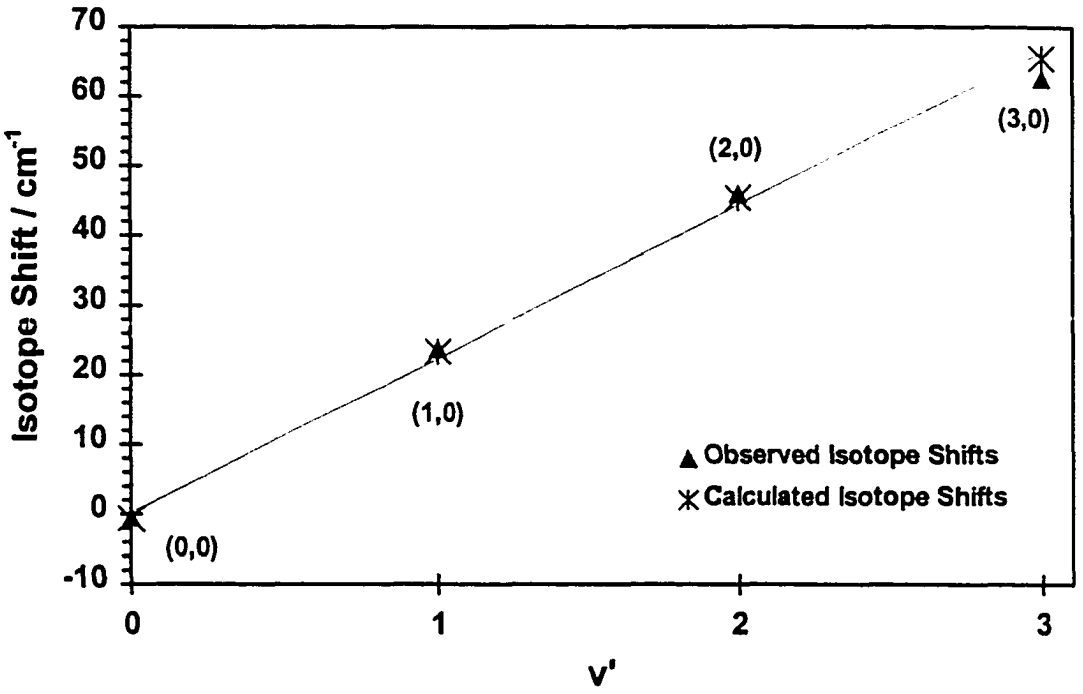

Fig. 5.8. Comparison of the observed and calculated isotope shifts for the bands of the [19.5]0^+-$X^1\Sigma^+$ system. (▲) represents measured isotope shifts whereas (*) represents the calculated isotope shifts. The solid line represents the best fit of the experimental data. Measurement errors are approximately ± 0.1 cm^{-1}.

In the $Rh^{14}N$ spectrum we observed three very weak bands associated with the [19.5]-$X^1\Sigma^+$ system that originate from the v = 1 level of the $^1\Sigma^+$ ground state. The (0,1), (2,1), and (3,1) bands are located at 537.70 nm, 493.84 nm, and 475.70 nm. Unfortunately, only the (0,1) band was observed in the LIF spectrum of the $Rh^{15}N$ isotopomer. This prevented a more detailed analysis of the $Rh^{15}N$ ground state.

The vibrational intervals for the [19.5] state of the $Rh^{15}N$ allowed for rough estimates of 851 cm^{-1} and 16.1 cm^{-1} for the values of ω_e' and $\omega_e x_e'$. With values of ω_e' and $\omega_e x_e'$ determined for both isotopomers, comparison can be drawn between calculated and experimental values of the isotope ratio ρ according to the relations [21]

$$\omega_e' / \omega_e = \rho \quad \text{and} \quad \omega_e' x_e' / \omega_e x_e = \rho^2 \qquad (5.6).$$

The measured ratio 0.9704 is in excellent agreement with theoretical value of 0.9703 determined from the reduced masses. The correlation between the calculated (0.9414) and experimentally determined ratio (0.9470) of ρ^2 determined from the anharmonicity constants is not as satisfactory as that found for the (ω_e' / ω_e) ratio and this is understandable from the error limits on $\omega_e x_e$.

Where there was sufficient intensity, the excited state lifetimes of the upper state vibronic levels of the [19.5] state were measured at the R-band heads and at any other distinguishable rotational line. Multiple measurements were made at each line in order to check reproducibility. The lifetimes determined for different vibronic levels of this state are much the same. The v = 0, 1, and 2 levels exhibit lifetimes of about 100 ± 25 ns. The lifetime of the v′ = 3 level departs from the consistent values obtained for the other members of the progression. The LIF decays recorded at 512.97 nm (v′ = 0 level) and 456.19 nm (v′ = 3 level) are shown in Fig. 5.9. Although there is not a huge difference in the excited state lifetime, the v′ = 3 vibronic level has a slightly longer lifetime of 145 ± 25 ns. The deviation suggests that the v′ = 3 level may be perturbed by a nearby state. The slightly longer lifetime is accompanied by a slight discrepancy in the isotope shift for this (3,0) band. Although these observations may be coincidences, evidence supporting a possible interaction with another state is mounting. There is no physical evidence of any other band within 10 nm of the 456.19 nm band that could be interacting with this band. However, there are a couple of extra lines that appear to higher energy of the R-head which cannot be explained at this time. The extra lines are likely due to some underlying

structure. One plausible supposition is that this vibrational level is interacting with another state, where the perturber is a "dark" state.

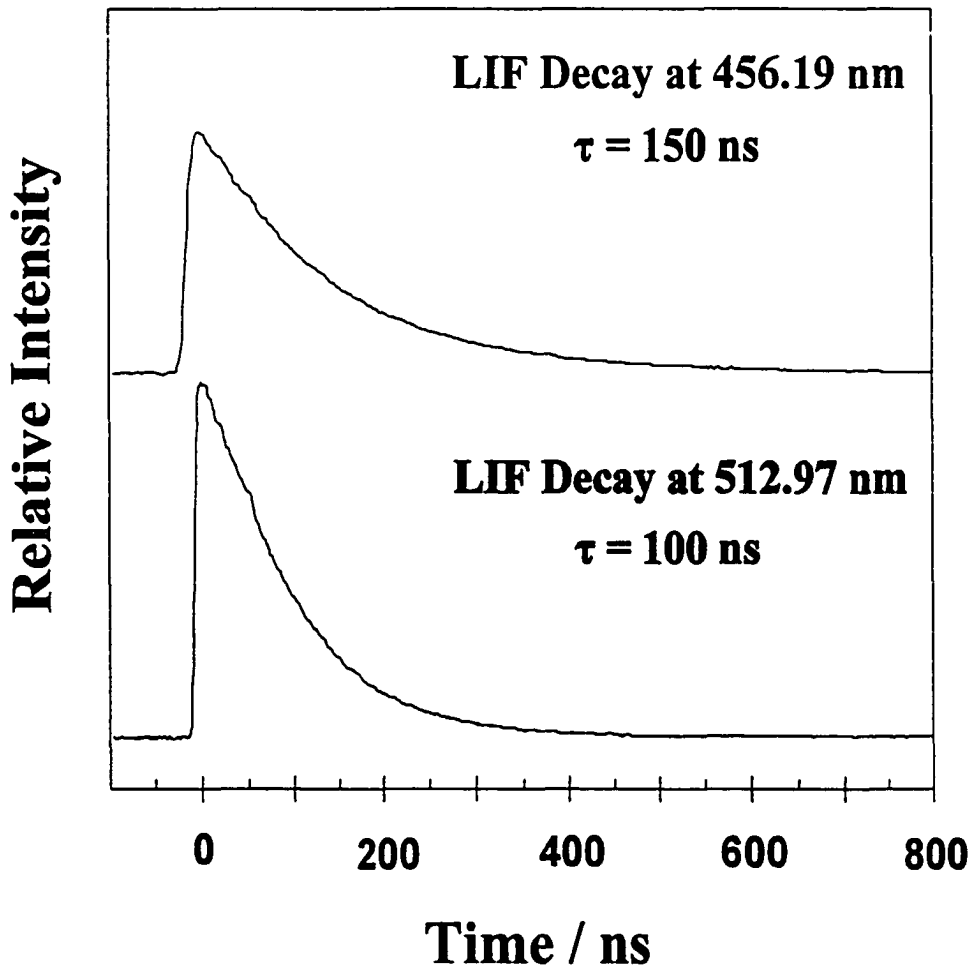

Fig. 5.9. The LIF decay profiles observed for the 512.97 nm (v′=0) band and the 456.19 nm (v′=3) band.

The simple rotational branch structure of the bands of this [19.5]-$X^1\Sigma^+$ system suggest the upper state has $\Omega = 0^+$, possibly of $^1\Sigma^+$symmetry. The first lines of the bands of the [19.5]0^+-$X^1\Sigma^+$ system, R(0) and P(1), support a 0^+-0^+ transition. Reproductions of the rotationally resolved spectra are shown in Fig. 5.10 - Fig. 5.13. Line positions and rotational assignments are listed for the (0,0), (1,0), (2,0), and (3,0) bands in Table 5.3 at the end of this section.

Rotational assignments were relatively straightforward for the bands of this system. The upper state rotational constants for each vibrational level of this electronic state were determined. The B_v values for the [19.5]$^1\Sigma^+$ state follow the equation:

$$B_v = 0.4669(5) - (v + ½)0.00582(6) \qquad (5.7).$$

An equilibrium bond length, r_e[19.5] = 01712 nm was calculated from the value of B_e.

Rotational assignments and line positions for the $Rh^{15}N$ corresponding bands are given in Table 5.4 at the end of this section. The B values obtained for the $Rh^{15}N$ species for the [19.5]0^+-$X^1\Sigma^+$ system were consistent with those obtained for $Rh^{14}N$. The value of the rotational constant B_e was determined to be 0.4394(5) cm^{-1}. Using the relationship

$$\rho^2 = B_e(Rh^{15}N)/B_e(Rh^{14}N) \qquad (5.8)$$

the experimentally determined $B_e(Rh^{15}N)/B_e(Rh^{14}N)$ ratio of rotational constants is 0.9413 in excellent agreement with the reduced mass-calculated ρ^2 value of 0.9414.

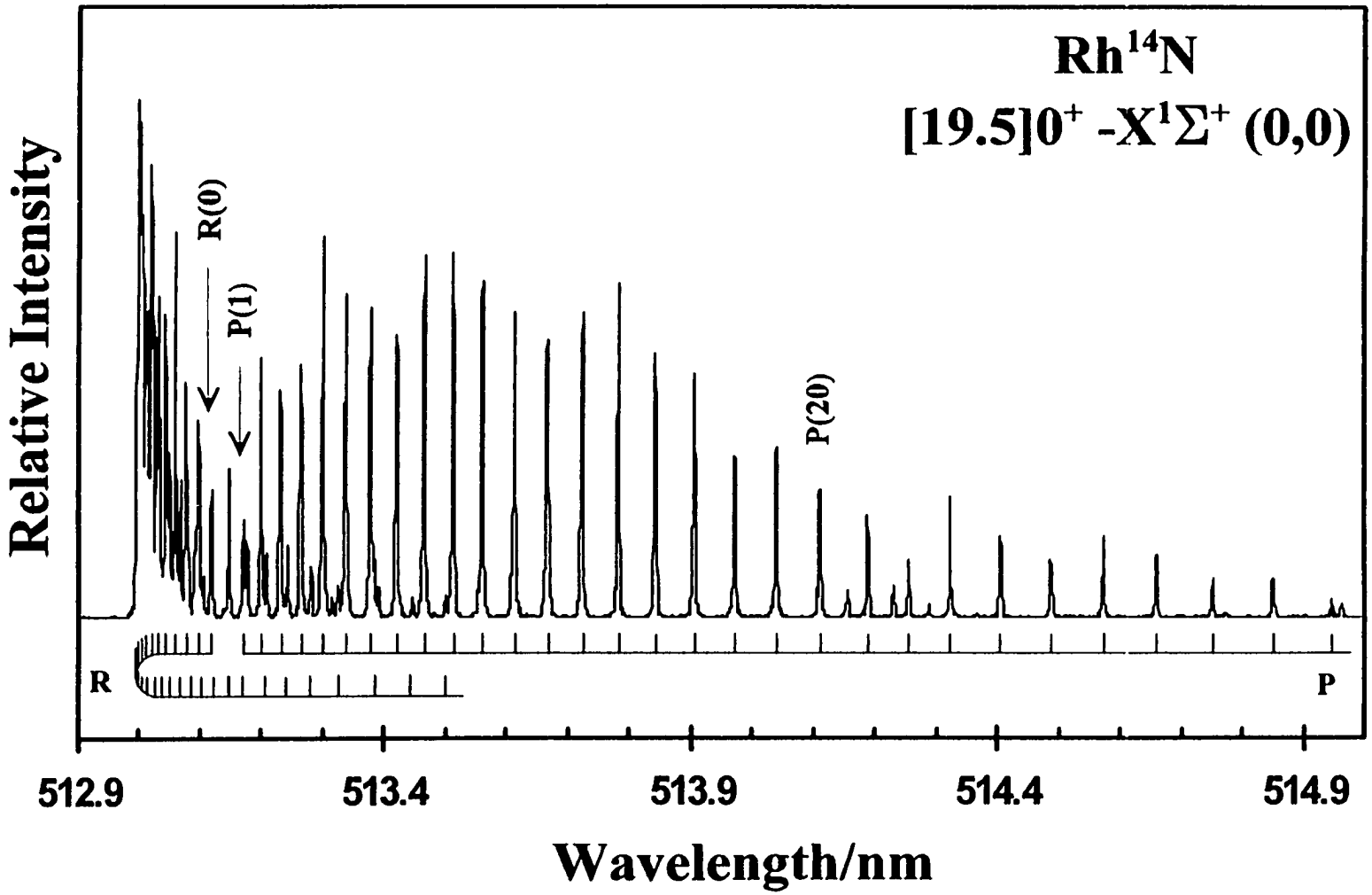

Fig. 5.10. The (0,0) band of the [19.5]0' - X¹Σ'. The first lines are marked.

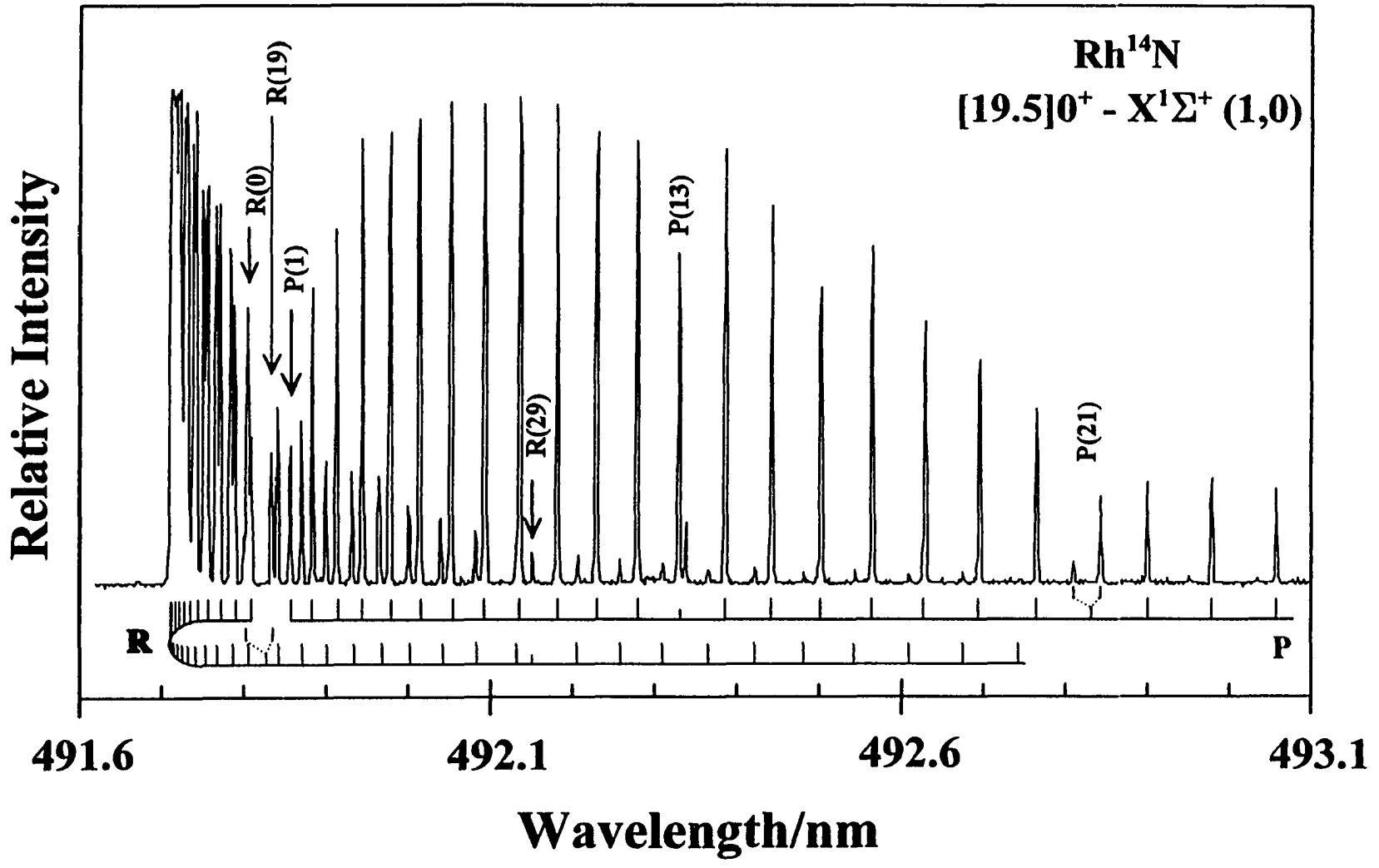

Fig. 5.11. The (1,0) band of the [19.5]0' - X¹Σ' system. The first lines of each branch are marked.

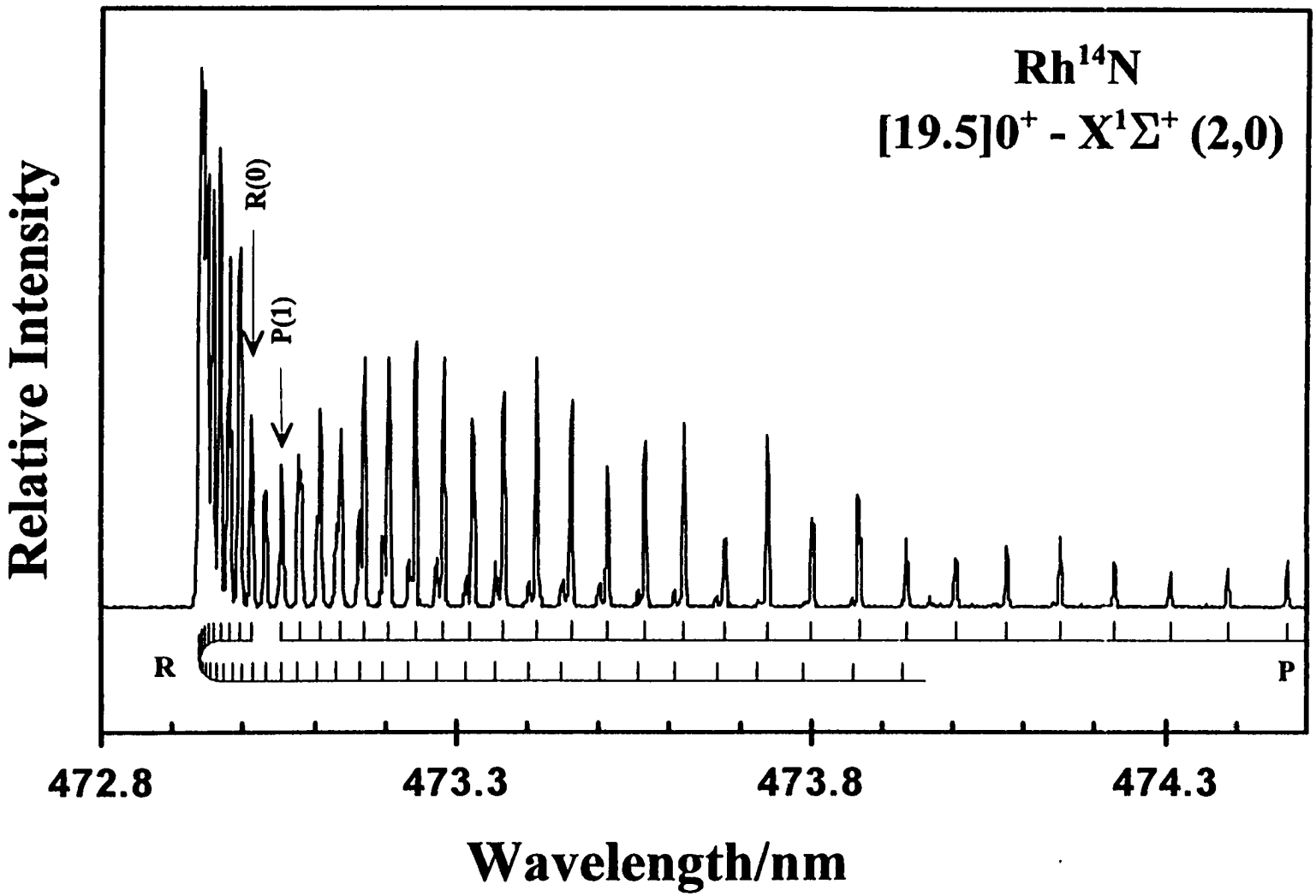

Fig. 5.12. The (2,0) band of the [19.5]0' - $X^1\Sigma^+$ system. The first lines of each branch are marked.

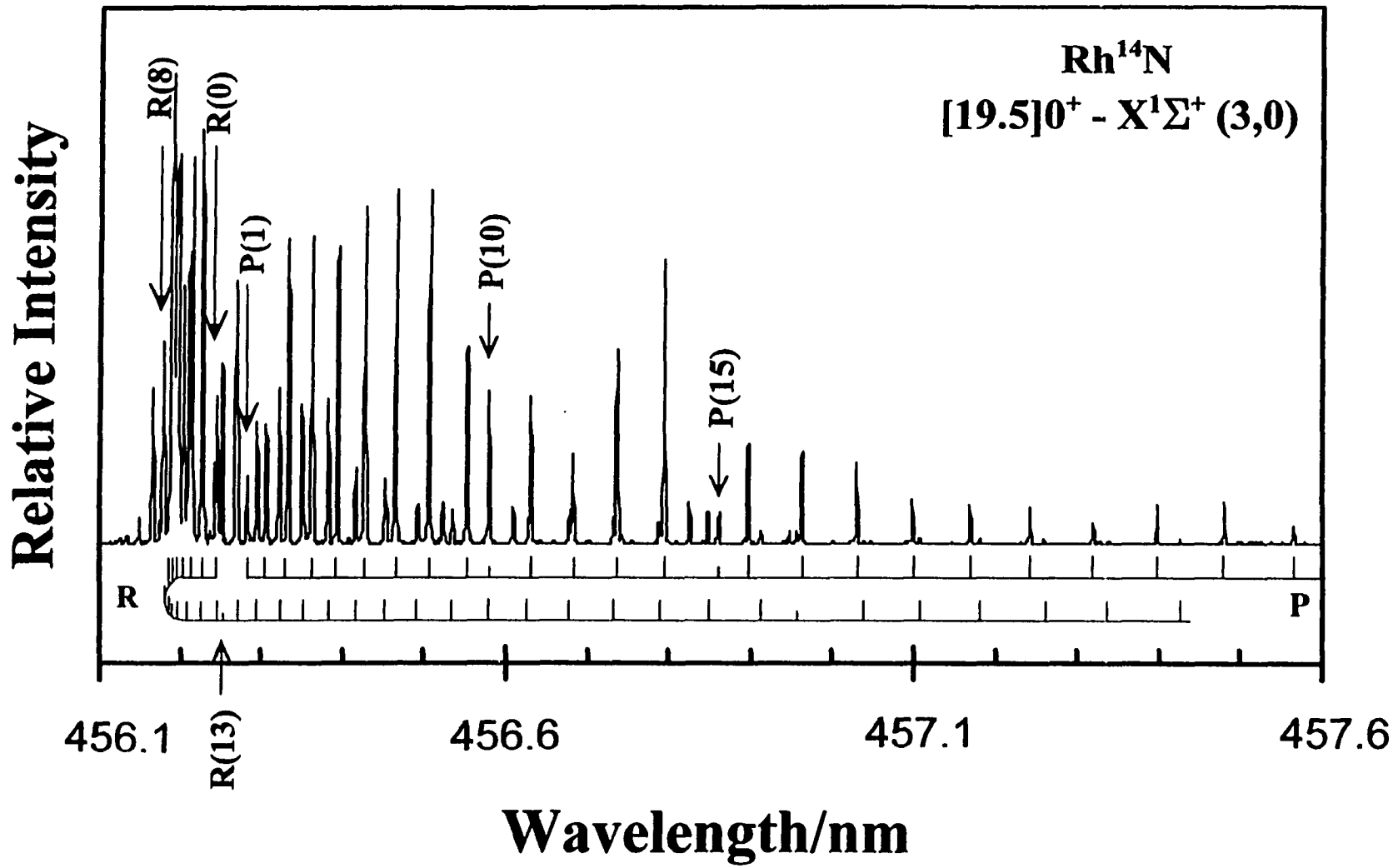

Fig. 5.13. The (3,0) band of the [19.5]0$^+$ - X$^1\Sigma^+$ system. The first lines of each branch are marked along with local rotational perturbations.

Several local rotational perturbations are evident in the bands of the [19.5]0^+ - $X^1\Sigma^+$ system of the $Rh^{14}N$ spectrum. They are associated with the upper state vibrational levels. By simple inspection of Fig. 5.10, one can see examples of these local perturbations in terms of line displacements, appearance of extra lines, and intensity disturbances near 514.2 nm. The perturbations occur in the upper J levels 20, 21, and 22 as three extra lines appear in the spectrum associated with these rotational levels. An extra line also appears for the upper J = 28 level. The reduced term plot for this band shows that the lines between J(22) and J(27) appear to be slightly displaced to higher energy from the regular course of the branch. There are three local perturbations in the v' = 1 level of the [19.5] state. These occur in the upper J levels 12, 20, and 29. These perturbations are labeled in the spectrum shown in Fig. 5.11. The branch pattern is disturbed slightly between J(20) and J(29) as is most clearly seen in the P-branch. A reduced term plot is shown in Fig. 5.14. The (2,0) band of this system shows no extra lines but the P(16) intensity is quite weak in comparison to the neighboring lines of the branch. The [19.5] v = 3 vibrational level exhibits local rotational perturbations in the upper J levels 9, 14, and 32. With the limited J structure and the number of local perturbations present in each spectrum, it is likely that more than one state is responsible for the observed perturbations in each band. This is not surprising given the number of electronic states observed for RhN.

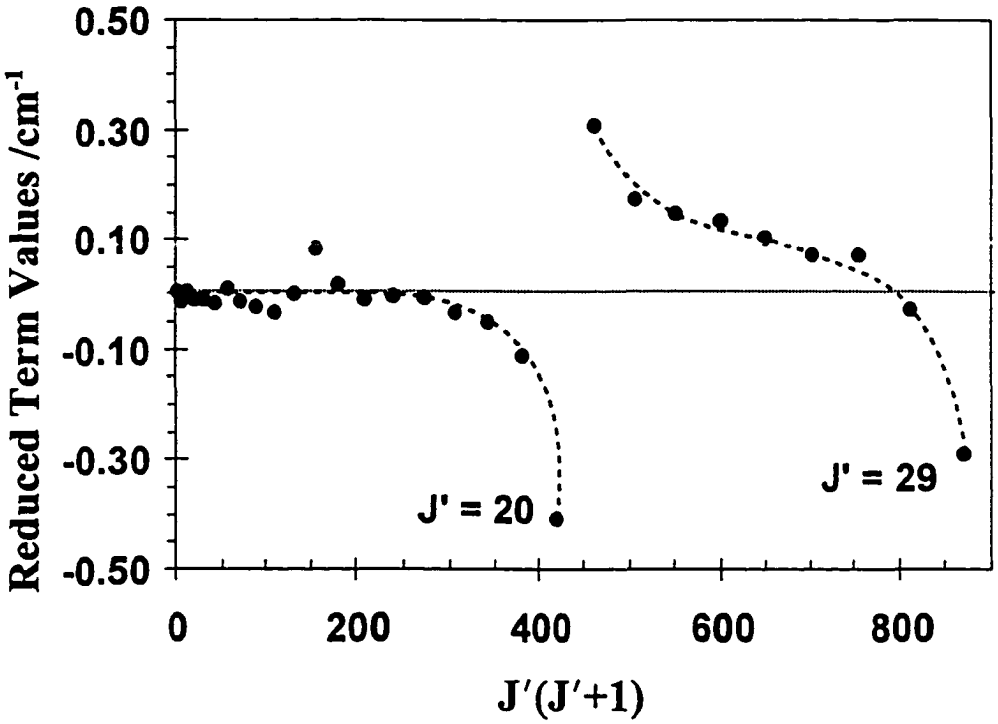

Fig. 5.14. Reduced term plot for the v = 1 level of the [19.5]0^+ state. Each rotational level is reduced by subtracting (T_0+B'J(J+1)).

Table 5.3. Rotational assignments and vacuum wavenumbers (cm^{-1}) for the [19.5]0^+ - $X^1\Sigma^+$ system of the $Rh^{14}N$ molecule.

	(0,0)		(1,0)	
J	R(J)	P(J)	R(J)	P(J)
0	19484.29		20327.47	
1	19485.12	19482.31	20328.30	20251.51
2	19485.88	19481.21	20329.04	20254.34
3	19486.53	19480.04	20329.66	20258.40
4	19487.10	19478.75	20330.20	20262.18
5	19487.67	19477.38	20330.65	20265.79
6	19488.04	19475.98	20331.02	20269.33
7	19488.35	19474.46	20331.23	20272.77
8	19488.54	19472.83	20331.39	20276.06
9	19488.77	19471.13	20331.46	20279.30
10	19488.88	19469.31	20331.45	20282.55
11	19488.77	19467.45	20331.39	20284.85
12	19488.61	19465.52	20331.15	20288.06
13	19488.42	19463.51	20330.77	20290.94
14	19488.27	19461.35	20330.36	20293.70
15	19487.89	19459.12	20329.87	20296.34
16	19487.48	19456.81	20329.20	20298.89
17	19486.91	19454.42	20328.50	20301.32
18	19486.22	19451.93	20327.64	20303.67
19	19485.27	19449.36	20326.44	20306.02
20	19484.82	19446.60	20326.17	20308.08
21	19484.29	19443.65	20324.95	20310.10
22	19483.19	19441.15	20323.75	20312.08
23	19482.09	19438.62	20322.43	20313.97
24	19480.87	19435.49	20321.03	20315.75
25	19479.58	19432.39	20319.54	20317.40
26	19478.10	19429.14	20317.98	20319.01
27	19476.43	19425.82	20316.20	20320.49
28	19474.18	19422.32	20314.18	20321.90
29	19473.93	19418.58	20313.35	20323.18
30		19414.32	20311.09	20324.41
31			20308.98	20325.53
32			20306.80	
33			20304.53	
34			20302.18	
35			20300.16	
36			20294.52	
37			20291.77	
38			20288.89	

Table 5.3 continued. Rotational assignments and vacuum wavenumbers (cm^{-1}) for the [19.5]0^+- $X^1\Sigma^+$ system of the $Rh^{14}N$ molecule.

	(2,0)		(3,0)	
J	R(J)	P(J)	R(J)	P(J)
0	21135.17		21911.81	
1	21135.93	21133.34	21912.68	21918.92
2	21136.60	21132.04	21913.30	21919.55
3	21137.18	21130.79	21913.83	21920.07
4	21137.67	21129.45	21914.17	21920.41
5	21137.99	21127.97	21914.45	21920.70
6	21138.26	21126.46	21914.55	21920.80
7	21138.39	21124.76	21914.29	21920.54
8	21138.42	21123.02	21914.98	21921.23
9	21138.39	21121.10	21914.55	21920.79
10	21138.26	21119.19	21914.07	21920.31
11	21137.99	21117.09	21913.30	21919.55
12	21137.68	21114.86	21912.68	21918.92
13	21137.18	21112.58	21911.53	21917.77
14	21136.60	21110.18	21911.81	21918.06
15	21135.93	21107.68	21910.66	21916.91
16	21135.17	21105.10	21909.41	21915.66
17	21134.28	21102.42	21908.17	21914.41
18	21133.34	21099.62	21906.78	21913.02
19	21132.22	21096.72	21905.24	21911.48
20	21131.02	21093.69	21903.56	21909.81
21	21129.72	21090.58	21901.83	21908.08
22	21128.29	21087.38	21899.92	21906.16
23	21126.82	21084.00	21897.86	21904.10
24	21125.17	21080.57	21895.70	21901.94
25	21123.43	21077.06	21893.21	21899.45
26	21121.60	21073.42	21890.91	21897.15
27	21119.63	21069.69	21888.32	21894.56
28	21117.58	21065.87	21885.64	21891.88
29	21115.39	21061.92	21882.72	21888.96
30	21113.07	21057.88	21879.61	
31	21110.67	21053.75		
32	21108.30			
33	21105.67			
34	21102.96			
35	21100.06			
36	21097.08			
37				
38				

Table 5.4. Rotational assignments and vacuum wavenumbers (cm^{-1}) for the $[19.5]0^+ - X^1\Sigma^+$ system of the $Rh^{15}N$ molecule.

	(0,0)		(1,0)	
J	R(J)	P(J)	R(J)	P(J)
0	19485.03		20304.52	
1	19485.78	19483.21	20305.26	20302.72
2	19486.50	19482.19	20305.96	20301.61
3	19487.15	19481.06	20306.49	20300.54
4	19487.71	19479.85	20307.31	20299.23
5	19488.24	19478.60	20307.64	20297.92
6	19488.62	19477.24	20307.93	20296.85
7	19488.89	19475.76	20308.18	20295.17
8	19489.11	19474.29	20308.26	20293.57
9	19489.30	19472.70	20308.34	20291.93
10	19489.38	19471.00	20308.26	20290.16
11	19489.38	19469.27	20308.18	20288.36
12	19489.30	19467.46	20307.93	20286.39
13	19489.11	19465.53	20307.64	20284.35
14	19488.89	19463.49	20307.31	20282.30
15	19488.42	19461.45	20306.86	20280.04
16	19488.02	19459.27	20306.29	20277.75
17	19487.52	19457.04	20305.67	20275.50
18	19486.82	19454.63	20304.89	20273.00
19	19486.28	19452.21	20304.03	20270.43
20	19485.44	19449.69	20303.17	20267.81
21	19484.57	19447.16	20302.14	20265.03
22	19483.44	19444.41	20301.08	20262.25
23	19482.04	19441.70	20299.84	20259.30
24	19479.66	19438.69	20298.57	20256.32
25	19479.32	19435.38	20297.20	20253.30
26	19477.73	19431.09	20295.78	20250.11
27	19475.95	19428.76	20294.22	20246.81
28	19474.52	19425.04	20292.58	20243.50
29	19472.70	19421.58	20290.82	20240.03
30		19418.12	20289.02	20236.44
31		19414.63	20286.99	
32			20285.33	20229.15
33				20225.32
34			20280.82	

Table 5.4 continued. Rotational assignments and vacuum wavenumbers (cm^{-1}) for the [19.5]0^+- $X^1\Sigma^+$ system of the $Rh^{15}N$ molecule.

	(2,0)		(3,0)	
J	R(J)	P(J)	R(J)	P(J)
0	21090.44		21843.98	
1	21091.19	21088.62	21844.69	21842.18
2	21091.90	21087.56	21845.12	21841.18
3	21092.43	21086.41	21845.69	21839.94
4	21092.88	21085.17	21846.07	21838.37
5	21093.23	21083.88	21846.26	21837.09
6	21093.54	21082.33	21846.36	21835.62
7	21093.60	21080.83	21846.36	21833.91
8	21093.65	21079.19	21846.26	21832.10
9	21093.65	21077.51	21845.98	21830.16
10	21093.54	21075.69	21845.60	21828.12
11	21093.23	21073.74	21845.12	21825.98
12	21092.88	21071.71	21844.50	21823.70
13	21092.43	21069.59	21843.79	21821.33
14	21091.95	21067.33	21842.98	21818.87
15	21091.32	21065.03	21842.03	21816.21
16	21090.57	21062.60	21841.46	21813.51
17	21089.86	21060.08	21840.09	21810.63
18	21088.89	21057.52	21838.80	21808.15
19	21087.82	21054.82	21837.42	21804.93
20	21086.67	21051.95	21835.95	21801.71
21	21085.52	21049.04	21834.34	21798.49
22	21084.15	21046.04	21832.58	21795.09
23	21083.26	21042.90	21830.73	21791.59
24	21081.58	21039.64	21828.78	21787.94
25	21079.90	21036.95	21826.69	21784.26
26	21078.12	21033.33	21824.46	21780.43
27			21822.14	21776.46
28			21819.72	21772.40
29			21817.11	21768.20

(iv) The [22.4]0^+ - $X^1\Sigma^+$ System

To this point the [15.1]1 - $X\ ^1\Sigma^+$ and [19.5] 0^+ - $X\ ^1\Sigma^+$ systems account for just about all the bands observed in the RhN LIF spectrum to wavelengths longer than 450 nm. To higher energy, four prominent features were detected that could be assigned to a third electronic transition. These four bands resemble those recorded for the [19.5]0^+ - $X^1\Sigma^+$ system. A simple R and P branch structure is exhibited by each band indicating that the excited state is of a singlet nature. The [22.4] excited state can be assigned as a $\Omega = 0^+$ state.

The first of the bands appears at 22385 cm^{-1} (446.59 nm) and exhibits the very small isotope shift (-0.55 cm^{-1}) which is expected for a (0,0) band. The LIF spectra for the $Rh^{14}N$ and $Rh^{15}N$ radicals recorded for this system are shown in Fig. 5.15 and Fig. 5.16. Rotational assignments and line positions for all bands associated with the [22.4]0^+ - $X^1\Sigma^+$ system of both isotopomers are listed in Table 5.5.

A very weak feature is observed approximately 900 cm^{-1} to the red of the 446.59 nm band in the $Rh^{14}N$ LIF spectra. It comes from the (0,1) transition. A similar hot band was identified for the [19.5]0^+ - $X^1\Sigma^+$ system. The isotope shift (–26.32 cm^{-1}) of this (0,1) band confirms the feature at 446.59 nm as the (0,0) band of this [22.4]0^+ - $X^1\Sigma^+$ system. The (1,0), (2,0), and (3,0) bands occur at respective vibrational intervals of 820, 798, and 717 cm^{-1}. Measured isotope shifts for the [22.4]0^+ - $X^1\Sigma^+$ system parallel observations for the 0–0 and 1–0 transitions for the [19.5]0^+ - X system. The observed shift for the (0,0) band agrees well with the calculated isotope shift of -0.58 cm^{-1}.

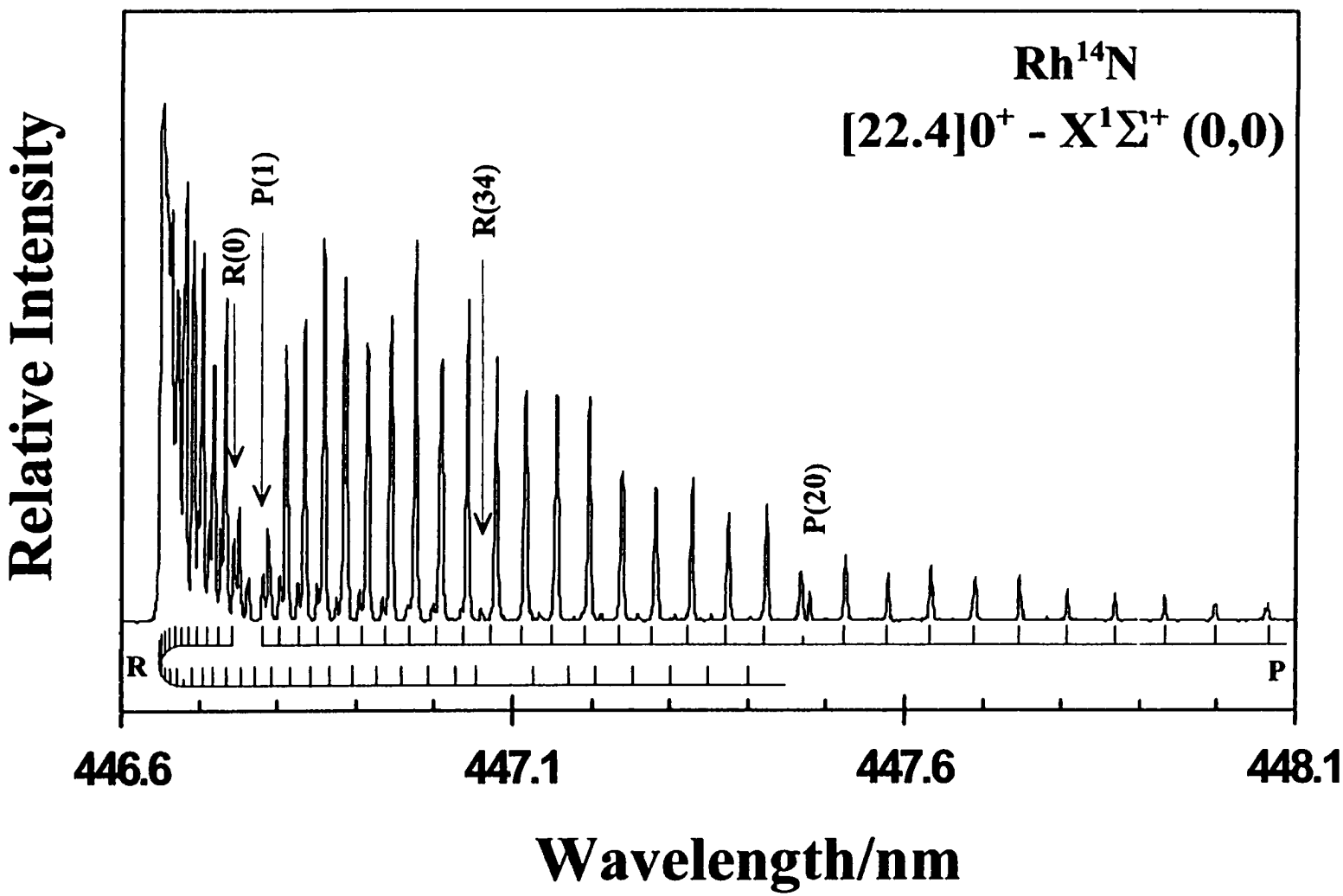

Fig. 5.15. The (0,0) band of the [22.4]0⁺ - X¹Σ⁺ system. The first lines are marked. The P(20) and R(34) lines are marked to indicate local rotational perturbations.

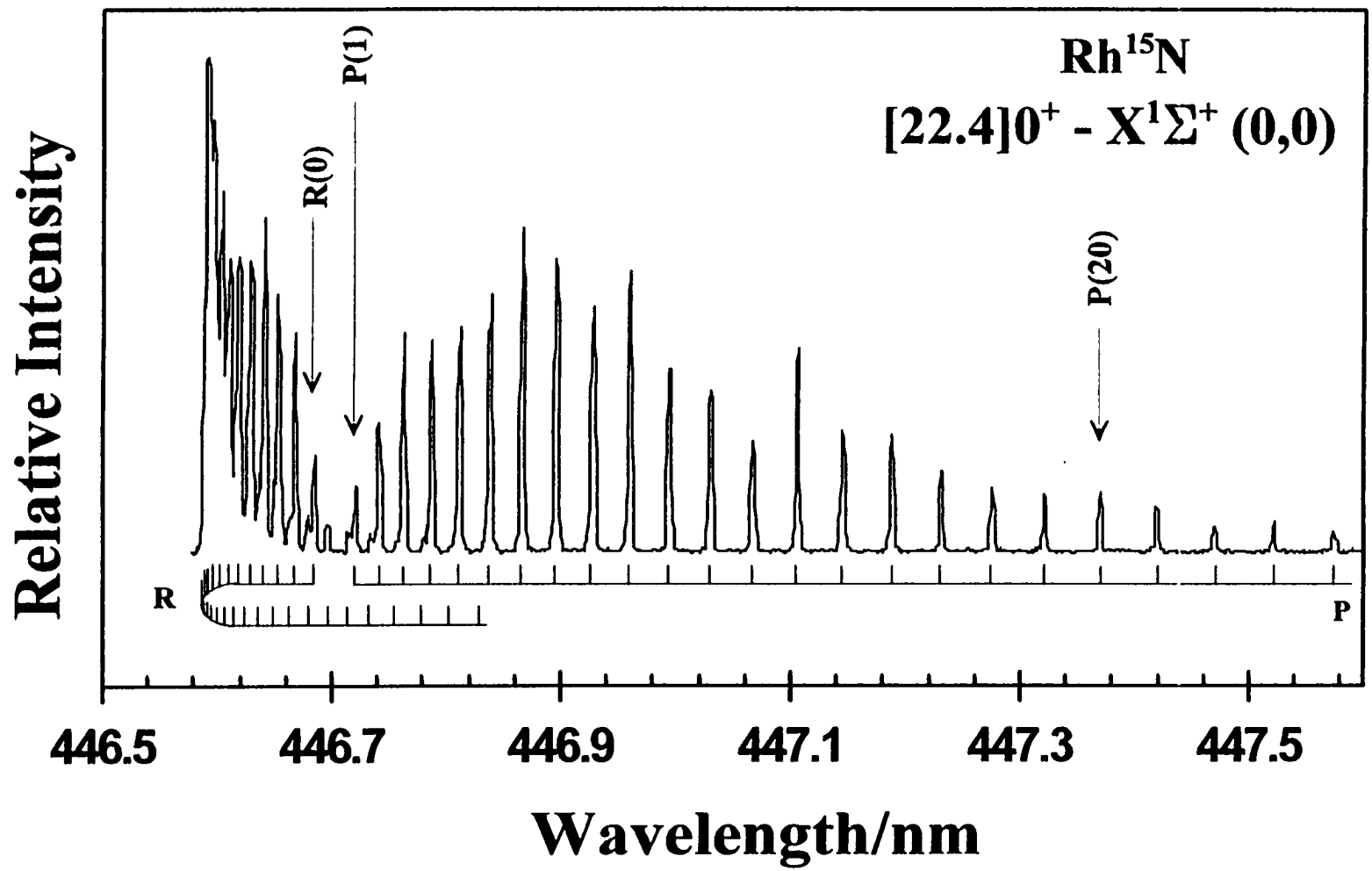

Fig. 5.16. The (0,0) band of the [22.4]0' - X¹Σ' system of $Rh^{15}N$. The first lines and P(20) are marked.

However, the difference between the calculated and observed shift for the (1,0) band is somewhat larger (~1.4 cm^{-1}) than expected. Isotope shifts for the bands of this system are listed in Table 5.1. These vibrational spacings in the [22.4]0^+ state are sufficiently regular to allow estimates for ω_e' and $\omega_e x_e'$ to be made: values of 881 and 13.7 cm^{-1} are found for these constants, respectively for $Rh^{14}N$. For $Rh^{15}N$, ω_e' and $\omega_e x_e'$ were found to be 816 and 14.3 cm^{-1} respectively. Values of 0.926 and 1.02 were determined for ρ from the expressions in equation 5.6. These values do not agree with the theoretical ratio from the reduced masses (0.941). The vibrational spacings for both the [19.5] and [22.4] states are not so free from perturbational disturbances that a very meaningful values of ω_e' and $\omega_e x_e'$ can be obtained.

Excited state lifetimes in the four v = 0 to 3 vibrational levels of the [22.4]0^+ state were measured. The lifetimes for the vibronic levels of this state were consistent as was the case for the levels of the [19.5]0^+ state. Lifetimes of about 75(5) ns were obtained. All measured lifetime measurements are included in Table 5.1. If the v = 1 level is perturbed as the isotope shift would seem to suggest, one would expect to note an anomaly in the lifetime as was the case in the v′ = 3 level of the [19.5]0^+ state. However, there is a uniformity to the excited state lifetimes for the [19.5]0^+ state which suggests that these $Rh^{14}N$ levels are not disturbed by any neighboring state(s). The possibility exists that the (1,0) band of the $Rh^{15}N$ isotopomer is perturbed and the discrepancy between the measured and calculated shift comes from $Rh^{15}N$ isotopomer and not $Rh^{14}N$. Unfortunately, no excited state lifetime measurements were made for the $Rh^{15}N$ isotopomer due to limitations on the amount of $^{15}NH_3$ available. It is, therefore,

impossible to confirm a disturbance in the $Rh^{15}N$ $v' = 1$ level at this time.

The rotational line assignments for the (0,0), (1,0), (2,0), and (3,0) bands were straightforward. As in the fits of the other bands, combination differences were used to determine the rotational constant B. A fit of the B_v values for the [22.4] 0^+ state generates the following relation:

$$B_v = 0.4651(7) - (v + ½)0.0075(6) \qquad (5.9).$$

An equilibrium bond length of 0.1715(4) nm was determined from the value of B_e, for this 0^+ state. This bond length is almost identical to that determined for the [19.5]0^+ excited state. Like the [19.5] 0^+ state, the relationship between B_e^i and B_e was satisfactory. A value of 0.4385_4 cm^{-1} was determined for B_e^i yielding a value of 0.9709 for ρ compared with the mass determined value of 0.9703.

Local perturbations are apparent at $J' = 21$ and 35 in the (0,0) band of the [22.4] $0^+ - X^1\Sigma^+$ system. These perturbations are indicated in the 446 nm band shown in Fig. 5.15. Similar rotational anomalies are evident in the other bands of this system. With the observed range of J being so limited in each of the observed bands, correlation between these perturbations is, at best, speculative. The perturbations are indicated in Fig. 5.17. It is likely that more than one state is responsible for the disturbances.

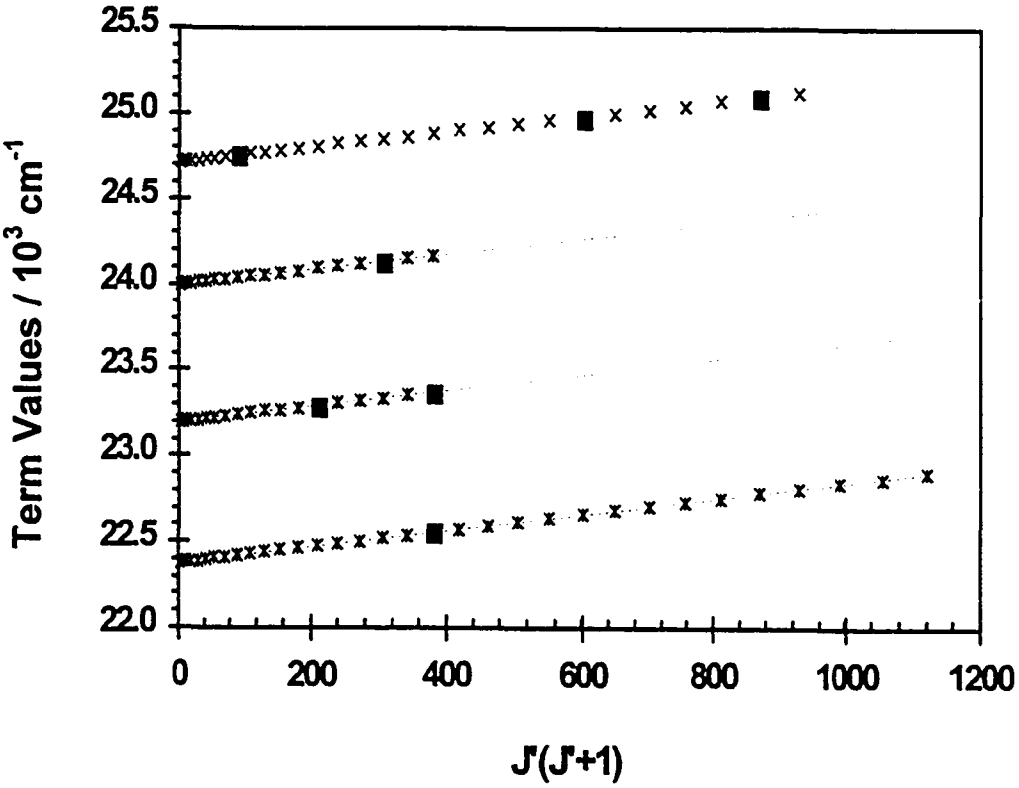

Fig. 5.17. Upper state term values for the [22.4] 0^+ electronic state of $Rh^{14}N$. Positions of local perturbations are marked with solid squares.

Table 5.5. Rotational assignments and vacuum wavenumbers (in cm^{-1}) for the $[22.4]0^+ - X^1\Sigma^+$ system of the $Rh^{14}N$ molecule.

	(0,0)		(1,0	
J	R(J)	P(J)	R(J)	P(J)
0	22380.15		23200.65	
1	22381.00	22378.20	23201.45	23198.77
2	22381.75	22377.15	23202.15	23197.65
3	22382.45	22375.94	23202.79	23196.42
4	22383.01	22374.69	23203.33	23195.13
5	22383.56	22373.39	23203.70	23193.74
6	22384.06	22371.99	23204.08	23192.24
7	22384.41	22370.49	23204.39	23190.69
8	22384.71	22368.94	23204.54	23189.03
9	22385.01	22367.29	23204.54	23187.26
10	22385.10	22365.59	23204.45	23185.44
11	22385.15	22363.79	23204.23	23183.41
12	22385.10	22361.94	23203.01	23181.32
13	22385.01	22359.94	23202.15	23178.97
14	22384.71	22357.94	23201.83	23175.76
15	22384.51	22355.79	23201.45	23173.09
16	22384.06	22353.59	23200.65	23170.52
17	22383.56	22351.34	23199.79	23167.91
18	22383.56	22348.94	23198.77	23165.18
19	22382.65	22346.50	23197.65	23162.46
20	22382.00	22344.30	23196.58	23159.57
21	22381.25	22341.46		23156.64
22	22380.42	22338.76		23153.60
23	22379.55	22336.02		23150.40
24	22378.60	22333.13		23147.25
25	22377.45	22330.18		23144.00
26	22376.33	22327.24		23140.59
27	22375.09	22324.10		23137.12
28	22373.89	22321.01		
29	22372.44			
30	22370.99			
31	22369.44			
32	22367.84			
33	22365.94			

Table 5.5 continued. Rotational assignments and vacuum wavenumbers (cm^{-1}) for the $[22.4]0^+ - X^1\Sigma^+$ system of the $Rh^{14}N$ molecule.

	(2,0)		(3,0)	
J	R(J)	P(J)	R(J)	P(J)
0	24000.26		24717.50	
1	24000.95	23998.26	24718.29	24715.68
2	24001.58	23997.28	24718.90	24714.58
3	24002.15	23996.02	24719.33	24713.24
4	24002.56	23994.59	24719.81	24711.91
5	24002.90	23993.10	24720.06	24710.33
6	24002.93	23991.49	24720.18	24708.68
7	24003.02	23989.78	24720.18	24706.92
8	24002.92	23987.94	24720.06	24704.92
9	24002.90	23985.94	24719.69	24702.79
10	24002.56	23983.88	24719.33	24700.85
11	24002.15	23981.65	24718.72	24698.48
12	24001.58	23979.30	24718.11	24695.99
13	24000.95	23976.95	24717.26	24693.50
14	24000.26	23974.44	24716.29	24690.71
15	23999.17	23971.75	24715.19	24687.91
16	23998.43	23969.00	24714.03	24684.94
17	23997.51	23966.03	24712.70	24681.79
18	23996.31	23963.34	24711.18	24678.57
19	23995.22	23960.26	24709.54	24675.24
20	23993.84	23957.12	24707.77	24671.66
21	23992.47	23953.80	24705.89	24668.03
22	23990.75	23950.49	24703.82	24664.27
23	23988.92		24701.88	24660.33
24	23986.68		24699.33	24656.34
25	23985.19		24696.84	24652.34
26	23983.08		24694.11	24647.81
27	23980.73		24691.56	24643.27
28			24688.46	
29			24685.37	

Table 5.6. Rotational assignments and vacuum wavenumbers (in cm^{-1}) for the $[22.4]0^+ - X^1\Sigma^+$ system of the $Rh^{15}N$ molecule.

	(0,0)		(1,0)	
J	R(J)	P(J)	R(J)	P(J)
0	22380.91		23200.65	
1	22381.76	22432.95	23201.45	23198.77
2	22382.51	22433.70	23202.15	23197.65
3	22383.06	22434.25	23202.79	23196.42
4	22383.70	22434.89	23203.33	23195.13
5	22384.20	22435.39	23203.70	23193.74
6	22384.70	22435.89	23204.08	23192.24
7	22384.91	22436.10	23204.39	23190.69
8	22385.17	22436.36	23204.54	23189.03
9	22385.45	22436.64	23204.54	23187.26
10	22385.55	22436.74	23204.45	23185.44
11	22385.65	22436.84	23204.23	23183.41
12	22385.55	22436.74	23203.01	23181.32
13	22385.45	22436.64	23202.15	23178.97
14	22385.30	22436.49	23201.83	23175.76
15	22385.04	22436.23	23201.45	23173.09
16	22384.70	22435.89	23200.65	23170.52
17	22384.29	22435.48	23199.79	23167.91
18	22383.80	22434.99	23198.77	23165.18
19	22383.31	22434.50	23197.65	23162.46
20	22382.66	22433.85	23196.58	23159.57
21	22382.01	22433.20		23156.64
22	22381.16	22432.35		23153.60
23	22380.41	22431.60		23150.40
24	22379.51	22430.70		23147.25
25	22378.52	22429.71		23144.00
26	22377.37	22428.56		23140.59
27	22376.12	22427.31		23137.12

(v) Other Bands of Note

A survey of the data in Table 5.1 shows there are sporadic instances throughout the LIF spectrum of RhN where isolated bands are observed with no obvious relationship to any of the main systems examined. Most of these bands are very weak with a few notable exceptions. The bands with appreciable intensity are located such that they are not obviously related to each other. A brief description of these bands will be given.

(a) Bands at 444.40 and 440.72 nm

Two weak red-degraded bands appear at slightly higher energy (~ 100 and 300 cm^{-1}) than the (0,0) band of the $[22.4]0^+ - X^1\Sigma^+$ system. It was first thought the bands might have been hot bands associated with the $[22.4]0^+ - X^1\Sigma^+$ system. However, no evidence was observed in the DF spectrum to suggest the 444.40 nm band is "hot", i.e., there is a complete absence of any DF feature(s) to the higher energy side of the exciting line. The DF spectrum for the 444.40 nm band is discussed in the next section. The 440.72 nm band is much weaker and no useful information was obtained from the DF spectrum. Also, measured isotope shifts of +36.57 cm^{-1} and +28.60 cm^{-1} were determined for the 444.4 and 440.7 nm bands respectively, possibly suggesting that the upper state vibrational quantum number may be two for the 444.4 nm band and one for the 440.7 nm band.

The excited state lifetimes for the 444.40 nm and 440.72 nm bands were determined to be ~ 300 ns and ~ 185 ns respectively, roughly two to three times longer than for the vibrational levels associated with the other 0^+ states observed in this study.

One can speculate that the bands are observed because of mixing with other states in the vicinity.

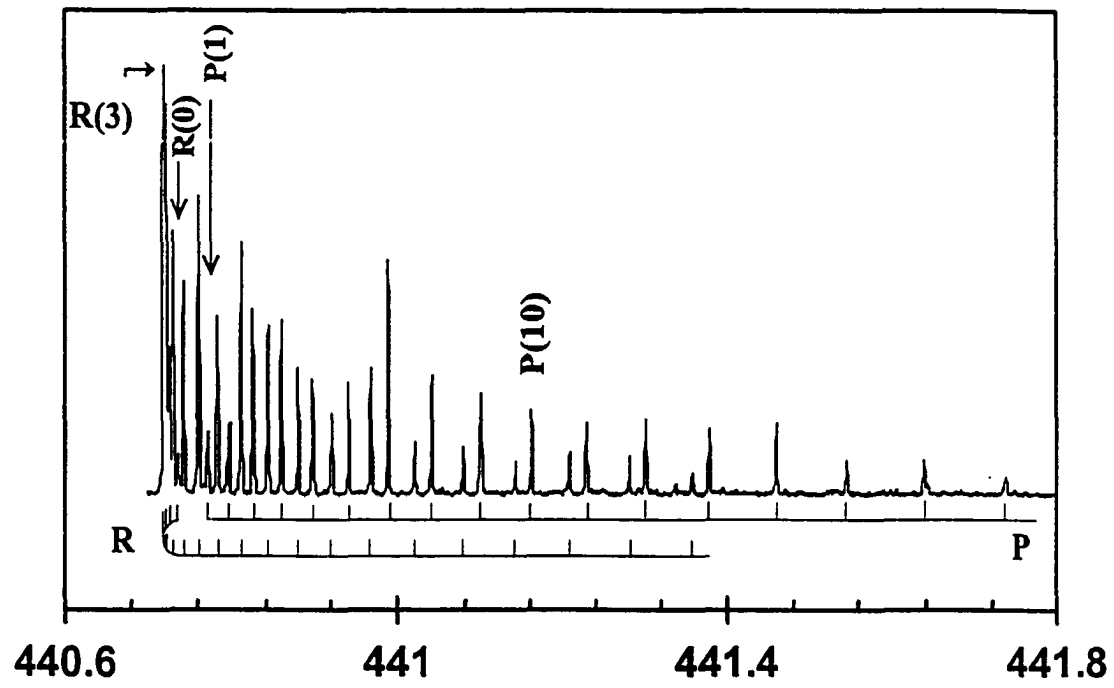

Fig. 5.18. The LIF spectrum for the 440.72 nm band of $Rh^{14}N$. The first lines are marked.

The simple R and P branch structure of these bands is similar to the band structures observed for the $[22.4]0^+ - X^1\Sigma^+$ and $[19.5]0^+ - X^1\Sigma^+$ transitions and the upper states can be assigned as 0^+ states. The LIF spectrum for the 440.72 nm band is shown in Fig. 5.18. The 444.40 nm band looks very similar. Combination differences and the DF spectrum confirm the bands belong to RhN with $^1\Sigma^+$, v = 0 as their lower level.

The 444.40 nm and 440.72 nm bands differ from the bands of the $[22.4]0^+ - X^1\Sigma^+$ and $[19.5]0^+ - X^1\Sigma^+$ systems in that the R branch band heads form very quickly, at R(3), reflecting small upper state B values. The B value for the upper state 444.40 nm band

was determined to be 0.3874(9) cm^{-1} while the 440.72 nm upper state has B′ = 0.3871(9) cm^{-1}. The bond lengths associated with these vibronic levels are, by far, the longest observed for RhN, *i.e.,* the molecule obviously undergoes a significant change in bonding upon excitation to these vibronic levels.

(b) The 429.85 nm band

The discovery of this band was rather by accident. In recording slow scans for the (1,0) band of the $[22.4]0^+ - X^1\Sigma^+$ system, it was noted that when the monochromator was set to certain wavelengths, extra features would appear on the higher energy side. As may be seen from the spectrum in Fig. 5.19, there are two significant bands in the region between 429.5 and 430.95 nm. With the photomultiplier set to record all wavelength fluorescence, the band located at 429.85 nm appeared only very weakly, whereas the band at 430.95 nm was quite intense. The head at 430.95 nm had been assigned previously as the (1,0) band of the $[22.4]0^+ - X^1\Sigma^+$ system {section 5.3(*iv*)}.

The DF spectra obtained following the excitation of each of the two bands are significantly different. They are shown in Fig. 5.20. Excitation within the 430.95 nm band gives strong fluorescence to a state 1740 cm^{-1} above the ground state; the strongest feature in the DF spectrum recorded for the 429.85 nm band appears 3920 cm^{-1} above the ground state. Since the strongest emission features appear at different energies, we could utilize a filtered fluorescence technique (section 3.3(*i*)) to record the LIF spectra by setting the monochromator to collect the fluorescence at the two different displacement wavelengths. The outcome of our efforts is displayed in Fig. 5.19.

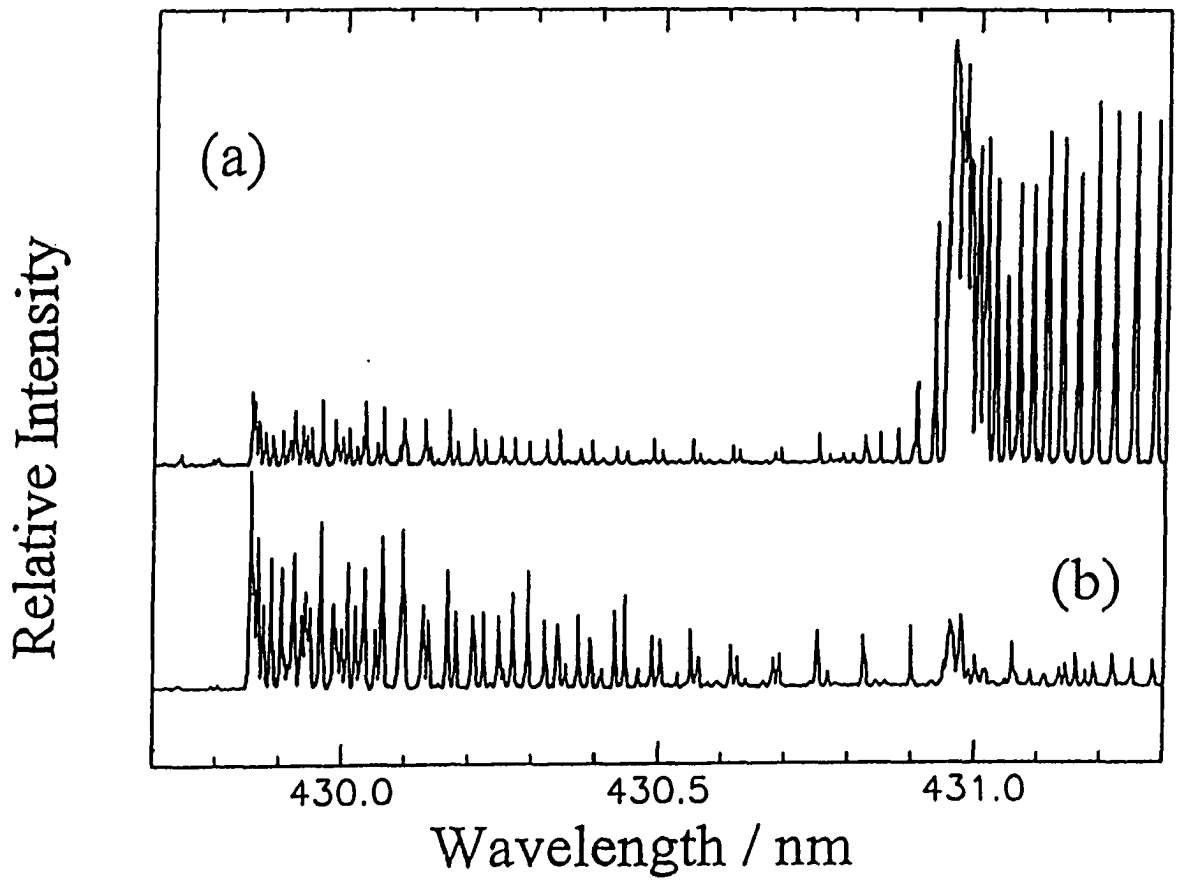

Fig. 5.19. The LIF spectrum of $Rh^{14}N$ recorded between 427.7 nm and 431.3 nm at two different monochromator settings. The fluorescence in the upper spectrum (a) was monitored at a displacement of 1740 cm^{-1} from the excitation frequency. The spectrum is dominated by the $[22.4]0^+ - X^1\Sigma^+$ emission from the (1,0) band. The weaker feature to shorter wavelength is the 429.85 nm band. The lower spectrum (b) was recorded with the monochromator set at a displacement of 3940 cm^{-1} from the excitation frequency. Here, the contribution from the [22.4]-X (1,0) band is all but eliminated.

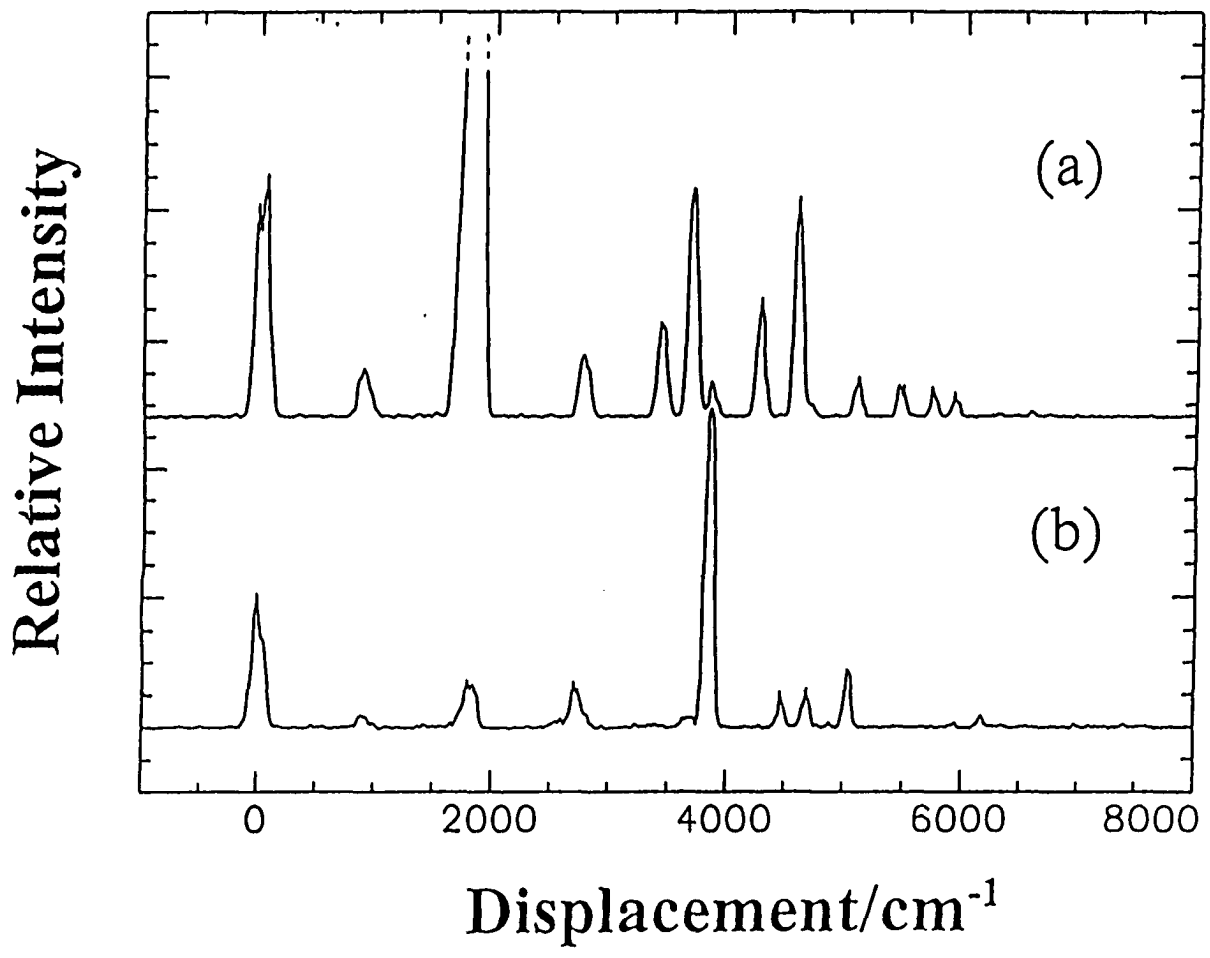

Fig. 5.20. The recorded DF spectra following the excitation in (a) the (1,0) band of the [22.4] 0' - X $^1\Sigma^+$ system observed at 430.82 nm and (b) the 429.85 nm band of $Rh^{14}N$.

It was first thought that the 429.85 nm band was a vibrational counterpart to the band at 444.40 nm since it is situated approximately 800 cm^{-1} to higher energy. The lifetime associated with this excited state vibrational level is approximately 225 ns which is similar to the 300 ns measured for the 444.40 nm band. These lifetimes are clearly longer than those recorded for the [19.5] and [22.4] states. Based on the aforementioned results, one can see why one would think that the two bands were related. The slow scans of the 429.85 nm band tell a different story, however. The 429.85 nm spectrum reveals the presence of a P (strong), Q (weak), and R (strong) branch structure (Fig. 5.19(b)). The three-branch structure suggests a $\Delta\Omega = 1$ transition, contradicting the assumption that it is related to the 444.40 nm band ($\Delta\Omega = 0$) as alluded to earlier. Rotational assignments and line positions for the 429.85 nm band are listed in Table 5.7.

Rotational analysis of the band revealed that the R(23) rotational line is displaced from its expected position. Unfortunately, the perturbation cannot be seen in the P-branch as the intensity of the branch dies out at P(20). First combination differences reveal that a combination defect is present in this band. However, the Λ-doubling is unlike that observed in the [15.1]1 state. The observed splitting is approximately 200 times larger than the values observed for the [15.1]1 state. The Λ-doubling observed in the 429 nm band varies linearly with J rather than with J(J+1) as expected in a $^1\Pi$ state, an interesting result which is currently being examined. The splitting is shown as a function of J in Fig. 5.21.

The Δ_2F'' combination differences indicate that the band's ground state is $X^1\Sigma^+$. The B value for the upper state was determined to be 0.4312(6) cm^{-1} yielding a bond

length of 0.1781(5) nm. This bond is longer than any of the other observed values except that determined for the 440.40 nm band. The upper state involved in the transition must have a fair amount of antibonding character since the change in bond length is quite significant.

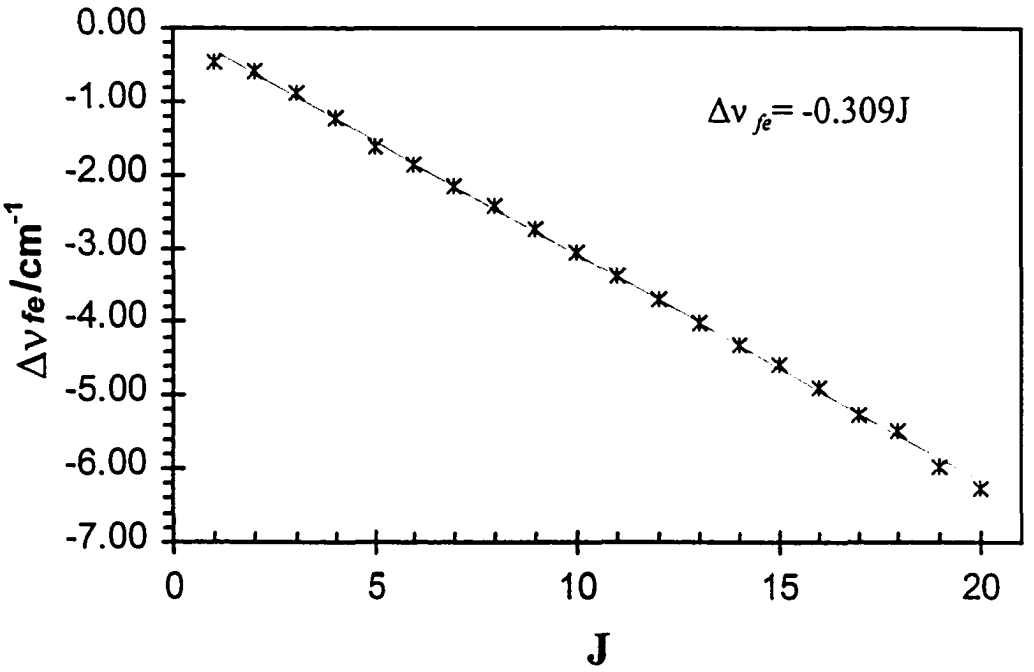

Fig. 5.21. The observed Λ-type doubling in the 429.85 nm band. The (*) represents the observed splittings and the line represents the fit of the data. The uncertainty in the slope is ± 0.002 cm^{-1}.

Table 5.8 lists the molecular constants for the $Rh^{14}N$ and $Rh^{15}N$ molecules respectively.

Table 5.7. Rotational assignments and vacuum wavenumbers (cm^{-1}) for the 444.40, 440.72, and 429.17 nm bands of the $Rh^{14}N$ molecule.

	444.40 nm 0^+ - $X^1\Sigma^+$		440.72 nm 0^+ - $X^1\Sigma^+$		429.17 nm 1 - $X^1\Sigma^+$		
J	R(J)	P(J)	R(J)	P(J)	R(J)	Q(J)	P(J)
0	22495.14	-	22630.27	-	23255.11	-	-
1	22495.70	22493.37	22630.80	22628.48	23255.66	23254.41	-
2	22496.02	22492.11	22631.19	22627.25	23256.30	23254.25	23252.09
3	22496.14	22490.64	22631.19	22625.76	23256.63	23253.87	23250.63
4	22495.95	22488.92	22631.09	22624.12	23256.90	23253.60	23249.06
5	22495.49	22487.00	22630.58	22622.13	23256.90	23253.17	23247.44
6	22494.89	22484.77	22629.96	22619.93	23256.90	23252.52	23245.54
7	22494.03	22482.40	22629.04	22617.47	23256.63	23251.76	23243.65
8	22492.91	22479.77	22627.96	22614.91	23256.30	23250.84	23241.65
9	22491.55	22476.89	22626.53	22611.89	23255.76	23249.71	23239.38
10	22489.93	22473.76	22624.89	22608.82	23255.11	23248.52	23236.95
11	22488.11	22470.38	22623.05	22605.40	23254.25	23247.11	23234.42
12	22485.99	22466.74	22620.95	22601.67	23253.17	23245.54	23231.66
13	22483.66	22462.86	22618.59	22597.84	23252.09	23243.87	23228.85
14	22481.03	22458.77	22615.88	22593.65	23250.73	23242.03	23225.78
15	22478.21	22454.34	22613.02	22589.21	23249.44	23239.98	23222.65
16	22475.12	22449.75	22609.80	22584.56	23247.87	23237.87	23219.25
17	22471.74	22444.82	22606.42	22579.62	23246.14	23235.66	23215.85
18	22468.06	22439.68	22602.69	22574.47	23244.30	23233.17	23212.19
19	22464.17	22434.29	22598.81	22569.06	23242.03	23230.58	23208.47
20	22459.98	22428.66	22594.01		23239.98	23227.83	23204.43
21	22455.50	22422.73				23224.97	23200.30
22	22450.76	22416.55				23221.84	
23	22445.72	22410.12				23218.71	
24	22440.43	22403.34				23215.26	
25	22434.85					23211.70	
26	22429.62					23208.47	

Table 5.8. Molecular constants (cm^{-1}) for $Rh^{14}N$.

$Rh^{14}N$

Level	T_0	B_v	$q_v / 10^3$	r_v/ nm
$X^1\Sigma^+$, v = 0	0	0.5075(3)	-	0.1642
v = 1	891	0.5041(5)	-	0.1648
[15.1] 1, v = 0	15065	0.4673(3)	2.59(3)	0.1711
v = 1		0.4588(6)	0.89(2)	0.1728
v = 2		0.4520(9)	0.59(5)	0.1740
[19.5] 0^+, v = 0	19483	0.4619(9)		0.1721
v = 1		0.4603(8)		0.1724
v = 2		0.4540(4)		0.1736
v = 3		0.4446(20)		0.1754
[22.4] 0^+, v = 0	22379	0.4634(6)		0.1719
v = 1		0.4516(8)		0.1741
v = 2		0.4443(5)		0.1755
v = 3		0.4407(6)		0.1762
Unclassified Bands				
444.40 nm band		0.3874(9)		0.1880
440.72 nm band		0.3871(9)		0.1880
429.17 nm band		0.4312(8)	-309(2)	0.1782
417.82 nm band		0.4030(6)		0.1843
408.33 nm band		0.4389(7)		0.1766
406.19 nm band		0.4064(9)		0.1836
400.85 nm band		0.4326(7)		0.1779

$Rh^{15}N$

Level	T_0	B_v	r_v/ nm
$X^1\Sigma^+$, v = 0	0	0.4754(3)	0.1642
[19.5] 0^+, v = 0	19483	0.4347(9)	0.17216
v = 1		0.4318(8)	0.17274
v = 2		0.4256(4)	0.17399
v = 3		0.4161(20)	0.17597
[22.4] 0^+, v = 0	22379	0.4373(6)	0.17166
v = 1		0.4306(8)	0.17298

5.4. Dispersed Fluorescence Spectra of RhN.

Dispersed fluorescence (DF) spectra were collected at wavelengths corresponding to all of the observed $Rh^{14}N$ bands of appreciable intensity. The excitation was to various vibrational levels (v'= 0, 1, 2, . . .) of the three excited states observed in the LIF spectrum of rhodium nitride. The procedure for the recording of the DF spectra has been described in the experimental section of this work (section 3.3.2). It should be noted that, most often, the spectra were recorded with the probe laser wavelength positioned on the strongest feature of the band in question. This feature was, more often than not, within the R-band head. The DF spectra of $Rh^{14}N$ are shown in Fig. 5.22 - Fig. 5.24. Each group of spectra reveals the presence of two or more low-lying electronic states (or substates) and the vibrational progressions provide valuable information on their vibrational spacings. A summary of the DF data associated with the ground state plus the newly observed low-lying electronic states is provided in Table 5.9 and a stick diagram summarizing the DF observations is shown in Fig. 5.25.

A comparison of the spectra for the three systems (Fig. 5.22 - Fig. 5.24) leads to two general observations. The first, mentioned above, is that more than one progression is present in all the DF spectra. Second, there is an additional progression in the DF spectra recorded from the [15.1]1 state that is not in the DF spectra from the $[19.5]0^+$ and $[22.4]0^+$ excited states. This extra progression involves a level 555 cm^{-1} above the ground state. We recall that emissions to this low-lying state were observed as "hot bands" in the LIF spectra associated with the bands of the [15.1]1 - $X^1\Sigma^+$ system. With the [15.1] excited state having $\Omega = 1$ and the [19.5] and [22.4] excited states having $\Omega =$

0^+, emission to different low-lying states may occur in the two instances. If fluorescence to the [0.55] state is only allowed from $\Omega = 1$ states and not from the 0^+ states this leads to the premise that the [0.55] state has $\Omega = 0^-$ or 2 neither of which are accessible from the [19.5] and [22.4] $\Omega = 0^+$ states due to selection rules on $\Delta\Omega$. We shall discuss which of the two possible Ω values 0^- or 2 is the more probable assignment for the [0.55] state in the next section. There is evidence for additional low-lying electronic states other than the ground state. These states have their electronic origins (T) 1739, 3922, 4956, and 7243 cm^{-1} above the ground state. This abundance of low-lying states observed for RhN is in marked contrast to observations in the DF spectra recorded for RhC (section 4.3).

The column on the far-right hand side of Table 5.9 lists the vibrational spacings of the low-lying electronic (sub)states. Immediately, one can see that the vibrational intervals are irregular. It is not that surprising given the number of low-lying states present and that these states must have $\Omega = 0^+$ or 1 (the [.55] state has $\Omega = 0^-$ or 2). The irregular spacings are more than likely a result of the interactions between the vibrational levels of these low-lying states. We used the information from the vibrational intervals to determine values for the vibrational constants ω_e and $\omega_e x_e$ for the three lowest lying states. From the least squares fit of the three states we find that the ground state has $\omega_e \approx$ 947 ±13 cm^{-1} and $\omega_e x_e \approx 4.0 \pm 1.1$ cm^{-1}, the [0.55] state has $\omega_e \approx 910 \pm 6$ cm^{-1} and $\omega_e x_e \approx 2.0 \pm 0.7$ cm^{-1}, and the [1.74] state has $\omega_e \approx 882 \pm 5$ cm^{-1} and $\omega_e x_e \approx 7.3 \pm 0.5$ cm^{-1}. Although the vibrational constants have large uncertainties associated with their values, the calculated values are reasonable based on comparison with other TM nitrides (section 5.6).

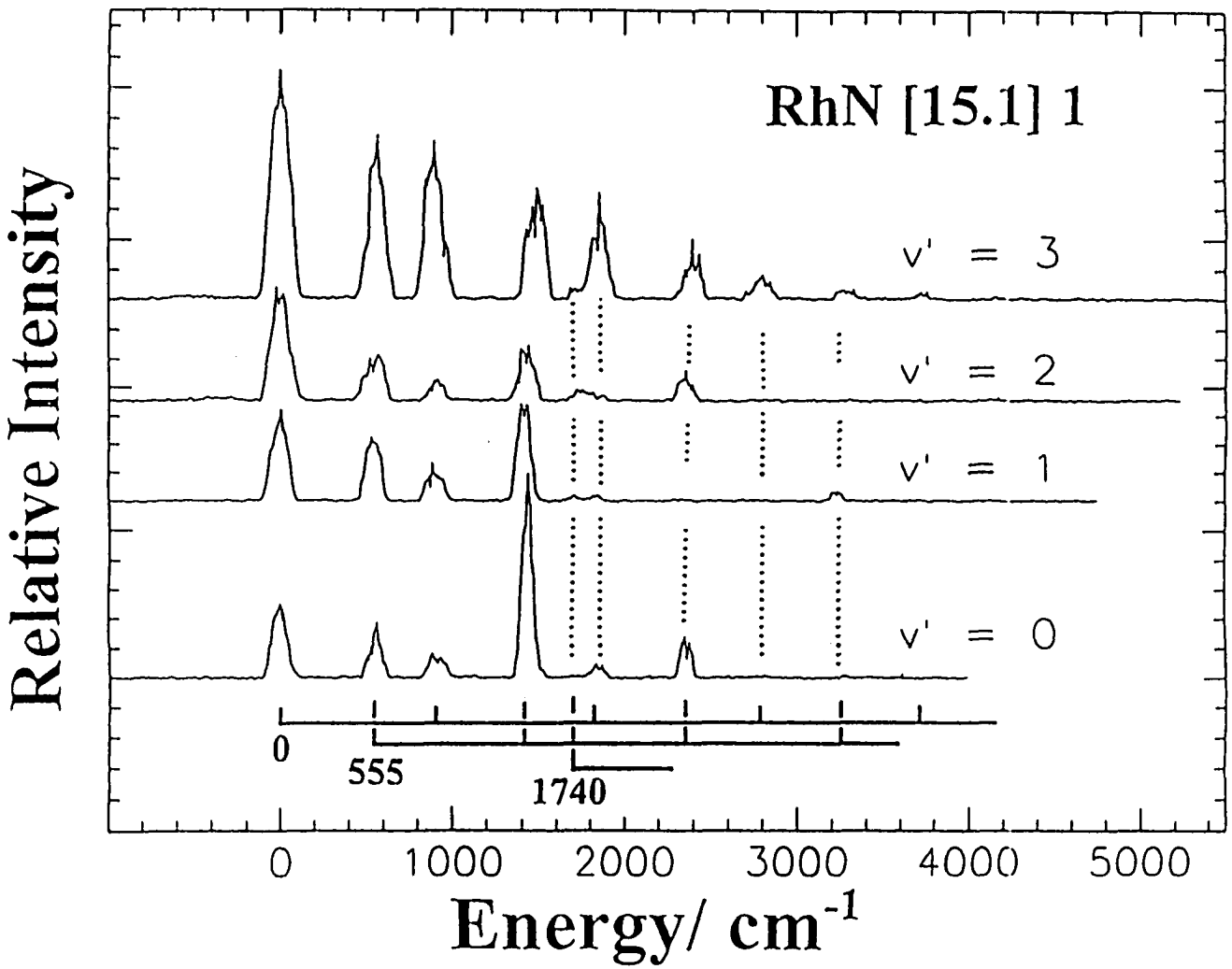

Fig. 5.22. $Rh^{14}N$ dispersed fluorescence spectra following excitation to various vibrational levels of the |15.1|1 state.

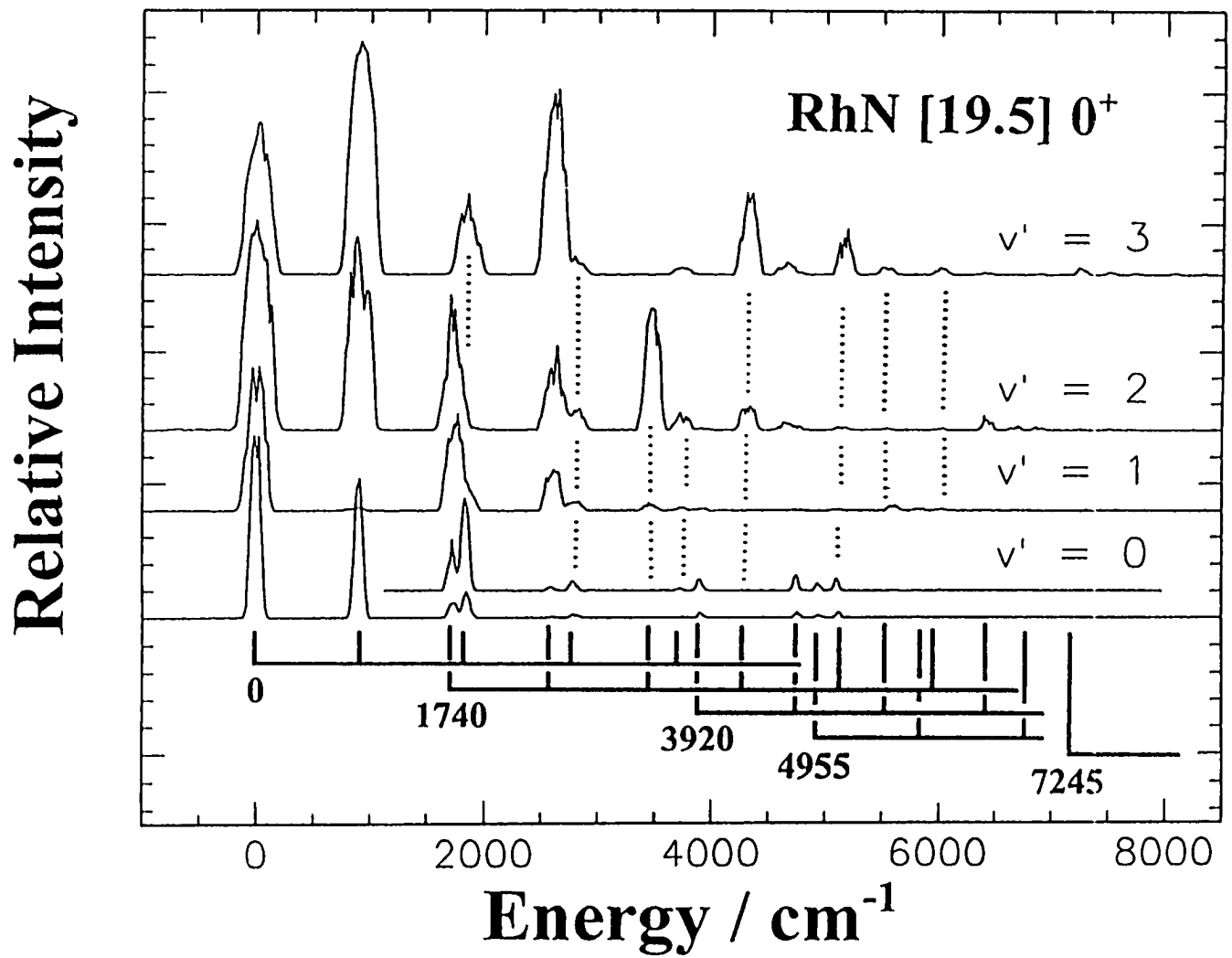

Fig. 5.23. $Rh^{14}N$ dispersed fluorescence spectra following excitation to various vibrational levels of the [19.5]0⁺ state.

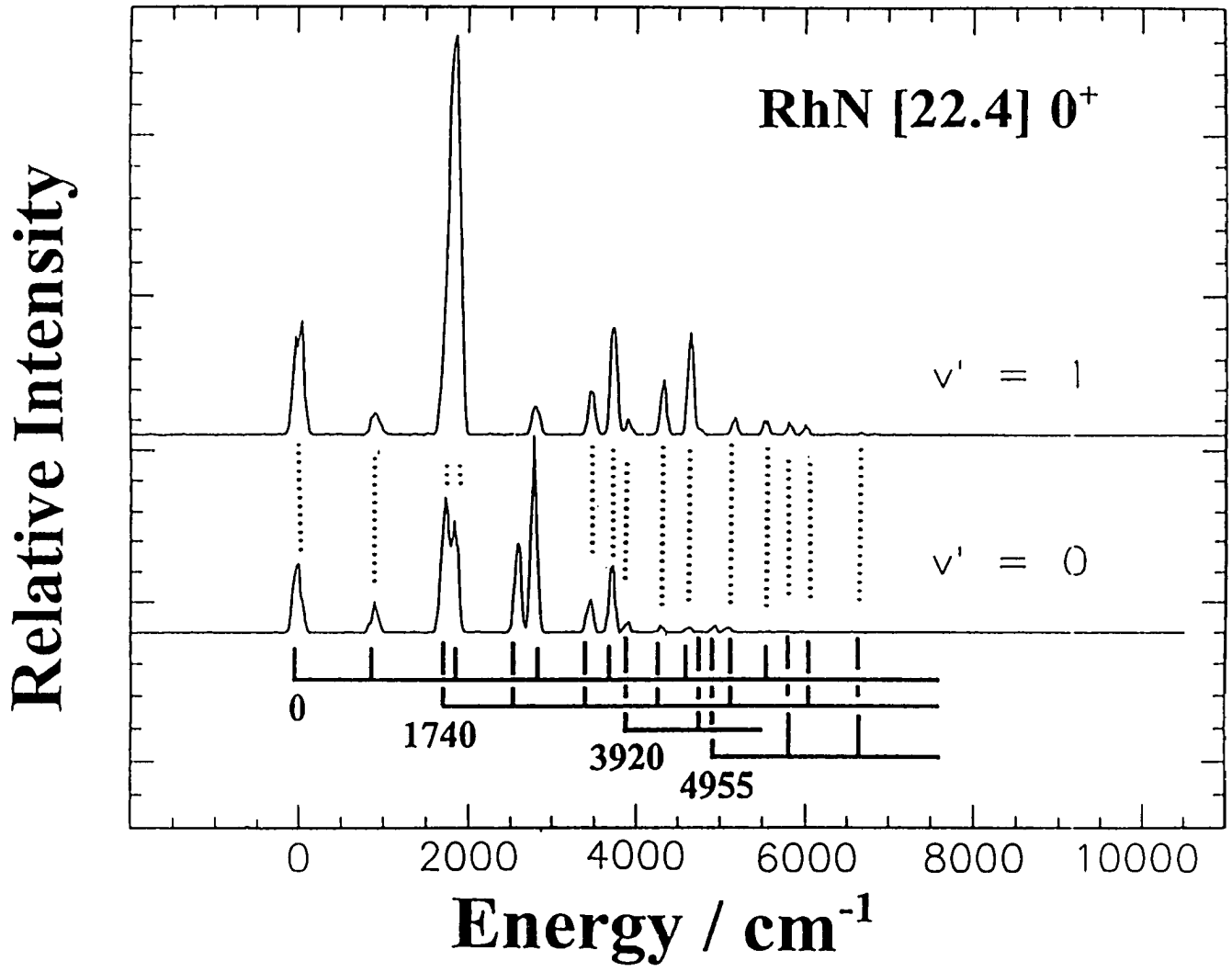

Fig. 5.24. $Rh^{14}N$ dispersed fluorescence spectra following excitation to various vibrational levels of the [22.4]0' state.

Table 5.9. Summary of the observed low-lying levels of $Rh^{14}N$ from dispersed fluorescence spectra.

Emitting State(s)	Lower State	Displacement (± 20 cm^{-1})	Separation cm^{-1}
[15.1] 1, [19.5] 0^+, and [22.4] 0^+	$X^1\Sigma^+$ v = 0	0	
			900
	1	900[a]	
			945
	2	1845	
			955
	3	2800	
			930
	4	3730	
			900
	5	4630	
			905
	6	5535	
			870
	7	6405	
[15.1] 1 only	[0.55] v = 0	555[b]	
			895
	1	1450	
			915
	2	2365	
			905
	3	3270	
			885
	4	4155	
[15.1] 1, [19.5] 0^+, and [22.4] 0^+	[1.74] v = 0	1740	
			865
	1	2605	
			850
	2	3455	
			855
	3	4310	
			815
	4	5125	
			870
	5	5995	
[19.5] 0^+ and [22.4] 0^+	[3.92] v = 0	3920	
			850
	1	4770	
[19.5] 0^+ and [22.4] 0^+	[4.90] v = 0	4955	
			845
	1	5800	
			810
	2	6610	
[19.5] 0^+	[7.20] v = 0 ?	7245	

[a] A value of 897 cm^{-1} is found for the $\Delta G(\frac{1}{2})$ interval in the $^1\Sigma^+$ state from the LIF spectra.

[b] Hot bands at v - 553 cm^{-1} are found in the [15.1] 1 - $X^1\Sigma^+$ LIF Spectra.

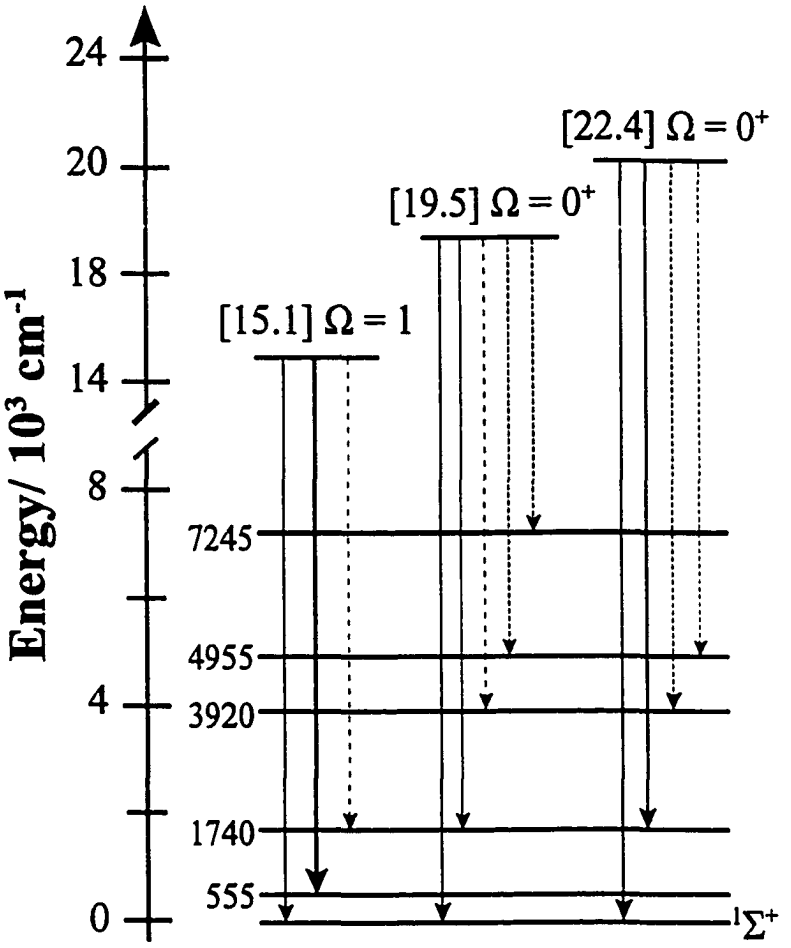

Fig. 5.25. A summary of the DF spectra recorded following excitation to the various vibronic states of $Rh^{14}N$. The thick solid lines (=) indicate strong emissions, the thin solid lines (-) represent medium strength transitions, the large dashed lines (- -) show weak transitions, and the thin dashed lines (--) indicate very weak transitions.

Lai and Wang [139] have recently published photoelectron spectra (PES) for the anions RhC^-, RhN^-, and RhO^-. Their publication also provides information on the low-lying states of the neutral species of these anions. The PE spectra of RhN display the same high density of low energy states as our DF spectra. The absence of such states in

the PE spectra for RhC [139] and RhO [139] also reflects our DF results. Electronic states were observed in the PE spectrum of RhN^- at 560, 970, 1900, 3000, 7800, and 12300 cm^{-1} with errors of ± 100 cm^{-1}. The state whose origin is at 560 cm^{-1} is clearly the state observed at 555 cm^{-1} in our DF spectra recorded from the [15.1]1 state as well as in "hot" bands in the LIF spectrum. Lai and Wang assigned this state as the 0^+ component of the anticipated low-lying $^3\Pi$ state and the states at 970 and 1900 cm^{-1} as the accompanying $^3\Pi_1$ and $^3\Pi_2$ substates (state designations will be discussed in the next section). Our experiments clearly argue against their conclusions. First, the absence of the [0.55] state from all DF spectra whose excited states have $\Omega = 0^+$ contradicts their 0^+ assignment of this electronic substate. Secondly, our DF spectra show no evidence of any feature at 970 cm^{-1}. If there is a substate there with $\Omega = 1$, we should have been able to observe it. We have, however, confidently assigned the feature at 900 cm^{-1} in the DF spectra to the v = 1 level of the ground state. Most of the apparent intensity of the 970 cm^{-1} PES feature comes from overlapping by the stronger 560 cm^{-1} feature so it is possible that the feature at 970 cm^{-1} is the v = 1 vibrational level of the ground state. The PES features at 7800 and 12,300 cm^{-1} were assigned by Lai and Wang as features emanating from a low-lying excited state of RhN^- (3900 cm^{-1}). However, if we assume the features originate from the ground state, the 7800 cm^{-1} feature then lies within a few wavenumbers of the 3900 cm^{-1} feature we observe in our DF spectrum and the 12,300 cm^{-1} feature should lie in the vicinity of 8400 cm^{-1}. We have not detected a level at 8400 cm^{-1} but we have detected a level at 7245 cm^{-1}.

5.5. Molecular Orbitals and the Nature of the Electronic States of RhN

The focus of this section is to attempt to assign the electronic states observed in the LIF and DF spectra of $Rh^{14}N$. The RhN molecular orbital diagram, in conjunction with electronic selection rules, comparison to isovalent molecules such as IrN [72, 126 - 128], PdC [56], and PtC [77] as well as the recent *ab initio* calculations of Shim *et al.* [4] were some points considered in determining the electronic nature of these RhN vibronic states. The above publication describes the calculations involved in the computation of symmetries, bond lengths, and vibrational energies for seven low-lying states (to 14,000 cm^{-1}) of RhN.

The molecular orbital (MO) diagram for the isovalent IrN [128] and PdC [56] radicals can serve as a guide to understanding the bonding in RhN. The trends across the 3*d*, 4*d*, and 5*d* transition series of TM nitrides are discussed in chapter 7. The MO diagram describing the metal mononitrides and metal monocarbides may be constructed using principles similar to those put forth by Merer [84] to characterize the 3*d* metal monoxides and are discussed in chapter 4. The result is shown in Fig. 5.26. For nitrogen the 2*s* and 2*p* atomic orbitals are closer to the valence AOs of the metal in energy than is the situation for oxygen but they are still well separated and the nitrogen 2*s* AO is essentially nonbonding and is not shown in the MO diagram. If shown, the 2*s* orbital of nitrogen would account for the 10σ orbital of RhN.

As in the rhodium monocarbide scenario, the 2*p* orbitals of nitrogen mix with the 4*d* orbitals of rhodium. The 11σ orbital would be the bonding combination of the rhodium 4*d*σ orbital and the 2*p*σ orbital of nitrogen. The 13σ orbital is the antibonding

counterpart to the 11σ orbital. Both the 2δ and 12σ molecular orbitals are essentially nonbonding and arise from the rhodium 4*d*δ and 5*s*σ orbitals respectively. Electrons in these orbitals are essentially metal-centered. The 5π and 6π orbitals are the bonding and antibonding combinations of the nitrogen 2*p*π and rhodium 4*d*π orbitals. The ordering of the MOs is shown in Fig. 5.26. Although the MO diagram is qualitatively correct, one must recognize that describing the electronic states solely by one electron configuration may not be entirely correct.

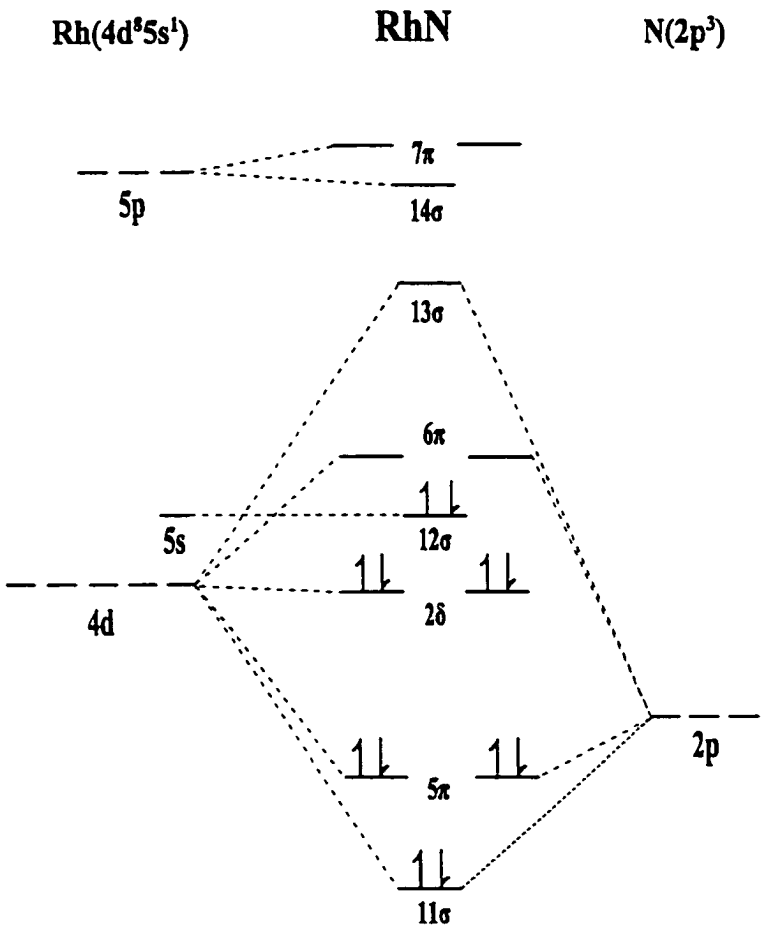

Fig. 5.26. The qualitative molecular orbital scheme for the RhN molecule. The 14σ and 7π MOs are essentially nonbonding. The 2*s* orbital of nitrogen is not shown as it is much lower in energy than the 2*p* orbital and is essentially the nonbonding 10σ molecular orbital. The ground state electron configuration is shown in the diagram and the excited states are described in Table 5.11.

Using the Aufbau (build-up) principle to place the valence electrons into the molecular orbitals, a ground state electron configuration of $...11\sigma^2 5\pi^2 2\delta^4 12\sigma^2$ arises for RhN. The resulting closed shell configuration (two electrons in the 12σ molecular orbital) produces just one possible symmetry for the ground state: $^1\Sigma^+$. A $^1\Sigma^+$ ground state is not surprising since the ground state of RhC [1, 69] is known to have a $...11\sigma^2 5\pi^2 2\delta^4 12\sigma^1$ electron configuration resulting in a $^2\Sigma^+$ ground state. The addition of an electron (nitrogen has one more electron than carbon) fills the 12σ orbital and a $^1\Sigma^+$ symmetry results.

With the symmetry of the ground state established, one must next consider the origin of the excited states observed in the LIF spectra and the nature of the low-lying states recorded in the DF spectra. According to Shim *et al.*, there are seven electronic states predicted for the RhN species below 14,000 cm^{-1}. The calculations do not provide any insight into the nature of the excited states that we have observed in the LIF spectrum between 14,000 and 24,000 cm^{-1}. Nonetheless, the calculations were quite useful in understanding the nature of the low-lying states. Some predicted electronic states cannot be observed by us experimentally because the transitions involved violate the electronic selection rules in some manner. Transitions to electronic states expected in the region 14,000 - 8,000 cm^{-1}, even when permissible, are not observable using the LIF or DF setup because of experimental limitations. A survey of this "dark zone" would unquestionably add to the characterization of the molecular states of RhN and essentially map out almost all the electronic states expected between 0 and 25,000 cm^{-1}.

If the ordering of the molecular orbitals in the MO diagram (Fig. 5.26) is

qualitatively correct, the reader can envision that the lowest lying electronic state(s) arise(s) when one of the electrons occupying the 12σ orbital is excited into one of the 6π orbitals ($\sigma \rightarrow \pi$). The resulting electron configuration would then be $...11\sigma^2 5\pi^4 2\delta^4 12\sigma^1 6\pi^1$. Two molecular electronic terms (states) are possible with a $\sigma\pi$ electron configuration: $^3\Pi_r$ and $^1\Pi$. The same electronic promotion ($12\sigma \rightarrow 6\pi$) in RhC leads to the $A^2\Pi$ state found near 10,000 cm^{-1} [57]. The energy of the 6π MO is expected to be lower in RhN compared to RhC since nitrogen has a higher electronegativity than carbon. The interaction between the carbon $2p\pi$ orbital and rhodium $4d\pi$ orbital is greater than that of the nitrogen $2p\pi$ orbital and rhodium $4d\pi$ orbital. The resulting separation between the bonding and antibonding π MOs is greater in RhC than in RhN. As a result the $12\sigma \rightarrow 6\pi$ promotion is of higher energy in RhC than in RhN. The $^3\Pi_r$ state, according to the predictions of Shim *et al.*, is the lowest energy state above the ground state. One must also consider a $...11\sigma^2 5\pi^4 2\delta^4 12\sigma^0 6\pi^2$ electron configuration as a plausible representation for low-lying electronic states of RhN. The possible molecular electronic terms from the doubly occupied 6π orbital are $^1\Sigma^+$, $^3\Sigma^-$ and $^1\Delta$. The $...11\sigma^2 5\pi^4 2\delta^4 12\sigma^0 6\pi^2$ configuration differs from the ground state by two electrons and is expected to lie at higher energies than the $^{1,3}\Pi$ states arising from the $11\sigma^2 5\pi^4 2\delta^4 12\sigma^1 6\pi^1$ confguration.

The exact ordering of the various Ω substates from the aforementioned configurations is dependent upon the spin-orbit interactions in the low-lying electronic states of RhN. The typical spin-orbit splitting pattern for the low-lying $^3\Pi_r$ places the substates at intervals of +A, 0, and -A for the $\Omega = 2$, 1, and 0 substates respectively in comparison to a $^3\Pi_r$ state that does not experience any spin-orbit coupling.

The spin-orbit constant A of a $^3\Pi$ state ($\sigma^1\pi^1$ configuration) is related to the one-electron parameter a_π [3] by

$$A = \tfrac{1}{2}\, a_\pi \qquad (5.8).$$

The value of a_π of RhN can be estimated from the experimental data available for $A^2\Pi$ state (π^1 configuration) of RhC [57] (A = +775.82 cm^{-1}). If we take the atomic spin-orbit value (ζ) of the rhodium atom as 1253 cm^{-1} [3], a rough estimate of a_π for RhN can be made. If then, for RhC $\zeta(4d)$ = 1253 cm^{-1} and a_π (RhC) = 775.82 cm^{-1}, then a_π = (775.82/1253)ζ = 61.9 % ζ. For comparison, in PdC (a_π = 661 cm^{-1}, $\zeta(4d)$ = 1495 cm^{-1}) and a_π is ~44% ζ [56]. The value of a_π is expected to be somewhat higher in RhN than RhC since nitrogen has a higher valence orbital ionization energy than carbon. There is less mixing of the $2p_\pi$ orbital with the metal $4d_\pi$ orbital. As a result, the S-O coupling in RhN should have more of the atomic character of rhodium than the S-O coupling in RhC. For RhN, it is reasonable to expect that 775.82 $cm^{-1} \le a_\pi \le$ 1253 cm^{-1}.

The precise ordering shown in Fig. 5.26 will depend upon the strength of the spin-orbit coupling. One would expect some degree of mixing between states with the same value of Ω (*e.g.* Ω = 1 components of the $^3\Pi$ and $^1\Pi$ states and interaction between the Ω = 2 states of the $^1\Delta$ and $^3\Pi$ states). With the mixing of the various substates and the proximity of the $^3\Pi_0$ substate to the $^1\Sigma^+$ ground state, it is reasonable to assume that there are, low-lying, one substate for each of $\Omega = 0^+$ and 0^-, and two for each Ω = 1, and one for Ω = 2. Given the number of low-lying states below 10,000 cm^{-1} a complex arrangement of the molecular substates is expected.

The ordering of the substates, based on the Shim's calculation [4], is predicted to

be

$$^3\Pi_0^+ \approx {}^3\Pi_0^- \approx {}^3\Pi_2 < {}^3\Pi_1 \approx {}^1\Pi_1 < {}^3\Sigma_1^- < {}^1\Delta_2 \quad .$$

Some doubt about the accuracy of this ordering exists. The first problem is that the $^3\Pi_2$ substate is predicted to be lower in energy than the $^3\Pi_1$ substate and about the same energy as the $^3\Pi_0$ substates. The $^3\Pi_2$ substate is calculated to be the only contributor to that molecular term (100% $^3\Pi_2$ character) so there should very small second order interaction with any other electronic state to displace the $^3\Pi_2$ state to even lower energy than the $^3\Pi_1$ state. The $^1\Delta_2$ state is calculated to be too far away from the $^3\Pi_2$ state to induce any shift in either of the states' positions. The interaction of the $^3\Pi_1$ substate with the $^1\Pi_1$ state that arises from the same electron configuration should push the $^3\Pi_1$ state to a lower energy than if it were "unperturbed". These points cast doubt on the validity of the calculated ordering of the RhN substates. The characterization of the DF spectra in the following paragraphs will hopefully clarify the confusion with the energy ordering of the substates.

A second observation about the predicted ordering of the substates involves the near degeneracy of the $^3\Pi_0^-$ and $^3\Pi_0^+$ substates. If one considers the interaction between the $^3\Pi_0^+$ substate with the ground state (0^+) as the predominant interaction in the $^3\Pi$ regime, the $^3\Pi_0^+$ substate should be displaced to higher energy than the $^3\Pi_0^-$ substate. Symmetry restrictions prohibit any interaction between the $^3\Pi_0^-$ substate and the $^1\Sigma_0^+$ ground state. With no close opportunity for interaction, the $^3\Pi_0^-$ substate should not undergo any displacement, making it the lowest energy state next to the ground state.

We have drawn these arguments to Ms. Shim's attention. A revised calculation

[119] by her has corrected the ordering of the low-lying states such that the ordering (transition energy) is now predicted to be $^3\Pi_0^-$(1826 cm^{-1}) < $^3\Pi_0^+$(1956 cm^{-1}) ≈ $^3\Pi_1$(1958 cm^{-1}) < $^3\Pi_2$(2113 cm^{-1}) < $^1\Pi_1$(4431 cm^{-1}). The revised ordering correlates with what is anticipated. The same ordering is also observed in the isoelectronic molecule, PdC [56].

The key to assigning the features in the DF spectra and the ordering of the substates is the progression anchored 555 cm^{-1} above the ground state. It is seen only in emission from the $\Omega = 1$ state and not from the 0^+ states. In light of the revised calculations, the progression anchored at 555 cm^{-1} is tentatively assigned as the 0^- component of the triplet pi state ($^3\Pi_0^-$).

The next higher levels, at 1740 cm^{-1} and 3920 cm^{-1} above the ground state, appear in all the DF spectra. The assignment of these lower energy levels is more complicated. Based on the expected spin-orbit splitting pattern of RhN, the lower of the two levels would be assigned to the $^3\Pi_0^+$ substate and the level at 3920 cm^{-1} to the $^3\Pi_1$ substate. However, this assignment is at odds with calculated transition energies and result in a spin-orbit coupling much larger than expected. With the closeness of the calculated and observed molecular constants (see Table 5.10 and 5.11) and with the many interactions occurring in this region, it is possible that the $\Omega = 0^+$ and 1 substates have very similar energies (≈ 1740 cm^{-1}) where with the resolution of our DF experiments, the two substates may not be distinguishable.

The level at 3920 cm^{-1} is reasonably situated that it is tentatively assigned to the $^1\Pi$ state arising from the same configuration as the $^3\Pi$ state. This would make the singlet-triplet splitting for the Π states arising from the same configuration approximately 2500

cm^{-1}. This splitting is quite reasonable given that the quartet-doublet splitting for the low-lying P atomic states in rhodium that result from the $4d^8 5s^1$ electron configuration is 2800 cm^{-1} [143]. Comparison of the metal and the molecule suggests that the $12\sigma \rightarrow 6\pi$ transition in RhN involves an electron in a metal-based orbital.

We did not assign the level at 3920 cm^{-1} to the $\Omega = 2$ spin component of the $^3\Pi$ state (the $^3\Pi_2$ state) since it was observed in the DF spectra from the 0^+ states. The [15.1]1 state is the only excited state that we have observed that can fluoresce to the $^3\Pi_2$ substate. One possible explanation for not observing the $^3\Pi_2$ substate is that the [15.1]1 - $^3\Pi_2$ transition might just be too weak.

Table 5.11. Summary of all the calculated[a] and observed[b] low-lying states of RhN and their electron configurations.

Electronic State Assignment	Calculated Transition Energy/cm^{-1}	Observed Energy/cm^{-1}	Valence Shell Configuration					
			11σ	12σ	13σ	5π	6π	2δ
$^1\Sigma^+$	0	0	2	2	0	4	0	4
$^3\Pi_0^-$	1826	555	2	1	0	4	1	4
$^3\Pi_0^+$	1956	1740	2	1	0	4	1	4
$^3\Pi_1$	1958	1740	2	1	0	4	1	4
$^3\Pi_2$	2113	-	2	1	0	4	1	4
$^1\Pi$	4431	3922	2	1	0	4	1	4

[a]See reference [4, 119].
[b]Data collected from DF spectra.

The natures of the two levels at 4955 and 7245 cm^{-1} are still unexplained at this time. Given that the levels are observed in the DF spectra recorded from the 0^+ states, the

levels must have $\Omega = 0^+$ or 1. One possible configuration that could account for both (sub)states is $11\sigma^2 5\pi^4 2\delta^3 12\sigma^2 6\pi^1$ which leads to $^{1,3}\Pi$ states. The term splitting is comparable to what was observed for the low-lying $^{1,3}\Pi$ states. However, this assignment is speculative at best.

The symmetries of the excited electronic states (> 13,000 cm^{-1}) were easily assigned from the simplicity of the LIF spectra. One must now identify the dominant electron configurations that lead to these molecular terms. It is already known that the excited states of the systems in question have very similar rotational constants to those of the ground. The small change in the RhN bond length signifies only modest antibonding character of the metal-centered orbitals to the antibonding orbitals on the metal. This is not surprising given that the bonding orbitals are mainly nitrogen-centered.

The first electronic state observed in the LIF spectrum of RhN situated at T = 15071 cm^{-1}, has $\Omega = 1$. Two possible electron configurations lead to a state with $\Omega = 1$. The first possibility results from the promotion of an electron residing in the 12σ orbital (HOMO) to the 13σ orbital (LUMO). The resulting $\sigma^1\sigma^1$ configuration can produce a $^1\Sigma^+$ or $^3\Sigma^+$ state with the $^3\Sigma^+$ state lower in energy. The $^1\Sigma^+$ state does not have an $\Omega = 1$ component but the $^3\Sigma^+$ state does. The second candidate is a $2\delta \rightarrow 6\pi$ transition. The $\delta\pi$ configuration leads to $^1\Pi$, $^1\Phi$, $^3\Pi$, and $^3\Phi$ states. The $^1\Phi$ and $^3\Phi$ states will not be observed. They are not accessible from the $^1\Sigma^+$ ground state. Physical evidence provided by the rotational analyses of the RhN spectra also plays a role in deciding the nature of the electron transition. A $2\delta \rightarrow 6\pi$ transition will have strong P, Q, and R branches. As mentioned earlier, the [15.1]1 - X system is weak. In this regard, our observations are

remarkably similar to what is seen in the [17.9]1 - X system of the isoelectronic PdC molecule [56]. The Morse group have confidently assigned the upper state of this system as $^3\Sigma_1^+$ based on the measured hyperfine splitting associated with the unpaired electron in the 12σ orbital. Normally, a transition to a $^3\Sigma_1^+$ state from $^1\Sigma^+$ is spin-forbidden but if the $^1\Sigma^+$ ground state is mixed through spin-orbit interaction (DF results confirm this to be true) with the low-lying $^3\Pi_0^+$ substate, then the transition would be weakly allowed.

With the large term splittings observed for the rhodium atom, it is conceivable that the $^1\Sigma^+$ state arising from the same configuration as the $^3\Sigma^+$ state is most likely the parentage of the electronic state originating at 19489 cm^{-1}.

Rotational analyses confirmed that the [22.4] electronic state has 0^+ symmetry. The parentage of the upper state is uncertain. A 0^+ state arises from the promotion of a 5π electron to the 6π orbital. The consequent $\pi^3\pi$ configuration generates singlet and triplet Σ and Δ states. A second possible configuration that would explain the nature of the [22.4] excited state results from a 12σ → 14σ electron transition. The σσ configuration produces $^1\Sigma^+$ and $^3\Sigma^+$ states as was the case for the [19.5]0^+ - $X^1\Sigma^+$ transition. Both electron excitations are probable and both configurations would lead to a lengthening of the Rh-N bond. The latter electron promotion is the more likely candidate for the parentage of the [22.4]0^+ electronic state. The 14σ orbital is relatively nonbonding since the rhodium 5*p*σ and 5*p*π orbitals are much higher in energy than the nitrogen 2p orbitals so the electron involved in the transition is essentially being promoted from a nonbonding orbital to another nonbonding orbital. In this case the 5π → 6π excitation is expected to weaken the bond more than the 12σ → 14σ transition because the 5π orbital is bonding

while the 6π is slightly antibonding. The fact that the bond length for the [22.4] state is comparable to those determined for the [15.1] and [19.5] states (ΔB is small) lends support to the idea that the [22.4]0^+ - $X^1\Sigma^+$ transition also involves the promotion of an electron from a nonbonding orbital to another nonbonding orbital. However, without detailed calculations, the nature of these 0^+ states remains tentative.

5.6. Concluding Remarks

The electronic spectrum of RhN was studied via laser-induced fluorescence and dispersed fluorescence spectroscopy. It is believed that this is the first observation of rhodium mononitride in the visible region. The vibronic bands have been assigned to three electronic transitions based on measured isotope shifts, excited state lifetimes, and rotational analyses. The lowest energy system involves a transition from the 0^+ ground state to an excited state with $\Omega = 1$. The two other systems involve no change in Ω. Our $^1\Sigma^+$ ($11\sigma^2 5\pi^4 2\delta^4 12\sigma^2$) assignment as the ground state is consistent with *ab initio* calculations and simple molecular orbital arguments. Rotational analyses of the bands of each system have provided molecular constants for the v = 0 to 3 vibrational levels in each of the three excited states and the v = 0 and 1 vibrational levels of the ground state. Several other "rogue" vibronic bands appear in the visible region but have yet to be vibronically classified. The ground state combination differences and dispersed fluorescence spectra confirm that these bands belong to RhN. The ground state equilibrium bond length was determined to be 0.1642(5) nm. This value is comparable to other TM mononitrides with triple bond character.

Dispersed fluorescence spectra were recorded following individual excitation to various levels in the three excited states identified in the LIF spectra. Each group of spectra revealed the presence of several low-lying electronic substates in the region just above the ground state (0 - 5000 cm^{-1}). All of the observed low-lying states but one have $\Omega = 0^+$ or 1, the exception being a low-lying 0^- substate that is only observed in emission from the $\Omega = 1$ excited state. A low-lying $^3\Pi_r$ electronic state that arises from a $...11\sigma^2 5\pi^4 2\delta^4 12\sigma^1 6\pi^1$ configuration is the likely parent of three of the low-lying substates observed in the DF spectra. The same configuration also accounts for a $^1\Pi$ electronic state that is also observed in the DF spectra. Our results sparked a reevaluation of the *ab initio* calculations [4] for RhN as our experimental data contradicted the calculated results.

It is hoped that this work will encourage further study in experimental areas such as the investigation of the infra red region of the spectrum to provide more detailed analyses of the electronic substates observed in our DF spectra. Our analyses of the excited states in the visible region should encourage additional theoretical studies of the excited electronic states.

Chapter 6

The Electronic Spectrum of Rhodium Monoxide

6.1. Introduction

As with their monocarbide and mononitride counterparts, interest in the transition metal oxides stems from their importance in catalysis, astrophysics, and bonding just to name a few examples. Perusal of Herzberg & Huber's tables shows that the 3*d* transition metal oxides have been studied extensively [144]. In fact, enough experimental work has been published on the 3*d* diatomic transition metal oxides that Merer [84] has reviewed their experimental properties. The 4*d* and 5*d* transition metal monoxides have not yet been afforded the same attention as their 3*d* relatives. One point of Merer's review was to emphasize that diatomic transition metal oxides exhibit very complicated spectra, even more so than their respective monocarbide and mononitrides.

Our investigation of rhodium monoxide (RhO) preceded our investigations of RhC and RhN. The high resolution spectrum of rhodium monoxide was photographed in Stockholm about the same time as the spectrum of RhC (late 1960's). As was the case for RhC, the spectrum was photographed "hot" due to the production of the RhO molecules in a King furnace. The high-temperature spectrum proved too complicated to assign due to the congestion and density of the spectrum. Many years passed before copies of the RhO emission spectra were passed on to our lab from the Scullman lab in the hope that a "fresh look" at the spectrum could lead to progress with the analysis. With the capability to produce molecules by jet-expansion, we could record a cold RhO spectrum. A cold spectrum, in conjunction with the high-resolution spectrum, may provide the information needed to achieve an analysis.

The LIF spectrum of RhO was produced in the same manner as the spectra of

RhC and RhN. Details of the experiments are provided in Chapter 3. The LIF spectrum of RhO was recorded between 700 and 380 nm. There are two distinct regions into which the spectrum can be divided: $\lambda < 550$ nm (~ 18,000 cm^{-1}) and $\lambda > 550$ nm. The energy region above 18,000 cm^{-1} is very dense with at least 25 bands observed, many of which were overlapped. Fourteen red-degraded bands were detected in the region between 640 nm (15600 cm^{-1}) and 550 nm (18200 cm^{-1}). $^{16}O/^{18}O$ isotope shifts confirm that the carrier of the spectrum is RhO. The $Rh^{16}O$ bands are listed in Table 6.1 and the individual bands are shown in Fig. 6.1.

Table 6.1. Positions* (nm) of the Observed RhO Features between 700 and 550 nm.

Wavelength (nm) $\lambda_{air} \pm 0.05$	Frequency (cm^{-1}) ν_{vac}	Isotope Shift (cm^{-1}) $\Delta\nu$ ($^{16}O-^{18}O$)
638.20	15665	- 3
629.84	15876	+ 6
625.82	15978	+ 29
618.40	16170	+ 3
608.80	16422	+ 30
598.05	16716	+ 38
594.41	16819	+ 42
588.67	16982	+ 43
584.16	17116	+ 59
573.77	17423	+ 55
569.31	17562	+ 73
562.22	17783	+ 79
553.52	18061	+ 89

*** The values reported are for the strongest feature in each band which, in all cases, is near the band center.**

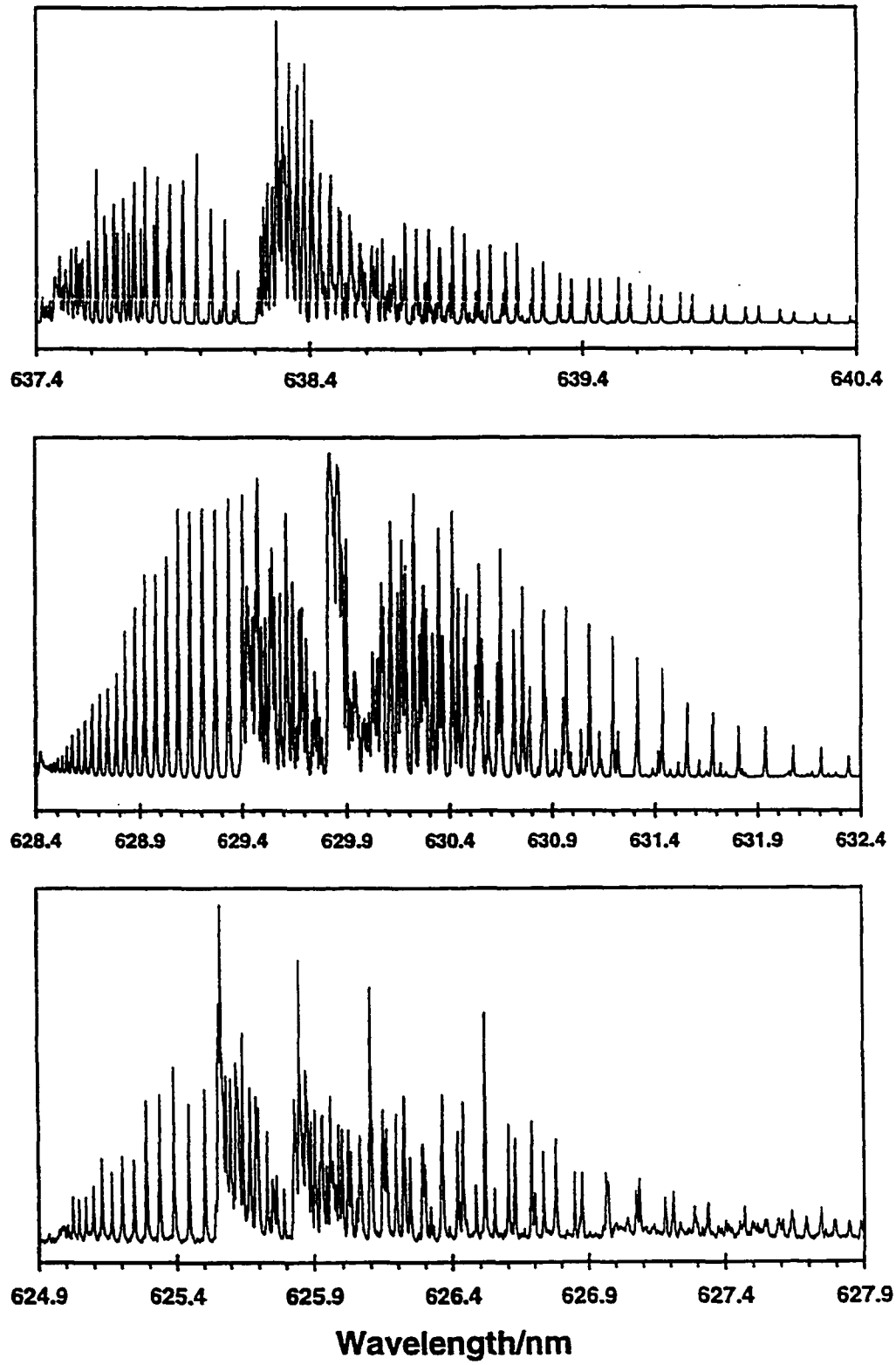

Fig. 6.1. The LIF spectra recorded for $Rh^{16}O$ in the 700 - 550 nm.

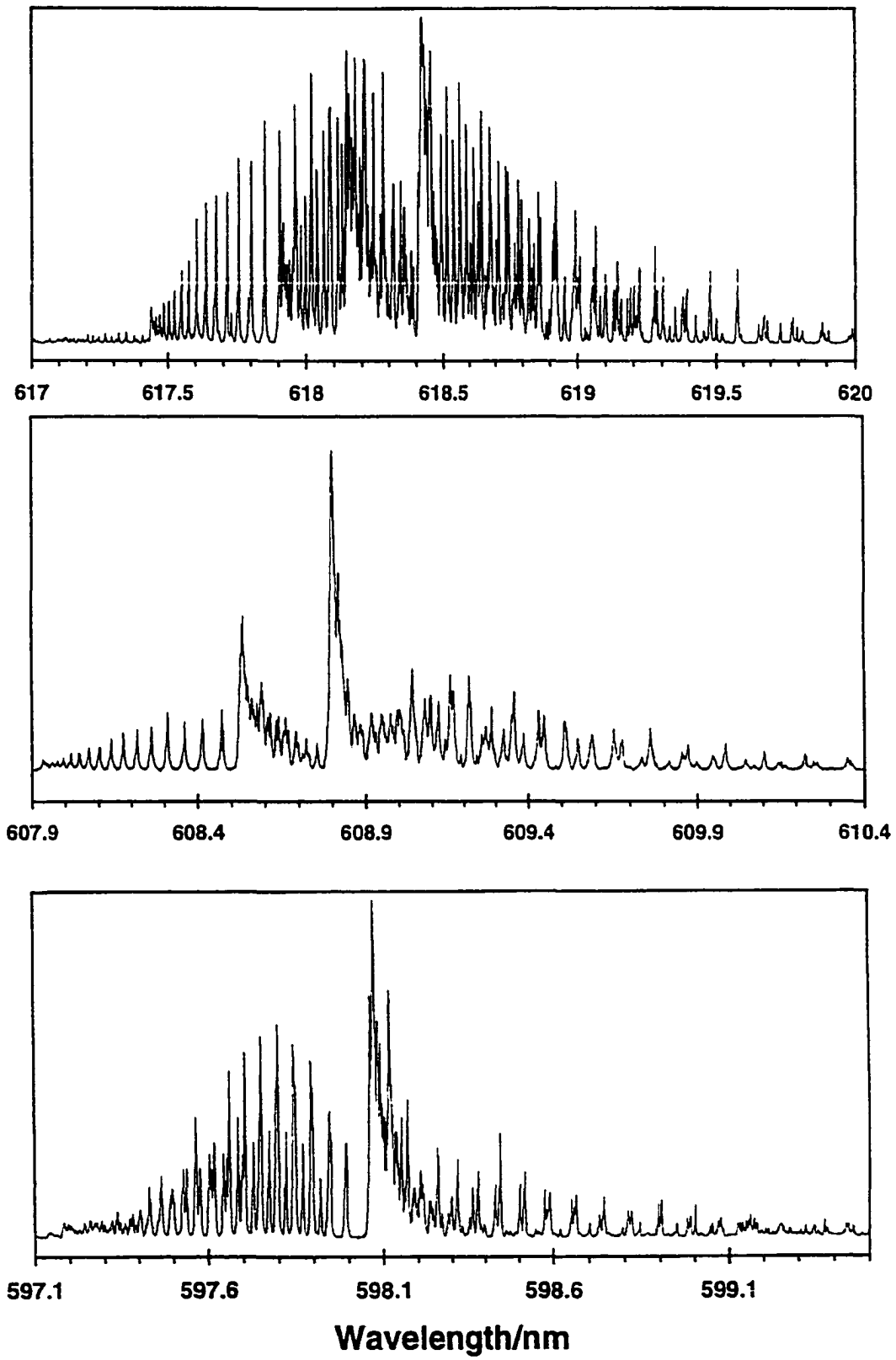

Fig. 6.1 continued. The LIF spectra recorded for $Rh^{16}O$ in the 700 - 550 nm.

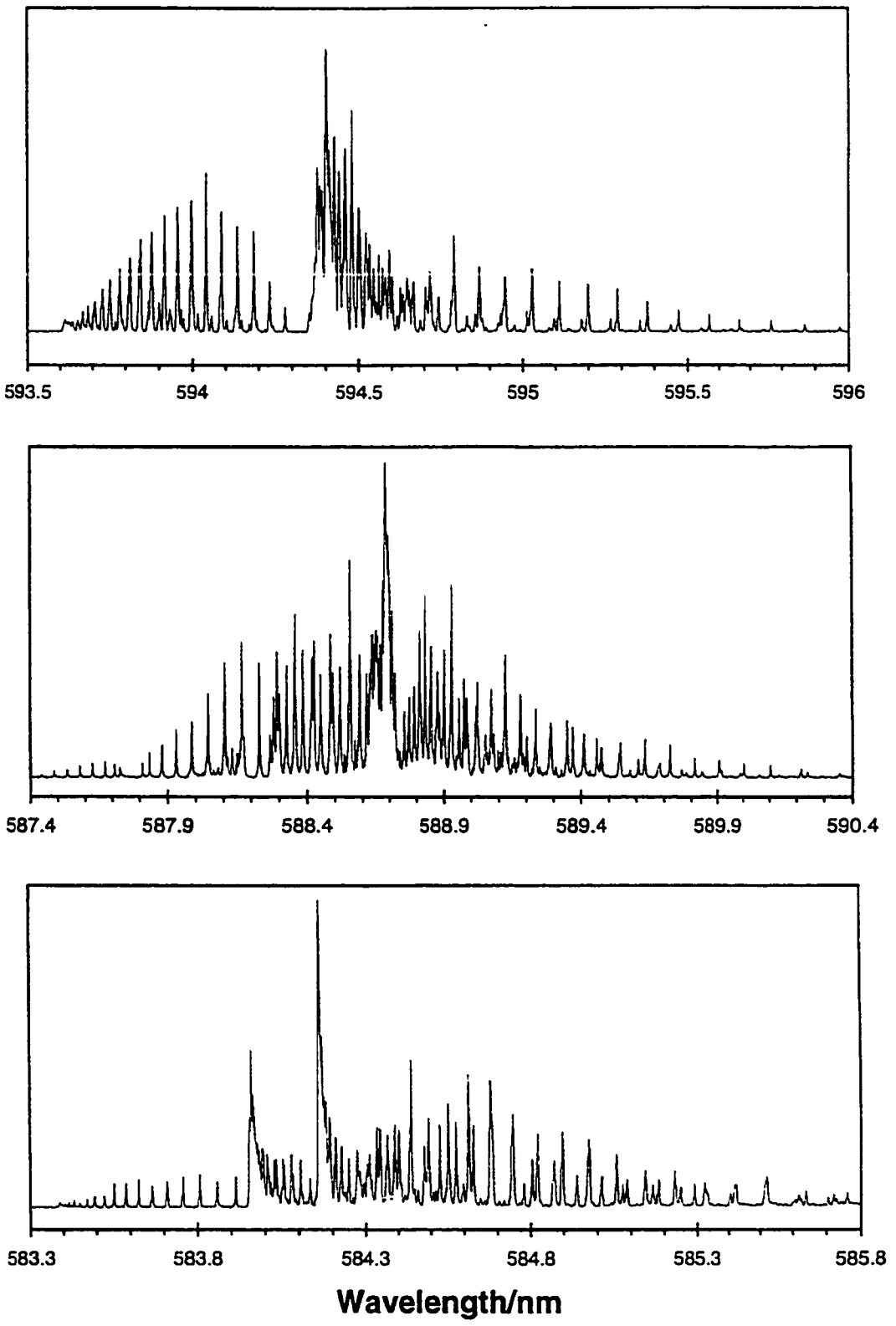

Fig. 6.1 continued. The LIF spectra recorded for $Rh^{16}O$ in the 700 - 550 nm.

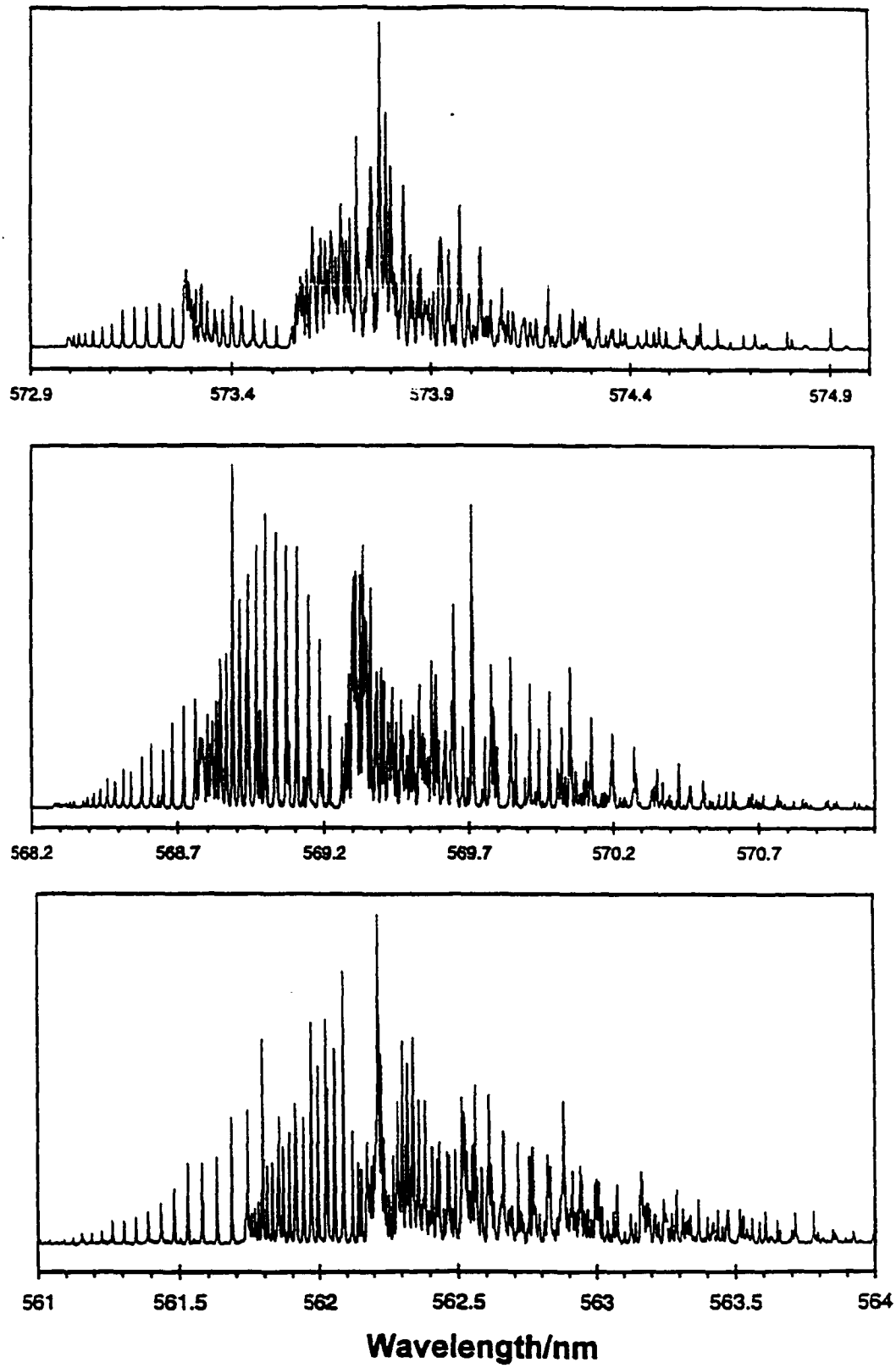

Fig. 6.1 continued. The LIF spectra recorded for $Rh^{16}O$ in the 700 - 550 nm.

6.2. Observations and Results

The bands shown in Fig. 6.1 appear very strongly. The same bands observed in the photographed high-resolution spectrum were also very intense. The high-resolution spectrum was photographed at a much higher temperature and its bands are even more congested than those recorded via the LIF technique. The spectral intensities alone suggest that the observed transitions are electronically allowed. The structure of the bands in both the LIF and high-resolution spectrum of RhO appears very complicated.

Comparison of the RhO bands presented in Fig. 6.1 with those of RhC and RhN displayed in Chapters 4 (RhC) and 5 (RhN) respectively, indicates a stark contradiction in profiles. The RhO bands have many more branches (approximately nine to twelve can be picked out in some cases) than are observed in RhC. The differences are even more notable when RhO is compared with RhN where spectra have only two or three branches depending on the states of the system under study. The RhC spectra involve doublet states, the RhN spectra singlet states. Besides the large number of branches in the RhO bands, the branch spacings of the RhO bands are significantly different from those found in RhC and RhN. Rudimentary fittings of the branches in the RhO bands suggest spacings of $\pm$ B, $\pm$ 3B, and $\pm$ 5B. These "global" observations (band profiles/ branch spacings) strongly suggest that the transitions involve states of high multiplicities. All of the RhO bands show strong intensity which implies that a "Q-type" structure is present. If these structures are, indeed, "Q-type" structures, the probability exists that these transitions have $\Delta\Lambda = \pm 1$. The number of observed branches, the spacings, and the presence of strong features near the band center suggest that the observed transition is

$^4\Pi - {}^4\Sigma$.

The structure of the bands associated with a $^4\Pi - {}^4\Sigma$ transition can be very complex. Limitations in our laser resolution have prohibited a detailed rovibrational analysis of the system. A simulation program [145] was written for each of the four subbands associated with a $^4\Pi - {}^4\Sigma$ transition to compare the simulated spectra with what was observed. Similar simulations proved very valuable in the fit of the $A^4\Pi - X^4\Sigma$ system of CrN [38, 97] recently studied by our group. The programs were written under the assumption that the $^4\Pi$ upper state belongs to Hund's case (a) or (ab) and the $^4\Sigma$ ground state falls under Hund's case (b). These assumptions were based on the number of CrN branches observed in the stronger bands of the spectrum. Energy expressions, including Λ-type doubling where applicable, used for the simulation were based on models used to fit known $^4\Pi - {}^4\Sigma$ transitions, MoN [111] and WN [122]. An example of the simulated spectrum of the 626 nm RhO band accompanies the recorded spectrum in Fig. 6.2. Qualitatively, the simulated spectrum bears a likeness to the observed spectrum. The resemblance supports our contention that the observed bands are a result of a $^4\Pi - {}^4\Sigma$ transition. Also, the structural parameters used to simulate the spectrum are reasonable approximations of the expected parameters and should be a good starting point to begin a detailed rotational analysis.

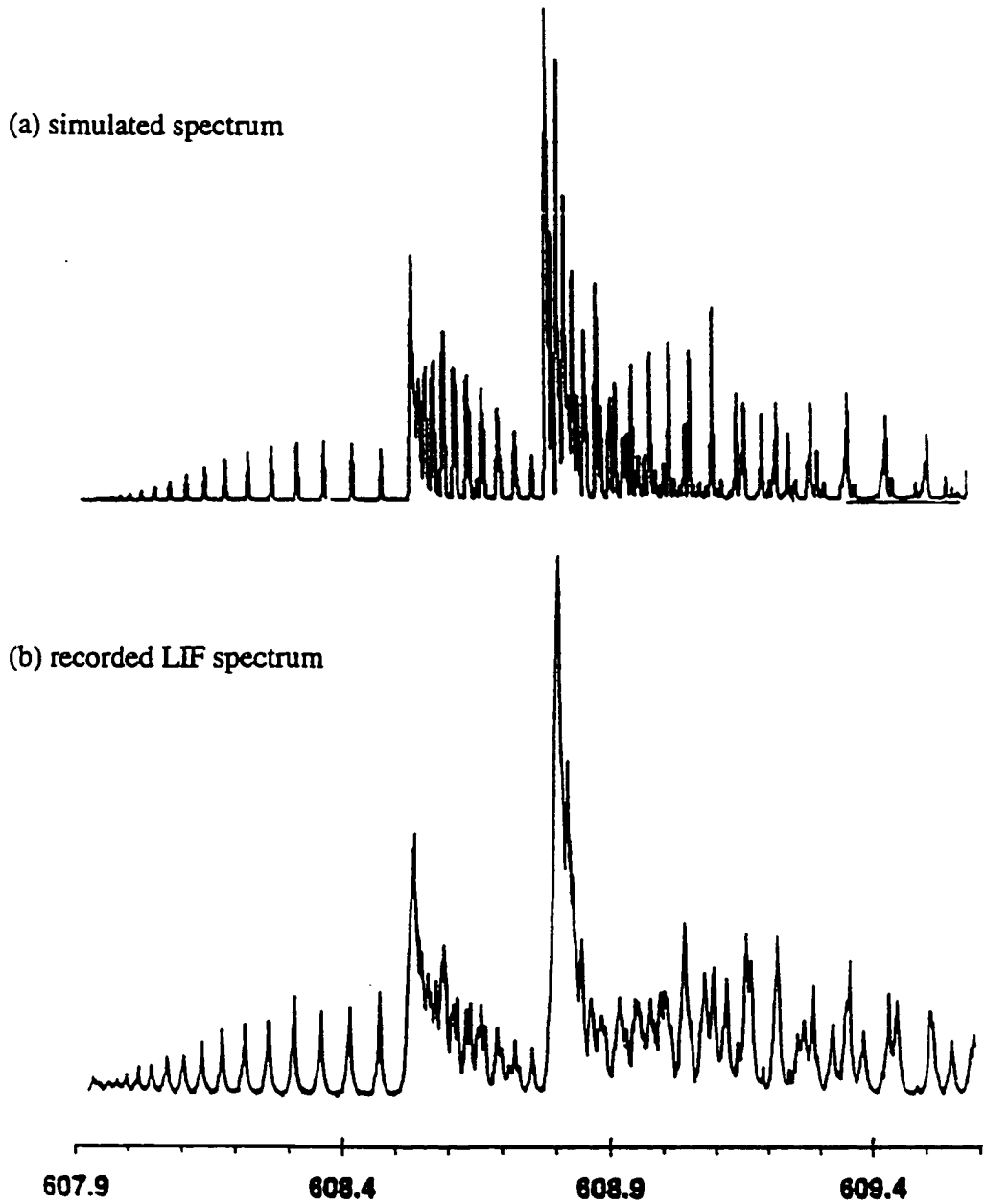

Fig. 6.2. (a) The simulated spectrum for the 608.80 nm band. In (b), a portion of the recorded LIF spectrum is shown.

6.3. A Molecular Orbital Picture of RhO

The qualitative MO diagram constructed for RhC and RhN can be used to propose logical low-energy configurations for RhO. As in RhC and RhN, ten electrons fill the 11σ, 5π, and 2δ orbitals. The placement of the three remaining electrons into the lowest unoccupied orbitals leads to several possible electron arrangements.

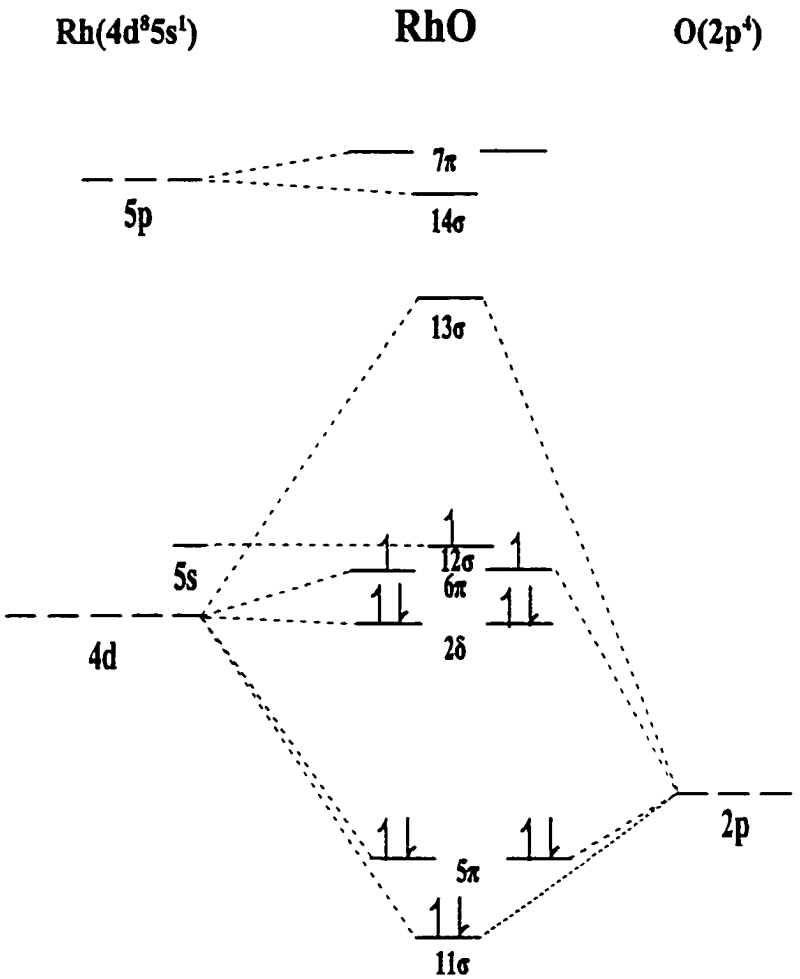

Fig. 6.3. The qualitative molecular orbital diagram for the RhO molecule.

From Fig. 6.3, we predict several low-energy configurations:

(i) ... $2\delta^4 6\pi^3$: $^2\Pi_i$

(ii) ... $2\delta^4 12\sigma^1 6\pi^2$: $^{2,4}\Sigma^-$, $^2\Delta$, $^2\Sigma^+$

(iii) ... $2\delta^4 12\sigma^2 6\pi^1$: $^2\Pi_r$

Unlike RhC and RhN, no detailed *ab initio* calculations that concentrate on the electronic states of RhO exist. If the 6π molecular orbitals are in close proximity to the 12σ orbital, simple arguments based on Hund's rule favor configuration (ii). The only theoretical work [146] on the electronic structure of RhO predicts the lowest energy state to be the $^4\Sigma^-$ state that arises from configuration (ii). It therefore appears very likely on both experimental and theoretical grounds that the RhO spectrum we have recorded involves a transition of a $^4\Pi - {}^4\Sigma^-$ nature.

Although the CoO and IrO are isoelectronic with RhO, the ground states of these molecules differ from each other and that proposed for RhO. States of $^4\Delta_i$ and $^2\Delta_r$ have been proposed for the ground states of CoO [147] and IrO [148, 149] respectively. Spectroscopic analyses have proven these assignments to be correct. The principal configuration that describes the ground state of CoO is $\sigma^2\pi^2\delta^3$. That proposed for the ground state of IrO is the same as that proposed for the ground state of RhO. The atomic ground state configurations are Co: $3d^7 4s^2$, Rh: $4d^8 5s^1$, Ir:$5d^7 6s^2$. With different atomic ground state electron configurations and the relative energy differences between the n*d* and (n + 1)*s* of the metal atomic orbitals, it is not unreasonable to observe different ground molecular states for the three monoxides.

Our attention now turns to the nature of the $^4\Pi$ excited state. If our prediction is

correct, the two likely configurations that lead to a $^4\Pi$ state are: (*i*) $2\delta^4 6\pi^1 12\sigma^1 13\sigma^1$ and (*ii*) $2\delta^3 6\pi^3 12\sigma^1$. Configuration (*i*) is preferred on energetic grounds, however, without further analysis, neither configuration should be rejected at this time. Experimental determination of whether the $^4\Pi$ state is regular or inverted will distinguish between the two choices.

6.4. Further Analysis of the RhO Spectrum

Given the complexity of the overall picture of RhO, we have deferred further analyses at this time pending the collection of higher resolution spectra. The branch structure in our spectra, although resolved for medium resolution work, is congested near the band center. This congestion prohibits the identification of the first lines for several branches associated with the $^4\Pi$ - $^4\Sigma$ transition. With higher resolution spectra, the lines of the branches near the band center should be clearly resolved. Experiments at 200 MHz resolution are scheduled (January 2000) in collaboration with Professor Adam at the University of New Brunswick, Fredericton. The clearer picture will enable assignment of the first rotational lines of each branch. Proper branch identification and assignment of appropriate rotational quantum numbers are key to any further investigation and assignments associated with the RhO spectrum.

Chapter 7

Bonding in Rhodium Diatomic Molecules

7.1. Introduction

The aim of this chapter is twofold. We will first give a brief overview of the bonding in diatomic molecules that contain the metal rhodium. The second goal is to present a brief review of the spectral and theoretical information obtained for the ground states of the transition metal carbides and nitrides. It is still rare to see an overview of spectral information that pertains to the bonding in transition metal carbides or nitrides like Merer's review of the 3*d* TM- oxides [84]. Siegbahn [150] and Armentrout *et al.* [151] have investigated the trends in metal carbon bond strengths in small TM complexes (M - H, and M - C) but this is a rare exception. The inclusion of such a section is not only to show the accomplishments of this work but also to convey just how much current interest there is in this field as evidenced by the number of different research institutes throughout the world that publish works in this area. This summary certainly demonstrates the scientific interest that transition metal diatomic molecules have attracted during the last thirty years. The reasons for this interest have been presented in the introduction to this dissertation. On the other hand, one can absorb the information conveyed in this work and realize that this field has a rich chemistry yet to be explored.

Although the bonding picture in most transition metal compounds is complex, simple MO arguments give insight on the possible ground states and low-lying electronic states that may or may not influence the bonding of the ground state. A qualitative MO diagram, no matter how simplistic, goes "hand-in-hand" with spectroscopic analyses to provide a clear picture for the nature of the bonding in the molecule.

7.2. Bonding in Rhodium Diatomic Molecules

Before we look at how the bonding in RhC and RhN compares with other transition metals, we will consider how the ground states of the Rh-X molecules change as the ligand changes. The MO picture for RhC, RhN, and RhO was already presented in each molecule's respective chapter however, a brief description of the bonding in diatomic Rh-X compounds, i.e., RhC, RhN, RhO, and RhF will be presented here. The obvious difference in these molecules is the one-electron increase from the ligand as we move from C → N → O → F. As we move across period 2, the electronegativity of the ligands increases and thus the ligand 2*p* orbitals drop in energy. The drop in atomic orbital energy directly affects the energies of the molecular orbitals that result from the mixing of the 2*p* ligand orbitals and the Rh 4*d* atomic orbitals. The 11σ, 13σ, 5π, and 6π molecular orbitals will decrease in energy as the ligand electronegativity increases.

Of importance to the ground state electron configurations of the rhodium molecules mentioned above, are the positions of the 11σ, 13σ, 5π, and 6π molecular orbitals in relation to the nonbonding orbitals which are predominantly the 5*s* (12σ) and 4*d*δ (2δ) orbitals of the rhodium atom. Since the 12σ and 2δ orbitals are metal-based orbitals, their energies are to a first approximation constant (equal to the energy of the atomic orbitals) despite the ligand attached to rhodium (or any other 4*d* transition metal). Because the relative energy orderings of the 12σ and 6π orbitals depends on the ligand atom, the 6π orbitals in RhN will lie lower than in RhC but the 12σ orbital will not change from RhC to RhN. This also means that the 13σ orbital in RhN will lie lower than in RhC. Support for the lower orbital energies comes from the

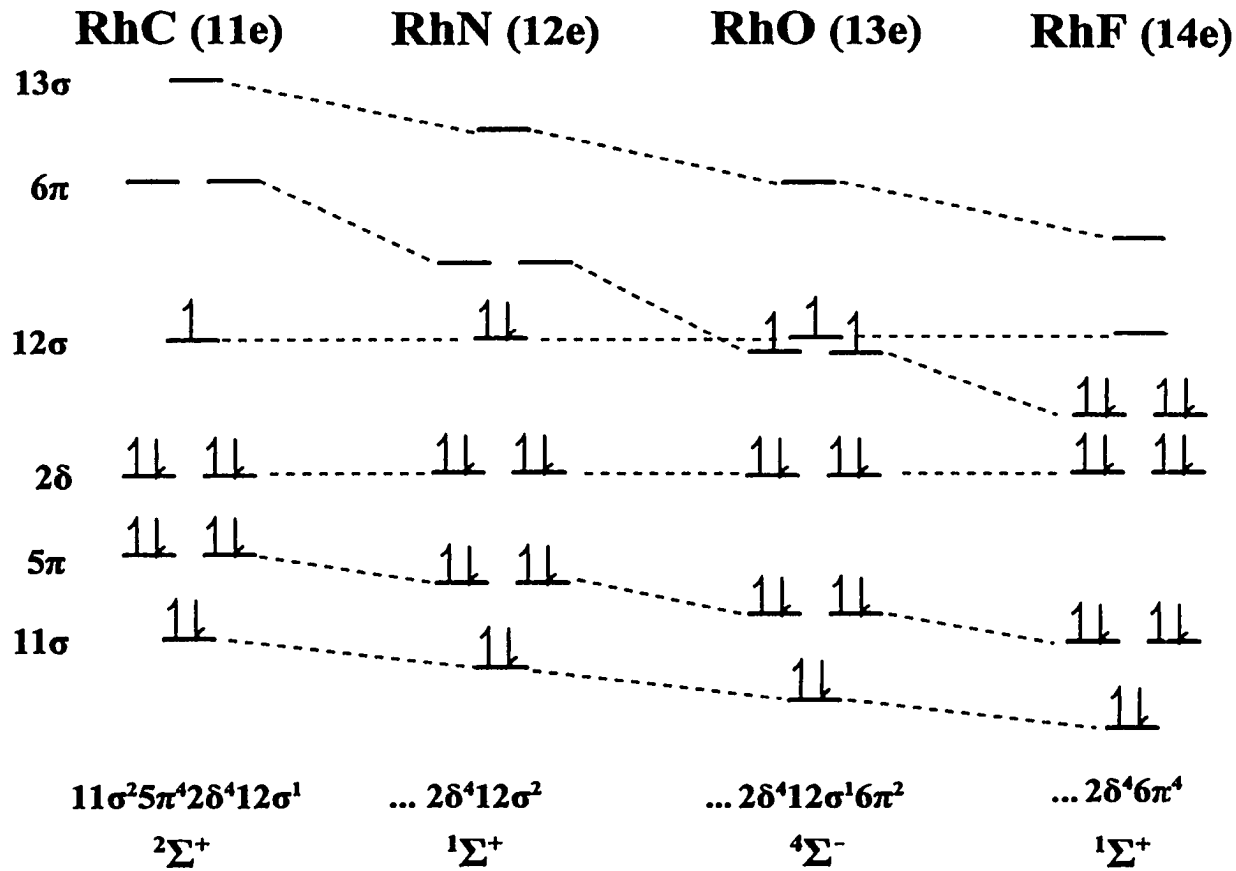

Fig. 7.1. The qualitative molecular orbital scheme, leading electron configurations and proposed ground electronic states of period 2 Rh-X diatomic molecules.

proposed electron configurations of the rhodium diatomic molecules. The qualitative effect of the increasing electronegativity of the ligand is shown in Fig. 7.1. The proposed ground state electronic configurations (and ground electronic states) of the Rh-X molecules were made based on our experimental observations in conjunction with the molecular orbital diagrams.

The placement of the valence electrons into the Rh-X molecular orbitals depends on the relative orderings of the 12σ and 6π orbitals. All the Rh-X species mentioned above have their first ten electrons completely filling the 11σ, 5π, and 2δ molecular orbitals. Successive electrons placed in the 12σ orbital accounts for the $^2\Sigma^+$ and $^1\Sigma^+$ ground electronic states of RhC and RhN respectively. The 6π orbitals lie higher than the 12σ in both molecules. From dispersed fluorescence spectra, we made a conservative estimate of the energy gap between these two orbitals in the two molecules. As can be seen in Fig. 7.1, the energy ordering of the 6π and 12σ orbitals is different in RhO. In the RhO molecular orbital description, we believe the 6π orbitals lie slightly lower in energy than the 12σ orbital. With the 6π and 12σ orbitals so close in energy, the three remaining electrons should singly occupy these orbitals. The resulting configuration ($^4\Sigma^-$ ground state) is the only logical scheme that accounts for the appearance of the bands in the RhO spectrum. If the energy of the $2p$ orbital continues to lower energy as we move to fluorine, we can assume the 6π molecular orbitals in RhF would be significantly lower in energy than the 12σ orbital. The relative difference should be large enough that the 12σ orbital would be unoccupied. The electrons should then completely fill the 6π orbitals giving a $...2\delta^4 6\pi^4$ ground state configuration for RhF. This configuration leads to a

ground state with $^1\Sigma^+$ symmetry. The electronic structure and spectrum of RhF have yet to be investigated by experimental or theoretical means.

From the MO description of the Rh-X species, we can infer that RhC and RhN molecules are triply-bonded to the ligand atom (Rh≡C and Rh≡N). The triple bond consists of a sigma bond between the metal and the ligand atom and two pi bonds that result from the overlap of the metal's d_π orbitals and the p_π orbitals of the ligand. The degree of overlap between these orbitals in RhC and RhN must be nearly identical. In other words, the attraction between rhodium and either of the ligand atoms is very similar. Evidence for this stems from the closeness of the ground state bond lengths in RhC and RhN molecules: $r_{RhC} = 0.161$ nm and $r_{RhN} = 0.164$ nm. The similarity in the bond lengths of the two molecules also implies that the 12σ orbital in both molecules is essentially nonbonding so the addition of a second electron, on going from RhC to RhN, does not affect the bonding in any significant manner. A similar trend is observed in the isoelectronic Ir-X molecules [70 - 72, 126 -128, 148, 149] but comparisons must be made with caution since the ordering of the molecular orbitals are slightly different in the two sets of molecules. With different relative orderings of the molecular orbitals, different electronic configurations may result. Such is the case when RhC is compared to IrC. We saw that RhC has a $...\sigma^1$ ground state configuration ($^2\Sigma^+$ molecular ground state). IrC, however, has a $...\delta^3\sigma^2$ configuration which yields a $^2\Delta_i$ ground state.

As for RhO and RhF, we would expect the ground state bond lengths of these molecules to be successively longer since the number of electrons that occupy the antibonding orbitals increases. This assumption is, of course, dependent on our assumed

ground state electron configurations being the true ground state configuration.

7.3. Property Trends of Transition Metal Carbides.

The focus of this section is to point out and discuss the general trends of transition metal carbides in their ground state. In Table 7.1, the spectroscopic constants that are presently known are listed. The majority of the presented data has come via experimental work, however, where no characterization of the carbides exists through experimental studies, the results of theoretical works have been used as a substitute. Although our work has not added any new information to the already well established ground state of RhC, a global summary of the bonding trends in the transition metal carbides is timely.

It is probably fair to state that when TM metal surveys are performed, in almost all cases it is the ligand that is changed in order to observe the effects the ligand(s) has(have) on the metal. However, for the present comparison, the ligand (in this case carbon) is kept constant and the transition metal is the variable. Establishing the trends in carbides as one goes from a d^1 to a d^{10} configuration across the periodic table is pertinent in predicting the chemical behavior of the metal-carbon interaction whether one is looking at bond strength or multiple bonding characteristics. The numbering of the d electrons is taken to be the valence electron configuration of neutral gas phase d-block atoms [87]. In this number scheme Sc, Y, and La would be considered d^1 metals and Zn, Cd, and Hg would be d^{10} metals.

Table 7.1. Gas Phase Spectroscopic Information for the Ground States of Transition Metal Carbides[a].

ScC b	[b,c]TiC [47] $...8\sigma^1 3\pi^4 9\sigma^1$ $(^3\Sigma^+)$ $\omega_e'' = 889$ $k = 449$ $B_0'' \approx 0.595$ $r_0'' \approx 0.176$	[b,c]VC [46] $...8\sigma^2 3\pi^4 1\delta^1$ $(^2\Delta)$ $\omega_e'' \approx 730$ $k = 306$ $B_0'' \approx 0.638$ $r_0'' = 0.165$	[b,c]CrC [48, 49] $...8\sigma^2 3\pi^4 1\delta^2$ $(^3\Sigma^-)$ $\omega_e'' \approx 675$ $k = 262$ $B_0'' \approx 610$ $r_0'' = 0.168$	MnC b	FeC [40] $...3\pi^4 9\sigma^1 1\delta^3$ $(^3\Delta_i)$ $\omega_e'' = 938$ $k = 514$ $B_0'' \approx 0.6698$ $r_0'' \approx 0.1596$	CoC [43] $...3\pi^4 9\sigma^1 1\delta^4$ $(^2\Sigma^+)$ $\omega_e'' \approx 940$ $k = 521$ $B_0'' \approx 0.6937$ $r_0'' \approx 0.1612$	NiC [45] $...3\pi^4 9\sigma^2 1\delta^4$ $(^1\Sigma^+)$ $\omega_e'' = 875$ $k = 451$ $B_0'' \approx 0.6374$ $r_0'' \approx 0.1631$	CuC b	ZnC b
YC [51] $11\sigma^1 5\pi^3 12\sigma^1$ $(^4\Pi_i)$ $\omega_e'' \approx 686$ $k = 294$ $B_0'' = 0.3788$ $r_0'' = 0.2050$	ZrC [52] $11\sigma^2 5\pi^4$ $(^1\Sigma^+)$ $\omega_e'' \approx 880$ $k = 486$ $B_0'' = 0.5265$ $r_0'' = 0.1739$	NbC [53] $...5\pi^4 2\delta^1$ $(^2\Delta_r)$ $\omega_e'' \approx 993$ $k = 620$ $B_0'' = 0.5487$ $r_0'' = 0.1723$	MoC [54] $...5\pi^4 2\delta^2$ $(^3\Sigma^-)$ $\omega_e'' = 1008$ $k = 641$ $B_0'' = 0.5536$ $r_0'' = 0.1688$	[b,c]TcC [61] $...5\pi^4 2\delta^2 12\sigma^1$ $(^4\Sigma^+)$ $\omega_e'' \approx 937$ $k = 556$ $B_0'' \approx 0.539$ $r_0'' \approx 0.171$	RuC [55, 81] $...5\pi^4 2\delta^4$ $(^1\Sigma^+)$ $\omega_e'' = 1100$ $k = 768$ $B_0'' = 0.6073$ $r_0'' = 0.1608$	RhC [1] $...5\pi^4 2\delta^4 12\sigma^1$ $(^2\Sigma^+)$ $\omega_e'' \approx 1049$ $k = 700$ $B_0'' = 0.6027$ $r_0'' \approx 0.1614$	PdC [56] $...5\pi^4 2\delta^4 12\sigma^2$ $(^1\Sigma^+)$ $\omega_e'' = 848$ $k = 458$ $B_0'' = 0.5336$ $r_0'' = 0.1712$	AgC b	CdC b
LaC b	HfC b	[b,c]TaC [79] $...8\pi^4 16\sigma^1$ $(^2\Sigma^+)$ $\omega_e'' \approx 748$ $k = 748$ $B_0'' \approx 0.401$	WC b	ReC b	OsC b	IrC [70, 71] $...8\pi^4 4\delta^3 16\sigma^2$ $(^2\Delta_i)$ $\omega_e'' \approx 1060$ $k = 751$ $B_0'' = 0.5252$ $r_0'' = 0.1683$	PtC [73 - 78] $...4\delta^4 16\sigma^2$ $(^1\Sigma^+)$ $\omega_e'' \approx 1051$ $k = 739$ $B_0'' = 0.5287$ $r_0'' = 0.1677$	AuC b	HgC b

[a] **All data represents the most abundant isotope: ω in cm^{-1}, k in N/m, B_0'' in cm^{-1}, r_0'' in nm.**

[b] **No experimental data are presently known**

[c] **Only theoretical data are available**

The method used to construct the MO diagram for RhC was described in chapter 4. In principle, the same diagram can be used for the other transition metal carbides. One must consider the differences in the metal atomic orbitals for the metal in question. The MOs of the M-C molecules will differ from metal to metal based on the n*d* and (n+1)*s* valence electrons of the metal and their interaction with the carbon 2*p* and to a lesser extent, the carbon 2*s* orbital. As one goes across the periodic table the energy of the metal n*d* orbital drops in energy more rapidly in comparison to the (n+1)*s* orbital [84]. As a direct consequence the δ molecular orbitals that are mostly of metal n*d* character decrease in energy relative the sigma nonbonding orbital that is primarily of (n+1)*s* metal character. Besides the δ molecular orbitals, those MOs with significant metal *d* character will also decrease in energy, *e.g.*, the antibonding (σ^* and π^*) orbitals. The drop in orbital energy is illustrated qualitatively in Fig. 7.2.

Based on experimental evidence, the early TM carbides (*e.g.* YC) have their nonbonding σ molecular orbitals filled prior to the δ orbitals. In all likelihood, the (n+1)*s* (for Y, 5*s*) atomic orbitals of the metal lie below the n*d* (Y: 4*d*) AOs. Once the d^3 metal is reached in the first and second row transition metals (V and Nb), the ordering is reversed. In the 5*d* series, where relativistic effects become important this is not the case. The molecule's δ orbitals become partially filled whereas the non-bonding σ orbital (σ_{nb}) remains unoccupied.

As Table 7.1 indicates, about half of the TM monocarbides have yet to be studied spectroscopically. This situation may be rectified shortly as studies on ZrC [52], TiC, VC, and CrC [45] are currently underway.

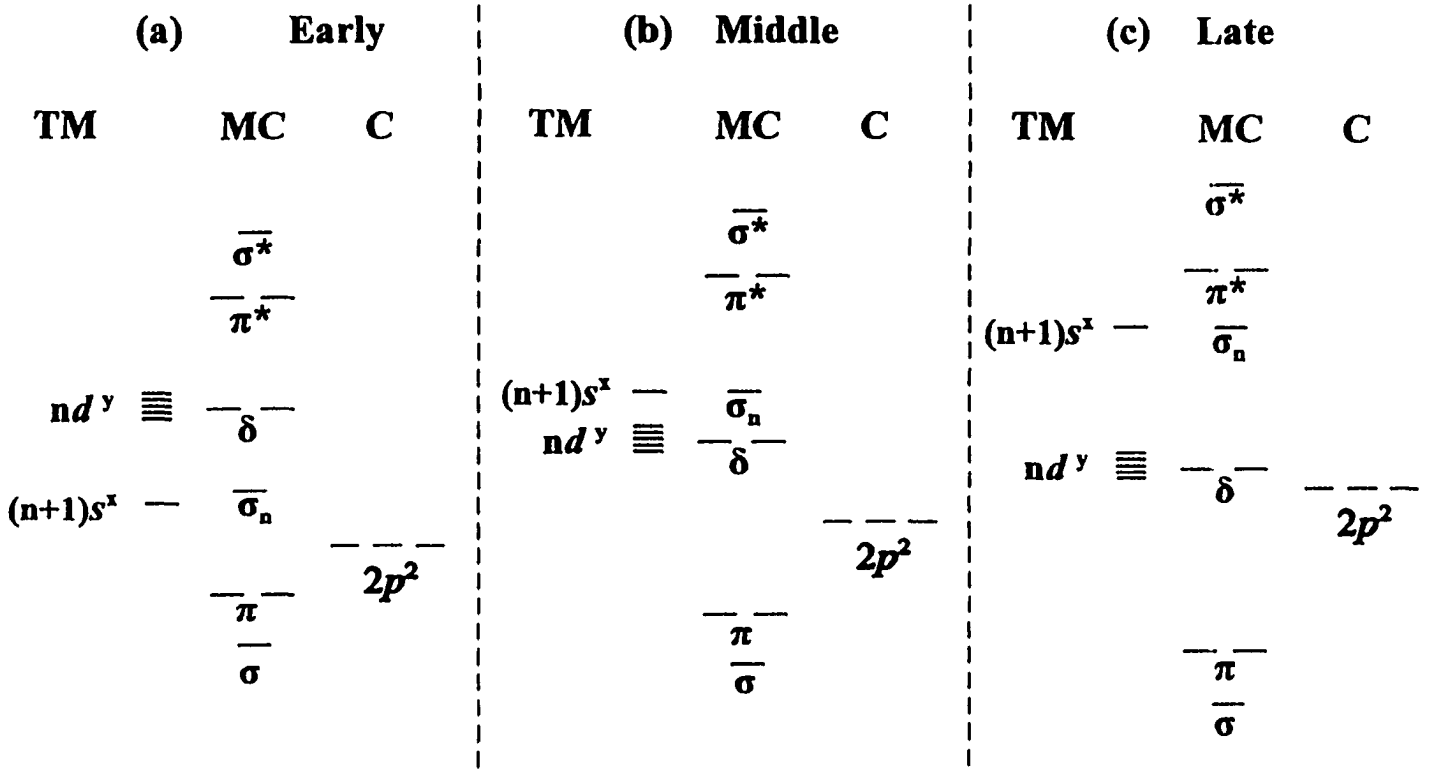

Fig. 7.2. Qualitative MO diagrams for the TM carbides showing the relative change in orbital energy between the *nd* and (n+1)*s* AOs of the metal across a row. (a) In the early part of the *nd* series, the *nd* orbital lies above the (n+1)*s* orbital. (b) As the atomic number increases towards the middle TM metals, the *nd* orbital and (n+1)*s* orbitals become nearly degenerate and finally for the late TM carbides (c), the *nd* drops below the (n+1)*s* orbital.

The 4*d* series is by far, the most extensively studied. Of the first eight metals of the series, all but technetium have been studied spectroscopically. The reason for technetium's absence is that all its isotopes are radioactive. It has, however, been the focus of a theoretical study [61]. Experiment proved that yttrium carbide has a $^4\Pi_i$ ground state [51]. The leading candidate for this symmetry is an $11\sigma^1 5\pi^3 12\sigma^1$ electron configuration. This electron configuration is somewhat surprising. If the MOs were filled on the Aufbau principle, an $11\sigma^2 5\pi^3$ electron configuration would be the most probable configuration, giving a $^2\Pi_i$ symmetry. Shim *et al.* have predicted a $^4\Pi_i$ ground state for YC as well as low-lying $^2\Pi_i$ and $^2\Sigma^+$ states [59]. The closeness of these states suggests that the 11σ, 5π, and 12σ molecular orbitals have similar energies. Although, there is no published work to date concerning ZrC, studies [52] currently in progress have shown ZrC to have a $^1\Sigma^+$ ground state. A $11\sigma^2 5\pi^4$ electron configuration yields a $^1\Sigma^+$ symmetry. As one moves across the row from niobium to ruthenium, the 2δ orbital fills until it becomes fully occupied for RuC ($^1\Sigma^+$: $5\pi^4 2\delta^4$). Technetium could be the exception to this δ orbital occupation. Theoretical studies [61] place the $^4\Sigma^+$ ($5\pi^4 2\delta^2 12\sigma^1$) electronic state at a lower energy than the $^2\Delta_i$ ($5\pi^4 2\delta^3$). With the $5\pi^4 2\delta^2 12\sigma^1$ configuration as the preferred configuration of the TcC ground state, the nonbonding sigma orbital (12σ) must lie close enough to the 2δ orbitals that it becomes more favorable for the electrons to occupy the three orbitals (one σ and two δ orbitals) singly as opposed to having three electrons in the 2δ orbitals. Further theoretical and experimental investigation would certainly provide insight into the true nature of the TcC ground state. The RhC and PdC species have $^2\Sigma^+$and $^1\Sigma^+$ ground states, respectively. These ground states are a direct

consequence of the successive TM electrons occupying the 12σ orbital.

With the lack of experimental information on the first and third row TM carbides, discussing trends in their ground state bond lengths is pointless. However, with seven second row TM carbides spectroscopically analyzed, a discussion of the bond lengths there is more meaningful. Across the second row the length of the M-C bond shortens from YC to RuC. The decreased bond length across the 4*d* series might lead one to suspect that the 2δ orbitals have a tendency to be slightly bonding for the TM carbides. However, since these do not mix with the carbon *p* orbitals, the 2δ orbitals are nonbonding.

The bond length ranges from 0.1723 nm in NbC [53] to 0.1608 nm in RuC [55]. This reduction can be attributed to the shrinking of the metal orbitals with increasing atomic number across the row. There is not much in the way of organometallic TM complexes with which to compare the above bond lengths. In what is an unfortunate circumstance, most of the metal-carbon triple-bonded complexes for which there are data, there is no spectroscopic information for the diatomic counterpart. Metals such as chromium, molybdenum, tantalum, tungsten, rhenium, and osmium have a propensity to form metal-carbon triply bonded complexes. However, no identification of the diatomic carbides of these metals has come through spectroscopic studies with the exception of molybdenum. A typical value for a Mo≡C bond length in metal-carbon complexes is 0.1795 nm [152]. The value in the diatomic Mo≡C bond length is shorter (0.1688 nm). It is likely that the Mo≡C bond length is longer in the complex due to ligand effects. If the donor ligand contributes electron density to the metal, the M–Ligand bond gains

strength at the expense of the M≡C bond. In tantalum-carbon complexes, the Ta≡C bond length ranges from 0.176 to 0.185 nm. These values may be compared with what was predicted via theory for the monocarbide: 0.179 nm [79].

For the first and second row series, the metal-carbon bond length begins to increase once the electrons of the d^n metal occupies their respective nonbonding sigma orbital. The TM carbide bond length (Table 7.1) exhibits a small increase in bond length as one goes from FeC to NiC. Occupation of this orbital introduces more σ-repulsion between the atoms so that they cannot approach one another closely enough to form the optimal π-bonds. The net result is an increase in bond length and a decrease in vibrational frequency. The increase in bond length is more dramatic in the second row. The metal-carbon bond increases from 0.1608 nm in RuC to 0.1712 nm in PdC .

Plenty of work still remains to be done for the first and third row TM carbides in order to establish a clear understanding of the trends in transition metal-carbon bonding.

7.4. Bonding in the Second-Row Transition Metal Mononitrides

The inclusion of a section correlating the bonding relationships between transition metals and nitrogen would have been nearly impossible if this dissertation were being written fifteen or even ten years ago. The main reason, as stated in the opening of this chapter, is that the spectroscopic understanding of small transition metal molecules has only emerged within this time frame. Before the mid-1980s, the detailed information did not exist to permit such a correlation. Improvements in both experimental and theoretical

strategies have removed such barriers. Information is now available for most of the second-row transition metal mononitrides enabling a detailed spectroscopic database to be constructed. The addition of this section is beneficial to the understanding of the bonding in TM mononitrides in that some perspective can be placed to the known spectroscopic information about the ground states of the TM mononitrides.

As was the case for the carbides, establishing the trends of the metal as one goes from a d^1 to a d^{10} electron configuration across the periodic table is pertinent to predicting the chemical behavior of the metal-ligand (in this case nitrogen) interaction. It is not the goal of this section to analyze the details of the experimental and calculated results for the TM mononitrides but instead, to present the spectroscopic information of the known mononitrides and in the case where no experimental data are known, the results of theoretical calculations to see just how rhodium mononitride fits into the transition metal mononitride scheme.

In relation to the metal atomic orbitals, two trends occur for metal orbitals across the 4*d* transition series. The first trend is the more dramatic decrease in the 4*d* orbital energy in comparison to the 5*s* orbital energy as the atomic number increases. Secondly, the energy gap between the N 2*p* orbital and the metal 4*d* orbital gets smaller as one goes left to right across the periodic table as the TM ionization potentials increase. This should allow for more interaction between the nitrogen *p* orbitals and the metal *d* orbitals. The ground electronic states of the 4*d*-TM nitrides follow these trends as evidenced in various spectroscopic investigations [85, 105 - 115]. Table 7.2 lists the spectroscopic constants that are presently known for the TM mononitrides.

In most transition metal complexes, one or more multiple bonds (π - bonds) involving the ligand (atom) *p* orbitals and the metal *d* orbitals [152] is present. It is the goal of scientists in organometallic chemistry to interpret the nature of this $d\pi$ - $p\pi$ bonding in order to understand the similarities and differences between metals and ligands. The resulting triple bond character of the early transition metal- nitrogen bonds due to the $d\pi$ - $p\pi$ bonding is supported by the bond lengths that are listed in Table 7.2.

To date, six of the ten 4*d*-block TM mononitrides have been spectroscopically characterized. Besides our study on rhodium, the early 4*d*-block metals, yttrium to molybdenum mononitrides, have been studied along with ruthenium.
The valence electrons are housed in the metal 5*s* and 4*d* orbitals. The electronic configurations leading to the ground states of the MN species are also shown in Table 7.2. The MO diagrams shown in Fig. 5.26 and Fig. 7.1 can be used as a qualitative model to derive the molecular electronic configurations.

Nitrogen will contribute three 2*p* electrons. These three valence electrons are "deposited" in the 1σ and 5π MOs. The 1σ and 5π are the bonding orbitals that result from the mixing of the metal $d\sigma$ -$p\sigma$ and $d\pi$ -$p\pi$ orbitals of the metal and nitrogen atoms respectively. It is from this point the MOs are filled with electrons from the metal in question. With the ground state of YN [105] being ...$1\sigma^2 5\pi^4$ ($^1\Sigma^+$) and the ground state configuration of ZrN [106] ...$1\sigma^2 5\pi^4 2\sigma^1$($^2\Sigma^+$), it is likely that the 2σ orbital lies lower in energy than the 2δ orbital. Successive electrons go into the 2σ and 2δ orbitals of the metal nitrides.

Table 7.2. Various Gas Phase Spectroscopic Information for the Transition [a]Metal Nitrides.

ScN [88] $8\sigma^2 3\pi^4$ ($^1\Sigma^+$) $\omega''_e \approx 795$ k = 399 $B''_0 = 0.5528$ $r''_0 = 0.1691$	TiN [89 - 92] $8\sigma^2 3\pi^4 9\sigma^1$ ($^2\Sigma^+$) $\omega''_e \approx 1049$ k = 705 $B''_0 = 0.6200$ $r''_0 = 0.1577$	VN [93 - 96] $...3\pi^4 9\sigma^1 1\delta^1$ ($^3\Delta$) $\omega''_e \approx 1003$ k = 653 $B''_0 = 0.6253$ $r''_0 = 0.1566$	CrN [38] $...3\pi^4 9\sigma^1 1\delta^2$ ($^4\Sigma^-$) $\omega''_e \approx 1000$ k = 652 $B''_0 = 0.6259$ $r''_0 = 0.1563$	MnN b	[b,c]FeN [103] $...3\pi^4 9\sigma^1 1\delta^4$ ($^2\Sigma^+$) [d]$\omega''_e \approx 938$ k = 582 $B''_0 \approx 0.5702$ $r''_0 \approx 0.1626$	CoN b	NiN b	CuN b	ZnN b
YN [105] $10\sigma^2 11\sigma^2 5\pi^4$ ($^1\Sigma^+$) $\omega''_e \approx 661$ k = 313 $B''_0 = 0.4267$ $r''_0 = 0.1807$	ZrN [106] $11\sigma^2 5\pi^4 12\sigma^1$ ($^2\Sigma^+$) $\omega''_e \approx ?$ k = ? $B''_0 = 0.4830$ $r''_0 = 0.1696$	NbN [109, 110] $...5\pi^4 12\sigma^1 2\delta^1$ ($^3\Delta$) $\omega''_e \approx ?$ k = ? $B''_0 = 0.5015$ $r''_0 = 0.1662$	MoN [111] $...5\pi^4 2\delta^2 12\sigma^1$ ($^4\Sigma^-$) $\omega''_e \approx 1057$ k = 807 $B''_0 = 0.5143$ $r''_0 = 0.1638$	TcN b	RuN [85] $...5\pi^4 2\delta^4 12\sigma^1$ ($^2\Sigma^+$) $\omega''_e = 1122$ k = 916 $B''_0 = 0.5528$ $r''_0 = 0.1574$	[d]RhN $...5\pi^4 2\delta^4 12\sigma^2$ ($^1\Sigma^+$) $\omega''_e \approx 900$ k = 617 $B''_0 = 0.5075$ $r''_0 = 0.1642$	PdN b	AgN b	CdN b
LaN b	HfN [120] $15\sigma^2 8\pi^4 16\sigma^1$ ($^2\Sigma^+$) $\omega''_e \approx 933$ k = 668 $B''_0 = 0.4349$ $r''_0 = 0.1729$	[c]TaN [121] ($^1\Sigma^+$)	WN [122] $...8\pi^4 4\delta^2 16\sigma^1$ ($^4\Sigma^-$) $\omega''_e \approx ?$ k = ? $B''_0 = 0.4664$ $r''_0 = 0.1667$	ReN [123] $...8\pi^4 4\delta^2 16\sigma^2$ ($^3\Sigma^-$) $\omega''_e \approx 1125$ k = 975 $B''_0 = 0.4812$ $r''_0 = 0.1641$	OsN [125] $...8\pi^4 4\delta^3 16\sigma^2$ ($^2\Delta_i$) $\omega''_e \approx 1148$ k = 1016 $B''_0 = 0.4920$ $r''_0 = 0.1620$	IrN [72, 128] $...8\pi^4 4\delta^4 16\sigma^2$ ($^1\Sigma^+$) $\omega''_e \approx 1126$ k = 979 $B''_0 = 0.4985$ $r''_0 = 0.1609$	PtN [78, 129] $...4\delta^4 16\sigma^2 9\pi^1$ ($^2\Pi_r$) $\omega''_e \approx 947$ k = 693 $B''_0 = 0.4540$ $r''_0 = 0.1686$	AuN b	HgN b

[a] All data represent the most abundant isotope: ω in cm^{-1}, k in N/m, B''_0 in cm^{-1}, r''_0 in nm.
[b] No experimental data are presently known
[c] Only theoretical data are available
[d] This work
[e] From matrix work

The addition of an extra electron on going from zirconium to niobium mononitride does not result in a filled 12σ orbital but instead the electron follows a high spin electron configuration [7] and is placed in the 2δ orbital which results in an ...$11\sigma^2 5\pi^4 12\sigma^1 2\delta^1$ ($^3\Delta$) configuration for the ground state. This suggests that in NbN the 12σ and 2δ orbitals are very close in energy.

The multiplicity of the ground electronic states top out at MoN ($^4\Sigma^-$: $5\pi^4 12\sigma^1 2\delta^2$). No experimental observations or theoretical calculations have been made on the ground state of TcN so there a definite ground state configuration has not been established to this point. Atomic technetium has a $4d^5 5s^2$ electron configuration. The likely candidates for the extra electron are the 12σ or 2δ molecular orbitals. The resulting electronic states are $^1\Sigma^+$,$^3\Sigma^-$, and $^1\Gamma$ (...$5\pi^4 12\sigma^2 2\delta^2$) or $^1\Delta$ and $^3\Delta_i$ (...$5\pi^4 12\sigma^1 2\delta^3$). In the case of the Tc atom, the 5*s* AO is higher in energy than the 4*d* AO. If both the 4*d* and 5*s* atomic orbitals are nonbonding, these orbitals will not participate in any bonding with the nitrogen 2*p* orbital. If this is the case, then the most likely symmetry of the TcN ground state is $^3\Delta_i$ arising from the ...$5\pi^4 12\sigma^1 2\delta^3$ configuration. The multiplicity of the ground states begins to decrease as one moves from TcN to RuN and RhN. At this point, one can cautiously surmise that the 12σ molecular orbital lies above the 2δ orbital as the 2δ orbital is filled completely leaving the 12σ orbital to be filled. Spectroscopic analyses have proved the ground state of RuN [85] to be of $^2\Sigma^+$ symmetry (...$5\pi^4 2\delta^4 12\sigma^1$) and in this thesis research has shown that the ground state of RhN is $^1\Sigma^+$.

The remaining nitrides associated with the 4*d*-block elements (Pd, Ag, and Cd) have not been identified spectroscopically or studied via any theoretical means. Once we

move to the right of rhodium (for the nitrides), the electrons must be placed in antibonding orbitals. The strength of the metal-nitrogen bond of the late 3*d*, 4*d*, and 5*d* transition series will decrease. One can still theorize about the nature of the ground states for these late metal nitrides based on simple MO arguments. It is likely that PdN would have a $^2\Pi_r$ ground state as a sole electron would occupy the antibonding 6π orbital. A ...$6\pi^2$ configuration is likely to occur for AgN resulting in a $^3\Sigma^-$ ground state with low-lying $^1\Sigma^+$ and $^1\Delta$ states. Depending on the energy gap between the 6π and 13σ orbital, the ground state of PdN can have one of various symmetries. If a high-spin configuration is considered a $6\pi^2 13\sigma^1$ configuration would account for the ground state of PdN. Four molecular electronic terms may result from this electron configuration: $^2\Sigma^+$, $^2\Sigma^-$, $^2\Delta$, and $^4\Sigma^-$. However, if the 6π/13σ gap is large, the 6π orbital is more likely to fill up before the addition of an electron to the 13σ orbital, resulting in a $6\pi^3$ configuration ($^2\Pi_i$). The group IIB metals, to which cadmium belongs, have much in common with the group IIA metals (Ca, Mg, ...), *i.e.*, filled 2*s* AOs. The mononitrides of these metals are not known either.

As we go from left to right across the 4*d* transition series, we find a decrease in bond length for the ground state from YN to RuN (0.1807 nm to 0.1574 nm). This shortening of the M-N bond across the 4*d* series follows the same principles discussed in the previous section on metal carbides. This trend is also observed in the 3*d* and 5*d* series. For all the transition metals, the experimentally determined M-N bond lengths fall in the range of 0.15 - 0.18 nm. A plot showing the M-N bond length for the *d*-block elements is shown in Fig. 7.3. As will be discussed shortly, these distances are typical of

a M-N triple bond. The bond lengths support the idea that a favorable orbital overlap is present between the metal and nitrogen. The experimentally determined bond lengths are very close to those determined for metal-nitrogen (nitrido) triple bonds in larger transition metal complexes [152]. The typical M-N bond length in these complexes varies but is typically in the range of 0.16 - 0.18 nm.

The decrease in bond length described in the last paragraph appears to stop as we get to RhN in the 4*d* transition series. On going from RuN to RhN the bond length increases slightly from 0.1574 to 0.1642 nm. This suggests the nitrides have become less bonding than in their TM mononitride predecessors. Similar increases in the M-N bond are also observed in the 3*d* and 5*d* transition series.

With the gaps in the spectroscopic data for the diatomic transition metal mononitrides it is difficult to make any predictions/statements regarding trends in vibrational stretching frequencies across any row or down a particular group. However, one can look at the vibrational stretching frequencies of the diatomic TM mononitrides and examine how the vibrational frequencies for the metal- nitrogen bond correlate to those that are part of a larger M-N complexes. Table 7.3 shows the vibrational frequencies and M-N bond lengths for both the diatomic M-N species and metal-nitrogen bond in various metal-nitrido complexes. The reader should be aware that these values are representative of a general range and not specific to a particular molecule. As one can see the vibrational frequencies for the diatomics are in good agreement with the $\nu(M \equiv N)$ reported for the larger metal nitrogen analogues. The variation in the stretching frequencies in the nitrido complexes are directly related to the effect of the various

ligands attached to the metal center.

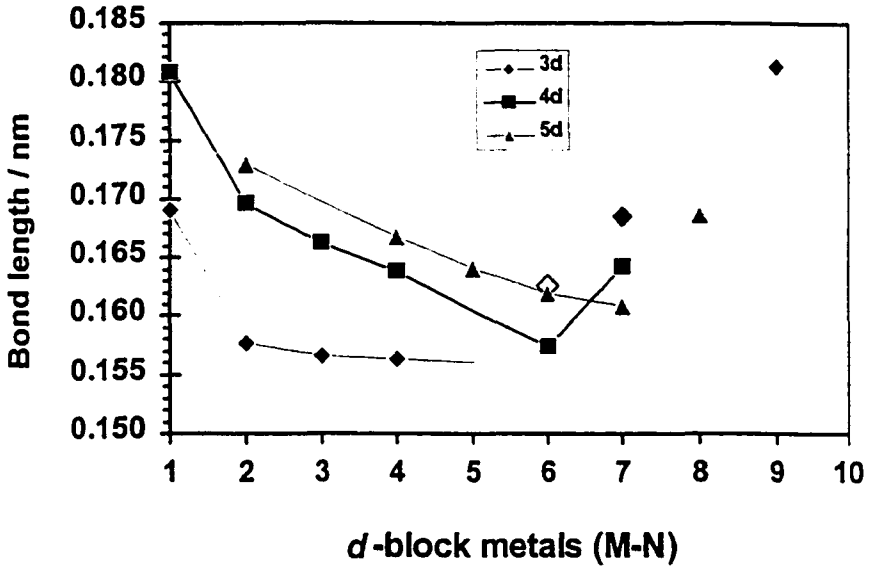

Fig. 7.3. A plot of metal-nitrogen bond lengths (r_0) for the first, second, and third row transition metal mononitrides. The values of r_0 are experimentally determined values except for FeN (open diamond). References are given in Table 7.2.

The excited states of the 4*d* mononitrides will, of course, vary as we go from one metal to another. The molecular orbitals associated with these excited states may undergo significant changes in geometry and energy due to the origin of the transition, configuration interactions, and perturbations from nearby states. Before one assigns configurations to any excited state, these factors have to be taken into account for, most often, the excited state molecular orbital cannot be described by a single configuration.

Table 7.3. Range of reported stretching frequencies and bond lengths of various nitrido complexes.

Metal	~Bond length[a] (nm) (M≡N complex)	Bond length[b] (nm) (M≡N diatomic)	ν(M≡N)[c]/ cm^{-1} (complex)	ν(M≡N)[b]/ cm^{-1} (diatomic)
V	0.157 - 0.173	0.1566	950 - 1050	1003
Cr	0.155 - 0.162	0.1563	1012 - 1017	1000
Fe	-	0.1626	915 - 1000	938
Nb	0.170 - 0.180	0.1662	835 - 1020	-
Mo	0.162 - 0.180	0.1638	945 - 1085	1057
Ru	0.158 - 0.184	0.1574	1025 - 1080	1122
W	0.168 - 0.184	0.1667	980 - 1135	-
Re	0.153 - 0.177	0.1641	950 - 1100	1125
Os	0.158 - 0.176	0.1620	1010 - 1140	1148

[a] Values of $r_{M\equiv N}$ taken from X-ray crystallographic data of various $L_3M\equiv N$ complexes. Note: the reported values are an average of several bond lengths.
[b] See Table 7.2 for references.
[c] The M≡N vibrational frequencies are based on IR or Raman spectra of $L_3M\equiv N$ complexes. Values taken from reference [152].

The excited states of the TM mononitrides, with the ideas in the previous paragraph considered, can be described using the same ideas used to describes the TM oxides [84]. Two types of excited states arise upon electron excitation. The first arises from the promotion of a bonding electron housed in the 11σ or 5π MO to a metal-centered MO (12σ or 2δ orbital) or to an antibonding molecular orbital (13σ or 6π orbital). These transitions essentially involve the migration of a nitrogen-based electron to the metal. This type of transition is called a "charge transfer" transition [21, 26]. The lowest lying excited electronic states in YN [105] are reached by such transitions. Low-

lying $^{1,3}\Sigma$ and $^{1,3}\Pi$ states result from the promotion of all σ or a 5π electron to the 12σ orbital. However, unlike the early TM oxides where the excited states of these charge transfer transitions have bond lengths that change by as much as 10%, the same electron promotion in the TM mononitrides does not produce as significant a change in bond length. Similar transitions in ScN [99] and YN [105] produce small changes in bond length (< 5%). Mixing between the orbitals of the nitrogen atom and metal atom may account for this, as the energy gap between nitrogen and the metals is not as large as the gap between oxygen and the metals. Rhodium nitride has two vibronic bands (444.4 and 440.7 nm) that fit the criteria of a "charge transfer" transition. A significant change in bond length between the ground state and these vibronic levels is observed (-15%). However, the nature of these transitions has yet to be determined.

The second type of transition involves the promotion of an electron from the metal- centered 2δ or 12σ molecular orbitals to the antibonding 6π or 13σ MOs. Most of the excited states for RhN involve this type of transition (see DF results). The 6π orbital may be only slightly antibonding in character in relation to the 2δ and12σ orbitals in RhN. The small difference in bond length between the $[19.5]0^+$ and $[22.4]0^+$ states suggests that they are very similar in character. The same trend is seen in NbN [109, 110], MoN [111 - 115], and RuN [85] where promotion of an electron to the 6π orbital from either the 12σ or 2δ orbitals produces small changes in bond length (< 7%), suggesting that the transitions involve metal- based electrons.

This section has presented information about the transition metal mononitrides that have been studied either spectroscopically or through various theoretical methods.

The ground state molecular terms have been characterized and the trends in the bond lengths across the 3*d*, 4*d*, and 5*d* series have been examined. The ground state bond length of the TM mononitrides can serve as a reference in determining metal- nitrogen distances of various metal- nitrido complexes. It is evident from a glance at Table 7.2, a fair number of TM nitrides have yet to be studied spectroscopically and theoretically. This emphasizes that there is still work to be done in the characterization of the TM mononitrides especially in the latter part of the transition series.

Chapter 8

Concluding Remarks and Future Work

8.1. Concluding Remarks

The work described in Chapters 1 through 7, represents the spectroscopic research carried out by the author. Detailed spectroscopic studies of two rhodium diatomic species, rhodium monocarbide and rhodium mononitride have been presented and the spectrum of a third rhodium diatomic species has been recorded. This latter spectrum was recorded after laser-ablated rhodium atoms were allowed to mix with oxygen gas. All the evidence points to rhodium monoxide as the carrier of the spectrum. Various techniques of laser-induced fluorescence and dispersed fluorescence have been used to study the visible region of all three molecules.

Previous studies of the RhC spectrum established the species as an excellent choice for an internal calibration of the RhX spectra we were to run. However, the questions that arose from careful interpretation of the original work on RhC led to the reinvestigation of its spectrum in the visible region between 400 - 530 nm. With the observation of new RhC bands, we were able to reinterpret the original analysis and present a clearer picture of the nature of the transitions in this region. Our study of RhC is now in print [153].

In chapter 5, we reported the first observation of the gas-phase electronic spectra for rhodium mononitride. Of the many vibronic bands recorded in the region 400 - 700 nm, we identified three electronic systems: $[15.1]1 - X^1\Sigma^+$, $[19.5]0^+ - X^1\Sigma^+$, and $[22.4]0^+ - X^1\Sigma^+$. Our assignment of $^1\Sigma^+$ as the symmetry of the ground state agrees with theoretical predictions. Dispersed fluorescence spectra revealed the presence at least three low-lying electronic states within 5,000 cm^{-1} of the ground state. Some of these

features are likely spin-orbit components of an expected low-lying $^3\Pi$ state and another of these features may be the $^1\Pi$ state that arises from the same electron configuration. Published results for RhN [154] appear in the *Journal of Molecular Spectroscopy*.

The spectrum of what has been tentatively identified as rhodium monoxide has been recorded in the 400 - 700 nm region using laser-induced fluorescence. The bands recorded between 550 and 640 nm appear to have a profile consistent with a $^4\Pi$ - $^4\Sigma$ transition. However, further rotational analyses of the individual bands has been hindered by the density of lines in several branches near the band center. An attempt to overcome this situation with increased resolution data is presently underway.

The reader, in the most general sense, can probably arrive at the conclusion that the spectrum of each RhX species presents quite different problems in terms of analysis. The recorded bands of rhodium mononitride had a simple profile but many bands in the spectrum did not quite fit into a regular scheme expected for an electronic system. The region in the vicinity of the ground state was rich in electronic states. The bands recorded for rhodium monocarbide can be thought of as having "fairly uncomplicated" profiles. Nevertheless, the analysis and interpretation of the spectrum was made difficult due to various interactions between the electronic states. And finally, the bands observed in the spectrum of rhodium monoxide were observed to have a complicated structure. The bands proved too complex for rotational study at his point. Hopefully the analysis will proceed after more detailed spectra have been recorded. The author has certainly gained a new appreciation for the methods of spectroscopic research and has especially achieved a greater understanding of the word "patience".

8.2. *Future Work*

"Where to go from here?" is a fundamental question that may be asked after any stage is completed. The same question can be posed after reading the work presented in this dissertation. In an attempt to answer this question, this section has been included to lay the groundwork for possible future work.

The first order of business is to complete the rovibrational analysis of RhO. Collaborative efforts are currently underway to record high resolution spectra of the lower energy bands. The high resolution spectra should identify the first lines associated with each branch located near the band center making a detailed rotational analysis possible. This further analysis should confirm our assumption the bands are part of a $^4\Pi$ - $^4\Sigma$ transition.

A second spin-off project that stems from the RhN analysis would be to investigate and analyze the lower energy states between 0 and 10,000 cm^{-1} of the RhN molecule. FT-IR emission spectroscopy is one tool that could be utilized to probe these states. If this study proves successful, RhN would be one of only a few examples of a transition metal diatomic species whose "energy map" would be characterized "completely" up to 25,000 cm^{-1} above the ground state. A detailed picture like this may provide the basis for an extensive theoretical study into the bonding in, and interactions between the electronic states of RhN.

To complete the spectroscopic study of period 2 main group rhodium diatomic molecules, an attempt to observe the spectrum of RhF should be made. It would be a logical extension to begin the search for the spectra of the period 3 molecules as well:

RhSi, RhP, RhS, and RhCl.

The production of rhodium radicals in jet-cooled beams is hopefully not limited to diatomic molecules. It is quite possible that we, or others, may study small polyatomic radicals containing rhodium. The importance of rhodium as a catalyst prompts one to search for, record and subsequently characterize the spectra of such molecules as $RhCH_3$, $RhCH_2$, RhCH, $RhNH_2$, RhNH, RhCO, RhNO, RhCN, RhOH, and RhCCH just to name a few. To date, there are only a few examples of spectroscopic investigation of such metal-containing species.

On another tangent, the information presented in chapter 7 shows there are still many transition metal diatomic monocarbides, mononitrides, and monoxides not yet discovered and spectroscopically characterized. The search for these molecules must not be overlooked either. To twist the words of Frost, "there are miles to go before a spectroscopist may sleep."

Bibliography

1. A. Lagerqvist, H. Neuhaus, and R. Scullman, Arkiv Fys. **32**, 479 (1966).

2. B. Simard, P. A. Hackett, and W. J. Balfour, Chem. Phys. **230**, 103 (1994).

3. H. Lefebvre-Brion and R. W. Field, *Perturbations in the Spectra of Diatomic Molecules*, Academic Press, Orlando, 1986.

4. I. Shim, K. Mandix, and K. A. Gingerich, J. Mol. Structure (Theochemistry) **393**, 127 (1997).

5. N.N. Greenwood and A. Earnshaw, *The Chemistry of the Elements, 2nd Edition*, Butterworth-Heinemann, Boston, 1997.

6. M. Gerloch and E. C. Constable, *Transition Metal Chemistry- The Valence Shell in d-Block Chemistry*, VCH Publishers, New York, 1994.

7. F. A. Cotton and G. Wilkinson, *Advanced Inorganic Chemistry, 5th Edition*, John Wiley & Sons, New York, 1988.

8. F. R. Hartley, *Chemistry of the Platinum Group Metals : Recent Developments*, edited by Frank R. Hartley, Elsevier, New York, 1991.

9. R. C. West - editor, *CRC Handbook of Chemistry and Physics, 1st Student Edition*, CRC Press, Boca Raton, 1988.

10. M. A. Freeman and D. A. Young, Inorg. Chem. **25**, 1296 (1986).

11. http://www.healthestores.com/racer/armagbiom.html,. http://www.lycaeum.org/drugs

12. R. F. Wing, J. Cohen, and J. W. Brault, Astrophys.l J. **216**, 659 (1977).

13. R. E. S. Clegg and D. L. Lambert, Astrophys. J. **226**, 931 (1978).

14. A. J. Merer, C. M. Walmsley, and E. Churchwell, Astrophys. J. **256**, 151 (1982).

15. Y. Kasai, K. Obi, Y. Ohshima, Y. Endo, and K. Kawaguchi, J. Chem. Phys.**103**, 90 (1995).

16. K. Kawaguchi, E. Kagi, T. Hirano, S. Tahano, and S. Saito, Astrophys. J. **406**, L39 (1993).

17. L. M. Ziurys, A. J. Apponi, M. Guelin, and J. Cernicharo, Astrophys. J. **445**, L47 (1995).

18. NASA, *Instruments and Calibration*, 17 June 1999, <http://www.stsci.edu/instruments> (18 August, 1999).

19. W. J. Balfour, Astrophys. J. **162**, 1031 (1970).

20. A. Neuhaus, R. Scullman, and B. Yttermo, Z. Naturforsch. **20a**, 751 (1965).

21. G. Herzberg, *Molecular Spectra and Molecular Structure, I. Spectra of Diatomic Molecules, 2nd Edition*, D. Van Nostrand, New York, 1950.

22. J. I. Steinfeld, *Molecules and Radiation: An Introduction to Molecular Spectroscopy*, Harper and Row, New York, 1974.

23. P. F. Bernath, *Spectra of Atoms and Molecules*, Oxford University Press, 1995.

24. J. Graybeal, *Molecular Spectroscopy,* McGraw- Hill, New York, 1988.

25. G. W. King, *Spectroscopy and Molecular Structure,* Holt, Rinehart, and Winston, New York, 1964.

26. P. W. Atkins, *Physical Chemistry, 3rd Edition*, W. H. Freeman, New York, 1986.

27. Webster's Dictionary, Warner Books, 1984.

28. J. N. Demas, *Lifetimes of the Excited States*, Academic Press, New York, 1983.

29. W. McGucken, *Nineteenth-Century Spectroscopy: Development of the Understanding of Spectra*, John Hopkins Press, Baltimore, 1969.

30. D. E. Powers, S. G. Hansen, M. E. Geusic, D. L. Michalopoulas, and R. E. Smalley, J. Chem. Phys. **74**, 6511 (1981).

31. B. Simard, P. A. Hackett, and W. J. Balfour, Chem. Phys. Lett. **230**, 103 (1994).

32. D. Proch and T. Trickl, Rev. Sci. Instrum. **60**, 713 (1989).

33. C. X. W. Qian and J. Cao, University of Victoria, 1991.

34. B. Edlén, J. Opt. Soc. Am. **43**, 339 (1953).

35. J. L. Kinsey, Ann. Rev. Phys. Chem. **28**, 349 (1977).

36. W. Demtröder, *Laser Spectroscopy*, Springer, Berlin, 1982.

37. D. L. Andrews (Editor), *Applied Laser Spectroscopy: Techniques, Instrumentation, and Applications*, VCH, New York, 1992.

38. W. J. Balfour, C. X. W. Qian, and C. Zhou, J. Chem. Phys. **107**, 4473 (1997).

39. J. Cao, W. J. Balfour, and C. X. W. Qian, J. Phys. Chem. B **101**, 6741 (1997).

40. W. J. Balfour, J. Cao, C. V. V. Prasad, and C. X. W. Qian, J. Chem. Phys. **103**, 4046 (1995).

41. M. D. Allen, T. C. Pesch, and L. M. Ziurys, Ap. J. **472**, L57 (1996).

42. D. J. Brugh and M. D. Morse, J. Chem. Phys. **107**, 9772 (1997).

43. M. Barnes, A. J. Merer, and G. F. Metha, J. Chem. Phys **103**, 8360 (1995).

44. A. G. Adam and J. R. D. Peers, J. Mol. Spectrosc. **181**, 24 (1997).

45. M. D. Morse, personal communication.

46. G. H. Jeung and J. Koutecký, J. Chem. Phys. **88**, 3747 (1988).

47. R. G. A. R. Maclagan and G. E. Scuseria, Chem. Phys. Lett. **262**, 87 (1996).

48. C. W. Bauschlicher and P. E. M. Siegbahn, Chem. Phys. Lett. **104**, 331 (1984).

49. I. Shim and K. Gingerich, Int. J. Quantum. Chem. **23**, 409 (1989); I. Shim and K. Gingerich, Int. J. Quantum. Chem. **42**, 349 (1992); M. D. Hack, R. G. A. R. Maclagan, G. E. Scuseria, and M. S. Gordon, J. Chem. Phys. **104**, 6628 (1996).

50. I. Shim and K. Gingerich, European Phys. J. **D7**, 163 (1999)

51. I. Shim and K. Gingerich, Z. Phys. D **12**, 373 (1989).

52. B. Simard, P. A. Hackett, and W. J. Balfour, Chem. Phys. Lett. **230**, 103 (1994).

54. A. J. Merer, unpublished results.

55. B. Simard, P. I. Presunka, H. P. Loock, and A. Berces, J. Chem. Phys. **107**, 307 (1997).

54. D. J. Brugh, T. J. Ronningen, and M. D. Morse, J. Chem. Phys. **109**, 7851 (1998).

55. J. D. Langenberg, R. S. DaBell, L. Shao, D. Dreessen, and M. D. Morse, J. Chem. Phys. **109**, 7863 (1998).

56. J. D. Langenberg, L. Shao, and M. D. Morse, J. Chem. Phys. **111**, 4077 (1999).

57. B. Kaving and R. Scullman, J. Mol. Spectrosc. **32**, 475 (1969).

58. J. M. Brom, W. R. M. Graham, and W. Weltner, J. Chem. Phys. **57**, 4116 (1972).

59. I. Shim, M. Pelino, and K. Gingerich, J. Chem. Phys. **97**, 9240 (1992).

60. I. Shim and K. Gingerich, J. Chem. Phys. **106**, 8093 (1997).

61. P. Jackson, G. E. Gadd, D. W. Mackey, H. v. d. Wall, and G. D. Willett, J. Phys. Chem. **102**, 8941 (1998).

62. I. Shim, H. C. Finkbeiner, and K. Gingerich, J. Phys. Chem. **91**, 3171 (1987).

63. I. Shim and K. Gingerich, J. Chem. Phys. **76**, 3833 (1982).

64. I. Shim and K. Gingerich, Surf. Sci. **156**, 623 (1985).

65. G. Pacchioni, J. Koutecký, and P. Fantucci, Chem. Phys. Lett. **92**, 486 (1982).

66. N. Russo, J. Andzelm, and D. R. Salahub, Chem. Phys. **114**, 331 (1987).

67. H. Tan, D. Dai, and K. Balasubramanian, Chem. Phys. Lett. **286**, 375 (1998).

68. I. Shim and K. Gingerich, J. Chem. Phys. **81**, 5937 (1984).

69. H. Tan, M. Liao, and K. Balasubramanian, Chem. Phys. Lett. **280**, 423 (1997).

70. K. Jansson, R. Scullman, and B. Yttermo, Chem. Phys. Lett. **4**, 188 (1969).

71. K. Jansson and R. Scullman, J. Mol. Spectrosc. **36**, 248 (1970).

72. A. J. Marr, M. E. Flores, and T. C. Steimle, J. Chem. Phys. **104**, 8183 (1996).

73. H. Neuhaus, R. Scullman, and B. Yttermo, Z. Naturf. **20a**, 1962 (1965).

74. R. Scullman, and B. Yttermo, Arkiv. Fys., **25**, 95 (1963).

75. O. Appelblad, R. F. Barrow, and R. Scullman, Proc. R. Soc. London **91**, 261 (1967).

76. O. Appelblad, C. Nilsson, and R. Scullman, Phys. Scr. **7**, 65 (1973).

77. T. C. Steimle, K. Y. Jung, and B.-Z. Li, J. Chem. Phys. **102**, 5937 (1995).

78. T. C. Steimle, K. Y. Jung, and B.-Z. Li, J. Chem. Phys. **103**, 1767 (1995).

79. D. Majumbar and K. Balasubramanian, Chem. Phys. Lett. **284**, 273 (1998).

80. H. Tan, M. Liao, and K. Balasubramanian, Chem. Phys. Lett. **280**, 219 (1997).

81. R. Scullman and B. Thelin, Phys. Scr. **3**, 19 (1971).

82. R. Scullman and B. Thelin, Phys. Scr. **5**, 201 (1972).

83. L. B. Knight Jr. and W. Weltner, J. Chem. Phys. **53**, 4111 (1970).

84. A. J. Merer, Ann. Rev. Phys. Chem. **40**, 407 (1989).

85. R. S. Ram, J. Liévin, and P. F. Bernath, J. Chem. Phys.**109**, 6329 (1998).

86. H. W. Kroto, *Molecular Rotation Spectra*, John Wiley & Sons, New York, 1975.

87. M. J. Winter, *d-Block Chemistry*, Oxford University Press, New York, 1994.

88. R. S. Ram and P. F. Bernath, J. Chem. Phys. **96**, 6344 (1992).

89. A. E. Douglas and P. M. Veillette, J. Chem. Phys. **72**, 5378 (1980).

90. B. Simard, H. Niki, and P. A. Hackett, J. Chem. Phys. **92**, 7012 (1990).

91. C. Athénour, J. L. Féménias, and T. M. Dunn, Can. J. Phys. **60**, 109 (1982).

92. K. Brabaharan, J. A. Coxon, and A. B. Yamashita, Can. J. Phys. **63**, 997 (1985).

93. B. Simard, C. Masoni, and P. A. Hackett, J. Mol. Spectrosc. **136**, 44 (1989).

94. S. L. Peter and T. M. Dunn, J. Chem. Phys. **90**, 5333 (1989).

95. W. J. Balfour, A. J. Merer, H. Niki, B. Simard, and P. A. Hackett, J. Chem. Phys. **99**, 3288 (1993).

96. T. C. Steimle, J. S. Robinson, and D. Goodridge, J. Chem. Phys. **110**, 881 (1999).

97. W. J. Balfour, C. X. W. Qian, and C. Zhou, J. Chem. Phys. **106**, 4383 (1997).

98. L. Andrews, W.D. Bare, and G. V. Chertihin, J. Phys. Chem. **101**, 8417 (1997).

99. K. L. Kunze and J. F. Harrison, J. Am. Chem. Soc. **112**, 3812 (1990).

100. C. W. Bauschlicher, Chem. Phys. Lett. **100**, 515 (1983).

101. J. F. Harrison, J. Chem. Phys. **100**, 3513 (1996).

102. S. M. Mattar, J. Chem. Phys. **97**, 3171 (1993).

103. A. Fielder and S. Iwata, Chem. Phys. Lett. **271**, 143 (1997).

104. A. Daoudi, A. T. Benjelloun, J. P. Flament, and G. Berthier, J. Mol. Spectrosc. **194**, 8 (1999).

105. R. S. Ram and P. F. Bernath, J. Mol. Spectrosc. **165**, 97 (1994).

106. J. K. Bates and T. M. Dunn, Can. J. Phys. **54**, 1216 (1976).

107. C. M-T. Chan, H. Li, N. S-K. Sze, and A. S-C. Cheung, J. Mol. Spectrosc. **180**, 145 (1996).

108. C. M-T. Chan, H. Li., and A. S-C. Cheung, Chem. Phys. Lett. **269**, 49 (1997).

109. J-L. Féménias, C. Athénour, K. M. Rao, and T. M. Dunn, J. Mol. Spectros. **130**, 269 (1988).

110. Y. Azuma, G. Huang, M. P. J. Lyne, A. J. Merer, and V. I. Srdanov, J. Chem. Phys. **100**, 4318 (1994).

111. R. C. Carlson, J. K. Bates, and T. M. Dunn, J. Mol. Spectros. **110**, 215 (1985).

112. E. A. Pazyuk, E. N. Moskvitina, Y. Y. Kyzyakov, Spectros. Letts. **21**, 447 (1988).

113. D. A. Fletcher, K. J. Jung, and T. C. Steimle, J. Chem. Phys. **99**, 901 (1993).

114. K. J. Jung, D. A. Fletcher, and T. C. Steimle, J. Mol. Spectros. **165**, 448 (1994).

115. N. S-K. Sze, and A. S-C. Cheung, J. Mol. Spectros. **173**, 194 (1995).

116. I. Shim and K. A. Gingerich, Int. J. Quantum. Chem. **46**, 145 (1993).

117. S. R. Langhoff and C. W. Bauschlicher, J. Mol. Spectros. **143**, 169 (1990).

118. J. N. Allison and W. A. Goddard III, Chem. Phys. **81**, 263 (1983).

119. I. Shim, private communication.

120. R. S. Ram and P. F. Bernath, J. Mol. Spectros. **184**, 401 (1997).

121. J. K. Bates and D. M. Gruen, J. Chem. Phys. **70**, 4428 (1979).

122. R. S. Ram and P. F. Bernath, J. Opt. Soc. Am. B **11**, 225 (1994).

123. R. S. Ram, P. F. Bernath, W. J. Balfour, J. Cao, C. X. W. Qian, and S. J. Rixon., J. Mol. Spectros. **168**, 350 (1994).

124. W. J. Balfour, J. Cao, and C. X. W. Qian, J. Mol. Spectros. **183**, 113 (1997).

125. R. S. Ram and P. F. Bernath, J. Chem. Phys. **111**, 349 (1999).

126. T. C. Steimle, private communication.

127. T. C. Steimle, A. J. Marr, S. A. Beaton, and J. M. Brown, J. Chem. Phys. **106**, 2073 (1997).

128. R. S. Ram and P. F. Bernath, J. Mol. Spectros. **193**, 363 (1999).

129. E. J. Friedman-Hill and R. W. Field, J. Chem. Phys. **100**, 6141 (1994).

130. D. Dai and K. Balasubramanian, J. Mol. Spectros. **172**, 421 (1995).

131. G. V. Chertihin, L. Andrews, and M. Neurock J. Phys. Chem. **100**, 14609 (1996).

132. L. Andrews, A. Citra, G. V. Chertihin, and M. Neurock, J. Phys. Chem. A. **102**, 2561 (1998).

133. J. K. Bates and D. M. Gruen, J. Chem. Phys. **70**, 4428 (1979).

134. L. Andrews, private communication.

135. J. K. Bates and D. M. Gruen, High Temp. Sci. **10**, 27 (1978).

136. J. K. Bates and D. M. Gruen, J. Mol. Spectros. **78**, 284 (1979).

137. L. B. Knight and J. Steadman, J. Chem. Phys. **76**, 3378 (1982).

138. D. W. Green, W. Kormfmacher, and D. M. Gruen, J. Chem. Phys. **58**, 404 (1973).

139. X. Li, and L-S. Wang, J. Chem. Phys. **109**, 5264 (1998).

140. A. Citra and L. Andrews, J. Phys. Chem. **103**, 3410 (1999).

141. F. Illas, J. Rubio, J. Cañellas, and J. M. Ricart, J. Chem. Phys. **93**, 2603 (1990).

142. W. J. Balfour, J. Cao, and C. X. W. Qian, J. Mol. Spectros. **201**, 244 (2000).

143. C. E. Moore, *Atomic Energy Levels Vol. III, Natl. Stand., USA, Circ. No. 467* (U.S. GPO, Washington) 1971.

144. K.-P. Huber and G. Herzberg, *Constants of Diatomic Molecules,* Van Nostrand - Reinhold, New York, 1979.

145. C. X. W. Qian and C. Zhou, University of Victoria, 1997.

146. J. White and G. Mains; J. Phys. Chem., **95** 112 (1991).

147. A. G. Adam, Y. Azuma, J. A. Barry, G. Huang, P. J. Lyne, A. J. Merer, and J. O. Schröder, J. Chem. Phys. **86**, 5231 (1987).

148. J. H. Norman, H. G. Stanley, and W. E. Bell, J. Chem. Phys. **42**, 1123 (1965).

149. K. Jansson and R. Scullman, J. Mol. Spectros. **36**, 248 (1972).

150. P. E. M. Siegbahn, J. Phys. Chem. **99**, 12723 (1995).

151. P. B. Armentrout and R. Georgiadis, Polyhedron, **7**, 1573 (1988).

152. W. A. Nugent and J. M. Mayer, *Metal - Ligand Multiple Bonds*, John Wiley & Sons, New York, 1988.

153. W. J. Balfour, S. G. Fougère, R. F. Heuff, C. X. W. Qian, and C. Zhou, J. Mol. Spectros. **198**, 393 (1999).

154. S. G. Fougère, W. J. Balfour, J. Cao, and C. X. W. Qian, J. Mol. Spectros. **199**, 18 (2000).